Master's thesis

NTNU
Norwegian University of Science and Technology
Faculty of Natural Sciences
Department of Physics

Jostein Negård Kløgetvedt

Topological Magnon-Phonon Hybrid Excitations and Hall Effects in Two-Dimensional Ferromagnets

Master's thesis in Applied Physics and Mathematics
Supervisor: Alireza Qaiumzadeh
June 2023

NTNU
Norwegian University of
Science and Technology

Jostein Negård Kløgetvedt

Topological Magnon-Phonon Hybrid Excitations and Hall Effects in Two-Dimensional Ferromagnets

Master's thesis in Applied Physics and Mathematics
Supervisor: Alireza Qaiumzadeh
June 2023

Norwegian University of Science and Technology
Faculty of Natural Sciences
Department of Physics

Preface

This master's thesis concludes my five-year study program, leading to a Master of Science degree in Applied Physics and Mathematics at the Norwegian University of Science and Technology. Throughout this project, I have thoroughly enjoyed the process and gained valuable knowledge along the way. It has provided me with a profound understanding of the challenges involved in navigating through a vast sea of information. I would like to thank my supervisor, Alireza Qaiumzadeh, for his invaluable guidance and insightful direction throughout this journey. His expertise and mentorship have been crucial in shaping and enriching my research experience. I would also like to express my gratitude to my friends and family for their encouragement and constant support.

Abstract

The interactions between magnons and phonons, which are fundamental excitations in magnetically ordered materials, have been the subject of intense investigation. It has been found that these interactions can give rise to magnon-polarons that can modify the system's topology, leading to intriguing transport phenomena. In this study, our focus is on examining magnons, phonons, and their interactions in a two-dimensional (2D) ferromagnetic (FM) honeycomb layer. A comprehensive topological analysis of the interacting bands is conducted, considering various magnetization directions. The interactions stem from different sources, including magnetic anisotropy and the in-plane Dzyaloshinskii-Moriya interaction (DMI), with the latter arising from mirror symmetry breaking.

The findings of this study reveal that the interactions between magnons and phonons have notable effects on the system's topology when the magnetization is perpendicular to the lattice plane and the initial magnon bands possess nontrivial topology. Specifically, the interactions induce Berry curvature at the avoided crossings between magnon and phonon bands, leading to a weak renormalization of the thermal Hall conductivity and the spin Nernst coefficient. On the other hand, when the magnetization lies in the plane and the initial bands are topologically trivial, the magnon-phonon interactions arising from anisotropy and in-plane nearest neighbour DMI result in a vanishing Berry curvature. However, the in-plane next-nearest neighbour DMI induces Berry curvature at the anticrossing regions. In this scenario, the transport properties are influenced by the magnetization direction within the plane. Particularly, a nonzero conductivity is observed in the $\hat{\boldsymbol{x}}$-direction, while the $\hat{\boldsymbol{y}}$-direction exhibits a vanishing conductivity due to the balanced distribution of Berry curvature, resulting in topologically trivial magnon-polaron bands. In contrast, a nonzero spin Nernst coefficient is observed in all magnetization directions examined.

Oppsummering

Mye forskning har hatt til hensikt å undersøke vekselvirkningene mellom magnoner og fononer, som utgjør fundamentale eksitasjoner i magnetisk ordnede materialer. Forskningsfunnene tyder på at disse vekselvirkningene kan danne magnon-polaroner, som i sin tur kan påvirke systemets topologi og føre til interessante transportfenomener. I denne studien er fokuset rettet mot undersøkelsen av magnoner, fononer og deres samspill i et todimensjonalt ferromagnetisk honeycombgitter. En grundig topologisk analyse av de interagerende båndene utføres med varierende magnetiseringsretninger tatt i betraktning. Vekselvirkningene har ulike kilder, inkludert magnetisk anisotropi og den planære Dzyaloshinskii-Moriya-vekselvirkningen, der sistnevnte oppstår som følge av symmetribrytelse av speilrefleksjonssymmetri.

Resultatene av denne studien avdekker at vekselvirkningene mellom magnoner og fononer har betydelige effekter på systemets topologi når magnetiseringen står vinkelrett på gitterplanet og de opprinnelige magnonbåndene har en ikke-triviell topologi. Spesifikt fører disse vekselvirkningene til uvikling av Berry-kurvatur ved unngåtte kryssinger mellom magnon- og fononbånd, som resulterer i en svak endring av den termiske Hall-konduktiviteten og spinn-Nernst-koeffisienten. Når magnetiseringen derimot ligger i gitterplanet og de opprinnelige båndene har en triviell topologi, fører de magnon-fonon vekselvirkningene som oppstår fra anisotropi og den planære Dzyaloshinskii-Moriya-vekselvirkningen for nærmeste naboer til en forsvinnende Berry-kurvatur. Imidlertid induserer den planære Dzyaloshinskii-Moriya-vekselvirkningen for nest nærmeste naboer Berry-kurvatur ved områder med antikryssinger. I dette tilfelle påvirkes transportegenskapene av magnetiseringsretningen i gitterplanet. Spesielt observeres en ikke-null konduktivitet i $\hat{\boldsymbol{x}}$-retningen, mens $\hat{\boldsymbol{y}}$-retningen viser en forsvinnende konduktivitet på grunn av en balansert fordeling av Berry-kurvatur, noe som resulterer i topologisk trivielle magnon-polaronbånd. Til forskjell observeres en ikke-null spinn-Nernst-koeffisient i alle undersøkte magnetiseringsretninger.

Contents

CHAPTER 1

Introduction

Phonons and magnons have been extensively studied since their discovery and are well-established concepts in the field of condensed matter physics. Phonons describe the collective modes of lattice vibrations and are useful in understanding thermal properties such as specific heat capacity and thermal conductivity in materials [1–3]. On the other hand, magnons are associated with deviations from the magnetic ordering in a material and provide a valuable model for, among other things, temperature-dependent magnetization in ferro- and antiferromagnetic materials at low temperatures [3, 4].

In the wake of the isolation of graphene in 2004 [5], a new class of 2D physics has emerged, presenting unique properties that require a revision of existing theories for crystalline systems with infinitesimal thickness [6]. While several models for 3D materials can also be applied to 2D materials, the latter have flexural out-of-plane vibration modes with a quadratic dispersion instead of the linear relation predicted by 3D models, as established in the theory of elasticity [6, 7]. In magnetic systems, the Mermin-Wagner theorem postulates that two-dimensional isotropic materials with only short-range interactions cannot have magnetic ordering at nonzero temperatures [8]. Nonetheless, magnetic ordering can be achieved by introducing anisotropy into the system [6, 9]. Van der Waals magnets (vdW magnets), which consists of covalently bonded layers and possess intrinsic magnetocrystalline anisotropy, provide an excellent platform for exploring magnetically ordered materials in the 2D limit [10]. Recent studies have provided evidence for magnetic ordering in 2D sheets derived from van der Waals materials, such as in the chromium trihalide CrI_3 [6, 10, 11]. As two-dimensional vdW magnets are sensitive to external stimuli such as electric fields, strain, and proximity effects, they are potential candidates to be used in spintronics devices such as sensors and memory [9, 11].

After the discovery of two-dimensional magnets, much attention has been focused on identifying and investigating materials that display topological spin excitations [12–14]. Such materials are characterized by unique edge modes that are resistant to external disturbances [15], making them particularly promising for potential use in dissipationless spintronics [13, 16]. Furthermore, topological materials are likely to exhibit Hall effects, including the magnon-mediated thermal Hall effect and spin Nernst effect, which may be present in topological magnon insulators [16]. These transport phenomena are significant because they provide a means of examining and comprehending the low-energy excitations of the materials [17]. Indeed, thermal Hall effects attributed to magnons and phonons, which can also display topological excitations, have been demonstrated [18, 19].

A polaron is a quasiparticle that emerges from the interaction of a charged particle with the lattice of a material [3]. Similarly, magnons and phonons can also be coupled in a way that gives rise to a hybridized magnon-polaron state. Recent studies have shown that this coupling exists in various materials, including bcc Fe [20], the insulating ferrimagnet yttrium iron garnet [21] and the antiferromagnetic monolayer $FePSe_3$ [22]. Understanding how stable magnons and phonons interact to affect the properties of solids is of great interest. Particularly, spin-lattice coupling plays a crucial role in comprehending the phonon-driven spin-Seebeck effect, the coupling between ferromagnetic and ferroelectric order parameters in multiferroic materials, and also enables the exploration of new concepts in spin-calorics [23, 24]. Additionally, the interaction can shed light on effects such as magnetostriction,

spin damping and magnon transport [25].

Much research has been devoted to investigating how the interaction between magnons and phonons can either produce nontrivial topological bands from trivial magnon and phonon bands, or strengthen the already existing topology. This is because Berry curvature, which is essential in displaying nontrivial topological bands, can be generated at the gap openings between magnon and phonon branches in the presence of interactions [18, 26]. The resulting Berry curvature contributes to the thermal Hall and spin Nernst effect. Studies have been conducted on two-dimensional square, honeycomb, triangular, and kagome lattices with different magnetic orderings [18, 19, 22, 26–29]. Moreover, it has been demonstrated that topological magnon-polaron bands can arise in the presence of magnetic interactions such as dipolar interaction [30], Dzyaloshinskii-Moriya interaction [18, 26, 28], magnetic anisotropy [27, 29], Heisenberg exchange interaction [19] and Kitaev interaction [22]. Due to the small wavelengths achievable in the hybridized magnon-phonon system, which can be as small as the atomic unit cell, it holds promising potential for applications in compact topological devices [22].

This thesis aims to develop a microscopic theory for spin-waves and lattice vibrations, as well as their interactions, in two-dimensional magnetic systems. The initial part of the thesis is a review of prior work on the square and honeycomb lattices, examining both ferro- and antiferromagnetic ordering of the spins. Chapter 2 and 3 introduce phonons and magnons, respectively, and provide a calculation of their dispersion. In Chapter 4, these two systems are combined to investigate the hybrid magnon-phonon energy spectrum and compare with previous results. The latter part of the thesis focuses on the ferromagnetic honeycomb lattice, specifically modifying the magnon dispersion for an arbitrary direction of the magnetization and exploring the effects of various magnetic exchange interactions in Chapter 6. Chapter 7 examines the magnetoelastic energy spectrum, where the hybridization arises from both magnetic anisotropy and Dzyaloshinskii-Moriya interaction, with a focus on the topological aspects of the bands introduced in Chapter 5. The results are compared for various magnetization directions and coupling terms, and a discussion of the thermal Hall conductivity and the spin Nernst coefficient in the different systems is given. Finally, Chapter 8 summarizes the findings of the thesis.

Some sections of this thesis are included to enhance the understanding of the underlying theory and may not have a direct impact on the final results. Furthermore, this thesis is a continuation of the specialization project report, which is concluded by the first part of the thesis. However, it should be noted that certain sections might have been revised in the final thesis.

Part I.

Microscopic Theory of Magnons, Phonons, and Their Interactions: An Introduction

CHAPTER 2

Phonons

To analyze the properties of a solid, it is essential to establish its geometric structure, which is known as the crystal lattice. The crystal lattice consists of arrays of lattice sites where the atoms lie when the specimen is in its ground state. This is a simplified picture as a real material can have impurities, vacant sites and grain boundaries [2]. A crystal is divided into geometrically identical unit cells that are connected through discrete translations, giving rise to the complete crystal structure. The position $\boldsymbol{R}$ of each unit cell is

$$\boldsymbol{R} = n_1\boldsymbol{a}_1 + n_2\boldsymbol{a}_2 + n_3\boldsymbol{a}_3,$$

where $\{n_1, n_2, n_3\}$ are integer numbers and $\{\boldsymbol{a}_1, \boldsymbol{a}_2, \boldsymbol{a}_3\}$ are the primitive lattice vectors. When a crystal lattice's unit cell contains multiple atoms, the organization of these atoms is determined by a group of vectors called the basis [2]. These vectors indicate the locations of each atom within the unit cell.

Atoms within lattices experience vibrations around their equilibrium positions due to thermal energy. The opposing forces that maintain the lattice structure originate from the chemical bonds between the atoms [31]. To establish a mathematical model for lattice dynamics, it is advantageous to replace the individual particle model with a collective model. This is appropriate because when a single atom is perturbed from its ground state, the energy quickly spreads throughout the lattice through interactions between the atoms, resulting in collective vibrations [31]. Within this description, it is possible to quantize the lattice vibrations, resulting in the emergence of fundamental excitations known as phonons. From this perspective, the lattice can be seen as a volume containing a 'gas' of phonons [2]. Phonons exhibit similar quantum behaviour to other particles, but the concept of assigning a conventional mass to phonons is not applicable [32]. The classical counterpart of phonons is represented by normal modes, which are single-frequency oscillations and form the basis for lattice vibrations.

In 1907, Einstein was the pioneer in introducing the concept of quantized lattice vibrations when he calculated the specific heat capacity in diamond [1]. The term 'phonon' was coined by J. Frenkel in 1932, drawing inspiration from the photon [32]. The word 'phonon' originates from the ancient Greek word for sound, highlighting the association with sound waves.

Phonons can be divided into two categories based on the atomic motion within the lattice: acoustic and optical [2]. Optical phonons are present in lattices with multiple atoms in the basis and exhibit asymmetric motion among the atoms. In the case of an ionic crystal, the asymmetry creates an electric dipole moment that can interact with the electromagnetic field, hence the name "optical". On the other hand, acoustic phonons involve symmetric atomic motion. In the case of longitudinal vibrations and in the limit of long wavelengths, acoustic phonons correspond to sound waves. The total number of eigenmodes, or branches, in a lattice depends on the number of atoms in the basis and the number of dimensions in which the atoms can move. In a lattice with a r-atomic basis and atoms capable of moving in d dimensions, there are a total of dr branches. Among these branches, d correspond to acoustic phonons while the remaining $dr - d$ are optical phonons [3].

2.1. Classical equation of motion

In order to determine the lattice dynamics, it is theoretically necessary to account for both the effects of the nuclei and the electrons. However, due to the much slower movement of the nuclei compared to the electrons, an approximation can be made by considering the electrons to be in their ground state for every nuclear position [2, 4]. This approximation, known as the adiabatic approximation, allows us to focus solely on the motion of the nuclei or ions in the following calculations.

Furthermore, we adopt the Born-von Karman model and impose a periodic boundary condition on the wavefunctions. This assumption is based on the idea that the bulk properties of the material remain unaffected by the chosen boundary condition [4]. The periodic boundary condition restricts the wavevector to certain allowed values, and the number of allowed values within the primitive cell of the reciprocal lattice is equal to the number of unit cells in the crystal. In the limit of a large sample, the wavevector can be considered approximately continuous.

Let us consider a lattice consisting of ions, with N_{uc} unit cells. The equilibrium position for each ion is given by $\boldsymbol{R}_{i\alpha} = \boldsymbol{R}_i + \boldsymbol{R}_\alpha$, where $\boldsymbol{R}_i$ is a vector pointing to a reference point inside the ith unit cell, and $\boldsymbol{R}_\alpha$ is the vector pointing to the αth ion within the unit cell. For a lattice with an r-atomic basis, the indices can take values $i = 1, \dots, N_{\text{uc}}$ and $\alpha = 1, \dots, r$. The instantaneous position vector of an ion is denoted as $\boldsymbol{r}_{i\alpha}(t) = \boldsymbol{R}_{i\alpha} + \boldsymbol{u}_{i\alpha}(t)$, where $\boldsymbol{u}_{i\alpha}(t)$ represents the displacement of the ion at time t. The Hamiltonian, which represents the total energy of the ions as a function of their positions and momenta, can be expressed as follows [33]

$$\mathcal{H} = T + V = \sum_{i,\alpha} \left(\frac{\boldsymbol{p}_{i\alpha}^2}{2M_\alpha} + \sum_{\substack{j,\beta \\ j,\beta \neq i,\alpha}} V(\boldsymbol{r}_{i\alpha} - \boldsymbol{r}_{j\beta}) \right),$$

where M_α is the mass of the αth ion in the unit cell. Classically, the momentum is given by $\boldsymbol{p}_{i\alpha} = \dot{\boldsymbol{r}}_{i\alpha} M_\alpha = \dot{\boldsymbol{u}}_{i\alpha} M_\alpha$ where the dot denotes the time-derivative. As small vibrations of the ions are expected, $|\boldsymbol{u}_{i\alpha}| << a$ (where a is the lattice constant), we can Taylor expand the potential $V(\boldsymbol{r}_{i\alpha} - \boldsymbol{r}_{j\beta})$ around the equilibrium position $\boldsymbol{R}_{i\alpha} - \boldsymbol{R}_{j\beta}$. The expansion is done as [2]

$$\sum_{\substack{j,\beta \\ j,\beta \neq i,\alpha}} V(\boldsymbol{r}_{i\alpha} - \boldsymbol{r}_{j\beta}) \approx \sum_{\substack{j,\beta \\ j,\beta \neq i,\alpha}} \left(V(\boldsymbol{R}_{i\alpha} - \boldsymbol{R}_{j\beta}) + \sum_\mu \frac{\partial V}{\partial R_{i\alpha\mu}} u_{i\alpha\mu} + \frac{1}{2} \sum_{\mu,\nu} \frac{\partial^2 V}{\partial R_{i\alpha\mu} \partial R_{j\beta\nu}} u_{i\alpha\mu} u_{j\beta\nu} \right).$$

The index $\mu = x, y, \dots$ denotes the spatial components of the vectors in $d-$dimensions and the first and second derivatives of the potential are evaluated at equilibrium. The termination of higher order terms in the expansion of the potential is called the harmonic approximation [31]. The first term yields a constant contribution and can be discarded in the following. The second term is the force on the $i\alpha$th ion that, by definition, is zero in equilibrium. We are left with the last term which may be written compactly as

$$\frac{1}{2} \sum_{\substack{i,\alpha,\mu \\ j,\beta,\nu}} \frac{\partial^2 V}{\partial R_{i\alpha\mu} \partial R_{j\beta\nu}} u_{i\alpha\mu} u_{j\beta\nu} = \frac{1}{2} \sum_{\substack{i,\alpha,\mu \\ j,\beta,\nu}} \Phi_{\mu\nu}^{\alpha\beta}(\boldsymbol{R}_j - \boldsymbol{R}_i) u_{i\alpha\mu} u_{j\beta\nu}.$$

The coefficient $\Phi_{\mu\nu}^{\alpha\beta}(\boldsymbol{R}_j - \boldsymbol{R}_i)$ is the force coefficient between the $i\alpha$th ion in the μth direction due to a displacement of the $j\beta$th ion in the νth direction. Note that we included the $i = j$ and $\alpha = \beta$ term in the summation, which introduces self-force coefficients that will be further explained below.

Due to translational invariance, the force coefficients depend only on the relative distance between the unit cells. Moreover, the second derivatives are symmetric under an interchange of indices and satisfy $\Phi^{\alpha\beta}_{\mu\nu}(\boldsymbol{R}_j - \boldsymbol{R}_i) = \Phi^{\beta\alpha}_{\nu\mu}(\boldsymbol{R}_i - \boldsymbol{R}_j)$. With these modifications, the Hamiltonian may be written

$$\mathcal{H} = \frac{1}{2}\sum_{i,\alpha,\mu} M_\alpha \dot{u}^2_{i\alpha\mu} + \frac{1}{2}\sum_{\substack{i,\alpha,\mu \\ j,\beta,\nu}} \Phi^{\alpha\beta}_{\mu\nu}(\boldsymbol{R}_j - \boldsymbol{R}_i) u_{i\alpha\mu} u_{j\beta\nu}. \tag{2.1}$$

From Newton's equation, the equation of motion is [31]

$$M_\alpha \ddot{u}_{i\alpha\mu} = -\frac{\partial V}{\partial u_{i\alpha\mu}} = -\sum_{j,\beta,\nu} \Phi^{\alpha\beta}_{\mu\nu}(\boldsymbol{R}_j - \boldsymbol{R}_i) u_{j\beta\nu}, \tag{2.2}$$

for each $i\alpha\mu$ set of indices, making a total of drN_{uc} equations. The harmonic nature of the equation motivates the search for harmonic plane wave solutions. We use the ansatz

$$u_{i\alpha\mu}(t) = \frac{1}{\sqrt{M_\alpha}} c_{\alpha\mu} \mathrm{e}^{\mathrm{i}(\boldsymbol{q}\cdot\boldsymbol{R}_{i\alpha} - \omega t)},$$

where $c_{\alpha\mu}$ is the amplitude, $\boldsymbol{q}$ is the wavevector in reciprocal space and ω is a frequency. By substituting the given expression into the equation of motion, it results in the following

$$\begin{aligned} -\sqrt{M_\alpha}\omega^2 c_{\alpha\mu}\mathrm{e}^{\mathrm{i}(\boldsymbol{q}\cdot\boldsymbol{R}_{i\alpha} - \omega t)} &= -\sum_{j,\beta,\nu} \Phi^{\alpha\beta}_{\mu\nu}(\boldsymbol{R}_j - \boldsymbol{R}_i) \frac{1}{\sqrt{M_\beta}} c_{\beta\nu}\mathrm{e}^{\mathrm{i}(\boldsymbol{q}\cdot\boldsymbol{R}_{j\beta} - \omega t)} \\ \implies \omega^2 c_{\alpha\mu} &= \sum_{j,\beta,\nu} \frac{1}{\sqrt{M_\alpha M_\beta}} \Phi^{\alpha\beta}_{\mu\nu}(\boldsymbol{R}_j - \boldsymbol{R}_j)\mathrm{e}^{\mathrm{i}\boldsymbol{q}\cdot(\boldsymbol{R}_{j\beta} - \boldsymbol{R}_{i\alpha})} c_{\beta\nu}. \end{aligned}$$

Let us denote the relative distance between the unit cells by $\boldsymbol{\Delta}_{\text{uc}} = \boldsymbol{R}_j - \boldsymbol{R}_i$ and $\boldsymbol{\Delta} = \boldsymbol{R}_{j\beta} - \boldsymbol{R}_{i\alpha}$ as the vector between two ions. Changing the summation index from j to Δ_{uc} and defining $D^{\alpha\beta}_{\mu\nu}(\boldsymbol{\Delta}_{\text{uc}}) = (M_\alpha M_\beta)^{-\frac{1}{2}} \Phi^{\alpha\beta}_{\mu\nu}(\boldsymbol{\Delta}_{\text{uc}})$, the equation of motion may be written [31]

$$\begin{aligned} \omega^2 c_{\alpha\mu} &= \sum_{\beta,\nu} c_{\beta\nu} \sum_{\Delta_{\text{uc}}} D^{\alpha\beta}_{\mu\nu}(\boldsymbol{\Delta}_{\text{uc}})\mathrm{e}^{\mathrm{i}\boldsymbol{q}\cdot\boldsymbol{\Delta}} \\ \implies \omega^2 c_{\alpha\mu} &= \sum_{\beta,\nu} D^{\alpha\beta}_{\mu\nu}(\boldsymbol{q}) c_{\beta\nu}, \quad D^{\alpha\beta}_{\mu\nu}(\boldsymbol{q}) = \sum_{\Delta_{\text{uc}}} D^{\alpha\beta}_{\mu\nu}(\boldsymbol{\Delta}_{\text{uc}})\mathrm{e}^{\mathrm{i}\boldsymbol{q}\cdot\boldsymbol{\Delta}}, \\ \implies \sum_{\beta,\nu} &\left[D^{\alpha\beta}_{\mu\nu}(\boldsymbol{q}) - \omega^2 \delta_{\alpha,\beta}\delta_{\mu,\nu}\right] c_{\beta\nu} = 0. \end{aligned} \tag{2.3}$$

The number of drN_{uc} equations is now reduced to a set of dr equations. Writing the equation in matrix form, the system of equations has nontrivial solutions if and only if ω^2 satisfies the equation [34]

$$\det\left(D(\boldsymbol{q}) - \omega^2 I\right) = 0. \tag{2.4}$$

$D(\boldsymbol{q})$ is the dynamical matrix with dimensions $dr \times dr$, I is the identity matrix with the same dimensions and the notation $\det(\cdot)$ indicates the determinant of the matrix. The dynamical matrix is Hermitian. This can be shown by noting that $D(\boldsymbol{\Delta}_{\text{uc}})$ is a real symmetric matrix and that taking the transpose of the neighbouring vector $\boldsymbol{\Delta}$ yields a sign change such that

$$(D^{\alpha\beta}_{\mu\nu}(\boldsymbol{q}))^\dagger = \sum_{\Delta_{\text{uc}}} (D^{\alpha\beta}_{\mu\nu}(\boldsymbol{\Delta}_{\text{uc}}))^\dagger (\mathrm{e}^{-\mathrm{i}\boldsymbol{q}\cdot\boldsymbol{\Delta}})^* = \sum_{\Delta_{\text{uc}}} D^{\alpha\beta}_{\mu\nu}(\boldsymbol{\Delta}_{\text{uc}})\mathrm{e}^{\mathrm{i}\boldsymbol{q}\cdot\boldsymbol{\Delta}} = D^{\alpha\beta}_{\mu\nu}(\boldsymbol{q}).$$

In general, a $n \times n$ Hermitian matrix has n orthonormal eigenvectors and is always diagonalizable by an unitary matrix [34]. Equation (2.4) is an eigenvalue problem with solutions $\omega_\lambda^2(\boldsymbol{q})$, $\lambda = 1, \ldots, dr$, and each eigenvalue has a corresponding eigenvector $\boldsymbol{c}^\lambda(\boldsymbol{q})$. The frequency $\omega_\lambda(\boldsymbol{q})$ is called the dispersion for eigenmode λ. The normalized eigenvectors are denoted by $\hat{\boldsymbol{e}}^\lambda(\boldsymbol{q})$ and the unitary matrix that diagonalizes $D(\boldsymbol{q})$ is on the form $U_{\text{ph}}(\boldsymbol{q}) = [\hat{\boldsymbol{e}}^1(\boldsymbol{q}), \ldots, \hat{\boldsymbol{e}}^{dr}(\boldsymbol{q})]$ where each $\hat{\boldsymbol{e}}^\lambda(\boldsymbol{q})$ is a column vector. The normalized eigenvectors are orthonormal and fulfill the relation

$$\begin{aligned} &\hat{\boldsymbol{e}}^{\lambda *}(\boldsymbol{q}) \cdot \hat{\boldsymbol{e}}^{\lambda'}(\boldsymbol{q}) = \sum_{\alpha,\mu} e_{\alpha\mu}^{\lambda *}(\boldsymbol{q}) e_{\alpha\mu}^{\lambda'}(\boldsymbol{q}) = \delta_{\lambda,\lambda'}, \\ &\text{or in matrix notation } U_{\text{ph}}^\dagger(\boldsymbol{q}) U_{\text{ph}}(\boldsymbol{q}) = I. \end{aligned} \tag{2.5}$$

Note that the number of different $\omega_\lambda(\boldsymbol{q})$ is drN_{uc} since there are dr eigenvalues of the dynamical matrix and the wavevector can take N_{uc} values in the Brillouin zone. This is equal to the number of internal degrees of freedom in the crystal.

2.2. Derivation of the quantized phonon Hamiltonian

The goal is to represent the harmonic Hamiltonian, as shown in equation (2.1), using bosonic operators, effectively quantizing the Hamiltonian. By denoting $Q_\lambda(\boldsymbol{q}, t)$ as the normal coordinate, the displacement can be expressed as a linear combination of the eigenvectors on the form [31]

$$u_{i\alpha\mu}(t) = \frac{1}{\sqrt{N_{\text{uc}} M_\alpha}} \sum_{q,\lambda} Q_\lambda(\boldsymbol{q}, t) e_{\alpha\mu}^\lambda(\boldsymbol{q}) \mathrm{e}^{\mathrm{i}\boldsymbol{q}\cdot\boldsymbol{R}_{i\alpha}}, \tag{2.6}$$

where the temporal part of the normal coordinate is $\mathrm{e}^{-\mathrm{i}\omega_\lambda(\boldsymbol{q})t}$. The inverse relation can be found by noting that $\sum_\lambda M_\alpha^{-\frac{1}{2}} Q_\lambda(\boldsymbol{q}, t) e_{\alpha\mu}^\lambda(\boldsymbol{q}) = u_{q\alpha\mu}(t)$ is the spatial Fourier-transformed of $u_{i\alpha\mu}(t)$. In matrix notation, this equation translates to $\text{diag}(1/\sqrt{M_\alpha}) U \boldsymbol{Q}(\boldsymbol{q}, t) = \boldsymbol{u}_q(t)$, where $\text{diag}(\cdot)$ denotes a diagonal matrix and the matrix elements $1/\sqrt{M_\alpha}$ correspond to the components of $\boldsymbol{u}_q$ which belongs to the αth ion in the unit cell. The inverse relation is then

$$\begin{aligned} &\boldsymbol{Q}(\boldsymbol{q}, t) = U^\dagger \text{diag}(\sqrt{M_\alpha}) \boldsymbol{u}_q(t), \\ \implies &Q_\lambda(\boldsymbol{q}, t) = \sum_{\alpha,\mu} M_\alpha^{\frac{1}{2}} e_{\alpha\mu}^{\lambda *}(\boldsymbol{q}) \tilde{u}_{q\alpha\mu}(t) = \frac{1}{\sqrt{N_{\text{uc}}}} \sum_{i,\alpha,\mu} M_\alpha^{\frac{1}{2}} e_{\alpha\mu}^{\lambda *}(\boldsymbol{q}) u_{i\alpha\mu}(t) \mathrm{e}^{-\mathrm{i}\boldsymbol{q}\cdot\boldsymbol{R}_{i\alpha}}. \end{aligned}$$

The displacement in real space, $u_{i\alpha\mu}(t)$, is a real quantity. This leads to the following restrictions for the normal coordinates and eigenvectors [31]

$$e_{\alpha\mu}^{\lambda *}(\boldsymbol{q}) = e_{\alpha\mu}^\lambda(-\boldsymbol{q}), \quad Q_\lambda^*(\boldsymbol{q}, t) = Q_\lambda(-\boldsymbol{q}, t). \tag{2.7}$$

These relations will be useful later on. Inserting the expression for $u_{i\alpha\mu}(t)$, equation (2.6), the first term in the harmonic Hamiltonian transforms to

$$\frac{1}{2} \sum_{i,\alpha,\mu} M_\alpha u_{i\alpha\mu}^2(t) = \frac{1}{2} \sum_{i,\alpha,\mu} \frac{1}{N_{\text{uc}}} \sum_{\substack{q,q' \\ \lambda,\lambda'}} \dot{Q}_\lambda(\boldsymbol{q}, t) \dot{Q}_{\lambda'}(\boldsymbol{q}', t) e_{\alpha\mu}^\lambda(\boldsymbol{q}) e_{\alpha\mu}^{\lambda'}(\boldsymbol{q}') \mathrm{e}^{\mathrm{i}(\boldsymbol{q}+\boldsymbol{q}')\cdot\boldsymbol{R}_{i\alpha}}.$$

With the help of the relation

$$\frac{1}{N_{\mathrm{uc}}}\sum_{i}\mathrm{e}^{\mathrm{i}\boldsymbol{q}\cdot\boldsymbol{R}_i}=\delta(\boldsymbol{q}), \tag{2.8}$$

a delta function appears, $\delta(\boldsymbol{q}+\boldsymbol{q'})$, which in combination with equation (2.7), yields

$$\begin{aligned}&\frac{1}{2}\sum_{\alpha,\mu}\sum_{q,\lambda,\lambda'}\dot{Q}_\lambda(\boldsymbol{q},t)\dot{Q}^*_{\lambda'}(\boldsymbol{q},t)e^{\lambda}_{\alpha\mu}(\boldsymbol{q})e^{\lambda'*}_{\alpha\mu}(\boldsymbol{q})\\ =&\frac{1}{2}\sum_{q,\lambda,\lambda'}\dot{Q}_\lambda(\boldsymbol{q},t)\dot{Q}^*_{\lambda'}(\boldsymbol{q},t)\delta_{\lambda,\lambda'}=\frac{1}{2}\sum_{q,\lambda}\dot{Q}_\lambda(\boldsymbol{q},t)\dot{Q}^*_{\lambda}(\boldsymbol{q},t),\end{aligned}$$

where we also used the orthonormality relation of the eigenvectors. In a similar fashion, the second term in the harmonic Hamiltonian transforms to

$$\begin{aligned}&\frac{1}{2}\sum_{\substack{i,\alpha,\mu\\ j,\beta,\nu}}\Phi^{\alpha\beta}_{\mu\nu}(\boldsymbol{\Delta}_{\mathrm{uc}})u_{i\alpha\mu}(t)u_{j\beta\nu}(t)\\ =&\frac{1}{2}\sum_{\substack{i,\alpha,\mu\\ j,\beta,\nu}}\Phi^{\alpha\beta}_{\mu\nu}(\boldsymbol{\Delta}_{\mathrm{uc}})\frac{1}{N_{\mathrm{uc}}}\sum_{\substack{q,q'\\ \lambda,\lambda'}}\frac{1}{\sqrt{M_\alpha M_\beta}}Q_\lambda(\boldsymbol{q},t)Q_{\lambda'}(\boldsymbol{q'},t)e^{\lambda}_{\alpha\mu}(\boldsymbol{q})e^{\lambda'}_{\beta\nu}(\boldsymbol{q'})\mathrm{e}^{\mathrm{i}(\boldsymbol{q}\cdot\boldsymbol{R}_{i\alpha}+\boldsymbol{q'}\cdot\boldsymbol{R}_{j\beta})}\\ =&\frac{1}{2}\sum_{\substack{q,q'\\ \lambda,\lambda'}}\sum_{\substack{\alpha,\mu\\ \beta,\nu}}\left\{\frac{1}{N_{\mathrm{uc}}}\sum_{i}\mathrm{e}^{\mathrm{i}(\boldsymbol{q}+\boldsymbol{q'})\cdot\boldsymbol{R}_i}\right\}Q_\lambda(\boldsymbol{q},t)Q_{\lambda'}(\boldsymbol{q'},t)e^{\lambda}_{\alpha\mu}(\boldsymbol{q})e^{\lambda'}_{\beta\nu}(\boldsymbol{q'})\sum_{\Delta_{\mathrm{uc}}}D^{\alpha\beta}_{\mu\nu}(\boldsymbol{\Delta}_{\mathrm{uc}})\mathrm{e}^{\mathrm{i}(\boldsymbol{q}\cdot\boldsymbol{R}_\alpha+\boldsymbol{q'}\cdot(\boldsymbol{R}_\beta+\boldsymbol{\Delta}_{\mathrm{uc}}))}\\ =&\frac{1}{2}\sum_{q,\lambda,\lambda'}\sum_{\substack{\alpha,\mu\\ \beta,\nu}}Q_\lambda(\boldsymbol{q},t)Q^*_{\lambda'}(\boldsymbol{q},t)e^{\lambda}_{\alpha\mu}(\boldsymbol{q})e^{\lambda'}_{\beta\nu}(-\boldsymbol{q})D^{\alpha\beta}_{\mu\nu}(-\boldsymbol{q}).\end{aligned}$$

The summation variables over the unit cells were changed from (i,j) to (i,Δ_{uc}) in order to employ relation (2.8). To move forward, note that the eigenvectors solve the equation of motion, equation (2.3). This can be combined with the time-reversal symmetry of the dispersion, $\omega_\lambda(\boldsymbol{q})=\omega_\lambda(-\boldsymbol{q})$ [31], such that the following useful relation appears

$$\sum_{\beta,\nu}D^{\alpha\beta}_{\mu\nu}(-\boldsymbol{q})e^{\lambda'}_{\beta\nu}(-\boldsymbol{q})=\omega^2_{\lambda'}(-\boldsymbol{q})e^{\lambda'}_{\alpha\mu}(-\boldsymbol{q})=\omega^2_{\lambda'}(\boldsymbol{q})e^{\lambda'*}_{\alpha\mu}(\boldsymbol{q}).$$

By using this relation, we are left with

$$\frac{1}{2}\sum_{q,\lambda,\lambda'}\omega^2_{\lambda'}(\boldsymbol{q})Q_\lambda(\boldsymbol{q},t)Q^*_{\lambda'}(\boldsymbol{q},t)\sum_{\alpha,\mu}e^{\lambda}_{\alpha\mu}(\boldsymbol{q})e^{\lambda'*}_{\alpha\mu}(\boldsymbol{q})=\frac{1}{2}\sum_{q,\lambda}\omega^2_{\lambda}(\boldsymbol{q})Q_\lambda(\boldsymbol{q},t)Q^*_{\lambda}(\boldsymbol{q},t).$$

Thus, in terms of the normal coordinate, the total Hamiltonian is on the the simple form

$$\mathcal{H}=\frac{1}{2}\sum_{q,\lambda}\left(\dot{Q}^2_\lambda(\boldsymbol{q},t)+\omega^2_\lambda(\boldsymbol{q})Q^2_\lambda(\boldsymbol{q},t)\right),$$

and the corresponding Lagrangian is

$$L=T-V=\frac{1}{2}\sum_{q,\lambda}\left(\dot{Q}^2_\lambda(\boldsymbol{q},t)-\omega^2_\lambda(\boldsymbol{q})Q^2_\lambda(\boldsymbol{q},t)\right).$$

The Hamiltonian may be expressed in terms of canonical variables. The canonical momentum is easily verified to be

$$P_\lambda(\boldsymbol{q},t)=\frac{\partial L}{\partial \dot{Q}_\lambda(\boldsymbol{q},t)}=\dot{Q}^*_\lambda(\boldsymbol{q},t)=\sum_{i,\alpha,\mu}\frac{1}{\sqrt{N_{\mathrm{uc}}M_\alpha}}e^\lambda_{\alpha\mu}(\boldsymbol{q})p_{i\alpha\mu}(t)\mathrm{e}^{\mathrm{i}\boldsymbol{q}\cdot\boldsymbol{R}_{i\alpha}}.$$

From the theory of quantum mechanics, the canonical variables should satisfy the commutation relation $[u_{i\alpha\mu},p_{j\beta\nu}]=\mathrm{i}\hbar\delta_{i,j}\delta_{\alpha,\beta}\delta_{\mu,\nu}$ [35]. We verify that $Q_\lambda(\boldsymbol{q})$ and $P_\lambda(\boldsymbol{q})$ are canonical variables by computing the commutator. The time-dependency is suppressed for compact notation.

$$\begin{aligned}[Q_\lambda(\boldsymbol{q}),P_{\lambda'}(\boldsymbol{q'})]=&\frac{1}{N_{\mathrm{uc}}}\sum_{\substack{i,\alpha,\mu\\j,\beta,\nu}}\sqrt{\frac{M_\alpha}{M_\beta}}e^{\lambda*}_{\alpha\mu}(\boldsymbol{q})e^{\lambda'}_{\beta\nu}(\boldsymbol{q'})[u_{i\alpha\mu},p_{j\beta\nu}]\mathrm{e}^{\mathrm{i}(\boldsymbol{q'}\cdot\boldsymbol{R}_{j\beta}-\boldsymbol{q}\cdot\boldsymbol{R}_{i\alpha})}\\=&\frac{\mathrm{i}\hbar}{N_{\mathrm{uc}}}\sum_{i,\alpha,\mu}e^{\lambda*}_{\alpha\mu}(\boldsymbol{q})e^{\lambda'}_{\alpha\mu}(\boldsymbol{q'})\mathrm{e}^{\mathrm{i}(\boldsymbol{q'}-\boldsymbol{q})\cdot\boldsymbol{R}_{i\alpha}}\\=&\mathrm{i}\hbar\delta(\boldsymbol{q}-\boldsymbol{q'})\sum_{\alpha,\mu}e^{\lambda*}_{\alpha\mu}(\boldsymbol{q})e^{\lambda'}_{\alpha\mu}(\boldsymbol{q})=\mathrm{i}\hbar\delta(\boldsymbol{q}-\boldsymbol{q'})\delta_{\lambda,\lambda'}.\end{aligned}$$

The Hamiltonian is now reduced to a set of drN_{uc} uncoupled harmonic oscillators [31]

$$\mathcal{H}=\frac{1}{2}\sum_{q,\lambda}\left(P^2_\lambda(\boldsymbol{q})+\omega^2_\lambda(\boldsymbol{q})Q^2_\lambda(\boldsymbol{q})\right).$$

The quantization procedure for harmonic oscillators is well known. By introducing the creation and annihilation operators $c^\dagger_\lambda(\boldsymbol{q})$ and $c_\lambda(\boldsymbol{q})$, defined by

$$c_\lambda(\boldsymbol{q})=\frac{1}{\sqrt{2\hbar\omega_\lambda(\boldsymbol{q})}}\left(\omega_\lambda(\boldsymbol{q})Q_\lambda(\boldsymbol{q})+\mathrm{i}P^*_\lambda(\boldsymbol{q})\right),\quad c^\dagger_\lambda(\boldsymbol{q})=\frac{1}{\sqrt{2\hbar\omega_\lambda(\boldsymbol{q})}}\left(\omega_\lambda(\boldsymbol{q})Q^*_\lambda(\boldsymbol{q})-\mathrm{i}P_\lambda(\boldsymbol{q})\right),$$

we may compute the quantity $c^\dagger_\lambda(\boldsymbol{q})c_\lambda(\boldsymbol{q})$

$$\begin{aligned}c^\dagger_\lambda(\boldsymbol{q})c_\lambda(\boldsymbol{q})=&\frac{1}{2\hbar\omega_\lambda(\boldsymbol{q})}\left[\omega^2_\lambda(\boldsymbol{q})Q^2_\lambda(\boldsymbol{q})+P^2_\lambda(\boldsymbol{q})+\mathrm{i}\omega_\lambda(\boldsymbol{q})\left(Q^*_\lambda(\boldsymbol{q})P^*_\lambda(\boldsymbol{q})-P_\lambda(\boldsymbol{q})Q_\lambda(\boldsymbol{q})\right)\right]\\=&\frac{\mathcal{H}_\lambda(\boldsymbol{q})}{\hbar\omega_\lambda(\boldsymbol{q})}+\frac{\mathrm{i}}{2\hbar}\left(P_\lambda(-\boldsymbol{q})Q_\lambda(-\boldsymbol{q})-P_\lambda(\boldsymbol{q})Q_\lambda(\boldsymbol{q})\right)-\frac{1}{2}\\\implies\mathcal{H}_\lambda(\boldsymbol{q})=&\hbar\omega_\lambda(\boldsymbol{q})\left(c^\dagger_\lambda(\boldsymbol{q})c_\lambda(\boldsymbol{q})+\frac{1}{2}\right)+\frac{\mathrm{i}\omega_\lambda(\boldsymbol{q})}{2}\left(P_\lambda(\boldsymbol{q})Q_\lambda(\boldsymbol{q})-P_\lambda(-\boldsymbol{q})Q_\lambda(-\boldsymbol{q})\right),\end{aligned}$$

where $\mathcal{H}=\sum_{q,\lambda}\mathcal{H}_\lambda(\boldsymbol{q})$. The summation over q is symmetric, which means that there is a $-q$ for every q, so the last term vanishes. We are then left with the phonon Hamiltonian [31]

$$\mathcal{H}=\sum_{q,\lambda}\hbar\omega_\lambda(\boldsymbol{q})\left(c^\dagger_\lambda(\boldsymbol{q})c_\lambda(\boldsymbol{q})+\frac{1}{2}\right).\tag{2.9}$$

The operator $\hat{n}_\lambda(\boldsymbol{q})=c^\dagger_\lambda(\boldsymbol{q})c_\lambda(\boldsymbol{q})$ is commonly referred to as the number operator. It possesses the property of counting the number of phonon excitations in mode λ, corresponding to a specific $\boldsymbol{q}$ value [35]. Each mode is associated with an energy $\varepsilon_\lambda(\boldsymbol{q})=\hbar\omega_\lambda(\boldsymbol{q})$, where $\omega^2_\lambda(\boldsymbol{q})$ are the eigenvalues of the dynamical matrix and represents the phonon energy spectrum. The total energy in the crystal resulting from lattice vibrations, for a given $\boldsymbol{q}$, is determined by summing the product of the number of phonons in a mode and the energy of that mode across all modes. In this picture, the many-particle state can be represented in the occupation number basis as $|n(\boldsymbol{q})\rangle=|n_1(\boldsymbol{q}),\ldots,n_\lambda(\boldsymbol{q}),\ldots\rangle$, where

$n_\lambda(\boldsymbol{q})$ denotes the number of particles in mode λ [35]. The creation operator $c_\lambda^\dagger(\boldsymbol{q})$ adds a particle to mode λ, while the annihilation operator removes a particle from the same mode. Expressing the Hamiltonian in this manner is commonly known as the second quantized formalism.

Depending on the nature of the creation and annihilation operators, the particles can either be bosons or fermions following Bose-Einstein or Fermi-Dirac statistics. In the case of phonon excitations, they are found to exhibit bosonic behaviour as the operators satisfy the commutation relation $[c_\lambda(\boldsymbol{q}), c_{\lambda'}^\dagger(\boldsymbol{q'})] = \delta(\boldsymbol{q}-\boldsymbol{q'})\delta_{\lambda,\lambda'}$. This implies that each state in the lattice vibration spectrum can accommodate an arbitrary number of phonons, and the phonon occupation in each mode is determined by the system's energy [31]. The commutation relation can be verified by

$$\begin{aligned}[c_\lambda(\boldsymbol{q}), c_{\lambda'}^\dagger(\boldsymbol{q'})] =& \frac{1}{2\hbar\sqrt{\omega_\lambda(\boldsymbol{q})\omega_{\lambda'}(\boldsymbol{q'})}}\left(-\mathrm{i}\omega_\lambda(\boldsymbol{q})[Q_\lambda(\boldsymbol{q}), P_{\lambda'}(\boldsymbol{q'})] + \mathrm{i}\omega_{\lambda'}(\boldsymbol{q'})[P_\lambda^*(\boldsymbol{q}), Q_{\lambda'}^*(\boldsymbol{q'})]\right) \\ =& \frac{1}{2\hbar\sqrt{\omega_\lambda(\boldsymbol{q})\omega_{\lambda'}(\boldsymbol{q'})}}(\omega_\lambda(\boldsymbol{q})\hbar\delta(\boldsymbol{q}-\boldsymbol{q'})\delta_{\lambda,\lambda'} + \omega_{\lambda'}(\boldsymbol{q'})\hbar\delta(\boldsymbol{q}-\boldsymbol{q'})\delta_{\lambda,\lambda'}) = \delta(\boldsymbol{q}-\boldsymbol{q'})\delta_{\lambda,\lambda'}.\end{aligned}$$

For later use, it is useful to write the ionic displacement $u_{i\alpha\mu}$ in terms of the bosonic operators. This is done by observing that

$$Q_\lambda(\boldsymbol{q}) = \sqrt{\frac{\hbar}{2\omega_\lambda(\boldsymbol{q})}}(c_\lambda(\boldsymbol{q}) + c_\lambda^\dagger(-\boldsymbol{q})),$$

such that

$$u_{i\alpha\mu} = \sum_{q,\lambda}\sqrt{\frac{\hbar}{2N_{\mathrm{uc}}M_\alpha\omega_\lambda(\boldsymbol{q})}}(c_\lambda(\boldsymbol{q}) + c_\lambda^\dagger(-\boldsymbol{q}))e_{\alpha\mu}^\lambda(\boldsymbol{q})\mathrm{e}^{\mathrm{i}\boldsymbol{q}\cdot\boldsymbol{R}_{i\alpha}}, \tag{2.10}$$

from the definition of the displacement in equation (2.6). By reinstating the temporal dependency, the bosonic operators behave as $c_\lambda(\boldsymbol{q},t) = c_\lambda(\boldsymbol{q},0)\mathrm{e}^{-\mathrm{i}\omega_\lambda(\boldsymbol{q})t}$.

2.3. Calculation of phonon dispersion

As discussed in section 2.1, calculating the phonon eigenmodes involves analyzing the lattice geometry and finding the eigenvalues of the dynamical matrix. In this study, our objective is to determine the phonon dispersion in two-dimensional square and honeycomb lattices. In these lattices, the ions are free to move in three dimensions, namely the x, y and z directions, while the lattice itself lies in the xy-plane. We include interactions up to third nearest neighbours, which is shown to yield accurate results in the honeycomb lattice [36], and consider limitations set by the symmetry of the lattice. For the sake of notation, we let $\Phi_{\mu\nu}^{\alpha\beta}(\boldsymbol{\Delta}_{\mathrm{uc}}) \to \Phi_{\mu\nu}^{\alpha\beta}(\boldsymbol{\Delta})$, knowing that $\boldsymbol{\Delta}$ is the vector connecting the neighbouring ions. This clarifies which pair of ions the force coefficient is associated with. In this notation, the elements in the dynamical matrix are

$$D_{\mu\nu}^{\alpha\beta}(\boldsymbol{q}) = \sum_{\Delta_{\mathrm{uc}}}\frac{1}{\sqrt{M_\alpha M_\beta}}\Phi_{\mu\nu}^{\alpha\beta}(\boldsymbol{\Delta})\mathrm{e}^{\mathrm{i}\boldsymbol{q}\cdot\boldsymbol{\Delta}}. \tag{2.11}$$

The lattice sheet has infinitesimal translational symmetry, for instance under the transformation $u_{i\alpha\mu} \to u_{i\alpha\mu} + a_\mu$. It follows that [37]

$$\sum_{j,\beta} \Phi_{\mu\nu}^{\alpha\beta}(\boldsymbol{\Delta}) = 0, \tag{2.12}$$

which is referred to as the stability condition. This can be seen by inserting the expression in the equation of motion (equation (2.2))

$$\begin{aligned} M_\alpha \ddot{u}_{i\alpha\mu} &= -\sum_{j,\beta,\nu} \Phi_{\mu\nu}^{\alpha\beta}(\boldsymbol{\Delta})(u_{j\beta\nu} + a_\nu) \\ \implies &\sum_\nu a_\nu \left(\sum_{j,\beta} \Phi_{\mu\nu}^{\alpha\beta}(\boldsymbol{\Delta}) \right) = 0 \\ \implies &\sum_{j,\beta} \Phi_{\mu\nu}^{\alpha\beta}(\boldsymbol{\Delta}) = 0, \end{aligned}$$

since the size of a_ν is arbitrary. The stability condition is used to find expressions for the self-force coefficients, the force coefficients where $\Phi_{\mu\nu}^{\alpha\alpha}(\boldsymbol{\Delta} = 0)$.

In addition, the lattice sheet has a mirror symmetry under $z \to -z$ [37]. The energy should be invariant under this transformation. Investigating the lattice deviation coupling terms in the Hamiltonian, equation (2.1), it implies that there can be no coupling between the in-plane and out-of-plane modes. As an example, $\Phi_{zx}^{\alpha\beta}(\boldsymbol{\Delta}) \to \Phi_{-zx}^{\alpha\beta}(\boldsymbol{\Delta}) = -\Phi_{zx}^{\alpha\beta}(\boldsymbol{\Delta})$, so in order for the energy terms to be invariant, all $\Phi_{zx}^{\alpha\beta}(\boldsymbol{\Delta})$ coefficients must be zero. This applies for all pairs of indices $\{\mu, z\}$ where $\mu = x, y$. Therefore, the phonon eigenmodes can either exist purely within the plane or extend out of the plane.

2.3.1. Square lattice

Considering a monoatomic square lattice, with a single atom in the basis, the (α, β) indices vanish. The square lattice is shown in Figure 2.1a where the primitive lattice vectors, with length a, coincide with $\boldsymbol{\delta}_1$ and $\boldsymbol{\delta}_2$ in the figure. We expect to find three acoustic branches, one for each spatial dimension. Each ion has four nearest neighbours, four next-nearest neighbours and four third nearest neighbours. The vectors $\boldsymbol{\Delta}$ connecting to the first, second and third nearest neighbours are labeled by

$$\begin{aligned} 1^{\text{st}}: &\quad \boldsymbol{\delta}_{1(3)} = \pm a\hat{\boldsymbol{x}}, && \boldsymbol{\delta}_{2(4)} = \pm a\hat{\boldsymbol{y}}, \\ 2^{\text{nd}}: &\quad \boldsymbol{\tau}_{1(3)} = \pm a(\hat{\boldsymbol{x}} + \hat{\boldsymbol{y}}), && \boldsymbol{\tau}_{2(4)} = \pm a(-\hat{\boldsymbol{x}} + \hat{\boldsymbol{y}}), \\ 3^{\text{rd}}: &\quad \boldsymbol{\upsilon}_{1(3)} = \pm 2a\hat{\boldsymbol{x}}, && \boldsymbol{\upsilon}_{2(4)} = \pm 2a\hat{\boldsymbol{y}}, \end{aligned} \tag{2.13}$$

and visualized in Figure 2.1a. The reciprocal lattice vectors $\boldsymbol{b}_1 = (2\pi/a)\hat{\boldsymbol{q}}_x$ and $\boldsymbol{b}_2 = (2\pi/a)\hat{\boldsymbol{q}}_y$ span the reciprocal lattice. This is illustrated in Figure 2.1b where also the first Brillouin zone and the symmetry points are shown. The symmetry points are given by $\Gamma = (0, 0)$, $X = (\pi/a, 0)$ and $M = (\pi/a, \pi/a)$.

Due to the mirror symmetry $z \to -z$, the dynamical matrix $D(\boldsymbol{q})$ can be written on the form

$$D(\boldsymbol{q}) = \begin{bmatrix} D_{xx}(\boldsymbol{q}) & D_{xy}(\boldsymbol{q}) & 0 \\ D_{yx}(\boldsymbol{q}) & D_{yy}(\boldsymbol{q}) & 0 \\ 0 & 0 & D_{zz}(\boldsymbol{q}) \end{bmatrix},$$

in the basis $[x, y, z]^T$.

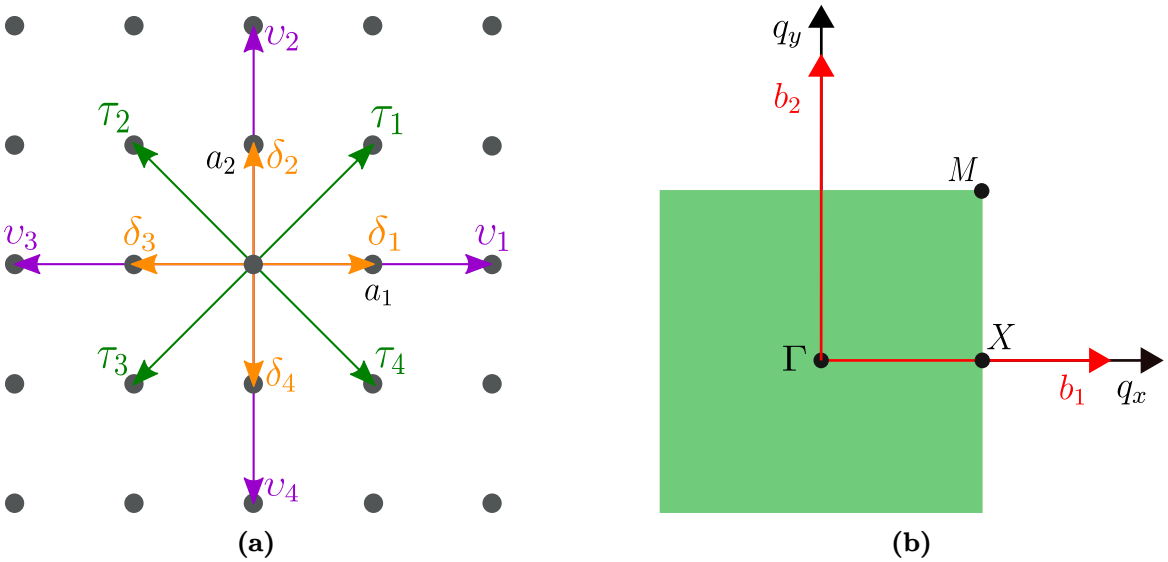

Figure 2.1.: The square lattice is illustrated in Figure 2.1a where the vectors to the first $\boldsymbol{\delta}$, second $\boldsymbol{\tau}$ and third $\boldsymbol{\upsilon}$ nearest neighbours are also shown. The first Brillouin zone, the marked green area, is visualized in Figure 2.1b, along with the symmetry points and the reciprocal lattice vectors.

Symmetry conditions are utilized to determine the independent force coefficients up to third nearest neighbours. First, a gentle reminder that the force coefficients are symmetric with respect to an interchange of indices, $\Phi_{\mu\nu}(\boldsymbol{\Delta}) = \Phi_{\nu\mu}(-\boldsymbol{\Delta})$. The square lattice possesses σ_x and σ_y mirror symmetries. This implies that the lattice remains unchanged under transformations of $(x, y) \to (-x, y)$ and $(x, y) \to (x, -y)$, respectively. Consequently, it follows that $\Phi_{\mu\nu}(\boldsymbol{\Delta}) = -\Phi_{\mu\nu}(\sigma_x\boldsymbol{\Delta})$ for $\mu \neq \nu$, and $\Phi_{\mu\nu}(\boldsymbol{\Delta}) = \Phi_{\mu\nu}(\sigma_x\boldsymbol{\Delta})$ for $\mu = \nu$. The same applies to σ_y. As a result, all $\Phi_{xy}(\boldsymbol{\Delta})$ values are zero except when $\boldsymbol{\Delta}$ belongs to the set $\{\boldsymbol{\tau}_1, \boldsymbol{\tau}_2, \boldsymbol{\tau}_3, \boldsymbol{\tau}_4\}$.

Furthermore, the square lattice also exhibits a four fold rotational symmetry, denoted as R_4, around the z-axis. The lattice can be rotated by an angle of $\phi = \pm\pi/2$ through transformations of $(x, y) \to (-y, x)$ and $(x, y) \to (y, -x)$. Therefore, we have the relations $\Phi_{xx}(\boldsymbol{\Delta}) = \Phi_{yy}(R_4\boldsymbol{\Delta})$ and the same holds true for interchanging x and y. Additionally, the force coefficients $\Phi_{zz}(\boldsymbol{\Delta}) = \Phi_{zz}(R_4\boldsymbol{\Delta})$ satisfy the rotational symmetry. When combined with the mirror symmetries, we find that $\Phi_{xx}(\boldsymbol{\tau}_i) = \Phi_{yy}(\boldsymbol{\tau}_j)$ for all $i, j = 1, 2, 3, 4$. Consequently, there are nine independent force coefficients, which are denoted by

$$
\begin{aligned}
\gamma_1 &= \Phi_{xx}(\boldsymbol{\delta}_1), & \gamma_2 &= \Phi_{yy}(\boldsymbol{\delta}_1), & \gamma_z &= \Phi_{zz}(\boldsymbol{\delta}_1),\\
\rho_1 &= \Phi_{xy}(\boldsymbol{\tau}_1), & \rho_2 &= \Phi_{xx}(\boldsymbol{\tau}_1), & \rho_z &= \Phi_{zz}(\boldsymbol{\tau}_1),\\
\eta_1 &= \Phi_{xx}(\boldsymbol{\upsilon}_1), & \eta_2 &= \Phi_{yy}(\boldsymbol{\upsilon}_1), & \eta_z &= \Phi_{zz}(\boldsymbol{\upsilon}_1).
\end{aligned}
$$

The stability condition, equation (2.12), yields

$$
\begin{aligned}
\Phi_{xx}(0) = \Phi_{yy}(0) &= -2(\gamma_1 + \gamma_2 + 2\rho_2 + \eta_1 + \eta_2),\\
\Phi_{zz}(0) &= -4(\gamma_z + \rho_z + \eta_z),
\end{aligned}
$$

and $\Phi_{xy}(0) = \Phi_{yx}(0) = 0$. To compute the matrix elements in the dynamical matrix, we employ equation (2.11), and find

$$
\begin{aligned}
D_{xx}(\boldsymbol{q}) = &\Big[\Phi_{xx}(0) + \Phi_{xx}(\boldsymbol{\delta}_1)(\mathrm{e}^{\mathrm{i}\boldsymbol{q}\cdot\boldsymbol{\delta}_1} + \mathrm{e}^{\mathrm{i}\boldsymbol{q}\cdot\boldsymbol{\delta}_3}) + \Phi_{xx}(\boldsymbol{\delta}_2)(\mathrm{e}^{\mathrm{i}\boldsymbol{q}\cdot\boldsymbol{\delta}_2} + \mathrm{e}^{\mathrm{i}\boldsymbol{q}\cdot\boldsymbol{\delta}_4}) + \Phi_{xx}(\boldsymbol{\tau}_1)(\mathrm{e}^{\mathrm{i}\boldsymbol{q}\cdot\boldsymbol{\tau}_1} + \\
&\mathrm{e}^{\mathrm{i}\boldsymbol{q}\cdot\boldsymbol{\tau}_2} + \mathrm{e}^{\mathrm{i}\boldsymbol{q}\cdot\boldsymbol{\tau}_3} + \mathrm{e}^{\mathrm{i}\boldsymbol{q}\cdot\boldsymbol{\tau}_4}) + \Phi_{xx}(\boldsymbol{\upsilon}_1)(\mathrm{e}^{\mathrm{i}\boldsymbol{q}\cdot\boldsymbol{\upsilon}_1} + \mathrm{e}^{\mathrm{i}\boldsymbol{q}\cdot\boldsymbol{\upsilon}_3}) + \Phi_{xx}(\boldsymbol{\upsilon}_2)(\mathrm{e}^{\mathrm{i}\boldsymbol{q}\cdot\boldsymbol{\upsilon}_2} + \mathrm{e}^{\mathrm{i}\boldsymbol{q}\cdot\boldsymbol{\upsilon}_4})\Big]/M \\
= &\frac{2}{M}[\gamma_1(\cos(q_x a) - 1) + \gamma_2(\cos(q_y a) - 1) + 2\rho_2(\cos(q_x a)\cos(q_y a) - 1) + \\
&2\eta_1(\cos^2(q_x a) - 1) + 2\eta_2(\cos^2(q_y a) - 1)].
\end{aligned}
$$

The same expression is obtained for $D_{yy}(\boldsymbol{q})$ where $\gamma_1 \leftrightarrow \gamma_2$ and $\eta_1 \leftrightarrow \eta_2$. Next, the $D_{xy}(\boldsymbol{q})$ matrix element is given by

$$
\begin{aligned}
D_{xy}(\boldsymbol{q}) &= \Big[\Phi_{xy}(\boldsymbol{\tau}_1)(\mathrm{e}^{\mathrm{i}\boldsymbol{q}\cdot\boldsymbol{\tau}_1} + \mathrm{e}^{\mathrm{i}\boldsymbol{q}\cdot\boldsymbol{\tau}_3}) + \Phi_{xx}(\boldsymbol{\tau}_2)(\mathrm{e}^{\mathrm{i}\boldsymbol{q}\cdot\boldsymbol{\tau}_2} + \mathrm{e}^{\mathrm{i}\boldsymbol{q}\cdot\boldsymbol{\tau}_4})\Big]/M \\
&= -\frac{4\rho_1}{M}\sin(q_x a)\sin(q_y a).
\end{aligned}
$$

By noting that $\Phi_{xy}(\boldsymbol{\tau}_i) = \Phi_{yx}(\boldsymbol{\tau}_i)$, we can establish that $D_{yx}(\boldsymbol{q}) = D_{xy}(\boldsymbol{q})$. The remaining out-of-plane matrix element is

$$
\begin{aligned}
D_{zz}(\boldsymbol{q}) = &[2\gamma_z(\cos(q_x a) + \cos(q_y a) - 2) + 4\rho_z(\cos(q_x a)\cos(q_y a) - 1) + \\
&4\eta_z(\cos^2(q_x a) + \cos^2(q_y a) - 2)\Big]/M.
\end{aligned}
$$

We can directly identify that the out-of-plane eigenvalue is $\omega_{\mathrm{ZA}} = \sqrt{D_{zz}(\boldsymbol{q})}$, and its corresponding eigenvector is $\hat{\boldsymbol{e}}^{\mathrm{ZA}} = [0, 0, 1]^T$. By renaming the in-plane matrix elements as $\mathcal{A} = D_{xx}(\boldsymbol{q})$, $\mathcal{B} = D_{xy}(\boldsymbol{q})$ and $\mathcal{C} = D_{yy}(\boldsymbol{q})$, we obtain the in-plane eigenvalues

$$
\begin{aligned}
\omega_{\mathrm{TA}} &= \frac{1}{\sqrt{2}}(\mathcal{A} + \mathcal{C} - \mathcal{D})^{1/2}, \\
\omega_{\mathrm{LA}} &= \frac{1}{\sqrt{2}}(\mathcal{A} + \mathcal{C} + \mathcal{D})^{1/2}, \\
\mathcal{D} &= \sqrt{(\mathcal{A} - \mathcal{C})^2 + 4\mathcal{B}^2},
\end{aligned}
$$

and the corresponding eigenvectors are

$$
\begin{aligned}
\hat{\boldsymbol{e}}^{\mathrm{TA}} &= \frac{1}{\sqrt{(\mathcal{A} - \mathcal{C} - \mathcal{D})^2 + 4\mathcal{B}^2}}[\mathcal{A} - \mathcal{C} - \mathcal{D}, 2\mathcal{B}, 0]^T, \\
\hat{\boldsymbol{e}}^{\mathrm{LA}} &= \frac{1}{\sqrt{(\mathcal{A} - \mathcal{C} + \mathcal{D})^2 + 4\mathcal{B}^2}}[\mathcal{A} - \mathcal{C} + \mathcal{D}, 2\mathcal{B}, 0]^T.
\end{aligned}
$$

By examining the dispersion along the symmetry line $\Gamma \to X$, where $q_y = 0$, the eigenfrequencies simplify to $\omega_{\mathrm{LA}} = \sqrt{D_{xx}(\boldsymbol{q})}$ and $\omega_{\mathrm{TA}} = \sqrt{D_{yy}(\boldsymbol{q})}$, and the eigenvectors are $\hat{\boldsymbol{e}}^{\mathrm{LA}} = [1, 0, 0]^T$ and $\hat{\boldsymbol{e}}^{\mathrm{TA}} = [0, 1, 0]^T$. Therefore, the LA mode exhibits **L**ongitudinal oscillations, while the TA mode exhibits **T**ransverse oscillations, which explains their respective names. The ZA branch indicates that it corresponds to the out-of-plane mode. All of these branches are classified as **A**coustic branches since their frequencies approach zero at the Γ-point, indicating their association with acoustic waves in the material.

It is widely known that in 2D crystals, the out-of-plane vibrations (flexural modes) exhibit a quadratic dispersion law in the long wavelength limit [6, 38]. This behaviour emerges due to the rotational and reflection symmetry of the crystal plane, which is distinct from the linear dispersion observed among transverse and longitudinal in-plane phonons [38]. The quadratic dispersion is a consequence of the zero Young modulus of the lattice sheet, indicating the absence of regular phonons propagating in this flexible medium and the presence of flexural waves instead [7]. This unique quadratic dispersion has notable consequences, such as the divergence of the number of phonons at nonzero temperatures in the long-wavelength limit [6]. However, the behaviour of 2D materials is influenced by their surroundings, including the substrate they are placed on, which dampens the oscillations and causes the dispersion to become increasingly linear with an increase in the number of layers [6]. Expanding the out-of-plane frequency around the $\Gamma-$point using a Taylor series, we obtain the lowest-order dependence on q

$$\omega_{\mathrm{ZA}}(\boldsymbol{q}) \approx \sqrt{\frac{-(\gamma_z + 2\rho_z + 4\eta_z)}{M}}|q|a.$$

The condition of a quadratic dispersion can be enforced by tuning the out-of-plane force coefficients such that the linear term vanishes.

Figure 2.2 illustrates the dimensionless dispersion plotted along the symmetry lines $\Gamma \to X$, $X \to M$ and $M \to \Gamma$ within the Brillouin zone. The dispersion is presented in units of $\sqrt{|\gamma_1|/M}$ with the following toy parameters as force coefficients

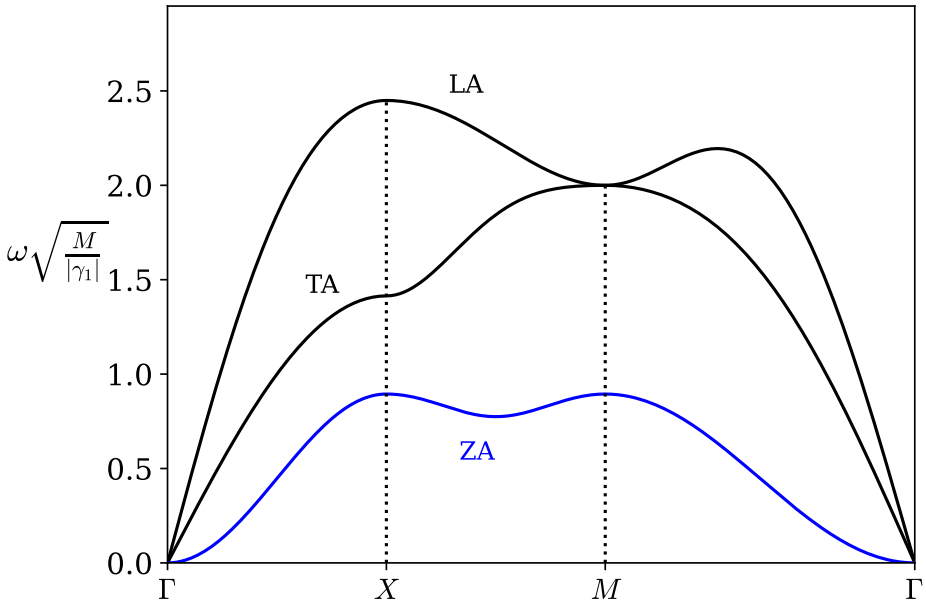

Figure 2.2.: The three acoustic branches of the phonon dispersion in a square lattice, longitudinal (LA), transverse (TA) and out-of-plane (ZA), are shown along the symmetry lines of the Brillouin zone. The frequency is given in units of $\sqrt{|\gamma_1|/M}$ and the values of the force coefficients are given in equation (2.14).

$$\begin{aligned} \rho_1 &= \rho_2 = \gamma_1/4, & \gamma_z &= \gamma_1/10, \\ \gamma_2 &= \eta_2 = 0, & \rho_z &= \gamma_1/20, \\ \eta_1 &= \gamma_1/10, & \eta_z &= -\gamma_1/20, \end{aligned} \tag{2.14}$$

where $\gamma_1 = -|\gamma_1|$ is a negative quantity. Note that η_z is positive in order to satisfy the requirement of a quadratic dispersion for the out-of-plane phonon mode. The degeneracy observed among the in-plane branches at the M point is a result of the preservation of reflection and rotational symmetries in the system.

The initial calculations were performed using a basic spring force model that considers only directional forces. The details and outcomes of these calculations can be found in Appendix A.1. The result obtained in this section are more comprehensive and reduce to the spring force model as a special case when certain conditions are met, specifically $\gamma_2 = 0$, $\rho_1 = \rho_2$, and the absence of third neighbour interactions. The dispersion is also depicted in the appendix, utilizing force coefficients that are approximately consistent with the values mentioned in this section.

2.3.2. Honeycomb lattice

The honeycomb lattice being examined consists of identical ions and can be divided into two sublattices: A and B. In other words, it has a two-atomic basis. The structure of the honeycomb lattice is depicted in Figure 2.3a. The primitive lattice vectors coincide with $\boldsymbol{\tau}_1^A$ and $\boldsymbol{\tau}_3^A$ in the figure and have a length of $a = a_0\sqrt{3}$, where a_0 represents the interatomic distance. We expect to find three acoustic and three optical branches. Each ion has three nearest neighbours, six next-nearest neighbours and three third nearest neighbours. The vectors $\boldsymbol{\Delta}$ connecting to the first, second and third nearest neighbours are labeled by

$$\begin{aligned} 1^{\text{st}}: \quad & \boldsymbol{\delta}_1^A = \frac{a}{\sqrt{3}}\hat{\boldsymbol{y}}, & \boldsymbol{\delta}_2^A &= -a\left(\frac{1}{2}\hat{\boldsymbol{x}} + \frac{1}{2\sqrt{3}}\hat{\boldsymbol{y}}\right), & \boldsymbol{\delta}_3^A &= a\left(\frac{1}{2}\hat{\boldsymbol{x}} - \frac{1}{2\sqrt{3}}\hat{\boldsymbol{y}}\right), \\ 2^{\text{nd}}: \quad & \boldsymbol{\tau}_{1(4)}^A = \pm a\hat{\boldsymbol{x}}, & \boldsymbol{\tau}_{2(5)}^A &= \pm a\left(\frac{1}{2}\hat{\boldsymbol{x}} + \frac{\sqrt{3}}{2}\hat{\boldsymbol{y}}\right), & \boldsymbol{\tau}_{3(6)}^A &= \pm a\left(-\frac{1}{2}\hat{\boldsymbol{x}} + \frac{\sqrt{3}}{2}\hat{\boldsymbol{y}}\right), \\ 3^{\text{rd}}: \quad & \boldsymbol{\upsilon}_1^A = -\frac{2a}{\sqrt{3}}\hat{\boldsymbol{y}}, & \boldsymbol{\upsilon}_2^A &= a\left(\hat{\boldsymbol{x}} + \frac{1}{\sqrt{3}}\hat{\boldsymbol{y}}\right), & \boldsymbol{\upsilon}_3^A &= a\left(-\hat{\boldsymbol{x}} + \frac{1}{\sqrt{3}}\hat{\boldsymbol{y}}\right), \end{aligned} \tag{2.15}$$

and illustrated in Figure 2.3a. Note that the above-mentioned vectors are based on sublattice A. Similarly, $\boldsymbol{\delta}_i^B$, $\boldsymbol{\tau}_i^B$ and $\boldsymbol{\upsilon}_i^B$ are the neighbouring vectors based on sublattice B. The first and third nearest neighbouring vectors satisfy $\boldsymbol{\delta}_i^B = -\boldsymbol{\delta}_i^A$ and $\boldsymbol{\upsilon}_i^B = -\boldsymbol{\upsilon}_i^A$ for $i = 1, 2, 3$, while the second neighbouring vectors are equal for both sublattices.

The reciprocal lattice is spanned by the reciprocal lattice vectors $\boldsymbol{b}_1 = \frac{2\pi}{\sqrt{3}a}(\sqrt{3}\hat{\boldsymbol{q}}_x + \hat{\boldsymbol{q}}_y)$ and $\boldsymbol{b}_2 = \frac{4\pi}{\sqrt{3}a}\hat{\boldsymbol{q}}_y$, which can be seen in Figure 2.3b. It is worth noting that the reciprocal lattice itself forms a honeycomb lattice. The highlighted green region in the figure represents the Wigner-Seitz-cell, which is the primitive reciprocal cell and serves as the first Brillouin zone. Additionally, the symmetry points $\Gamma = (0, 0)$, $M = (0, \frac{2\pi}{\sqrt{3}a})$, $K = (\frac{2\pi}{3a}, \frac{2\pi}{\sqrt{3}a})$ and $K' = (\frac{4\pi}{3a}, 0)$ are frequently referred to in the text.

The dynamical matrix $D(\boldsymbol{q})$ may be written as

$$D(\boldsymbol{q}) = \begin{bmatrix} D_{\text{in-plane}}(\boldsymbol{q}) & 0 \\ 0 & D_{\text{out-of-plane}}(\boldsymbol{q}) \end{bmatrix},$$

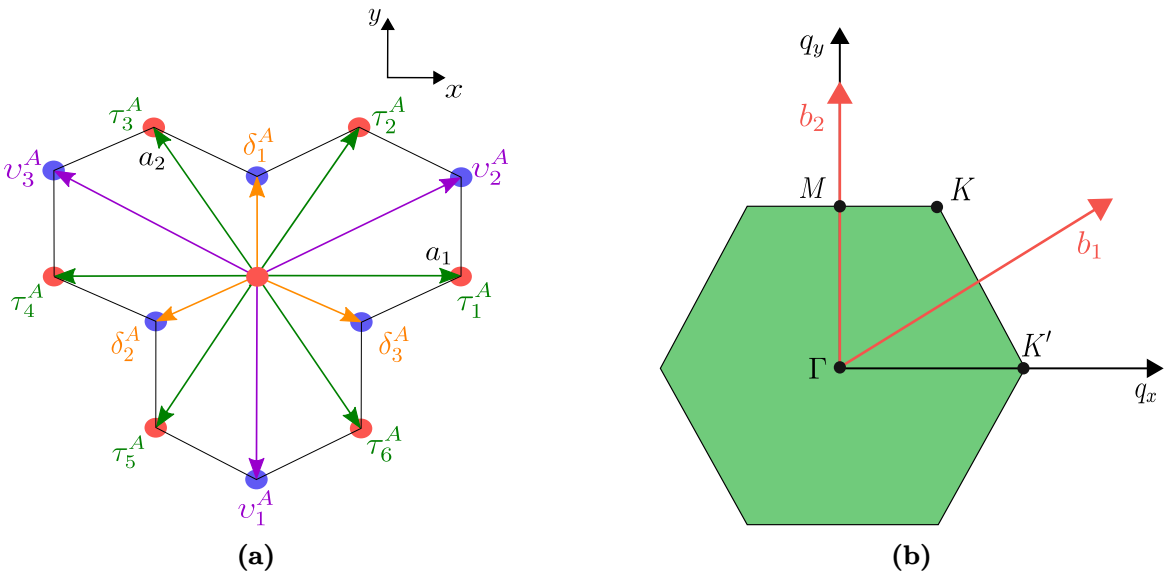

Figure 2.3.: Figure 2.3a illustrates the geometry of the honeycomb lattice where the $A(B)$ atoms constituting the two-atomic basis are marked in red (blue). The vectors to the first $\boldsymbol{\delta}^A$, second $\boldsymbol{\tau}^A$ and third $\boldsymbol{\upsilon}^A$ nearest neighbours based on sublattice A are also shown. The first Brillouin zone is visualized in Figure 2.3b, along with the symmetry points and the reciprocal lattice vectors. Figure 2.3a is inspired by Ref. [37].

in the basis $[x^A, y^A, x^B, y^B, z^A, z^B]^T$. $D_{\text{in-plane}}(\boldsymbol{q})$ is a 4×4 matrix which can further be separated into four matrices

$$D_{\text{in-plane}}(\boldsymbol{q}) = \begin{vmatrix} D^{AA}(\boldsymbol{q}) & D^{AB}(\boldsymbol{q}) \\ D^{BA}(\boldsymbol{q}) & D^{BB}(\boldsymbol{q}) \end{vmatrix},$$

where each $D^{\alpha\beta}(\boldsymbol{q})$ has four entries $D^{\alpha\beta}_{\mu\nu}(\boldsymbol{q})$ for $\mu, \nu \in \{x, y\}$. $D_{\text{out-of-plane}}(\boldsymbol{q})$ is a 2×2 matrix with entries $D^{\alpha\beta}_{zz}$ for $\alpha, \beta \in \{A, B\}$.

Symmetry considerations

The lattice exhibits sublattice symmetry due to its composition of identical ions, where both sublattices share the same next-nearest neighbour vectors. As a result, all force coefficients between A-A ions, Φ^{AA}, are equal to those between B-B ions, Φ^{BB}. To easily exploit the rotational and mirror symmetries of the lattice, it is convenient to change basis. By introducing the chiral basis

$$\xi = x + \mathrm{i}y, \quad \eta = x - \mathrm{i}y,$$

we ensure that rotating the lattice sheet by an angle ϕ around the $z-$axis does not result in a mixing of the new coordinates. They transform as $\xi \to \xi \mathrm{e}^{\mathrm{i}\phi}$ and $\eta \to \eta \mathrm{e}^{-\mathrm{i}\phi}$. The force coefficients in the new basis can be expressed in terms of the old ones via [37]

$$\begin{aligned}
\Phi_{\xi\xi} &= (\Phi_{xx} - \Phi_{yy} - \mathrm{i}\Phi_{xy} - \mathrm{i}\Phi_{yx})/4, \\
\Phi_{\eta\eta} &= (\Phi_{xx} - \Phi_{yy} + \mathrm{i}\Phi_{xy} + \mathrm{i}\Phi_{yx})/4, \\
\Phi_{\xi\eta} &= (\Phi_{xx} + \Phi_{yy} + \mathrm{i}\Phi_{xy} - \mathrm{i}\Phi_{yx})/4, \\
\Phi_{\eta\xi} &= (\Phi_{xx} + \Phi_{yy} - \mathrm{i}\Phi_{xy} + \mathrm{i}\Phi_{yx})/4.
\end{aligned}$$

With the new chiral basis, the application of the C_3 symmetry under 3-fold rotations R_3 around the $z-$axis becomes straightforward. The force coefficients undergo the following transformation [37]

$$\begin{aligned}\Phi^{\alpha\beta}_{\xi\xi}(R_3\boldsymbol{\Delta}) &= \Phi^{\alpha\beta}_{\xi\xi}(\boldsymbol{\Delta})\mathrm{e}^{+\mathrm{i}2\pi/3},\\ \Phi^{\alpha\beta}_{\eta\eta}(R_3\boldsymbol{\Delta}) &= \Phi^{\alpha\beta}_{\eta\eta}(\boldsymbol{\Delta})\mathrm{e}^{-\mathrm{i}2\pi/3},\end{aligned} \tag{2.16}$$

while the force coefficients with different $\{\xi,\eta\}$ or out-of-plane coordinates $\{z,z\}$ are equal to one another. These relations connect the force coefficients for the neighbouring ions $\{\boldsymbol{\delta}_1^A,\boldsymbol{\delta}_2^A,\boldsymbol{\delta}_3^A\}$, $\{\boldsymbol{\tau}_1^A,\boldsymbol{\tau}_3^A,\boldsymbol{\tau}_5^A\}$, $\{\boldsymbol{\tau}_2^A,\boldsymbol{\tau}_4^A,\boldsymbol{\tau}_6^A\}$ and $\{\boldsymbol{v}_1^A,\boldsymbol{v}_2^A,\boldsymbol{v}_3^A\}$ together. For instance, we have $\Phi^{AB}_{\xi\xi}(\boldsymbol{\delta}_1^A) = \Phi^{AB}_{\xi\xi}(\boldsymbol{\delta}_2^A)\mathrm{e}^{+\mathrm{i}2\pi/3} = \Phi^{AB}_{\xi\xi}(\boldsymbol{\delta}_3^A)\mathrm{e}^{-\mathrm{i}2\pi/3}$.

In addition to the rotational symmetry, the lattice has σ_x mirror symmetry, resulting in the following relations [37]

$$\Phi^{\alpha\beta}_{\mu\nu}(\boldsymbol{\Delta}) = \Phi^{\alpha\beta}_{\bar{\mu}\bar{\nu}}(\sigma_x\boldsymbol{\Delta}), \tag{2.17}$$

with $\bar{\xi}=\eta$, $\bar{\eta}=\xi$ and $\bar{z}=z$. Moreover, as we require a real potential, the relation

$$\Phi^{\alpha\beta}_{\mu\nu}(\boldsymbol{\Delta}) = \Phi^{\alpha\beta*}_{\bar{\mu}\bar{\nu}}(\boldsymbol{\Delta}) \tag{2.18}$$

must be met. The symmetry conditions yield nine independent force coefficients denoted by

$$\begin{aligned}\gamma_1 &= \Phi^{AB}_{\xi\xi}(\boldsymbol{\delta}_1^A), & \gamma_2 &= \Phi^{AB}_{\xi\eta}(\boldsymbol{\delta}_1^A), & \gamma_z &= \Phi^{AB}_{zz}(\boldsymbol{\delta}_1^A),\\ \rho_1 &= \Phi^{AA}_{\xi\xi}(\boldsymbol{\tau}_1^A), & \rho_2 &= \Phi^{AA}_{\xi\eta}(\boldsymbol{\tau}_1^A), & \rho_z &= \Phi^{AA}_{zz}(\boldsymbol{\tau}_1^A),\\ \eta_1 &= \Phi^{AB}_{\xi\xi}(\boldsymbol{v}_1^A), & \eta_2 &= \Phi^{AB}_{\xi\eta}(\boldsymbol{v}_1^A), & \eta_z &= \Phi^{AB}_{zz}(\boldsymbol{v}_1^A).\end{aligned} \tag{2.19}$$

By combining equation (2.17) and (2.18), we find the relation $\Phi^{\alpha\beta}_{\mu\nu}(\boldsymbol{\Delta}) = \Phi^{\alpha\beta*}_{\mu\nu}(\sigma_x\boldsymbol{\Delta})$ [37]. Thus, all force coefficients that belong to neighbouring ions with vectors parallel to the $y-$axis, which is invariant under σ_x mirror symmetry, are real. This includes $(\gamma_1,\gamma_2,\gamma_z,\eta_1,\eta_2,\eta_z)$. Moreover, ρ_z and ρ_1 are real since

$$\begin{aligned}\rho_z &= \Phi^{AA}_{zz}(\boldsymbol{\tau}_1^A) = \Phi^{AA*}_{zz}(\boldsymbol{\tau}_4^A) = \Phi^{AA*}_{zz}(\boldsymbol{\tau}_1^A),\\ \rho_1 &= \Phi^{AA}_{\xi\xi}(\boldsymbol{\tau}_1^A) = \Phi^{AA*}_{\xi\xi}(\boldsymbol{\tau}_4^A) = \Phi^{AA*}_{\xi\xi}(\boldsymbol{\tau}_1^A),\end{aligned}$$

where the symmetry by interchange of indices was used. However, ρ_2 may be a complex quantity [37]. This is in contrary to what Refs. [36, 39] claim, where they instead suggest that ρ_1 is the only complex parameter.

Out-of-plane modes

Utilizing the stability condition for the out-of-plane force coefficients, the self-force coefficients are given by

$$\Phi^{AA}_{zz}(0) = \Phi^{BB}_{zz}(0) = -3\gamma_z - 6\rho_z - 3\eta_z,$$

and the matrix elements in $D_{\text{out-of-plane}}(\boldsymbol{q})$ are

$$
\begin{aligned}
D_{zz}^{AA}(\boldsymbol{q}) &= \left[\Phi_{zz}^{AA}(0) + \Phi_{zz}^{AA}(\boldsymbol{\tau}_1^A)\left(\mathrm{e}^{\mathrm{i}\boldsymbol{q}\cdot\boldsymbol{\tau}_1^A} + \mathrm{e}^{\mathrm{i}\boldsymbol{q}\cdot\boldsymbol{\tau}_2^A} + \mathrm{e}^{\mathrm{i}\boldsymbol{q}\cdot\boldsymbol{\tau}_3^A} + \mathrm{e}^{\mathrm{i}\boldsymbol{q}\cdot\boldsymbol{\tau}_4^A} + \mathrm{e}^{\mathrm{i}\boldsymbol{q}\cdot\boldsymbol{\tau}_5^A} + \mathrm{e}^{\mathrm{i}\boldsymbol{q}\cdot\boldsymbol{\tau}_6^A}\right)\right]/M \\
&= -3\frac{\gamma_z+\eta_z}{M} + 2\frac{\rho_z}{M}[\cos(q_x a) + 2\cos(\frac{1}{2}q_x a)\cos(\frac{\sqrt{3}}{2}q_y a) - 3], \\
D_{zz}^{AB}(\boldsymbol{q}) &= \left[\Phi_{zz}^{AB}(\boldsymbol{\delta}_1^A)\left(\mathrm{e}^{\mathrm{i}\boldsymbol{q}\cdot\boldsymbol{\delta}_1^A} + \mathrm{e}^{\mathrm{i}\boldsymbol{q}\cdot\boldsymbol{\delta}_2^A} + \mathrm{e}^{\mathrm{i}\boldsymbol{q}\cdot\boldsymbol{\delta}_3^A}\right) + \Phi_{zz}^{AB}(\boldsymbol{\upsilon}_1^A)\left(\mathrm{e}^{\mathrm{i}\boldsymbol{q}\cdot\boldsymbol{\upsilon}_1^A} + \mathrm{e}^{\mathrm{i}\boldsymbol{q}\cdot\boldsymbol{\upsilon}_2^A} + \mathrm{e}^{\mathrm{i}\boldsymbol{q}\cdot\boldsymbol{\upsilon}_3^A}\right)\right]/M \\
&= \frac{\gamma_z}{M}\mathrm{e}^{\frac{\mathrm{i}}{\sqrt{3}}q_y a}[1 + 2\cos(\frac{1}{2}q_x a)\mathrm{e}^{-\mathrm{i}\frac{\sqrt{3}}{2}q_y a}] + \frac{\eta_z}{M}\mathrm{e}^{-\mathrm{i}\frac{2}{\sqrt{3}}q_y a}[1 + 2\cos(q_x a)\mathrm{e}^{\mathrm{i}\sqrt{3}q_y a}], \\
D_{zz}^{BA}(\boldsymbol{q}) &= D_{zz}^{AB*}(\boldsymbol{q}), \\
D_{zz}^{BB}(\boldsymbol{q}) &= D_{zz}^{AA}(\boldsymbol{q}).
\end{aligned}
$$

The eigenvalue problem to be solved is on the form

$$
\omega^2 = \begin{bmatrix} z^A & z^B \end{bmatrix} \begin{bmatrix} D_{zz}^{AA}(\boldsymbol{q}) & D_{zz}^{AB}(\boldsymbol{q}) \\ D_{zz}^{AB*}(\boldsymbol{q}) & D_{zz}^{AA}(\boldsymbol{q}) \end{bmatrix} \begin{bmatrix} z^A \\ z^B \end{bmatrix},
$$

which yields the following eigenvalues

$$
\omega_{\mathrm{ZO}}(\boldsymbol{q}) = \sqrt{D_{zz}^{AA}(\boldsymbol{q}) + |D_{zz}^{AB}(\boldsymbol{q})|}, \quad \omega_{\mathrm{ZA}}(\boldsymbol{q}) = \sqrt{D_{zz}^{AA}(\boldsymbol{q}) - |D_{zz}^{AB}(\boldsymbol{q})|},
$$

with the corresponding eigenvectors

$$
\hat{\boldsymbol{e}}^{\mathrm{ZO}}(\boldsymbol{q}) = \frac{1}{\sqrt{2}}\begin{bmatrix} \frac{|D_{zz}^{AB}(\boldsymbol{q})|}{D_{zz}^{AB*}(\boldsymbol{q})} \\ 1 \end{bmatrix}, \quad \hat{\boldsymbol{e}}^{\mathrm{ZA}}(\boldsymbol{q}) = \frac{1}{\sqrt{2}}\begin{bmatrix} -\frac{|D_{zz}^{AB}(\boldsymbol{q})|}{D_{zz}^{AB*}(\boldsymbol{q})} \\ 1 \end{bmatrix}. \tag{2.20}
$$

In the vicinity of the Brillouin zone center, where D_{zz}^{AB} takes negative values, the **A**coustic branch is characterized by symmetrical motion between the sublattices, while the **O**ptical branch exhibits asymmetrical motion. When $q = 0$, the out-of-plane acoustic mode corresponds to a translation of the honeycomb layer perpendicular to the plane, whereas the optical mode involves out-of-phase oscillations of neighbouring ions perpendicular to the lattice plane [6]. In this limit, the acoustic mode has a zero energy or frequency since there are no lattice vibrations, whereas the optical mode possesses a nonzero energy.

Expanding the out-of-plane eigenvalues around the $\Gamma-$point, we find

$$
\begin{aligned}
\omega_{\mathrm{ZO}}(\boldsymbol{q}) &\approx \sqrt{\frac{-6(\gamma_z+\eta_z)}{M}} + \frac{(\gamma_z - 6\rho_z + 4\eta_z)}{8\sqrt{-6(\gamma_z+\eta_z)M}}(qa)^2, \\
\omega_{\mathrm{ZA}}(\boldsymbol{q}) &\approx \sqrt{\frac{-(\frac{1}{4}\gamma_z + \frac{3}{2}\rho_z + \eta_z)}{M}}|q|a,
\end{aligned}
$$

to lowest order in q. We observe that the ZA branch typically exhibits a linear dispersion, which contradicts the expectations of elasticity theory, where a quadratic dispersion for the out-of-plane modes is anticipated [7]. To address this inconsistency, one can modify the values of the out-of-plane force coefficients to eliminate the linear term in the ZA branch.

In-plane modes

Proceeding in a similar fashion, the stability condition yields the following self-force coefficients

$$\Phi^{AA}_{\xi\eta}(0) = \Phi^{AA}_{\eta\xi}(0) = -3\gamma_2 - 6\,\mathrm{Re}\,(\rho_2) - 3\eta_2,$$

and $\Phi^{AA}_{\xi\xi}(0) = \Phi^{AA}_{\eta\eta}(0) = 0$. The same expressions apply for the force coefficients at sublattice B. Computing the matrix elements in $D^{AA}(\boldsymbol{q})$, we find

$$\begin{aligned}
D^{AA}_{\xi\eta}(\boldsymbol{q}) &= \left[\Phi^{AA}_{\xi\eta}(0) + \Phi^{AA}_{\xi\eta}(\boldsymbol{\tau}^A_1)(\mathrm{e}^{\mathrm{i}\boldsymbol{q}\cdot\boldsymbol{\tau}^A_1} + \mathrm{e}^{\mathrm{i}\boldsymbol{q}\cdot\boldsymbol{\tau}^A_3} + \mathrm{e}^{\mathrm{i}\boldsymbol{q}\cdot\boldsymbol{\tau}^A_5}) + \Phi^{AA}_{\xi\eta}(\boldsymbol{\tau}^A_4)(\mathrm{e}^{\mathrm{i}\boldsymbol{q}\cdot\boldsymbol{\tau}^A_2} + \mathrm{e}^{\mathrm{i}\boldsymbol{q}\cdot\boldsymbol{\tau}^A_4} + \mathrm{e}^{\mathrm{i}\boldsymbol{q}\cdot\boldsymbol{\tau}^A_6})\right]/M \\
&= \left[\Phi^{AA}_{\xi\eta}(0) + \rho_2\mathrm{e}^{\mathrm{i}q_x a}(1 + 2\cos(\frac{\sqrt{3}}{2}q_y a)\mathrm{e}^{-\mathrm{i}\frac{3}{2}q_x a}) + \rho_2^*\mathrm{e}^{-\mathrm{i}q_x a}(1 + 2\cos(\frac{\sqrt{3}}{2}q_y a)\mathrm{e}^{\mathrm{i}\frac{3}{2}q_x a})\right]/M \\
&= \left[-3(\gamma_2 + \eta_2) - 2\,\mathrm{Re}\left(\rho_2[3 - \mathrm{e}^{\mathrm{i}q_x a} - 2\cos(\frac{\sqrt{3}}{2}q_y a)\mathrm{e}^{-\frac{\mathrm{i}}{2}q_x a}]\right)\right]/M.
\end{aligned}$$

The calculation for $D^{AA}_{\eta\xi}(\boldsymbol{q})$ is similar with $\Phi^{AA}_{\eta\xi}(\boldsymbol{\tau}^A_1) = \rho_2^*$ and $\Phi^{AA}_{\eta\xi}(\boldsymbol{\tau}^A_4) = \rho_2$, which results in

$$D^{AA}_{\eta\xi}(\boldsymbol{q}) = \left[-3(\gamma_2 + \eta_2) - 2\,\mathrm{Re}\left(\rho_2[3 - \mathrm{e}^{-\mathrm{i}q_x a} - 2\cos(\frac{\sqrt{3}}{2}q_y a)\mathrm{e}^{\frac{\mathrm{i}}{2}q_x a}]\right)\right]/M.$$

Continuing, we investigate $D^{AA}_{\xi\xi}(\boldsymbol{q})$ and remember that $\Phi^{AA}_{\xi\xi}(\boldsymbol{\tau}^A_1) = \Phi^{AA}_{\xi\xi}(\boldsymbol{\tau}^A_4)$ since ρ_1 is real. We obtain

$$\begin{aligned}
D^{AA}_{\xi\xi}(\boldsymbol{q}) &= \Big[\Phi^{AA}_{\xi\xi}(\boldsymbol{\tau}^A_1)(\mathrm{e}^{\mathrm{i}\boldsymbol{q}\cdot\boldsymbol{\tau}^A_1} + \mathrm{e}^{\mathrm{i}(\boldsymbol{q}\cdot\boldsymbol{\tau}^A_3 + \frac{2\pi}{3})} + \mathrm{e}^{\mathrm{i}(\boldsymbol{q}\cdot\boldsymbol{\tau}^A_5 - \frac{2\pi}{3})}) \\
&\quad + \Phi^{AA}_{\xi\xi}(\boldsymbol{\tau}^A_4)(\mathrm{e}^{\mathrm{i}\boldsymbol{q}\cdot\boldsymbol{\tau}^A_4} + \mathrm{e}^{\mathrm{i}(\boldsymbol{q}\cdot\boldsymbol{\tau}^A_6 + \frac{2\pi}{3})} + \mathrm{e}^{\mathrm{i}(\boldsymbol{q}\cdot\boldsymbol{\tau}^A_2 - \frac{2\pi}{3})})\Big]/M \\
&= \frac{2\rho_1}{M}\left[\cos(q_x a) + \cos(\frac{1}{2}q_x a - \frac{2\pi}{3})\mathrm{e}^{\mathrm{i}\frac{\sqrt{3}}{2}q_y a} + \cos(\frac{1}{2}q_x a + \frac{2\pi}{3})\mathrm{e}^{-\mathrm{i}\frac{\sqrt{3}}{2}q_y a}\right].
\end{aligned}$$

The matrix element $D^{AA}_{\eta\eta}(\boldsymbol{q})$ is calculated similarly, but the coefficients $\Phi^{AA}_{\eta\eta}(\boldsymbol{\Delta})$ transform oppositely according to equation (2.16), which results in $D^{AA}_{\eta\eta}(\boldsymbol{q}) = D^{AA*}_{\xi\xi}(\boldsymbol{q})$. We turn our focus to the $D^{AB}(\boldsymbol{q})$ matrix and compute

$$\begin{aligned}
D^{AB}_{\xi\eta}(\boldsymbol{q}) &= \frac{\Phi^{AB}_{\xi\eta}(\boldsymbol{\delta}^A_1)}{M}[\mathrm{e}^{\mathrm{i}\boldsymbol{q}\cdot\boldsymbol{\delta}^A_1} + \mathrm{e}^{\mathrm{i}\boldsymbol{q}\cdot\boldsymbol{\delta}^A_2} + \mathrm{e}^{\mathrm{i}\boldsymbol{q}\cdot\boldsymbol{\delta}^A_3}] + \frac{\Phi^{AB}_{\xi\eta}(\boldsymbol{\upsilon}^A_1)}{M}[\mathrm{e}^{\mathrm{i}\boldsymbol{q}\cdot\boldsymbol{\upsilon}^A_1} + \mathrm{e}^{\mathrm{i}\boldsymbol{q}\cdot\boldsymbol{\upsilon}^A_2} + \mathrm{e}^{\mathrm{i}\boldsymbol{q}\cdot\boldsymbol{\upsilon}^A_3}] \\
&= \frac{\gamma_2}{M}\mathrm{e}^{\frac{\mathrm{i}}{\sqrt{3}}q_y a}[1 + 2\cos(\frac{1}{2}q_x a)\mathrm{e}^{-\mathrm{i}\frac{\sqrt{3}}{2}q_y a}] + \frac{\eta_2}{M}\mathrm{e}^{-\mathrm{i}\frac{2}{\sqrt{3}}q_y a}[1 + 2\cos(q_x a)\mathrm{e}^{\mathrm{i}\sqrt{3}q_y a}].
\end{aligned}$$

The presence of σ_x mirror symmetry leads to the equality of $\Phi^{AB}_{\eta\xi}(\boldsymbol{\delta}^A_1) = \Phi^{AB}_{\xi\eta}(\boldsymbol{\delta}^A_1)$ and $\Phi^{AB}_{\eta\xi}(\boldsymbol{\upsilon}^A_1) = \Phi^{AB}_{\xi\eta}(\boldsymbol{\upsilon}^A_1)$. As a result, $D^{AB}_{\eta\xi}(\boldsymbol{q}) = D^{AB}_{\xi\eta}(\boldsymbol{q})$. Additionally, we have

$$\begin{aligned}
D^{AB}_{\xi\xi}(\boldsymbol{q}) &= \frac{\Phi^{AB}_{\xi\xi}(\boldsymbol{\delta}^A_1)}{M}[\mathrm{e}^{\mathrm{i}\boldsymbol{q}\cdot\boldsymbol{\delta}^A_1} + \mathrm{e}^{\mathrm{i}(\boldsymbol{q}\cdot\boldsymbol{\delta}^A_2 + \frac{2\pi}{3})} + \mathrm{e}^{\mathrm{i}(\boldsymbol{q}\cdot\boldsymbol{\delta}^A_3 - \frac{2\pi}{3})}] + \frac{\Phi^{AB}_{\xi\xi}(\boldsymbol{\upsilon}^A_1)}{M}[\mathrm{e}^{\mathrm{i}\boldsymbol{q}\cdot\boldsymbol{\upsilon}^A_1} + \mathrm{e}^{\mathrm{i}(\boldsymbol{q}\cdot\boldsymbol{\upsilon}^A_2 + \frac{2\pi}{3})} + \mathrm{e}^{\mathrm{i}(\boldsymbol{q}\cdot\boldsymbol{\upsilon}^A_3 - \frac{2\pi}{3})}] \\
&= \frac{\gamma_1}{M}\mathrm{e}^{\frac{\mathrm{i}}{\sqrt{3}}q_y a}[1 + 2\cos(\frac{1}{2}q_x a - \frac{2\pi}{3})\mathrm{e}^{-\mathrm{i}\frac{\sqrt{3}}{2}q_y a}] + \frac{\eta_1}{M}\mathrm{e}^{-\mathrm{i}\frac{2}{\sqrt{3}}q_y a}[1 + 2\cos(q_x + \frac{2\pi}{3})\mathrm{e}^{\mathrm{i}\sqrt{3}q_y a}], \\
D^{AB}_{\eta\eta}(\boldsymbol{q}) &= \frac{\gamma_1}{M}\mathrm{e}^{\frac{\mathrm{i}}{\sqrt{3}}q_y a}[1 + 2\cos(\frac{1}{2}q_x a + \frac{2\pi}{3})\mathrm{e}^{-\mathrm{i}\frac{\sqrt{3}}{2}q_y a}] + \frac{\eta_1}{M}\mathrm{e}^{-\mathrm{i}\frac{2}{\sqrt{3}}q_y a}[1 + 2\cos(q_x - \frac{2\pi}{3})\mathrm{e}^{\mathrm{i}\sqrt{3}q_y a}].
\end{aligned}$$

In order to calculate the entries in $D^{BA}(\boldsymbol{q})$, we note that the neighbouring vectors $\boldsymbol{\Delta}^B$ of interest are now $\boldsymbol{\delta}^B_i$ and $\boldsymbol{\upsilon}^B_i$ for $i = 1, 2, 3$. The transformation of the force coefficients $\Phi^{BA}_{\mu\nu}(\boldsymbol{\Delta}^B)$ is similar to

that of $\Phi^{AB}_{\mu\nu}(\boldsymbol{\Delta}^A)$. Moreover, $\gamma_1 = \Phi^{AB}_{\xi\xi}(\boldsymbol{\delta}_1^A) = \Phi^{BA}_{\xi\xi}(\boldsymbol{\delta}_1^B)$ and $\gamma_2 = \Phi^{AB}_{\xi\eta}(\boldsymbol{\delta}_1^A) = \Phi^{BA}_{\xi\eta}(\boldsymbol{\delta}_1^B)$ since γ_2 is real, and the same applies for η_1 and η_2. Thus, in computing $D^{BA}_{\mu\nu}(\boldsymbol{q})$, the only difference compared to finding $D^{AB}_{\mu\nu}(\boldsymbol{q})$ is that the neighbouring vectors $\boldsymbol{\Delta}^B$ are directed oppositely as $\boldsymbol{\Delta}^A$. By setting $\boldsymbol{q} \to -\boldsymbol{q}$ in $D^{AB}_{\mu\nu}(\boldsymbol{q})$, we obtain the $D^{BA}_{\mu\nu}(\boldsymbol{q})$ elements. This results in the following relations

$$\begin{aligned} D^{BA}_{\xi\eta}(\boldsymbol{q}) &= D^{AB*}_{\xi\eta}(\boldsymbol{q}), \quad D^{BA}_{\eta\xi}(\boldsymbol{q}) = D^{AB*}_{\eta\xi}(\boldsymbol{q}), \\ D^{BA}_{\xi\xi}(\boldsymbol{q}) &= D^{AB*}_{\eta\eta}(\boldsymbol{q}), \quad D^{BA}_{\eta\eta}(\boldsymbol{q}) = D^{AB*}_{\xi\xi}(\boldsymbol{q}). \end{aligned}$$

Furthermore, the $D^{BB}(\boldsymbol{q})$ matrix is equal to $D^{AA}(\boldsymbol{q})$ due to the sublattice symmetry. By renaming the six unique matrix elements as

$$\begin{aligned} \mathcal{A} &= D^{AA}_{\xi\eta}(\boldsymbol{q}), & \mathcal{B} &= D^{AA}_{\eta\xi}(\boldsymbol{q}), & \mathcal{C} &= D^{AA}_{\xi\xi}(\boldsymbol{q}), \\ \mathcal{D} &= D^{AB}_{\xi\eta}(\boldsymbol{q}), & \mathcal{E} &= D^{AB}_{\xi\xi}(\boldsymbol{q}), & \mathcal{F} &= D^{AB}_{\eta\eta}(\boldsymbol{q}), \end{aligned}$$

the eigenvalue problem may be written in the following form

$$\omega^2 = \begin{bmatrix} \xi^A & \eta^A & \xi^B & \eta^B \end{bmatrix} \begin{bmatrix} \mathcal{A} & \mathcal{C} & \mathcal{D} & \mathcal{E} \\ \mathcal{C}^* & \mathcal{B} & \mathcal{F} & \mathcal{D} \\ \mathcal{D}^* & \mathcal{F}^* & \mathcal{A} & \mathcal{C} \\ \mathcal{E}^* & \mathcal{D}^* & \mathcal{C}^* & \mathcal{B} \end{bmatrix} \begin{bmatrix} \eta^A \\ \xi^A \\ \eta^B \\ \xi^B \end{bmatrix}.$$

The different ordering of the first vector is due to the hermitian conjugation where $\bar{\xi}^{A(B)} = \eta^{A(B)}$. The characteristic polynomial can be expressed as follows

$$\lambda^4 + A\lambda^3 + B\lambda^2 + C\lambda + D = 0, \quad \lambda = \omega^2,$$

where the coefficients are determined by the matrix elements from the following formulas

$$\begin{aligned} A =& -2(\mathcal{A} + \mathcal{B}), \\ B =& \mathcal{A}^2 + 4\mathcal{A}\mathcal{B} + \mathcal{B}^2 - 2|\mathcal{C}|^2 - 2|\mathcal{D}|^2 - |\mathcal{E}|^2 - |\mathcal{F}|^2, \\ C =& (\mathcal{A} + \mathcal{B})(-2\mathcal{A}\mathcal{B} + 2|\mathcal{C}|^2 + 2|\mathcal{D}|^2 + |\mathcal{E}|^2 + |\mathcal{F}|^2) - 4\,\mathrm{Re}\left(\mathcal{C}\mathcal{D}\mathcal{E}^* + \mathcal{C}\mathcal{D}^*\mathcal{F}\right), \\ D =& \mathcal{A}\mathcal{B}(\mathcal{A}\mathcal{B} - 2|\mathcal{C}|^2 - |\mathcal{E}|^2 - |\mathcal{F}|^2) + 2(\mathcal{A} + \mathcal{B})(\mathrm{Re}\left(\mathcal{C}\mathcal{D}^*\mathcal{F}\right) + \mathrm{Re}\left(\mathcal{C}\mathcal{D}\mathcal{E}^*\right)) + |\mathcal{E}|^2|\mathcal{F}|^2 + |\mathcal{C}|^4 \\ & - |\mathcal{D}|^2(\mathcal{A}^2 + \mathcal{B}^2 + 2|\mathcal{C}|^2 - |\mathcal{D}|^2) - 2\,\mathrm{Re}\left(\mathcal{D}^2\mathcal{E}^*\mathcal{F}^*\right) - 2\,\mathrm{Re}\left(\mathcal{C}^2\mathcal{E}^*\mathcal{F}\right). \end{aligned}$$

The roots of the characteristic polynomial, and the eigenvalues of the matrix, are

$$\begin{aligned} \omega^2_{\mathrm{LA}} &= -\frac{A}{4} - \zeta + \frac{1}{2}\sqrt{-4\zeta^2 - 2p_1 + \frac{p_2}{\zeta}}, \quad \omega^2_{\mathrm{TA}} = -\frac{A}{4} - \zeta - \frac{1}{2}\sqrt{-4\zeta^2 - 2p_1 + \frac{p_2}{\zeta}}, \\ \omega^2_{\mathrm{TO}} &= -\frac{A}{4} + \zeta + \frac{1}{2}\sqrt{-4\zeta^2 - 2p_1 - \frac{p_2}{\zeta}}, \quad \omega^2_{\mathrm{LO}} = -\frac{A}{4} + \zeta - \frac{1}{2}\sqrt{-4\zeta^2 - 2p_1 - \frac{p_2}{\zeta}}, \end{aligned} \tag{2.21}$$

where the new helping variables are defined as

$$
\begin{aligned}
\zeta &= \frac{1}{2}\sqrt{-\frac{2p_1}{3} + \frac{1}{3}(\xi + \frac{p_3}{\xi})}, & \xi &= \left(\frac{p_4 + \sqrt{p_4^2 - 4p_3^3}}{2}\right)^{\frac{1}{3}}, \\
p_1 &= \frac{8B - 3A^2}{8}, & p_2 &= \frac{A^3 - 4AB + 8C}{8}, \\
p_3 &= B^2 - 3AC + 12D, & p_4 &= 2B^3 - 9ABC + 27A^2D + 27C^2 - 72BD.
\end{aligned} \tag{2.22}
$$

The corresponding eigenvectors can be written in a non-normalized form as

$$
\boldsymbol{e}^\lambda = \begin{bmatrix} 1 & G_\lambda/K_\lambda & J_\lambda/K_\lambda & L_\lambda/K_\lambda \end{bmatrix}^T, \tag{2.23}
$$

with the components in the eigenvector defined by

$$
\begin{aligned}
G_\lambda =& (\mathcal{E}\mathcal{F} - \mathcal{D}^2)(\bar{\mathcal{B}}_\lambda \mathcal{D}^* - \mathcal{C}\mathcal{E}^*) + (\bar{\mathcal{A}}_\lambda \mathcal{D} - \mathcal{C}^*\mathcal{E})(\bar{\mathcal{A}}_\lambda \bar{\mathcal{B}}_\lambda - |\mathcal{C}|^2), \\
J_\lambda =& (\bar{\mathcal{A}}_\lambda \mathcal{D} - \mathcal{C}^*\mathcal{E})(\mathcal{C}\mathcal{D}^* - \bar{\mathcal{B}}_\lambda \mathcal{F}^*) - (\bar{\mathcal{B}}_\lambda \mathcal{D}^* - \mathcal{C}\mathcal{E}^*)(\bar{\mathcal{B}}_\lambda \mathcal{E} - \mathcal{C}\mathcal{D}), \\
K_\lambda =& (\bar{\mathcal{A}}_\lambda \bar{\mathcal{B}}_\lambda - |\mathcal{C}|^2)(\bar{\mathcal{B}}_\lambda \mathcal{E} - \mathcal{C}\mathcal{D}) + (\mathcal{C}\mathcal{D}^* - \bar{\mathcal{B}}_\lambda \mathcal{F}^*)(\mathcal{E}\mathcal{F} - \mathcal{D}^2), \\
L_\lambda =& -(\mathcal{E}^* K_\lambda + \mathcal{D}^* G_\lambda + \mathcal{C}^* J_\lambda)/\bar{\mathcal{B}},
\end{aligned}
$$

and we also defined $\bar{\mathcal{A}}_\lambda = \mathcal{A} - \omega_\lambda^2$ and $\bar{\mathcal{B}}_\lambda = \mathcal{B} - \omega_\lambda^2$. It is important to note that this expression is not well-defined where the branches are degenerate. Moreover, the eigenvectors are written in terms of the chiral basis, related to the Cartesian components by

$$
\begin{bmatrix} x^A \\ y^A \\ x^B \\ y^B \end{bmatrix} = \frac{1}{2} P \begin{bmatrix} \eta^A \\ \xi^A \\ \eta^B \\ \xi^B \end{bmatrix}, \quad P = \begin{bmatrix} 1 & 1 & 0 & 0 \\ \mathrm{i} & -\mathrm{i} & 0 & 0 \\ 0 & 0 & 1 & 1 \\ 0 & 0 & \mathrm{i} & -\mathrm{i} \end{bmatrix}.
$$

Denoting the unitary matrix $U_{\text{ph}}^{\eta,\xi} = [\hat{\boldsymbol{e}}_{\eta,\xi}^1, \dots]^T$ as the matrix that diagonalizes the dynamical matrix in the $\{\eta, \xi\}$ chiral basis, the relation to the unitary matrix $U_{\text{ph}}^{x,y}$ in the Cartesian basis is

$$
U_{\text{ph}}^{x,y} = \frac{1}{\sqrt{2}} P U_{\text{ph}}^{\eta,\xi}. \tag{2.24}
$$

It can be shown that $(1/\sqrt{2})P$ is in fact also an unitary matrix.

Phonon dispersion in graphene

Figure 2.4 displays the energy corresponding to each eigenfrequency, $\hbar\omega$, for a graphene layer, measured in electronvolts. The phonon dispersion is depicted along the symmetry lines $\Gamma \to M$, $M \to K$ and $K \to \Gamma$ of the Brillouin zone. The values of the force coefficients Φ/M are gathered from Ref. [36] and takes the values

$$
\begin{aligned}
\gamma_1 &= -1.645, & \gamma_2 &= -4.095, & \gamma_z &= -1.415, \\
\rho_1 &= 0.690, & \rho_2 &= -0.209, & \rho_z &= 0.171, \\
\eta_1 &= 0.375, & \eta_2 &= -0.072, & \eta_z &= 0.085,
\end{aligned} \tag{2.25}
$$

in units of 10^5 cm^{-2}. The values are given in spectroscopic units, related to the frequency through a factor of $2\pi c$ where c is the speed of light. The dispersions shown in the figure align with findings from more sophisticated approaches, such as density-functional perturbation theory [40], and experimental measurements [41]. The specific values employed for the out-of-plane force coefficients were determined through fitting with the Raman frequency and smallest elastic constant C_{44} [36], which may not inherently fulfill the quadratic dispersion criterion. Nevertheless, it can be observed from the figure that the dispersion is approximately quadratic. At the K symmetry point in graphene, both the in-plane LA/LO branches and the out-of-plane ZA/ZO branches exhibit double degeneracy. Similarly, at the $\Gamma-$point, the LO/TO branches also display double degeneracy. This degeneracy occurs due to the preservation of $C_{3,v}$ symmetry in graphene at these points in the Brillouin zone. A splitting of those modes would signify a breakdown of symmetry in the crystal [36]. An example of such splitting can be observed in hexagonal boron nitride (h-BN), where the lattice exhibits sublattice asymmetry [37].

Initially, the phonon dispersion was calculated using a spring force model. The calculations and outcomes are described extensively in Appendix A.2. However, as the spring force model yielded distinct results from previous studies [36, 37, 39], we adopted the method employed in those studies, which takes into account interactions up to third nearest neighbours. The results obtained using this method align with the findings of the spring force model when $\gamma_1 = -\gamma_2$, $\rho_1 = \rho_2$, and all third-neighbour interactions are zero.

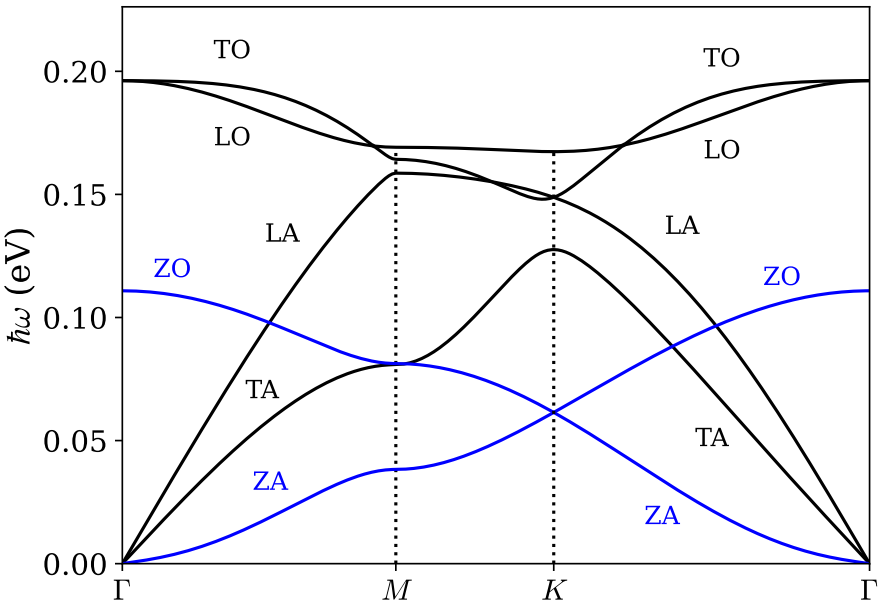

Figure 2.4.: The six branches of the phonon dispersion in graphene are shown along the symmetry lines of the Brillouin zone. The six branches are longitudinal acoustic (optical) [LA (LO)], transverse acoustic (optical) [TA (TO)] and out-of-plane acoustic (optical) [ZA (ZO)]. The values of the force coefficients are taken from Ref. [36].

CHAPTER 3

Magnetism

In this chapter, we will delve into the diverse types of magnetism with a special focus on ferromagnetism and antiferromagnetism. The fundamental concept of spin-waves and their corresponding magnons will be qualitatively elaborated. Additionally, we will introduce several common magnetic interactions, which will later be employed to calculate magnon dispersions in two-dimensional magnetic systems.

3.1. Magnetic materials

The magnetic moment of a free atom can have three sources, the angular momentum about the nucleus, the spin of the atom and the change in orbital momentum when an external magnetic field is present [3]. The magnetization $\boldsymbol{m}$ is defined as the magnetic moment $\boldsymbol{\mu}$ per unit volume

$$\boldsymbol{m} = \lim_{V \to 0} \sum_{V} \frac{\boldsymbol{\mu}}{V}.$$

It is customary to distinguish between the main types of magnetism; diamagnetism, paramagnetism, ferromagnetism and antiferromagnetism. There exist more variants such as ferrimagnetism and magnetic glass that are to some extent similar [42]. The different types of magnetism are classified by how the magnetization of a material changes as a function of an external magnetic field $\boldsymbol{B}$. The susceptibility characterizes this behaviour and can be defined as [3]

$$\chi = \frac{\mu_0 m}{B},$$

where μ_0 is the permeability in vacuum. Diamagnetic materials exhibit a magnetization field that is directed oppositely to the external field, resulting in a negative susceptibility ($\chi < 0$). In contrast, paramagnetic materials have a positive susceptibility ($\chi > 0$), leading to an enhancement of the magnetic field inside the material due to the magnetization. Once the external magnetic field is turned off, the magnetization vanishes for both dia- and paramagnetic materials due to the random ordering of the magnetic moments, resulting in a net zero magnetic moment. These materials are referred to as disordered states, which differs from the ordered ferro- and antiferromagnetic states. It is important to note that the various types of magnetism represent different phases, and a material can undergo a phase transition at a temperature specific to the material, causing it to change phases.

3.1.1. Ferromagnetism

Ferromagnetism is an ordered state where the magnetic moments are arranged such that a spontaneous magnetization arises, called the saturation moment, even in the absence of an external field. Macroscopically, a ferromagnet is typically divided into smaller regions called domains [3]. Each domain has their local magnetization saturated with different orientations. The regions are separated by finite thick domain walls, where the magnetization direction changes gradually along the normal direction of the domain wall. When an external magnetic field is applied, the increase in magnetization occurs either by an increase in volume of domains with favourable orientations or by a rotation of the domain magnetization towards alignment with the field [3]. The susceptibility of ferromagnetic materials is typically a large positive value and is a complicated function of temperature and the external field [42]. The susceptibility also depends on the history of the magnetization, and a hysteresis loop can be

observed where the domain volumes and directions change continuously. This loop encompasses both the maximum magnetization achieved by the sample under an applied field (total saturation magnetization) and the residual magnetization that remains once the external field is removed (remanent magnetization).

As the temperature increases, thermal fluctuations become stronger, leading to a reduction in the alignment of magnetic moments, and consequently, a decrease in magnetization. At the transition temperature, T_C, also known as the Curie temperature, the magnetization becomes zero, and the system undergoes a phase transition to the paramagnetic phase. The ferromagnetic $\leftrightarrow$ paramagnetic transition is classified as a second-order phase transition, indicating that the order parameter, which is a quantity that is nonzero in the ordered state, changes continuously at the transition temperature [3]. For ferromagnetic materials, the magnetization serves as the order parameter. A second-order transition typically indicates that there is a broken symmetry in the transition, where in the case of spontaneous magnetization, the rotational invariance of the magnetic moments is broken [43].

3.1.2. Antiferromagnetism

In an antiferromagnet, the magnetic moments are arranged into two or more sublattices, with equal magnitude and direction within each sublattice. Similar to diamagnetic and paramagnetic phases, the net magnetization in an antiferromagnet is zero in the absence of an external field due to the antialignment of magnetic moments between sublattices [42]. However, unlike diamagnetism and paramagnetism, antiferromagnetism is an ordered phase with fixed direction of the average atomic magnetic moments. The Néel temperature, T_N, is the transition temperature for the antiferromagnetic phase. The susceptibility is finite at zero temperature and increases with temperature until T_N, where it exhibits a cusp and then decreases into the paramagnetic phase [3]. Domain separation also occurs in antiferromagnets, and the phase transition is of the second-order type. If the lattice can be split into two sublattices A and B, where the magnetic moments within each sublattice are equal, then the antiferromagnetic order parameter takes the form [44]

$$\boldsymbol{l} = \frac{\hat{\boldsymbol{m}}_A - \hat{\boldsymbol{m}}_B}{2},$$

called the Néel vector. The direction of magnetization of sublattice A is denoted by $\hat{\boldsymbol{m}}_A$ and similarly, the direction of magnetization of sublattice B is denoted by $\hat{\boldsymbol{m}}_B$. The unit length magnetization direction is defined as $\hat{\boldsymbol{m}} = \boldsymbol{m}/|\boldsymbol{m}|$.

3.1.3. Magnons

When an ordered ferromagnetic or antiferromagnetic material is disturbed from its ground state, the magnetization direction at the lattice sites is modified, causing the perturbed magnetization to rotate around the preferred ground state axis at a slight tilt. This rotation results in the precession of magnetization at neighbouring sites, with the same frequency but different phases, due to magnetic interactions. This chain of lattice sites, with a linearly varying precession phase, is referred to as a spin-wave [45]. A spin-wave propagates through the material, carrying both energy and momentum, and represents a deviation in the net magnetization.

The idea of spin-waves was initially proposed by Felix Bloch in 1930 as a means of computing the temperature-dependent behaviour of ferromagnetic materials [46]. Bloch demonstrated that these waves are made up of quantized modes called magnons [47], much like phonons represent the quantized vibrations of the lattice. To consider magnons from a particle perspective, one could think of them

as particles whose motion along the chain increases the probability of a spin flip in the corresponding region [45].

The number of branches in the magnon dispersion in a magnetic lattice is determined by the symmetry of the lattice and the arrangement of magnetic atoms within it. Typically, in ferromagnetic or antiferromagnetic systems, the number of branches equals the number of independent magnetic atoms present in the magnetic unit cell. The magnetic unit cell is the smallest repeating unit of the crystal structure containing one or more magnetic atoms. For instance, a ferromagnetic square lattice with one magnetic atom per magnetic unit cell will have one branch in its magnon dispersion, while an antiferromagnetic version of the same lattice with two magnetic atoms per magnetic unit cell will have two branches. The ordered ferro- and antiferromagnetic states remain symmetric under rotations around an axis parallel to the magnetization direction. More complex spin systems, such as a spin spiral state, break additional symmetries and consequently have an increased number of magnon branches [48].

3.2. Magnetic interactions

Collective (or cooperative) magnetism, such as ferro-, ferri-, and antiferromagnetism, is dependent on interactions and cannot be explained without them. The most crucial interactions are known as exchange interactions, which determine the magnetic properties of the material. We separate between two cases, insulators and metals. In insulators, there are localized magnetic moments of a partially filled shell, which are well described by the Heisenberg model. In metals or band magnets, the net magnetization is produced by the conduction electrons, and the exchange interaction creates a spin-dependent band shift, which favours one particular spin orientation. The Hubbard model is a simplified but effective way to model this scenario [49].

We examine the fundamental physics of insulators and focus on the most influential interactions. Contrary to what one might expect, the main contributor to collective magnetism is not the magnetic dipole-dipole interactions or spin-orbit coupling. Instead, the electrostatic electron-electron interaction, in combination with the Pauli principle, is the most significant dynamic in magnetic materials. This is a quantum mechanical effect known as the direct exchange interaction [4]. When localized magnetic moments are separated by nonmagnetic ions, causing a large distance between the moments and thus a weak direct exchange interaction, the exchange interaction can be transmitted through the nonmagnetic ions. This is referred to as the superexchange interaction and is an indirect exchange interaction [50]. In this case, the indirect exchange is the primary contributor to magnetism. Both the direct and indirect exchange can be modeled using the Heisenberg exchange interaction.

3.2.1. Heisenberg exchange interaction

The direct exchange interaction can be illustrated by studying a system of two electrons with Coulomb interactions and a spin-independent Hamiltonian. In this system, the spin angular momentum, denoted by $\boldsymbol{S}$, is measured in units of the reduced Planck constant $\hbar$. Electrons are spin-1/2 particles, meaning that the eigenvalue of the squared spin $\boldsymbol{S}^2$ is $S(S+1)$, with $S = 1/2$. Combining two electron spin-1/2 states, $|\psi_1\rangle$ and $|\psi_2\rangle$, results in either a singlet or a triplet state with spin $S = 0$ or $S = 1$, respectively [4, 50]. Since electrons are fermionic particles, they obey the Pauli exclusion principle. Therefore, the total wavefunction must be antisymmetric under an interchange of coordinates $1 \leftrightarrow 2$. The spin singlet state is antisymmetric and requires a symmetric orbital wavefunction, while the symmetric spin triplet state requires an antisymmetric orbital wavefunction. The ground state energy in each state, denoted as E_s for the singlet and E_t for the triplet, is a solution of the spin-independent Schrodinger

equation and is distinct because the orbital wavefunctions are different [4]. The ground state is four-fold degenerate when the electrons are far apart due to the different spin configurations. However, bringing the electrons closer together breaks the degeneracy and allows for the construction of a spin Hamiltonian that produces the correct eigenvalues. Furthermore, the eigenfunctions yield the spin of the corresponding state. By using that the eigenvalue of $\boldsymbol{S}_1 \cdot \boldsymbol{S}_2$ is

$$\boldsymbol{S}_1 \cdot \boldsymbol{S}_2 = \frac{1}{2}(\boldsymbol{S}^2 - \boldsymbol{S}_1^2 - \boldsymbol{S}_2^2) = \frac{\boldsymbol{S}^2}{2} - \frac{3}{4} = \begin{cases} -\frac{3}{4} & \text{if S=0 in singlet state} \\ \frac{1}{4} & \text{if S=1 in triplet state} \end{cases},$$

the spin Hamiltonian [4, 50]

$$\mathcal{H} = \frac{1}{4}(E_s + 3E_t) - (E_s - E_t)\boldsymbol{S}_1 \cdot \boldsymbol{S}_2,$$

yields the correct energies $E_{s(t)}$ in both cases. By omitting the first term which is simply a constant, the spin Hamiltonian is

$$\mathcal{H} = -J\boldsymbol{S}_1 \cdot \boldsymbol{S}_2.$$

The exchange coupling coefficient J appears in the Hamiltonian, which can be extended to a system with many particles by summing over all pairs of atoms located at sites i and j. The resulting Hamiltonian is known as the Heisenberg Hamiltonian [4]

$$\mathcal{H}_{\text{Heis}} = -\sum_{i,j} J_{ij}\boldsymbol{S}_i \cdot \boldsymbol{S}_j.$$

If J is positive, the Hamiltonian prefers parallel spins, while if it is negative, it prefers anti-parallel spin alignment. As a result, this leads to ferro- and antiferromagnetism, respectively.

3.2.2. Zeeman coupling

The magnetic moment of atomic electrons in an external field is given by [3]

$$\boldsymbol{\mu} = -\mu_B(g_L\boldsymbol{L} + g_S\boldsymbol{S}),$$

where μ_B is the Bohr magneton, $\boldsymbol{L}$ and $\boldsymbol{S}$ represent the total (dimensionless) orbital and spin angular momentum of the atomic electrons, and g is the Landé g-factor. Specifically, $g_L = 1$ and g_S is approximately equal to 2. The induced magnetic moment, which arises in the presence of an external field and is responsible for diamagnetism, is neglected in this case. This term is usually insignificant and only becomes relevant when the electron shells are completely filled, resulting in a permanent magnetic moment of zero [50].

The energy associated with a magnetic moment in an external magnetic field directed along the $z-$axis is [35]

$$E = -\boldsymbol{\mu} \cdot \boldsymbol{B} = \mu_B(L_z + 2S_z)B_0,$$

where B_0 is the strength of the magnetic field and L_z (S_z) are the $z-$components of the orbital (spin) angular momentum. Some textbooks use a different sign convention, where the energy is defined as the negative of the expression above [49]. This convention suggests that the magnetic moments prefer to align parallel with the magnetic field, rather than anti-parallel. For example, in this convention, the state with $S_z = +1/2$ is energetically favourable instead of the $S_z = -1/2$ spin state. We will use this convention in the following. The term that describes this energy shift is known as the Zeeman

term and is responsible for the anomalous Zeeman effect, which is the splitting of the energy levels based on the orbital and spin momenta, breaking the degeneracy [35].

For a many-particle system, the Zeeman term may be added to the Hamiltonian via [49]

$$\mathcal{H}_Z = -g_J \mu_B B_0 \sum_i S_{iz} \equiv -h \sum_i S_{iz},$$

where the summation is over all lattice sites and g_J is the Landé g-factor associated with the total angular momentum $\boldsymbol{J} = \boldsymbol{L} + \boldsymbol{S}$. Moreover, we defined $h = g_J \mu_B B_0$ as the effective strength of the Zeeman coupling. If the localized moments consist solely of spin moments, the Landé g-factor is equal to 2. Otherwise, its value is determined by the following expression

$$g_J = 1 + \frac{J(J+1) - L(L+1) + S(S+1)}{2J(J+1)},$$

and S_{iz} must be replaced with J_{iz}.

3.2.3. Dipole-dipole interaction

The interaction energy of two magnetic dipoles separated by the vector $\boldsymbol{r}$ is [50]

$$U = \frac{\mu_0}{4\pi} \frac{1}{r^3} \left[\boldsymbol{\mu}_1 \cdot \boldsymbol{\mu}_2 - 3(\boldsymbol{\mu}_1 \cdot \hat{\boldsymbol{r}})(\boldsymbol{\mu}_2 \cdot \hat{\boldsymbol{r}}) \right].$$

The energy can be estimated using the values $\mu_1 = \mu_2 = \mu_B$ and $r = 2\text{Å}$, assuming that all vectors are aligned $\boldsymbol{\mu}_1 \parallel \boldsymbol{\mu}_2 \parallel \boldsymbol{r}$. The resulting energy is approximately $1 \times 10^{-24}\,\text{J}$. Based on the thermal energy $k_B T$, the corresponding temperature is well below 1K [50]. This demonstrates that magnetic dipole-dipole interactions do not play a major role in collective magnetism. The exchange interaction between nearest neighbours is typically a thousand times stronger than the dipole-dipole coupling [4].

Disregarding the dipole-dipole interaction is a valid approximation only when the separation distance is relatively small [49]. This is due to the fact that the direct exchange is a short-range interaction, where its strength decreases exponentially with the separation distance in ferromagnetic insulators [4]. On the other hand, the dipolar coupling strength decreases as the inverse cube of the separation distance, making it comparable to the exchange interaction at larger distances.

Dipole-dipole interactions can give rise to novel long-range and direction-dependent phenomena. Macroscopic domain formation, for instance, is primarily driven by dipolar coupling [4]. When domains are formed, the dipolar energy of each spin is reduced due to the long-range interaction. As the exchange interaction is a short-ranged interaction, only spins located close to the domain boundary will experience unfavourable exchange interactions, competing with the dipolar energy reduction caused by the formation of domains. Another example illustrating the influence of dipole-dipole interactions is the partial demagnetization of an isotropic ferromagnet in its ground state, which deviates from the completely ordered state and is attributed to the presence of these interactions [49].

3.2.4. Anisotropy

The Heisenberg Hamiltonian, which is completely isotropic, predicts that the magnetization will always be zero in the absence of an external magnetic field if only the exchange term is considered [50]. However, real materials exhibit anisotropy and should be modeled accordingly. Magneto-crystalline anisotropy, which arises from spin-orbit coupling between electrons, is a significant contribution to the

anisotropy [50]. The preference of the spins to align with the crystallographic axes arises from the fact that the spin-orbit coupling connects the spins to the electronic orbitals, which themselves are correlated with the crystallographic axes.

To account for anisotropy in a material, it is necessary to take into account the material's lattice geometry. In many cases, adding the uniaxial anisotropy term to the Hamiltonian is sufficient, and can be written mathematically as [49]

$$\mathcal{H}_{\text{ani}} = -\sum_{i,j} K_{ij} S_{iz} S_{jz},$$

where K_{ij} is the anisotropy constant between sites i and j and the preferred spin direction due to anisotropy is along the z-axis. The diagonal terms in the summation, when $i = j$, are called the single-ion anisotropy terms. One often speaks of easy and hard axes of magnetization, and as the names suggest, give rise to a preferred and unpreferred axis of magnetization. To incorporate these effects into the model, one can include the following terms in the Hamiltonian

$$\mathcal{H}_{\text{ani}} = -K_{\text{easy}} \sum_i (\boldsymbol{S}_i \cdot \hat{\boldsymbol{e}}_{\text{easy}})^2 + K_{\text{hard}} \sum_i (\boldsymbol{S}_i \cdot \hat{\boldsymbol{e}}_{\text{hard}})^2,$$

with the direction of the easy and hard axes given by the unit vectors $\hat{\boldsymbol{e}}_{\text{easy}}$ and $\hat{\boldsymbol{e}}_{\text{hard}}$.

3.2.5. Dzyaloshinskii–Moriya interaction

The Dzyaloshinskii-Moriya interaction (DMI) is a type of antisymmetric exchange interaction between spins that may be included in the Hamiltonian depending on the lattice geometry. Dzyaloshinskii demonstrated, through a phenomenological approach, that the weak ferromagnetic properties of α-Fe_2O_3 perpendicular to the trigonal axis arise because the antiferromagnetic spin structure has the same symmetry as a canted spin arrangement, while the free energy contains a term that favours canted spins, which is the DMI term [51]. Moriya expanded the theory of superexchange interaction, which was developed by Anderson [52], to incorporate the impact of spin-orbit coupling [53]. Using perturbation theory, Moriya derived an expression for the DMI term.

To introduce the Dzyaloshinskii-Moriya interaction, it should be noted that it requires low crystal symmetries, for instance a broken inversion symmetry, and that it is induced by spin-orbit coupling. In the Heisenberg formalism, the DMI-term is usually written as [26, 54, 55]

$$\mathcal{H}_{\text{DMI}} = -\sum_{i,j} \boldsymbol{D}_{ij} \cdot [\boldsymbol{S}_i \times \boldsymbol{S}_j].$$

The DM vector, $\boldsymbol{D}_{ij}$, determines the strength of the interaction and its direction is given by crystal symmetry rules [53]. The interaction is proportional to the cross-product of neighbouring spins and promotes perpendicular alignment between them. The energy is minimized when the spins lie in the plane that is normal to the DM vector. This interaction competes with the direct Heisenberg exchange, which prefers collinear alignment, and as a result, can cause the formation of chiral magnetic solitons, such as skyrmions, and affect the behaviour of spin-waves [12].

3.3. Calculation of ferromagnetic magnon dispersion

Our objective is to calculate the ferromagnetic magnon dispersion in the two-dimensional square and honeycomb lattices. We focus on a single ferromagnetic domain and exclude the consideration

of domain walls. The lattices are assumed to lie in the $xy-$plane. For simplicity, we employ a simplified model that incorporates only nearest-neighbour interactions for the Heisenberg exchange. The Hamiltonian takes into account the magnetic anisotropy, the Dzyaloshinskii-Moriya interaction, and the Zeeman term due to an external magnetic field $\boldsymbol{B} = B_0\hat{\boldsymbol{z}}$. The Hamiltonian can be expressed as

$$\mathcal{H} = -\sum_{<i,j>} J_{ij}\boldsymbol{S}_i \cdot \boldsymbol{S}_j - h\sum_i S_{iz} - K_z\sum_i S_{iz}^2 - \sum_{i,j} \boldsymbol{D}_{ij} \cdot [\boldsymbol{S}_i \times \boldsymbol{S}_j]. \tag{3.1}$$

The notation $\sum_{<i,j>}$ represents a summation over all pairs of nearest neighbours. The lattice possesses a single-ion anisotropy with an easy axis, where $K_z > 0$ favours an out-of-plane orientation [28]. We assume that the exchange coupling coefficients are equal for all pairs of neighbouring spins, denoted as $J_{ij} = J$. It is required that $J > 0$ to maintain ferromagnetic ordering. Both the Zeeman term and anisotropy term promote an out-of-plane alignment, indicating an expected ferromagnetic ordering along the z-axis. As the spin is measured in units of the Planck constant, the parameters J, h, K_z and $\boldsymbol{D}_{ij}$ are given in units of energy. The calculations include the DMI exclusively for the honeycomb lattice, as the square lattice does not exhibit a broken inversion symmetry.

To obtain the magnon dispersion, it is advantageous to represent the Hamiltonian in the second quantized form. This is achieved by employing the Holstein-Primakoff transformation, which converts spin operators into bosonic creation and annihilation operators, and is on the form [56]

$$\begin{aligned} S_{i+} &= S_{ix} + \mathrm{i}S_{iy} = \sqrt{2S}(1 - \frac{a_i^\dagger a_i}{2S})^{\frac{1}{2}} a_i \approx \sqrt{2S}a_i, \\ S_{i-} &= S_{ix} - \mathrm{i}S_{iy} = \sqrt{2S}a_i^\dagger(1 - \frac{a_i^\dagger a_i}{2S})^{\frac{1}{2}} \approx \sqrt{2S}a_i^\dagger, \\ S_{iz} &= S - a_i^\dagger a_i. \end{aligned} \tag{3.2}$$

We treat S_{iz} differently because we anticipate that the ground state consists of spins aligned perfectly along the z-axis. Any excitations created by $a_i^\dagger a_i$ would reduce S_{iz} and disrupt the ferromagnetic ordering. The approximations made in equation (3.2) is known as linear spin-wave theory and is applicable for systems with nearly ordered spins, where neglecting cubic and higher-order terms in boson operators is appropriate [33]. We employ this approximation in the subsequent calculations.

3.3.1. Square lattice

Starting from the Hamiltonian given in equation (3.1) without considering the DMI, the Heisenberg exchange part can be written as [45]

$$\mathcal{H}_{\text{Heis}} = -J\sum_{<i,j>} \boldsymbol{S}_i \cdot \boldsymbol{S}_j = -J\sum_{<i,j>} \left[S_{iz}S_{jz} + \frac{1}{2}(S_{i+}S_{j-} + S_{i-}S_{j+})\right].$$

Utilizing the Holstein-Primakoff transformation, the expression is further transformed to

$$\mathcal{H}_{\text{Heis}} = -JS\sum_{<i,j>} \left[S - (a_i^\dagger a_i + a_j^\dagger a_j - a_i^\dagger a_j - a_j^\dagger a_i)\right].$$

Likewise, the terms related to anisotropy and Zeeman effects can be expressed as follows

$$\begin{aligned}\mathcal{H}_Z &= -h\sum_i (S - a_i^\dagger a_i),\\ \mathcal{H}_{\text{ani}} &= -K_z \sum_i (S - a_i^\dagger a_i)(S - a_i^\dagger a_i) = -K_z \sum_i (S^2 - 2S a_i^\dagger a_i + a_i^\dagger a_i a_i^\dagger a_i).\end{aligned} \tag{3.3}$$

The fourth-order term can be rewritten as $a_i^\dagger a_i a_i^\dagger a_i = a_i^\dagger a_i^\dagger a_i a_i + a_i^\dagger a_i$, which introduces an additional-second order contribution [28, 57]. As a result, the total Hamiltonian up to second order in bosonic operators is [45]

$$\begin{aligned}\mathcal{H} = &- J \sum_{<i,j>} S^2 - h\sum_i S - K_z \sum_i S^2 + JS \sum_{<i,j>} (a_i^\dagger a_i + a_j^\dagger a_j - a_i^\dagger a_j - a_j^\dagger a_i)\\ &+ (h + (2S-1)K_z)\sum_i a_i^\dagger a_i.\end{aligned}$$

The first three terms in the equation contribute a constant energy term that either raises or lowers the energy spectrum. By adjusting the reference energy, we can neglect these terms. By interchanging $i \leftrightarrow j$ in $a_j^\dagger a_j$ and $a_j^\dagger a_i$, the fourth term becomes

$$\begin{aligned}&JS \sum_{<i,j>} (a_i^\dagger a_i + a_j^\dagger a_j - a_i^\dagger a_j - a_j^\dagger a_i)\\ &\qquad = 2JS \sum_{<i,j>} (a_i^\dagger a_i - a_i^\dagger a_j).\end{aligned}$$

We transform the summation indices to $< i, j > \to i, \delta$, where i spans the entire lattice and δ represents the nearest neighbours. To avoid double counting, we divide by 2 to account for this [42]. Here, $\boldsymbol{\delta} = \boldsymbol{R}_j - \boldsymbol{R}_i$ belongs to the set $\{\boldsymbol{\delta}_1, \boldsymbol{\delta}_2, \boldsymbol{\delta}_3, \boldsymbol{\delta}_4\}$. In effect, this implies that

$$\sum_{<i,j>} \to \frac{1}{2}\sum_{i,\delta},$$

such that we are left with a Hamiltonian on the form

$$\begin{aligned}\mathcal{H} &= JS\sum_{i,\delta}(a_i^\dagger a_i - a_i^\dagger a_{i+\delta}) + (h + (2S-1)K_z)\sum_i a_i^\dagger a_i\\ &= (JS\mathcal{Z} + \Delta)\sum_i a_i^\dagger a_i - JS\sum_{i,\delta} a_i^\dagger a_{i+\delta}.\end{aligned}$$

Here, we used that $\sum_{i,\delta} a_i^\dagger a_i = \mathcal{Z}\sum_i a_i^\dagger a_i$ with $\mathcal{Z}$ as the number of nearest neighbours, and we defined $\Delta = h + (2S-1)K_z$. Next, we introduce the Fourier-transformed operators

$$a_i^\dagger = \frac{1}{\sqrt{N}}\sum_k a_k^\dagger \mathrm{e}^{-\mathrm{i}\boldsymbol{k}\cdot\boldsymbol{R}_i}, \quad a_i = \frac{1}{\sqrt{N}}\sum_k a_k \mathrm{e}^{\mathrm{i}\boldsymbol{k}\cdot\boldsymbol{R}_i}, \tag{3.4}$$

where $\boldsymbol{k}$ is the wavevector and N is the number of lattice sites. The operators $a_k^\dagger$ and a_k are bosonic operators in $\boldsymbol{k}-$space that create or annihilate magnon excitations, the quantized spin-waves [45]. By utilizing this expression, the first term transforms to

$$\sum_i a_i^\dagger a_i = \frac{1}{N}\sum_i \sum_{k,k'} a_k^\dagger a_{k'} e^{i(\boldsymbol{k'}-\boldsymbol{k})\cdot \boldsymbol{R}_i} = \sum_{k,k'} a_{k'}^\dagger a_k \delta(\boldsymbol{k}-\boldsymbol{k'}) = \sum_k a_k^\dagger a_k,$$

with the help of relation (2.8). Similarly, the second term becomes

$$\begin{aligned}\sum_{i,\delta} a_i^\dagger a_{i+\delta} &= \frac{1}{N}\sum_{i,\delta}\sum_{k,k'} a_k^\dagger a_{k'} e^{i(\boldsymbol{k'}-\boldsymbol{k})\cdot\boldsymbol{R}_i} e^{i\boldsymbol{k'}\cdot\boldsymbol{\delta}} \\ &= \sum_{k,\delta} a_k^\dagger a_k e^{i\boldsymbol{k}\cdot\boldsymbol{\delta}} = \sum_k a_k^\dagger a_k f(\boldsymbol{k}),\end{aligned}$$

where we defined the structure factor $f(\boldsymbol{k}) = \sum_\delta e^{i\boldsymbol{k}\cdot\boldsymbol{\delta}}$. Thus, the Hamiltonian is reduced to the simple form [42]

$$\begin{aligned}\mathcal{H} &= \sum_k [JS(\mathcal{Z} - f(\boldsymbol{k})) + \Delta] a_k^\dagger a_k \\ &= \sum_k E_k a_k^\dagger a_k.\end{aligned} \tag{3.5}$$

The energy of the magnons is denoted as $E_k = \hbar\omega_k$, where ω_k represents the frequency, and its relation to the wavevector is known as the magnon dispersion relation. In a square lattice, the structure factor is given by

$$f(\boldsymbol{k}) = \sum_\delta e^{i\boldsymbol{k}\cdot\boldsymbol{\delta}} = e^{i\boldsymbol{k}\cdot\boldsymbol{\delta}_1} + e^{i\boldsymbol{k}\cdot\boldsymbol{\delta}_2} + e^{i\boldsymbol{k}\cdot\boldsymbol{\delta}_3} + e^{i\boldsymbol{k}\cdot\boldsymbol{\delta}_4} = 2\cos(k_x a) + 2\cos(k_y a),$$

with a as the lattice constant. The magnon dispersion is then

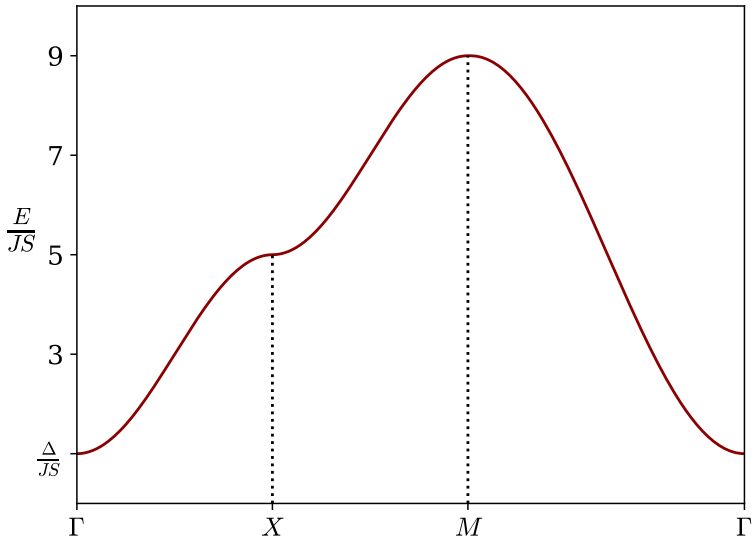

Figure 3.1.: Magnon dispersion in a ferromagnetic square lattice along the symmetry lines of the Brillouin zone, in units of JS. The energy gap is $\Delta/JS = 1$.

$$E_k = JS\left[\mathcal{Z} - 2\cos\left(k_x a\right) - 2\cos\left(k_y a\right)\right] + \Delta, \tag{3.6}$$

with $\mathcal{Z} = 4$ nearest neighbours and the energy gap Δ is proportional to the magnetic field and anisotropy. In the limit of large wavelengths, $|\boldsymbol{k}\cdot\boldsymbol{\delta}| << 1$, the approximation [33]

$$\mathcal{Z} - f(\boldsymbol{k}) \approx \mathcal{Z} - (\mathcal{Z} - \frac{1}{2}\sum_{\delta}(\boldsymbol{k}\cdot\boldsymbol{\delta})^2) = (ka)^2,$$

is valid. Thus, the dispersion in this limit is given by

$$E_k \approx JS(ka)^2 + \Delta, \tag{3.7}$$

and scales quadratically. The dispersion, measured in units of JS, is illustrated in Figure 3.1 along the symmetry lines of the Brillouin zone where $\Delta > 0$. The presence of an energy gap Δ results in an elevation of the entire energy spectrum. This can be explained by the influence of the magnetic field and anisotropy, which increases the energy required to excite magnons. In other words, it becomes more energetically costly to deviate from the ferromagnetic ground state. Additionally, the global minimum is situated at the Γ-point where $\boldsymbol{k} = 0$. This corresponds to the uniform mode, where all spins undergo precession with the same phase.

The angular momentum of a specific spin-wave with wavevector $\boldsymbol{k}$ can be determined by evaluating the expectation value of S_z in the state $a_k^\dagger\left|0\right\rangle$. The $z-$component of the spin may be written as

$$S_z = \sum_i S_{iz} = \sum_i (S - a_i^\dagger a_i) = SN - \sum_k a_k^\dagger a_k,$$

such that the angular momentum is

$$\begin{aligned}
\left\langle 0\right| a_k S_z a_k^\dagger \left|0\right\rangle &= SN\left\langle 0\right| a_k a_k^\dagger \left|0\right\rangle - \sum_{k'}\left\langle 0\right| a_k a_{k'}^\dagger a_{k'} a_k^\dagger \left|0\right\rangle \\
&= SN\left\langle 0\right| a_k a_k^\dagger \left|0\right\rangle - \sum_{k'}\left\langle 0\right| a_k a_{k'}^\dagger(\delta(\boldsymbol{k}-\boldsymbol{k'}) + a_k^\dagger a_{k'}) \left|0\right\rangle \\
&= (SN-1)\left\langle 0\right| a_k a_k^\dagger \left|0\right\rangle = SN - 1.
\end{aligned} \tag{3.8}$$

Here we used that $a_k\left|0\right\rangle = 0$ and the result is in units of $\hbar$. The generation of a single magnon causes a reduction of the total angular momentum by $\hbar$. In a semiclassical view, flipping a single spin in a ferromagnetic lattice with an ordered arrangement leads to an angular momentum of $S_z = \hbar S(N-2)$. This implies that the creation of a single magnon, with $S = 1/2$, corresponds to the same angular momentum as flipping a single spin [3]. Consequently, a magnon can be regarded as a collective excitation where a single spin flip is spread out over multiple lattice sites, giving rise to a spin-wave.

3.3.2. Honeycomb lattice

In order to calculate the magnon dispersion in a honeycomb lattice, we utilize the Hamiltonian presented in equation (3.1), which includes the DMI. Specifically, we allow for a next-nearest neighbour (NNN) DMI with an out-of-plane DM vector, as the midpoints of the second neighbouring bonds lack inversion symmetry [47]. Inspired by the Haldane model in electronic systems, we express the DM vector as $\boldsymbol{D}_{ij} = D_z^{\text{nnn}}\nu_{ij}\hat{\boldsymbol{z}}$ [12, 27, 55], where the Haldane sign is determined by $\nu_{ij} = \pm 1$ between next-nearest neighbours that are oriented clockwise and counterclockwise to each other, as depicted in Figure 3.2. Utilizing this expression, the DMI-part of the Hamiltonian is

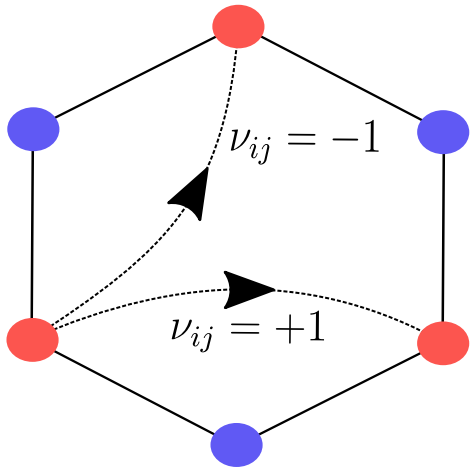

Figure 3.2.: An illustration of how the Haldane sign can be either $\nu_{ij} = +1$ or $\nu_{ij} = -1$ between next-nearest neighbours that are oriented clockwise or counterclockwise to each other. The illustration draws inspiration from Ref. [12].

$$\begin{aligned}\mathcal{H}_{\mathrm{DMI}} &= -D_z^{\mathrm{nnn}} \sum_{<<i,j>>} \nu_{ij}\hat{\boldsymbol{z}} \cdot [\boldsymbol{S_i} \times \boldsymbol{S_j}] \\ &= -D_z^{\mathrm{nnn}} \sum_{<<i,j>>} \nu_{ij}(S_{ix}S_{jy} - S_{iy}S_{jx}) = \mathrm{i}\frac{D_z^{\mathrm{nnn}}}{2} \sum_{<<i,j>>} \nu_{ij}(S_{i-}S_{j+} - S_{i+}S_{j-}).\end{aligned} \tag{3.9}$$

The honeycomb lattice, with a 2-atomic basis, is expected to exhibit two magnon branches. It is beneficial to separate the lattice into two sublattices, A and B, each associated with spins $\boldsymbol{S}_{iA}$ and $\boldsymbol{S}_{iB}$, respectively, as well as the corresponding bosonic operators a_i and b_i. In order to avoid double counting, the summation $\sum_{<i,j>}$ is transformed into $\sum_{i,\delta_A}$, where i iterates over the sites in sublattice A, and $\boldsymbol{\delta}_A \in \{\boldsymbol{\delta}_1^A, \boldsymbol{\delta}_2^A, \boldsymbol{\delta}_3^A\}$ represents the vectors to the nearest neighbouring atoms based on sublattice A [58]. Moreover, the summation involving pairs of next-nearest neighbours is transformed to [58]

$$\begin{aligned}\sum_{<<i,j>>} &= \sum_{\substack{<<i,j>> \\ i\in A}} + \sum_{\substack{<<i,j>> \\ i\in B}} \\ &= \frac{1}{2}\sum_{\substack{i,\tau_A \\ i\in A}} + \frac{1}{2}\sum_{\substack{i,\tau_B \\ i\in B}},\end{aligned}$$

where $\boldsymbol{\tau}_A \in \{\boldsymbol{\tau}_1^A, \boldsymbol{\tau}_2^A, \boldsymbol{\tau}_3^A, \boldsymbol{\tau}_4^A, \boldsymbol{\tau}_5^A, \boldsymbol{\tau}_6^A\}$ are the vectors to the next-nearest neighbours based on sublattice A and similarly are $\boldsymbol{\tau}_B$ based on sublattice B. The Hamiltonian is split into the following

$$\begin{aligned}\mathcal{H} =& -J\sum_{\substack{i,\delta_A \\ i\in A}}[S_{iAz}S_{i+\delta_A,Bz} + \frac{1}{2}(S_{iA+}S_{i+\delta_A,B-} + S_{iA-}S_{i+\delta_A,B+})] - h\sum_{\substack{i \\ i\in A}} S_{iAz} - K_z\sum_{\substack{i \\ i\in A}} S_{iAz}^2 \\ &+ \mathrm{i}\frac{D_z^{\mathrm{nnn}}}{4}\sum_{\substack{i,\tau_A \\ i\in A}} \nu_{\tau_A}(S_{iA-}S_{i+\tau_A,A+} - S_{iA+}S_{i+\tau_A,A-}) - h\sum_{\substack{i \\ i\in B}} S_{iBz} - K_z\sum_{\substack{i \\ i\in B}} S_{iBz}^2 \\ &+ \mathrm{i}\frac{D_z^{\mathrm{nnn}}}{4}\sum_{\substack{i,\tau_B \\ i\in B}} \nu_{\tau_B}(S_{iB-}S_{i+\tau_B,B+} - S_{iB+}S_{i+\tau_B,B-}).\end{aligned} \tag{3.10}$$

The Haldane sign solely depends on the relative vector connecting the sites. Specifically, for the summation over sublattice A or B, we have $\nu_{ij} = \nu_{\tau_A}$ or $\nu_{ij} = \nu_{\tau_B}$, respectively. By employing the Holstein-Primakoff transformation and disregarding the constants, we can express the Hamiltonian in terms of bosonic operators as follows

$$\begin{aligned}\mathcal{H} = JS\sum_{\substack{i,\delta_A\\ i\in A}}(a_i^\dagger a_i + b_{i+\delta_A}^\dagger b_{i+\delta_A} - a_i^\dagger b_{i+\delta_A} - b_{i+\delta_A}^\dagger a_i) + \Delta\sum_{\substack{i\\ i\in A}} a_i^\dagger a_i + \Delta\sum_{\substack{i\\ i\in B}} b_i^\dagger b_i \\ + \mathrm{i}\frac{D_z^{\mathrm{nnn}}S}{2}\sum_{\substack{i,\tau_A\\ i\in A}}\nu_{\tau_A}(a_i^\dagger a_{i+\tau_A} - a_{i+\tau_A}^\dagger a_i) + \mathrm{i}\frac{D_z^{\mathrm{nnn}}S}{2}\sum_{\substack{i,\tau_B\\ i\in B}}\nu_{\tau_B}(b_i^\dagger b_{i+\tau_B} - b_{i+\tau_B}^\dagger b_i).\end{aligned}$$

By substituting the Fourier-transformed bosonic operators, where a normalization factor of $\sqrt{2/N}$ is included due to the summation being limited to a single sublattice, the non-DMI part of the Hamiltonian becomes

$$\begin{aligned}\mathcal{H}_{\text{non-DMI}} &= JS\sum_k\sum_{\delta_A}(a_k^\dagger a_k + b_k^\dagger b_k - a_k^\dagger b_k \mathrm{e}^{\mathrm{i}\boldsymbol{k}\cdot\boldsymbol{\delta}_A} - b_k^\dagger a_k \mathrm{e}^{-\mathrm{i}\boldsymbol{k}\cdot\boldsymbol{\delta}_A}) + \Delta\sum_k a_k^\dagger a_k + \Delta\sum_k b_k^\dagger b_k \\ &= \sum_k\left[(JS\mathcal{Z}+\Delta)(a_k^\dagger a_k + b_k^\dagger b_k) - JSf_{\delta_A}(\boldsymbol{k})a_k^\dagger b_k - JSf_{\delta_A}^*(\boldsymbol{k})b_k^\dagger a_k\right],\end{aligned}$$

where the structure factor is defined by $f_{\delta_A}(\boldsymbol{k}) = \sum_{\delta_A}\mathrm{e}^{\mathrm{i}\boldsymbol{k}\cdot\boldsymbol{\delta}_A}$. Continuing, the DMI contribution to the Hamiltonian for sublattice A becomes

$$\begin{aligned}\mathcal{H}_{\mathrm{DMI}}^A =& \mathrm{i}\frac{D_z^{\mathrm{nnn}}S}{2}\frac{2}{N}\sum_{\substack{i,\tau_A\\ i\in A}}\sum_{k,k'}\nu_{\tau_A}(a_k^\dagger a_{k'}\mathrm{e}^{\mathrm{i}(\boldsymbol{k}'-\boldsymbol{k})\cdot\boldsymbol{R}_i}\mathrm{e}^{\mathrm{i}\boldsymbol{k}'\cdot\boldsymbol{\tau}_A} - a_k^\dagger a_{k'}\mathrm{e}^{\mathrm{i}(\boldsymbol{k}'-\boldsymbol{k})\cdot\boldsymbol{R}_i}\mathrm{e}^{-\mathrm{i}\boldsymbol{k}\cdot\boldsymbol{\tau}_A}) \\ =& \mathrm{i}\frac{D_z^{\mathrm{nnn}}S}{2}\sum_{k,\tau_A}\nu_{\tau_A}a_k^\dagger a_k 2\mathrm{i}\sin(\boldsymbol{k}\cdot\boldsymbol{\tau}_A) \\ =& \sum_k SD_{\tau_A}(\boldsymbol{k})a_k^\dagger a_k, \quad D_{\tau_A}(\boldsymbol{k}) = -D_z^{\mathrm{nnn}}\sum_{\tau_A}\nu_{\tau_A}\sin(\boldsymbol{k}\cdot\boldsymbol{\tau}_A).\end{aligned}$$

The DMI contribution for sublattice B is found by switching $A \leftrightarrow B$ and $a_k \leftrightarrow b_k$ in the obtained result for sublattice A. The entire Hamiltonian is then

$$\begin{aligned}\mathcal{H} = \sum_k\Big[&(JS\mathcal{Z}+\Delta+SD_{\tau_A}(\boldsymbol{k}))a_k^\dagger a_k + (JS\mathcal{Z}+\Delta+SD_{\tau_B}(\boldsymbol{k}))b_k^\dagger b_k \\ &-JSf_{\delta_A}(\boldsymbol{k})a_k^\dagger b_k - JSf_{\delta_A}^*(\boldsymbol{k})b_k^\dagger a_k\Big].\end{aligned}$$

It can be easily be verified that $D_{\tau_A}(\boldsymbol{k}) = -D_{\tau_B}(\boldsymbol{k})$. This relationship holds because $\boldsymbol{\tau}_A$ and $\boldsymbol{\tau}_B$ encompass the same vectors set, but the Haldane sign for sublattice B is the negative counterpart of sublattice A. By exploiting this symmetry, the Hamiltonian simplifies to

$$\mathcal{H} = \sum_k \boldsymbol{\psi}_k^\dagger H_{\mathrm{m}}(\boldsymbol{k})\boldsymbol{\psi}_k, \quad H_{\mathrm{m}}(\boldsymbol{k}) = \begin{bmatrix} JS\mathcal{Z}+\Delta+SD_{\tau_A}(\boldsymbol{k}) & -JSf_{\delta_A}(\boldsymbol{k}) \\ -JSf_{\delta_A}^*(\boldsymbol{k}) & JS\mathcal{Z}+\Delta-SD_{\tau_A}(\boldsymbol{k})\end{bmatrix}, \tag{3.11}$$

with $\boldsymbol{\psi}_k = [a_k, b_k]^T$ as the basis. The eigenvalues are given by [55, 59]

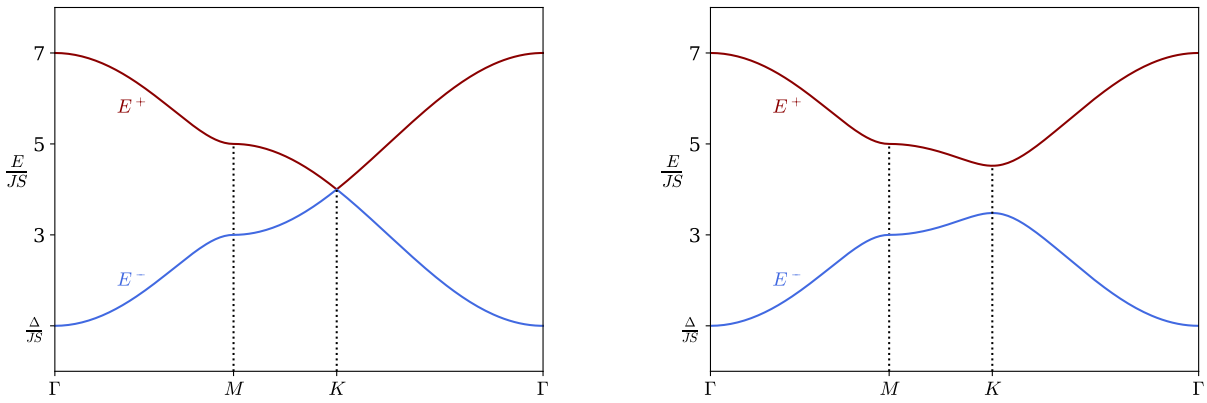

(a) $D_z^{\text{nnn}}/J = 0.$ **(b)** $D_z^{\text{nnn}}/J = 0.1.$

Figure 3.3.: Magnon dispersion in a ferromagnetic honeycomb lattice along the symmetry lines of the Brillouin zone, in units of JS. The dispersion is shown with the energy gap $\Delta/JS = 1$ both with and without DMI present.

$$E_k^{\pm} = JS\left(\mathcal{Z} \pm \sqrt{\frac{D_{\tau_A}^2(\boldsymbol{k})}{J^2} + |f_{\delta_A}(\boldsymbol{k})|^2}\right) + \Delta, \tag{3.12}$$

where $\mathcal{Z} = 3$ and

$$\begin{aligned}
f_{\delta_A}(\boldsymbol{k}) &= \mathrm{e}^{\mathrm{i}\boldsymbol{k}\cdot\boldsymbol{\delta}_1^A} + \mathrm{e}^{\mathrm{i}\boldsymbol{k}\cdot\boldsymbol{\delta}_2^A} + \mathrm{e}^{\mathrm{i}\boldsymbol{k}\cdot\boldsymbol{\delta}_3^A} \\
&= \mathrm{e}^{\frac{\mathrm{i}}{\sqrt{3}}k_y a} + 2\cos(\frac{1}{2}k_x a)\mathrm{e}^{-\frac{\mathrm{i}}{2\sqrt{3}}k_y a}, \\
\implies |f_{\delta_A}(\boldsymbol{k})|^2 &= 1 + 4\cos(\frac{1}{2}k_x a)\left(\cos(\frac{1}{2}k_x a) + \cos(\frac{\sqrt{3}}{2}k_y a)\right), \\
D_{\tau_A}(\boldsymbol{k}) &= -D_z^{\text{nnn}}\left(\sin(\boldsymbol{k}\cdot\boldsymbol{\tau}_1^A) - \sin(\boldsymbol{k}\cdot\boldsymbol{\tau}_2^A) + \sin(\boldsymbol{k}\cdot\boldsymbol{\tau}_3^A) - \sin(\boldsymbol{k}\cdot\boldsymbol{\tau}_4^A) + \sin(\boldsymbol{k}\cdot\boldsymbol{\tau}_5^A) - \sin(\boldsymbol{k}\cdot\boldsymbol{\tau}_6^A)\right) \\
&= -2D_z^{\text{nnn}}\left(\sin(k_x a) - 2\sin(\frac{1}{2}k_x a)\cos(\frac{\sqrt{3}}{2}k_y a)\right).
\end{aligned} \tag{3.13}$$

The corresponding eigenvectors are

$$\hat{\boldsymbol{e}}^{\pm}(\boldsymbol{k}) = \frac{\left[Jf_{\delta_A}(\boldsymbol{k}), D_{\tau_A}(\boldsymbol{k}) \mp \sqrt{D_{\tau_A}^2(\boldsymbol{k}) + J^2|f_{\delta_A}(\boldsymbol{k})|^2}\right]^T}{\left[J^2|f_{\delta_A}(\boldsymbol{k})|^2 + \left(D_{\tau_A}(\boldsymbol{k}) \mp \sqrt{D_{\tau_A}^2(\boldsymbol{k}) + J^2|f_{\delta_A}(\boldsymbol{k})|^2}\right)^2\right]^{1/2}}.$$

Denoting α_k as the linear combination of a_k and b_k that diagonalizes the Hamiltonian with eigenvalue E_k^+, and similarly β_k with the eigenvalue E_k^-, the transformation to the new basis can be expressed as

$$\begin{bmatrix}\alpha_k \\ \beta_k\end{bmatrix} = U_{\text{m}}^{\dagger}(\boldsymbol{k})\begin{bmatrix}a_k \\ b_k\end{bmatrix}, \quad U_{\text{m}}(\boldsymbol{k}) = [\hat{\boldsymbol{e}}^+(\boldsymbol{k}), \hat{\boldsymbol{e}}^-(\boldsymbol{k})],$$

and $U_{\mathrm{m}}(\boldsymbol{k})$ is an unitary matrix. The calculated normal modes of the system, $\{\alpha_k, \beta_k\}$, have been found to fulfill the bosonic commutation relation.

In the absence of DMI, the dispersion simplifies to

$$E_k^{\pm} = JS(\mathcal{Z} \pm |f_{\delta_A}(\boldsymbol{k})|) + \Delta.$$

The E_k^- branch exhibit a similar dispersion relation to the one observed in the square lattice (equation (3.5)), albeit with a distinct structure factor. Correspondingly, the eigenvectors are simplified to $\hat{\boldsymbol{e}}^{\pm}(\boldsymbol{k}) = (1/\sqrt{2})[\mathrm{e}^{\mathrm{i}\phi_k/2}, \mp\mathrm{e}^{-\mathrm{i}\phi_k/2}]^T$, with $\phi_k = \arg(f_{\delta_A}(\boldsymbol{k}))$. In the limit of small wavevectors ($|\boldsymbol{k}| \to 0$), it becomes apparent that the E_k^+ mode is asymmetric, causing the two sublattices to possess in-plane spin components pointing in opposite directions. On the other hand, the E_k^- mode is symmetric, representing a uniform precession of the entire lattice in the same direction.

The dimensionless dispersion along the symmetry lines of the Brillouin zone is illustrated in Figure 3.3 with and without the presence of DMI. Like the magnon spectrum in the ferromagnetic square lattice, the magnon spectrum is lifted by Δ. In the absence of DMI, a Dirac cone emerges at the $K-$point, as seen in Figure 3.3a. The two branches are degenerate and have a linear dispersion at this point, creating a Dirac point. We can demonstrate the linear relationship by Taylor expanding the dispersion around this point. We find that $|f_{\delta_A}(\boldsymbol{u})| \approx \frac{\sqrt{3}}{2}a|\boldsymbol{u}|$, where $\boldsymbol{u} = \boldsymbol{k} - \boldsymbol{K}$, suggesting that $E_k^{\pm} \sim k$. As a result, the effective Hamiltonian is the massless 2D Dirac equation [47], hence the name. Similar to how an external magnetic field breaks the time-reversal symmetry, the ferromagnetic ordering of spins also breaks the time-reversal symmetry. However, there may be an *effective* time-reversal symmetry that remains intact, consisting of a combined time-reversal symmetry and either a crystal symmetry or a lattice translation that preserves the magnetic unit cell [60]. As long as the effective time-reversal symmetry is preserved, the Dirac points will remain [47].

In the presence of DMI, the situation changes, as illustrated in Figure 3.3b, and a band gap emerges due to the broken inversion symmetry caused by DMI. The size of the band gap at the $K-$point is determined to be $\Delta_{\mathrm{K}} = 6\sqrt{3}D_z^{\mathrm{nnn}}S$. The presence of a band gap in the system leads to an intriguing feature called Berry curvature, which can give rise to the emergence of topological magnons. Chapter 5 will provide a more in-depth exploration of this concept, specifically focusing on the principles of topological band theory.

We evaluate the expectation value of the angular momentum S_z in each normal mode. The expression for S_z is given by

$$\begin{aligned} S_z &= \sum_{\substack{i \\ i\in A}} S_{iAz} + \sum_{\substack{i \\ i\in B}} S_{iBz} = \frac{1}{2}SN - \sum_{\substack{i \\ i\in A}} a_i^\dagger a_i + \frac{1}{2}SN - \sum_{\substack{i \\ i\in B}} b_i^\dagger b_i \\ &= SN - \sum_k (a_k^\dagger a_k + b_k^\dagger b_k) = SN - \sum_k (\alpha_k^\dagger \alpha_k + \beta_k^\dagger \beta_k). \end{aligned}$$

Hence, the expectation value of S_z in the state $\alpha_k^\dagger |0\rangle$ and $\beta_k^\dagger |0\rangle$ is

$$\langle 0| \alpha_k S_z \alpha_k^\dagger |0\rangle = SN - 1, \quad \langle 0| \beta_k S_z \beta_k^\dagger |0\rangle = SN - 1.$$

As expected, the magnon excitation decreases the angular momentum by an equivalent amount as described in equation (3.8) for the ferromagnetic square lattice.

3.4. Calculation of antiferromagnetic magnon dispersion

We calculate the magnon dispersion for the antiferromagnetic square and honeycomb lattices using the nearest neighbour Heisenberg exchange interaction. In this case, the exchange coupling coefficient J is negative ($J < 0$), resulting in antiferromagnetic ordering of the spins. In the Hamiltonian, as depicted in equation (3.1), the DMI term is exclusively included for the honeycomb lattice.

We examine an antiferromagnetic system with a checkerboard-like arrangement, where spins at nearest neighbouring sites exhibit opposite ordering. This arrangement is illustrated for the square lattice in Figure 3.4. Consequently, we can divide the lattice into two sublattices, A and B, with their belonging spins $\boldsymbol{S}_{iA}$ and $\boldsymbol{S}_{iB}$ and corresponding bosonic operators a_i and b_i. By assigning up-spins to sublattice A and down-spins to sublattice B, we establish a classical ground state with $\boldsymbol{S}_{iA} = S\hat{\boldsymbol{z}}$ and $\boldsymbol{S}_{iB} = -S\hat{\boldsymbol{z}}$. To analyze the system using bosonic operators, we apply the Holstein-Primakoff transformation, which, at the lowest order, takes the following form

$$\begin{aligned} S_{iA+} &= \sqrt{2S}a_i, & S_{iB+} &= \sqrt{2S}b_i^\dagger, \\ S_{iA-} &= \sqrt{2S}a_i^\dagger, & S_{iB-} &= \sqrt{2S}b_i, \\ S_{iAz} &= S - a_i^\dagger a_i, & S_{iBz} &= -S + b_i^\dagger b_i, \end{aligned} \tag{3.14}$$

and we define the Fourier-transformed operators as

$$\begin{aligned} a_i^\dagger &= \sqrt{\frac{2}{N}}\sum_k a_k^\dagger \mathrm{e}^{-\mathrm{i}\boldsymbol{k}\cdot\boldsymbol{R}_i}, \quad a_i = \sqrt{\frac{2}{N}}\sum_k a_k \mathrm{e}^{\mathrm{i}\boldsymbol{k}\cdot\boldsymbol{R}_i}, \\ b_i^\dagger &= \sqrt{\frac{2}{N}}\sum_k b_k^\dagger \mathrm{e}^{\mathrm{i}\boldsymbol{k}\cdot\boldsymbol{R}_i}, \quad b_i = \sqrt{\frac{2}{N}}\sum_k b_k \mathrm{e}^{-\mathrm{i}\boldsymbol{k}\cdot\boldsymbol{R}_i}. \end{aligned} \tag{3.15}$$

3.4.1. Square lattice

Similar to before, we transform the summation $\sum_{<i,j>}$ to $\sum_{i,\delta}$, where i solely belongs to sublattice A. This allows us to write the Hamiltonian as

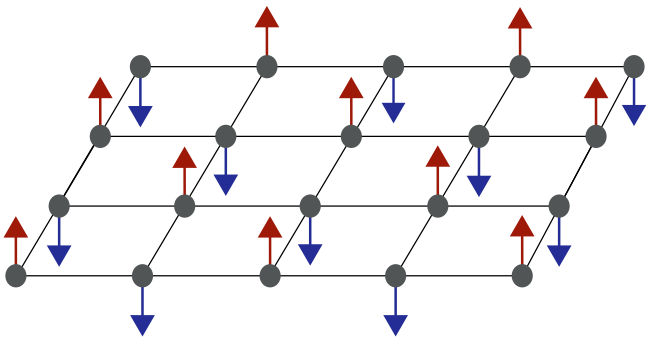

Figure 3.4.: Illustration of the magnetic ordering in the square checkerboard-type antiferromagnet. The direction of the spins is out of the lattice plane where the two sublattices, marked in red and blue, have an opposing arrangement.

$$\begin{aligned}\mathcal{H} = &- J \sum_{\substack{i,\delta \\ i\in A}} [S_{iAz}S_{i+\delta,Bz} + \frac{1}{2}(S_{iA+}S_{i+\delta,B-} + S_{iA-}S_{i+\delta,B+})] - h\sum_{\substack{i \\ i\in A}} S_{iAz} - K_z \sum_{\substack{i \\ i\in A}} S_{iAz}^2 \\ &- h\sum_{\substack{i \\ i\in B}} S_{iBz} - K_z \sum_{\substack{i \\ i\in B}} S_{iBz}^2.\end{aligned}$$

By inserting the Holstein-Primakoff transformation and omitting the constant terms, we obtain

$$\mathcal{H} = - JS \sum_{\substack{i,\delta \\ i\in A}} (a_i^\dagger a_i + b_{i+\delta}^\dagger b_{i+\delta} + a_i^\dagger b_{i+\delta}^\dagger + a_i b_{i+\delta}) + (\mathcal{K}+h)\sum_{\substack{i \\ i\in A}} a_i^\dagger a_i + (\mathcal{K}-h)\sum_{\substack{i \\ i\in B}} b_i^\dagger b_i, \tag{3.16}$$

with $\mathcal{K} = (2S-1)K_z$. By utilizing the magnon operators in $\boldsymbol{k}-$space, we can express the Hamiltonian in terms of these operators. The diagonal terms are transformed as

$$\sum_{\substack{i \\ i\in A}} a_i^\dagger a_i = \sum_k a_k^\dagger a_k, \quad \sum_{\substack{i \\ i\in B}} b_i^\dagger b_i = \sum_k b_k^\dagger b_k.$$

Likewise, the off-diagonal terms become

$$\begin{aligned}\sum_{\substack{i,\delta \\ i\in A}} (a_i b_{i+\delta} + a_i^\dagger b_{i+\delta}^\dagger) =& \frac{2}{N}\sum_{\substack{i,\delta \\ i\in A}}\sum_{k,k'} \left(a_k b_{k'} \mathrm{e}^{\mathrm{i}(\boldsymbol{k}-\boldsymbol{k'})\cdot\boldsymbol{R}_i} \mathrm{e}^{-\mathrm{i}\boldsymbol{k'}\cdot\boldsymbol{\delta}} + a_k^\dagger b_{k'}^\dagger \mathrm{e}^{-\mathrm{i}(\boldsymbol{k}-\boldsymbol{k'})\cdot\boldsymbol{R}_i} \mathrm{e}^{\mathrm{i}\boldsymbol{k'}\cdot\boldsymbol{\delta}} \right) \\ =& \sum_k \left(a_k b_k f^*(\boldsymbol{k}) + a_k^\dagger b_k^\dagger f(\boldsymbol{k}) \right).\end{aligned} \tag{3.17}$$

As the structure factor for the square lattice is a real quantity, we end up with

$$\begin{aligned}\mathcal{H} =& \sum_k \left[(\kappa+h) a_k^\dagger a_k + (\kappa-h) b_k^\dagger b_k - JSf(\boldsymbol{k})(a_k b_k + a_k^\dagger b_k^\dagger) \right] \\ =& \sum_k \boldsymbol{\psi}_k^\dagger H_{\mathrm{m}}(\boldsymbol{k}) \boldsymbol{\psi}_k, \quad H_{\mathrm{m}}(\boldsymbol{k}) = \begin{bmatrix} \kappa+h & -JSf(\boldsymbol{k}) \\ -JSf(\boldsymbol{k}) & \kappa-h \end{bmatrix}, \quad \boldsymbol{\psi}_k = [a_k, b_k^\dagger]^T.\end{aligned}$$

where $\kappa = -JS\mathcal{Z} + \mathcal{K}$. The Hamiltonian contains terms like $a_k b_k$ and $a_k^\dagger b_k^\dagger$, which suggests that these operators do not represent long-lived quantized spin-excitations [33]. In order to diagonalize the Hamiltonian, we perform a Bogoliubov transformation. This is done by introducing the bosonic operators α_k and β_k, defined by

$$\begin{aligned}\alpha_k &= u_k a_k + v_k b_k^\dagger, & \alpha_k^\dagger &= u_k a_k^\dagger + v_k b_k, \\ \beta_k &= v_k a_k^\dagger + u_k b_k, & \beta_k^\dagger &= v_k a_k + u_k b_k^\dagger,\end{aligned}$$

where the Bogoliubov coefficients (u_k, v_k) are yet to be determined. To ensure that the new operators are bosonic, they must satisfy the commutation relation $[\alpha_k, \alpha_{k'}^\dagger] = \delta(\boldsymbol{k}-\boldsymbol{k'})$, and the same applies for β_k. This condition is met when the following equation hold

$$\begin{aligned}[u_k a_k + v_k b_{-k}^\dagger, u_{k'} a_{k'}^\dagger + v_{k'} b_{-k'}] &= u_k u_{k'} [a_k, a_{k'}^\dagger] + v_k v_{k'} [b_{-k}^\dagger, b_{-k'}] \\ &= \delta(\boldsymbol{k}-\boldsymbol{k'})(u_k^2 - v_k^2) \quad \implies u_k^2 - v_k^2 = 1.\end{aligned} \tag{3.18}$$

The inverse relations are

$$\begin{bmatrix} a_k \\ b_k^\dagger \end{bmatrix} = \begin{bmatrix} u_k & -v_k \\ -v_k & u_k \end{bmatrix} \begin{bmatrix} \alpha_k \\ \beta_k^\dagger \end{bmatrix}, \tag{3.19}$$

such that the Hamiltonian, expressed in terms of the new bosonic operators, is on the form

$$\begin{aligned} \mathcal{H} = \sum_k \Big[& 2\kappa v_k^2 + 2JSf(\boldsymbol{k})u_k v_k + (\kappa(u_k^2 + v_k^2) + h + 2JSf(\boldsymbol{k})u_k v_k)\alpha_k^\dagger \alpha_k \\ & + (\kappa(u_k^2 + v_k^2) - h + 2JSf(\boldsymbol{k})u_k v_k)\beta_k^\dagger \beta_k \Big], \end{aligned} \tag{3.20}$$

where the coefficients in front of the terms $\alpha_k\beta_k$ and $\alpha_k^\dagger\beta_k^\dagger$ are set equal to zero. To be more specific, u_k and v_k must satisfy the equation

$$|J|Sf(\boldsymbol{k})(u_k^2 + v_k^2) = 2\kappa u_k v_k. \tag{3.21}$$

With the help of relation (3.18), the equation is solved with

$$u_k^2 = \frac{1}{2}\left(1 + \frac{\kappa}{\sqrt{\kappa^2 - J^2S^2f^2(\boldsymbol{k})}}\right), \quad v_k^2 = \frac{1}{2}\left(-1 + \frac{\kappa}{\sqrt{\kappa^2 - J^2S^2f^2(\boldsymbol{k})}}\right),$$
$$\text{and} \qquad u_k v_k = \frac{|J|Sf(\boldsymbol{k})}{2\sqrt{\kappa^2 - J^2S^2f^2(\boldsymbol{k})}}.$$

The first two terms in the Hamiltonian, as given in equation (3.20), represent a quantum correction to the classical magnetization and arise from the bosonic commutation relation [33]. Since these terms do not contribute to the magnon dispersion, they can be omitted. Therefore, the diagonalized Hamiltonian is expressed as follows

$$\begin{aligned} \mathcal{H} &= \sum_k \left[(\sqrt{\kappa^2 - J^2S^2f^2(\boldsymbol{k})} + h)\alpha_k^\dagger \alpha_k + (\sqrt{\kappa^2 - J^2S^2f^2(\boldsymbol{k})} - h)\beta_k^\dagger \beta_k \right], \\ &= \sum_k \left[E_k^+ \alpha_k^\dagger \alpha_k + E_k^- \beta_k^\dagger \beta_k \right]. \end{aligned}$$

The dispersion relations for the Bogoliubov quasiparticles are then

$$E_k^+ = |J|S\sqrt{(\mathcal{Z} + \frac{\mathcal{K}}{|J|S})^2 - f^2(\boldsymbol{k})} + h, \qquad E_k^- = |J|S\sqrt{(\mathcal{Z} + \frac{\mathcal{K}}{|J|S})^2 - f^2(\boldsymbol{k})} - h, \tag{3.22}$$

where $f(\boldsymbol{k}) = 2\cos(k_x a) + 2\cos(k_y a)$ and $\mathcal{Z} = 4$. This is in accordance with the findings in Ref. [61], with the exception of the anisotropy term, which is $\mathcal{K} = 2SK_z$ and does not account for the contribution from the fourth-order term presented in equation (3.3). Figure 3.5a illustrates the dimensionless dispersion along the symmetry lines of the Brillouin zone with $h/(|J|S) = 1$ and $\mathcal{K}/(|J|S) = 0.2$. The Bogoliubov quasiparticles, which are linear combinations of the original bosonic operators, exhibit minima at the Γ-point and all corners of the Brillouin zone where $f^2(\boldsymbol{k}) = \mathcal{Z}^2$.

By examining the influence of anisotropy, we investigating two scenarios: one where $h = 0$ without

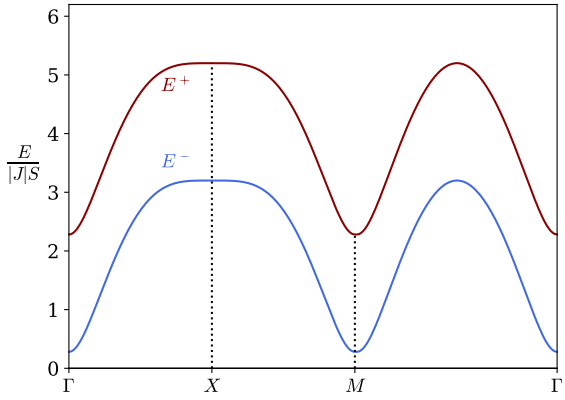

(a) $h/(|J|S) = 1$ and $\mathcal{K}/(|J|S) = 0.2$.

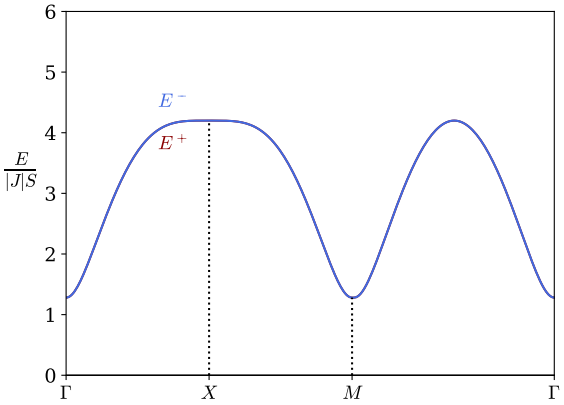

(b) $h/(|J|S) = 0$ and $\mathcal{K}/(|J|S) = 0.2$.

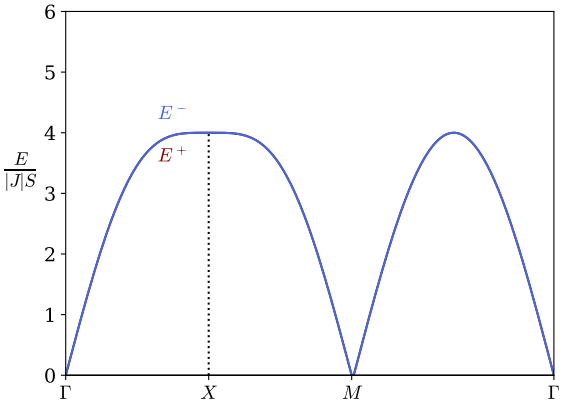

(c) $h/(|J|S) = 0$ and $\mathcal{K}/(|J|S) = 0$.

Figure 3.5.: Magnon dispersion in an antiferromagnetic square lattice along the symmetry lines of the Brillouin zone, with different values of the magnetic field and anisotropy strength, in units of $|J|S$.

anisotropy, and the other with the presence of anisotropy. This comparison is depicted in Figure 3.5b and 3.5c. The introduction of anisotropy results in a general energy increase and a quadratic dependence of E_k in the vicinity of the minima. In simpler terms, the anisotropy requires more energy to excite magnons and deviate from the Néel ground state, similar to the observations made in the ferromagnetic scenario. When expanding the dispersions around the Γ-point with $K_z = 0$, we observe that the dispersions scale linearly, as seen from the following equations

$$E_k^+ \approx |J|S\sqrt{2\mathcal{Z}}|k|a + h, \quad E_k^- \approx |J|S\sqrt{2\mathcal{Z}}|k|a - h.$$

This is in contrast to the ferromagnetic case where the dispersion scales quadratically regardless of the presence of anisotropy, as described in equation (3.7).

The two modes, E_k^+ and E_k^-, can be distinguished by their opposite chirality. The E_k^+ mode is characterized by right-handed spins while the E_k^- mode possesses left-handed spins. This distinction can be demonstrated by evaluating the expectation value of S_z for each mode, as done in Ref. [14,

57]. The $z-$component of the total spin can be written like

$$\begin{aligned} S_z &= \sum_{\substack{i \\ i\in A}} S_{iAz} + \sum_{\substack{i \\ i\in B}} S_{iBz} = \frac{1}{2}SN - \sum_{\substack{i \\ i\in A}} a_i^\dagger a_i - \frac{1}{2}SN + \sum_{\substack{i \\ i\in B}} b_i^\dagger b_i \\ &= \sum_k (-a_k^\dagger a_k + b_k^\dagger b_k) = \sum_k (-\alpha_k^\dagger \alpha_k + \beta_k^\dagger \beta_k), \end{aligned}$$

after substituting the Holstein-Primakoff and Bogoliubov transformation. The expectation value in each mode is then

$$\langle 0|\, \alpha_k S_z \alpha_k^\dagger \,|0\rangle = -1, \quad \langle 0|\, \beta_k S_z \beta_k^\dagger \,|0\rangle = +1, \tag{3.23}$$

with the corresponding angular momentum $\mp\hbar$. The next step is to establish a connection between angular momentum and chirality. This can be achieved by calculating the resonance frequencies using a macrospin approximation, where the magnetization of each sublattice is given by $\boldsymbol{m}_{A(B)} = \frac{1}{2} g_J \mu_B N \boldsymbol{S}_{A(B)}$, similar to the approach outlined in Ref. [61]. The resonance frequency corresponds to the frequency of the uniform precession modes, where the wavevector is $\boldsymbol{k} = 0$. The energy per unit volume is

$$E = -B_0(m_{Az} + m_{Bz}) + \frac{H_E}{m}(\boldsymbol{m}_A \cdot \boldsymbol{m}_B) - \frac{H_{\text{ani}}}{2m}(m_{Az}^2 + m_{Bz}^2),$$

where $H_E = \frac{|J|SZ}{g_J \mu_B}$, $H_{\text{ani}} = \frac{2SK_z}{g_J \mu_B}$ and m is the saturation magnetization at zero temperature, equal for both sublattices. We solve the Landau-Lifshitz equation

$$\begin{aligned} \frac{\mathrm{d}\boldsymbol{m}_{A(B)}}{\mathrm{d}t} &= \gamma \boldsymbol{m}_{A(B)} \times \boldsymbol{\mathcal{H}}_{\text{eff}}^{A(B)}, \\ \boldsymbol{\mathcal{H}}_{\text{eff}}^{A(B)} &= -\nabla_{\boldsymbol{m}_{A(B)}} E(\boldsymbol{m}_A, \boldsymbol{m}_B) \\ &= (B_0 + \frac{H_{\text{ani}}}{m} m_{A(B)z})\hat{\boldsymbol{z}} - \frac{H_E}{m}(m_{B(A)x}\hat{\boldsymbol{x}} + m_{B(A)y}\hat{\boldsymbol{y}} + m_{B(A)z}\hat{\boldsymbol{z}}), \end{aligned}$$

with $\gamma = g_J \mu_B / \hbar$ as the gyromagnetic ratio. Postulating a magnetization on the form $\boldsymbol{m}_{A(B)} = m_{A(B)z}\hat{\boldsymbol{z}} + (\bar{m}_{A(B)x}\hat{\boldsymbol{x}} + \bar{m}_{A(B)y}\hat{\boldsymbol{y}})\mathrm{e}^{-\mathrm{i}\omega t}$, with $m_{Az} = m$ and $m_{Bz} = -m$, the equation reduces to the eigenvalue problem $F\bar{\boldsymbol{m}} = \omega \bar{\boldsymbol{m}}$ with

$$F = \begin{bmatrix} 0 & F_{2\times 2} \\ F_{2\times 2} & 0 \end{bmatrix}, \; F_{2\times 2} = \begin{bmatrix} -\gamma(H_{\text{ani}} + H_E + B_0) & -\gamma H_E \\ \gamma H_E & \gamma(H_{\text{ani}} + H_E - B_0) \end{bmatrix},$$

and $\bar{\boldsymbol{m}} = [m_{Ax}, m_{Bx}, \mathrm{i}m_{Ay}, \mathrm{i}m_{By}]^T$. The eigenvalue problem yields four eigenvalues, but only two of them are physically meaningful as they are positive. The positive eigenvalues are

$$\begin{aligned} \omega^+ = \gamma(H_c + B_0), \quad \omega^- = \gamma(H_c - B_0), \\ H_c = \sqrt{H_{\text{ani}}^2 + 2H_{\text{ani}}H_E}. \end{aligned} \tag{3.24}$$

The eigenvalues $\hbar\omega^\pm$ correspond to the ones calculated in the second quantized form when $\boldsymbol{k} = 0$, equation (3.22), except for the anisotropy lacking the contribution from the fourth order term. The corresponding eigenvectors are given by

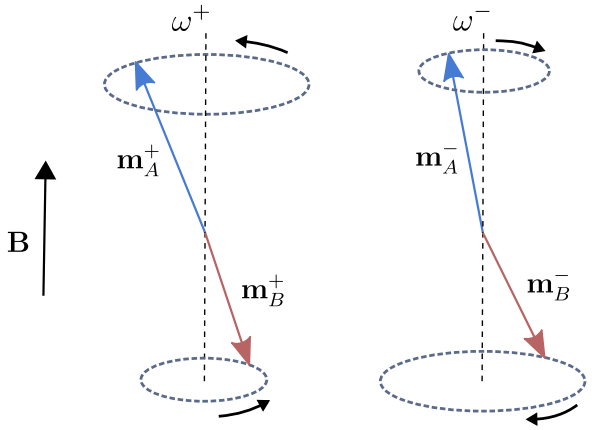

Figure 3.6.: An illustration of the precession of the the sublattice magnetizations in the two resonance modes, ω^+ and ω^-, of a square antiferromagnet is depicted in the figure. The illustration is inspired by Ref. [61].

$$\bar{\boldsymbol{m}}^+ = C_+ \begin{bmatrix} \eta_+ \\ -1 \\ -\eta_+ \\ 1 \end{bmatrix}, \quad \bar{\boldsymbol{m}}^- = C_- \begin{bmatrix} \eta_- \\ -1 \\ \eta_- \\ -1 \end{bmatrix},$$

with

$$\eta_\pm = \frac{H_{\text{ani}} + H_E \pm H_c}{H_E},$$

and $C_+(C_-)$ determine the amplitude. By examining the ansatz for $\boldsymbol{m}_{A(B)}$ in each mode, assuming C_+ and C_- are both equal to one for simplicity, we obtain the following expressions for each sublattice

$$\begin{aligned} \boldsymbol{m}_A^+ &= m\hat{\boldsymbol{z}} + \eta_+(\cos(\omega t)\hat{\boldsymbol{x}} + \sin(\omega t)\hat{\boldsymbol{y}}), \quad & \boldsymbol{m}_B^+ &= -m\hat{\boldsymbol{z}} - (\cos(\omega t)\hat{\boldsymbol{x}} + \sin(\omega t)\hat{\boldsymbol{y}}), \\ \boldsymbol{m}_A^- &= m\hat{\boldsymbol{z}} + \eta_-(\cos(\omega t)\hat{\boldsymbol{x}} - \sin(\omega t)\hat{\boldsymbol{y}}), \quad & \boldsymbol{m}_B^- &= -m\hat{\boldsymbol{z}} - (\cos(\omega t)\hat{\boldsymbol{x}} - \sin(\omega t)\hat{\boldsymbol{y}}). \end{aligned}$$

It is evident that both sublattices rotate counterclockwise in the ω^+ mode, where counterclockwise rotation is defined as the observed rotation when looking down on the $xy-$plane from $z > 0$. The radius, which represents the size of the precession circle, is larger for the A sublattice due to $\eta_+ > 1$. This implies that the magnetization at sublattice A has a smaller out-of-plane component compared to the magnetization at sublattice B. When summing over the entire lattice, a net magnetization along the $-\hat{\boldsymbol{z}}$ direction is obtained, resulting in a net negative angular momentum. This aligns with what we observed in equation (3.23) and is illustrated in Figure 3.6. Conversely, in the ω^- mode, both sublattices exhibit clockwise rotation. Analysis reveals that η_- is always less than unity, meaning that the magnetization at sublattice A has the largest m_z component, resulting in a net positive angular momentum. Therefore, the right-handed (counterclockwise) spin mode carries a negative angular momentum, while the left-handed (clockwise) spin mode carries a positive angular momentum. The locking of chirality to the expectation values of S_z remains unaffected by the wave vector $\boldsymbol{k}$, ensuring that this result holds true even for $\boldsymbol{k} \neq 0$ [57]. It is important to note that these findings are specific to our model with only an easy-axis anisotropy. The relationships described are disrupted if the rotational symmetry around the z-axis is broken, such as by introducing an in-plane easy-axis anisotropy [57]. According to this argument, ferromagnetic modes with negative angular momentum are expected to

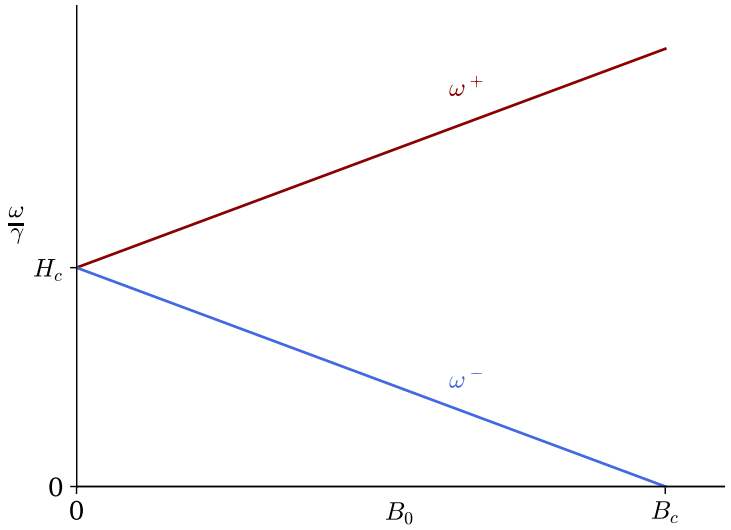

Figure 3.7.: Illustration of how the quantity ω/γ, proportional to the magnon frequency at $\boldsymbol{k} = 0$, behaves as a function of the magnetic field B_0 for the two branches in the antiferromagnetic square lattice.

exhibit a right-handed chirality, and a detailed exploration of ferromagnetic right-handedness can be found in Ref. [62].

Comparing the resonance frequencies of ferromagnetic and antiferromagnetic systems yields interesting insights. Typically, the anisotropy energy is much smaller compared to the exchange energy, allowing us to neglect the H_{ani}^2 in equation (3.24) in relation to $2H_{\text{ani}}H_E$. Consequently, in the absence of a magnetic field, the antiferromagnetic resonance frequency (AFMR) is given by $\omega_{\text{AFMR}} = \gamma\sqrt{2H_{\text{ani}}H_E}$. Similarly, according to equation (3.6), the ferromagnetic resonance frequency (FMR) is $\omega_{\text{FMR}} = \gamma H_{\text{ani}}$. As $H_{\text{ani}} << H_E$, it follows that $\omega_{\text{FMR}} << \omega_{\text{AFMR}}$. The AFMR typically falls within the range of hundreds of gigahertz [44]. Due to this characteristic, along with their zero net magnetic moment, antiferromagnetic materials have gained significant attention for their potential in ultrafast magnetization dynamics [63].

In the absence of an external magnetic field, the two branches of the magnon dispersion are degenerate, as depicted in Figure 3.5c and 3.5b. However, when an external magnetic field is applied, these branches spilt and become nondegenerate. One way to interpret this is by considering the addition of a Larmor precession, $\omega = \gamma B_0$, which occurs counterclockwise around the direction of B_0. Consequently, the Larmor precession introduces an additional positive contribution to the ω^+ branch, while it subtracts from the clockwise ω^- branch [62].

The frequency of the dispersion minima, described by equation (3.24), depends on the strength of the applied magnetic field. Figure 3.7 provides an illustration of how the frequency of both branches changes linearly with the external field. Specifically, the ω^- mode reaches zero frequency when the magnetic field reaches a critical value, denoted as $B_c = H_c \approx \sqrt{2H_{\text{ani}}H_E}$. At this critical field, a phase transition occurs, leading to a spin-flop state where the spins are bent nearly perpendicular to the magnetic, causing the Néel vector to lie in the plane [61, 64]. With further increase in the

magnetic field, another phase transition occurs, resulting in a spin-saturated flip state where all spins align parallel to the magnetic field [64].

3.4.2. Honeycomb lattice

The Hamiltonian, given by equation (3.10), includes an out-of-plane DMI contribution described by equation (3.9). The exchange coupling coefficient is negative, $J < 0$, indicating a Néel ordered ground state. A and B represents the two sublattices with spins arranged in opposite order. The non-DMI part of the Hamiltonian is treated in an equal manner as for the antiferromagnetic square lattice (as seen in equations (3.16) to (3.17)). By employing the Holstein-Primakoff transformation and substituting the Fourier-transformed operators, the DMI contribution to the Hamiltonian becomes

$$\begin{aligned}
\mathcal{H}_{\text{DMI}} =& \mathrm{i}\frac{D_z^{\text{nnn}}S}{2}\sum_{\substack{i,\tau_A\\ i\in A}}\nu_{\tau_A}(a_i^\dagger a_{i+\tau_A} - a_{i+\tau_A}^\dagger a_i) - \mathrm{i}\frac{D_z^{\text{nnn}}S}{2}\sum_{\substack{i,\tau_B\\ i\in B}}\nu_{\tau_B}(b_i^\dagger b_{i+\tau_B} - b_{i+\tau_B}^\dagger b_i)\\
=& \mathrm{i}\frac{D_z^{\text{nnn}}S}{2}\sum_{k,\tau_A}\nu_{\tau_A}a_k^\dagger a_k(\mathrm{e}^{\mathrm{i}\boldsymbol{k}\cdot\boldsymbol{\tau}_A} - \mathrm{e}^{-\mathrm{i}\boldsymbol{k}\cdot\boldsymbol{\tau}_A}) - \mathrm{i}\frac{D_z^{\text{nnn}}S}{2}\sum_{k,\tau_B}\nu_{\tau_B}b_k^\dagger b_k(\mathrm{e}^{-\mathrm{i}\boldsymbol{k}\cdot\boldsymbol{\tau}_B} - \mathrm{e}^{\mathrm{i}\boldsymbol{k}\cdot\boldsymbol{\tau}_B})\\
=& S\sum_k D_{\tau_A}(\boldsymbol{k})a_k^\dagger a_k + S\sum_k D_{\tau_B}(\boldsymbol{k})b_k^\dagger b_k\\
=& S\sum_k D_{\tau_A}(\boldsymbol{k})(a_k^\dagger a_k - b_k^\dagger b_k).
\end{aligned}$$

The total Hamiltonian is then

$$\begin{aligned}
\mathcal{H} =& \sum_k \left[(\kappa + SD_{\tau_A}(\boldsymbol{k}) + h)a_k^\dagger a_k + (\kappa - SD_{\tau_A}(\boldsymbol{k}) - h)b_k^\dagger b_k - JSf_{\delta_A}^*(\boldsymbol{k})a_k b_k - JSf_{\delta_A}(\boldsymbol{k})a_k^\dagger b_k^\dagger\right]\\
=& \sum_k \boldsymbol{\psi}_q^\dagger H_{\text{m}}(\boldsymbol{k})\boldsymbol{\psi}_q, \quad H_{\text{m}}(\boldsymbol{k}) = \begin{bmatrix}\kappa + SD_{\tau_A}(\boldsymbol{k}) + h & -JSf_{\delta_A}(\boldsymbol{k})\\ -JSf_{\delta_A}^*(\boldsymbol{k}) & \kappa - SD_{\tau_A}(\boldsymbol{k}) - h\end{bmatrix}, \boldsymbol{\psi}_k = [a_k, b_k^\dagger]^T.
\end{aligned}$$

Once more, the Hamiltonian is diagonalized using the Bogoliubov transformation. In this case, the structure factor $f_{\delta_A}(\boldsymbol{k})$ is complex, allowing the (u_k, v_k) coefficients to also be complex numbers. We define the transformation as

$$\begin{bmatrix}\alpha_k\\ \beta_k^\dagger\end{bmatrix} = \begin{bmatrix}u_k & v_k^*\\ v_k & u_k^*\end{bmatrix}\begin{bmatrix}a_k\\ b_k^\dagger\end{bmatrix}, \quad \begin{bmatrix}a_k\\ b_k^\dagger\end{bmatrix} = \begin{bmatrix}u_k^* & -v_k^*\\ -v_k & u_k\end{bmatrix}\begin{bmatrix}\alpha_k\\ \beta_k^\dagger\end{bmatrix},$$

where

$$|u_k|^2 - |v_k|^2 = 1.$$

This results in a Hamiltonian on the form

$$\begin{aligned}
\mathcal{H} =& \sum_k 2|v_k|^2\kappa + JS(f_{\delta_A}^*(\boldsymbol{k})u_k^*v_k^* + f_{\delta_A}(\boldsymbol{k})u_k v_k)\\
&+ \left[\kappa(|u_k|^2 + |v_k^2|) + SD_{\tau_A}(\boldsymbol{k}) + h + JS(f_{\delta_A}^*(\boldsymbol{k})u_k^*v_k^* + f_{\delta_A}(\boldsymbol{k})u_k v_k)\right]\alpha_k^\dagger\alpha_k\\
&+ [\kappa(|u_k|^2 + |v_k^2|) - SD_{\tau_A}(\boldsymbol{k}) - h + JS(f_{\delta_A}^*(\boldsymbol{k})u_k^*v_k^* + f_{\delta_A}(\boldsymbol{k})u_k v_k)]\beta_k^\dagger\beta_k,
\end{aligned}$$

where the coefficients must satisfy

$$JS(f^*_{\delta_A}(\boldsymbol{k})(u^*_k)^2 + f_{\delta_A}(\boldsymbol{k})v_k^2) = -2\kappa u^*_k v_k \quad \text{and} \quad JS(f_{\delta_A}(\boldsymbol{k})u_k^2 + f^*_{\delta_A}(\boldsymbol{k})(v^*_k)^2) = -2\kappa u_k v^*_k.$$

The two equations are each other's complex conjugates. To simplify the expression, we can represent the complex quantities in polar form, with ϕ_u, ϕ_v and ϕ_f representing the phases for u_k, v_k and $f_{\delta_A}(\boldsymbol{k})$, respectively. Using this representation, the first equation can be rewritten as follows

$$\begin{aligned} &|J|S|f_{\delta_A}(\boldsymbol{k})|(|u_k|^2 \mathrm{e}^{-\mathrm{i}(\phi_f+2\phi_u)} + |v_k|^2 \mathrm{e}^{\mathrm{i}(\phi_f+2\phi_v)}) = 2\kappa|u_k||v_k|\mathrm{e}^{\mathrm{i}(\phi_v-\phi_u)} \\ \implies &|J|S|f_{\delta_A}(\boldsymbol{k})|(2\cos(\Phi)|u_k|^2\mathrm{e}^{-\mathrm{i}\Phi} - 1) = 2\kappa|u_k||v_k|\mathrm{e}^{-\mathrm{i}\Phi}, \end{aligned}$$

where $\Phi = \phi_u + \phi_v + \phi_f$. By equating the real and imaginary parts, we obtain

$$\begin{aligned} &\text{(i)} \quad |J|S|f_{\delta_A}(\boldsymbol{k})|(2\cos^2(\Phi)|u_k|^2 - 1) = 2\kappa|u_k||v_k|\cos(\Phi), \\ &\text{(ii)} \quad |J|S|f_{\delta_A}(\boldsymbol{k})|\cos(\Phi)\sin(\Phi)|u_k|^2 = \kappa|u_k||v_k|\sin(\Phi). \end{aligned}$$

The second equation is solved with $\Phi = 0$ or $\cos(\Phi) = \frac{\kappa|v_k|}{|J|S|f_{\delta_A}||u_k|}$. Inserting the solutions into the first equation, only the $\Phi = 0$ solution yields physical results. Therefore, we end up with

$$|J|S|f_{\delta_A}(\boldsymbol{k})|(|u_k|^2 + |v_k|^2) = 2\kappa|u_k||v_k|,$$

which is the same equation as (3.21), with solutions

$$|u_k|^2 = \frac{1}{2}\left(1 + \frac{\kappa}{\sqrt{\kappa^2 - J^2S^2|f_{\delta_A}(\boldsymbol{k})|^2}}\right), \quad |v_k|^2 = \frac{1}{2}\left(-1 + \frac{\kappa}{\sqrt{\kappa^2 - J^2S^2|f_{\delta_A}(\boldsymbol{k})|^2}}\right).$$

The phases ϕ_u and ϕ_v may be chosen freely as long as $\Phi = 0$. We choose $\phi_u = -\phi_f$ and $\phi_v = 0$. This leads to the following Hamiltonian

$$\mathcal{H} = \sum_k \left[E^+_k \alpha^\dagger_k \alpha_k + E^-_k \beta^\dagger_k \beta_k\right],$$

where

$$\begin{aligned} E^+_k &= |J|S\sqrt{(\mathcal{Z} + \frac{\mathcal{K}}{|J|S})^2 - |f_{\delta_A}(\boldsymbol{k})|^2} + SD_{\tau_A}(\boldsymbol{k}) + h, \\ E^-_k &= |J|S\sqrt{(\mathcal{Z} + \frac{\mathcal{K}}{|J|S})^2 - |f_{\delta_A}(\boldsymbol{k})|^2} - SD_{\tau_A}(\boldsymbol{k}) - h, \end{aligned} \tag{3.25}$$

$|f_{\delta_A}(\boldsymbol{k})|^2$ and $D_{\tau_A}(\boldsymbol{k})$ are defined in equation (3.13), and $\mathcal{Z} = 3$. This is consistent with the findings reported in Ref. [57], where they utilize a different definition of the Fourier-transformed operators. The branches are degenerate when both the Zeeman and DMI terms are zero. Additionally, in the absence of anisotropy ($K_z = 0$), the branches scale linearly from the $\Gamma-$point, similar to the antiferromagnetic square lattice. Figure 3.8a shows the dimensionless magnon dispersion with the presence of a magnetic field, along with relatively weak DMI and anisotropy strengths compared to the exchange coupling coefficient. The dispersion is displayed along the symmetry lines of the Brillouin zone, including

the $K' = (4\pi/3a, 0)$ point situated at the corner of the Brillouin zone. The chosen parameters in this illustrative example are $h/|J|S = 1$, $D_z^{\text{nnn}}/|J| = 0.1$ and $\mathcal{K}/|J|S = 0.2$. The branches exhibit a minimum at the Γ-point, where their energy exceeds the Zeeman energies (h and $-h$) due to the anisotropy energy. When a strong magnetic field, $B_0 = B_c$, is applied, the antiferromagnetic resonance frequency of the lower branch reaches zero, leading to a phase transition into the spin-flop phase, as discussed in section 3.4.1.

In the absence of an external magnetic field, Figures 3.8b and 3.8c present the magnon dispersion for weak and strong DMI, respectively. Specifically, the DMI values used in the two cases are $D_z^{\text{nnn}}/|J| = 0.05$ and $D_z^{\text{nnn}}/|J| = 0.4$, with $\mathcal{K}/(|J|S) = 0.2$. Due to the linear dependence of $D_{\tau_A}(\boldsymbol{k})$ and its odd nature in $\boldsymbol{k}$, the branches are nonreciprocal, meaning E_k does not equal E_{-k} [14]. Furthermore, along the symmetry line $\Gamma \to M$, the branches are degenerate because $D_{\tau_A}(\boldsymbol{k})$ becomes zero when $k_x = 0$. A strong DM coupling leads to a relatively large band gap, which can be significant enough to shift the global minima to a location other than the $\Gamma-$point in the Brillouin zone. In order

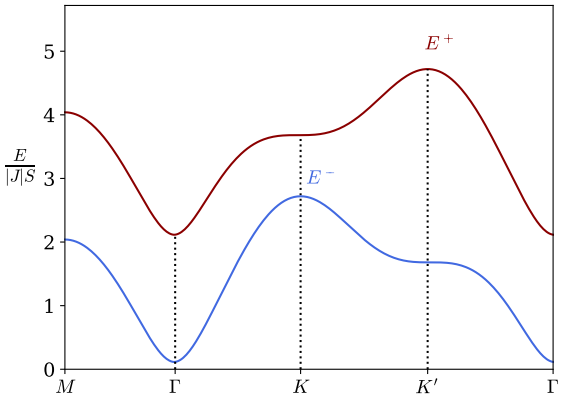

(a) $h/(|J|S) = 1$ and $D_z^{\text{nnn}}/|J| = 0.1$.

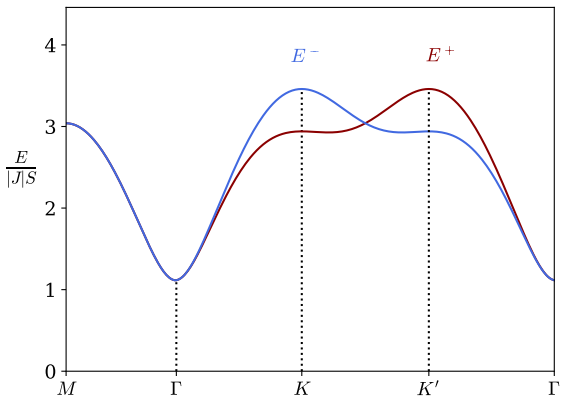

(b) $h/(|J|S) = 0$ and $D_z^{\text{nnn}}/|J| = 0.05$.

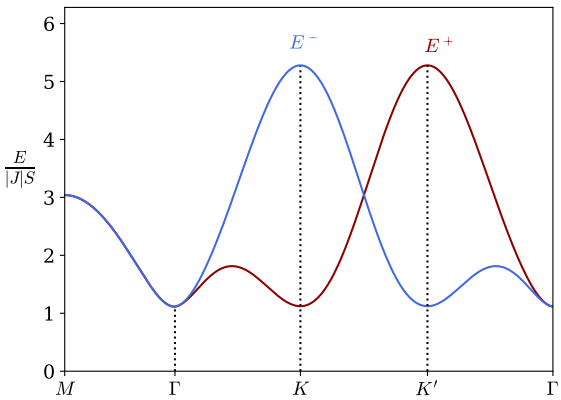

(c) $h/(|J|S) = 0$ and $D_z^{\text{nnn}}/|J| = 0.4$.

Figure 3.8.: Magnon dispersion in an antiferromagnetic honeycomb lattice along the symmetry lines of the Brillouin zone, in units of $|J|S$. The dispersion is shown for different values of the magnetic field and DMI strength, with $\mathcal{K}/(|J|S) = 0.2$.

for the branches to be positive across the Brillouin zone in the absence of an external field, the inequality $D_z^{\mathrm{nnn}}/|J| < (3+\mathcal{K}/|J|S)/3\sqrt{3}$ must be met. The expression reduces to $D_z^{\mathrm{nnn}}/|J| < 1/\sqrt{3}$, as suggested by Ref. [59] as the upper limit for D_z^{nnn} in the absence of anisotropy and under ferromagnetic ordering. This upper limit represents a breakdown of the linear spin-wave theory as the expected Néel ground state deviates from the true ground state, a spin spiral, rendering the Holstein-Primakoff transformation assumption of a collinear arrangement unsuitable [57]. It is worth noting that in contrast to the ferromagnetic case, where a nonzero DMI is required to induce Berry curvature, the Néel ordering of spins inherently possesses intrinsic Berry curvature [57]. Surprisingly, the presence or absence of DMI does not affect the Berry curvature in this scenario.

Following a similar approach to the previous cases, we evaluate the expectation value of S_z in the two magnon modes, yielding $\langle 0|\, \alpha_k S_z \alpha_k^\dagger \,|0\rangle = -1$ and $\langle 0|\, \beta_k S_z \beta_k^\dagger \,|0\rangle = 1$. Consequently, the E_k^+ branch exhibits right-handedness, while the E_k^- branch displays left-handedness [14].

CHAPTER 4

Hybridization in magnetic systems with out-of-plane magnetization direction

The preceding chapters have laid the foundation for understanding elastic vibrations and spin-waves in materials with magnetic order. In this chapter, we aim to merge these concepts and explore systems that exhibit magnetoelastic interactions. Specifically, we will investigate the coupling between magnons and phonons, which are the corresponding quasiparticles. In general, the Hamiltonian can be divided into the interacting part and the non-interacting part as

$$\mathcal{H} = \mathcal{H}_0 + \mathcal{H}_{\text{int}},$$

where $\mathcal{H}_0 = \mathcal{H}_{\text{ph}} + \mathcal{H}_{\text{m}}$ is the non-interacting phonon and magnon Hamiltonian. The magnetoelastic energy, denoted as $\mathcal{H}_{\text{int}}$, represents the portion of energy in a crystalline material that emerges from the interaction between the magnetization and lattice strain [65]. The magnetoelastic coupling can give rise to various phenomena, including magnetostriction, which involves the generation of spontaneous stress induced by magnetization, leading to alterations in the shape of the crystal [66]. Furthermore, it contributes to the damping of spin-waves [67].

The interacting Hamiltonian allows for magnon and phonon bosonic operators of various orders. The cubic terms are linked to the Kasuya-LeCraw process, where magnons scatter and either absorb or emit phonons. Additionally, the Confluent process, where two magnons of opposite polarization decay into a phonon, becomes possible for antiferromagnets [25]. Scattering processes play a crucial role in nonequilibrium calculations as they help to determine the equilibration times of spin and lattice systems and the lifetimes of their excitations [25, 67]. The quadratic terms, also known as linear magnetoelastic coupling terms, are associated with hybridization. These linear magnetoelastic coupling terms create hybridized magnon-polarons that produce anticrossing gap openings at the intersections of magnon and phonon dispersions [63]. The objective of this chapter is to compute the energy spectrum of magnetoelastic interactions in various two-dimensional systems with out-of-plane magnetic ordering and compare these findings to previous research. To accomplish this, we will employ the approximation that considers only the linear magnetoelastic coupling terms, which has been proven to be a valid approach [67]. A comprehensive examination of how the inclusion of magnon-phonon interactions can result in nontrivial topology will be presented in Chapter 7.

The magnetoelastic energy can be obtained through various methods, such as a phenomenological or microscopic approach. In the phenomenological approach, there are two main contributions: exchange modulation due to lattice vibrations, as the exchange coupling coefficients J_{ij} depend on phonon coordinates, and relativistic effects such as spin-orbit coupling and dipole-dipole interactions [67]. In the present chapter, we will employ a microscopic approach to derive the interacting Hamiltonian. This will be achieved by expanding the magnetic exchange interactions that are position-dependent on the lattice sites.

4.1. Derivation of the interacting Hamiltonian via Taylor expansion

As previously stated, the position of the ions in the lattice affects the exchange coupling coefficient J_{ij} in the magnon Hamiltonian, equation (3.1). This also applies for the DM vector $\boldsymbol{D}_{ij}$. Assuming small displacements, $\boldsymbol{u}_i = \boldsymbol{r}_i - \boldsymbol{R}_i$, the functions can be Taylor-expanded around their equilibrium positions $\boldsymbol{R}_i - \boldsymbol{R}_j$. Our investigation starts with exploring the exchange coupling coefficient.

4.1.1. Exchange coupling coefficient

To first order in the displacement, the Taylor-expanded exchange coupling coefficient is [25, 26]

$$J(\boldsymbol{r}_{ij}) \approx J(\boldsymbol{R}_{ij}) + \nabla_{\boldsymbol{r}_{ij}} J(\boldsymbol{r}_{ij})\Big|_{\boldsymbol{R}_{ij}} \cdot \boldsymbol{u}_{ij},$$

where $\boldsymbol{r}_{ij} = \boldsymbol{r}_i - \boldsymbol{r}_j$, $\boldsymbol{R}_{ij} = \boldsymbol{R}_i - \boldsymbol{R}_j$ and $\boldsymbol{u}_{ij} = \boldsymbol{u}_i - \boldsymbol{u}_j$. The operator $\nabla_{\boldsymbol{r}_{ij}}$ is defined as $\nabla_{\boldsymbol{r}_{ij}} = (\frac{\partial}{\partial r_{ij}^x}, \frac{\partial}{\partial r_{ij}^y}, \frac{\partial}{\partial r_{ij}^z})$ in Cartesian coordinates. The first term is the constant coupling coefficient, already used in calculating the non-interacting magnon dispersion. The second term, however, contributes to the interacting part of the Hamiltonian. A general expression for the exchange contribution to the interacting Hamiltonian is

$$\mathcal{H}_{\text{int}}^{\text{ex}} = -\sum_{i,j}\sum_{\mu} \frac{\partial J(\boldsymbol{r}_{ij})}{\partial r_{ij}^{\mu}}\bigg|_{\boldsymbol{R}_{ij}} (u_{i\mu} - u_{j\mu})(\boldsymbol{S}_i \cdot \boldsymbol{S}_j).$$

As shown in equation (2.10), the phonon annihilation and creation operators are proportional to the ionic displacements. The specific form of the expression and its dependence on magnon and phonon operators may vary depending on the crystal geometry and spin alignment. In the case of collinear spin alignment, the exchange part of the interacting Hamiltonian incorporates linear, cubic, and higher-order terms, as dictated by the dot product of the spins. Consequently, the Heisenberg exchange interaction does not contribute to hybridization. In contrast, the scenario would be modified in the case of a noncollinear antiferromagnet, where the presence of quadratic terms would have an impact [19].

4.1.2. Dzyaloshinskii–Moriya vector

In order to derive linear magnetoelastic terms, we will utilize an extended form of the DM vector that goes beyond the DM vector perpendicular to the plane, as discussed in section 3.3.2. More specifically, we introduce an additional in-plane component to the DM vector, leading to the following modified form [18, 26, 28]

$$\boldsymbol{D}(\boldsymbol{r}_{ij}) = D_{\perp}^{\text{nnn}}(\boldsymbol{r}_{ij})\hat{\boldsymbol{z}} + \boldsymbol{D}_{||}^{\text{nn}}(\boldsymbol{r}_{ij}). \tag{4.1}$$

The in-plane part is represented by $\boldsymbol{D}_{||}^{\text{nn}}(\boldsymbol{r}_{ij}) = D_{xy}^{\text{nn}}(\boldsymbol{r}_{ij})(\hat{\boldsymbol{z}} \times \hat{\boldsymbol{r}}_{ij})$, while the out-of-plane component is denoted as $D_{\perp}^{\text{nnn}}(\boldsymbol{r}_{ij}) = D_{z}^{\text{nnn}}(\boldsymbol{r}_{ij})\nu_{ij}$. The out-of-plane contribution is exclusively observed between next-nearest neighbours, while the in-plane components are between the nearest neighbours (NN). Moreover, the out-of-plane component can be understood as an intrinsic DMI resulting from the lack of inversion symmetry in the midpoints of the second neighbouring bonds. Conversely, the in-plane DMI arises when the mirror symmetry relative to the lattice plane is broken, which can occur when growing a 2D plate on a substrate [26]. Figure 4.1 displays the orientation of the in-plane DM vector for both the honeycomb and square lattices. Beginning with the out-of-plane DMI, the Taylor expansion is performed as

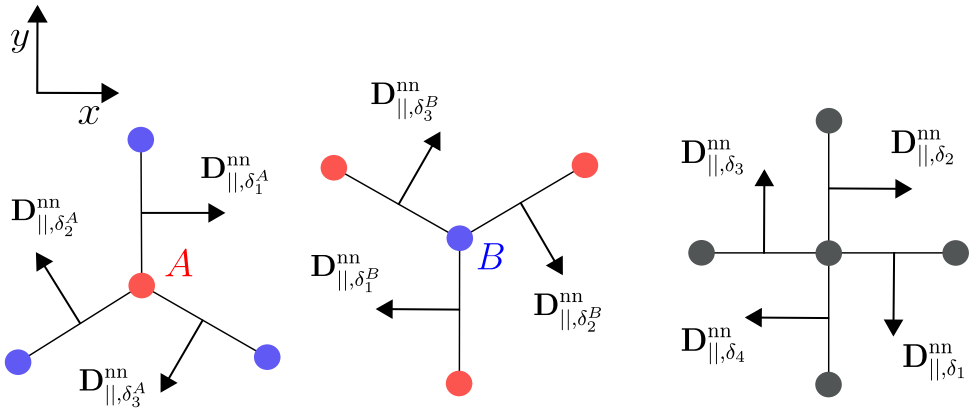

Figure 4.1.: The figures illustrate the orientation of the in-plane nearest neighbour DM vector for both the honeycomb lattice (two figures on the left) and the square lattice (on the right). These vectors are perpendicular to the neighbouring bonds and lie in the plane. Specifically, for the honeycomb lattice, we present the DM vectors associated with lattice sites belonging to sublattice A (far left figure) and sublattice B (middle figure), with their orientations being opposite to each other.

$$D_{\perp}(\boldsymbol{r}_{ij})^{\mathrm{nnn}} \approx D_{\perp}^{\mathrm{nnn}}(\boldsymbol{R}_{ij}) + \nabla_{\boldsymbol{r}_{ij}} D_{\perp}^{\mathrm{nnn}}(\boldsymbol{r}_{ij})\Big|_{\boldsymbol{R}_{ij}} \cdot \boldsymbol{u}_{ij},$$

resulting in the following contribution to the interacting Hamiltonian

$$\mathcal{H}_{\mathrm{int}}^{D\perp} = -\sum_{<<i,j>>} \sum_{\mu} \frac{\partial D_{\perp}^{\mathrm{nnn}}(\boldsymbol{r}_{ij})}{\partial r_{ij}^{\mu}}\Big|_{\boldsymbol{R}_{ij}} (u_{i\mu} - u_{j\mu})(\boldsymbol{S}_i \times \boldsymbol{S}_j)_z. \tag{4.2}$$

Unlike the exchange contribution to the interacting Hamiltonian, this term establishes a coupling between spins of different spatial components, thanks to the presence of the cross product. Upon closer examination of the in-plane DMI, it can be expressed in a general form as follows

$$\mathcal{H}^{D||} = -\sum_{<i,j>} D_{xy}^{\mathrm{nn}}(\boldsymbol{r}_{ij})(\hat{\boldsymbol{z}} \times \hat{\boldsymbol{r}}_{ij}) \cdot (\boldsymbol{S}_i \times \boldsymbol{S}_j). \tag{4.3}$$

The in-plane DM strength $D_{xy}^{\mathrm{nn}}(\boldsymbol{r}_{ij})$ as well as the unit vector $\hat{\boldsymbol{r}}_{ij}$ connecting the lattice sites both rely on the phonon coordinates. By performing a Taylor expansion, we obtain [28, 68]

$$\begin{aligned} D_{xy}^{\mathrm{nn}}(\boldsymbol{r}_{ij}) &\approx D_{xy}^{\mathrm{nn}}(\boldsymbol{R}_{ij}) + \nabla_{\boldsymbol{r}_{ij}} D_{xy}^{\mathrm{nn}}(\boldsymbol{r}_{ij})\Big|_{\boldsymbol{R}_{ij}} \cdot \boldsymbol{u}_{ij}, \\ \hat{\boldsymbol{r}}_{ij} &\approx \frac{\boldsymbol{R}_{ij} + \boldsymbol{u}_{ij}}{|\boldsymbol{R}_{ij} + \boldsymbol{u}_{ij}|} = \frac{\boldsymbol{R}_{ij} + \boldsymbol{u}_{ij}}{\sqrt{\boldsymbol{R}_{ij}^2 + 2\boldsymbol{R}_{ij} \cdot \boldsymbol{u}_{ij} + \boldsymbol{u}_{ij}^2}} \approx \frac{\boldsymbol{R}_{ij} + \boldsymbol{u}_{ij}}{|\boldsymbol{R}_{ij}|}\left(1 - \frac{\boldsymbol{R}_{ij} \cdot \boldsymbol{u}_{ij}}{|\boldsymbol{R}_{ij}|^2}\right). \end{aligned}$$

By substituting these expressions into equation (4.3) and considering only the first-order terms in displacement, the in-plane DMI contribution to the interacting Hamiltonian can be expressed as

$$\begin{aligned} \mathcal{H}_{\mathrm{int}}^{D||} &= -\sum_{<i,j>} \frac{D_{xy}^{\mathrm{nn}}(\boldsymbol{R}_{ij})}{|\boldsymbol{R}_{ij}|}\left[\hat{\boldsymbol{z}} \times \left(\boldsymbol{u}_{ij} - \hat{\boldsymbol{R}}_{ij}\left(\hat{\boldsymbol{R}}_{ij} \cdot \boldsymbol{u}_{ij} - \frac{|\boldsymbol{R}_{ij}|}{D_{xy}^{\mathrm{nn}}(\boldsymbol{R}_{ij})} \nabla_{\boldsymbol{r}_{ij}} D_{xy}^{\mathrm{nn}}(\boldsymbol{r}_{ij})\Big|_{\boldsymbol{R}_{ij}} \cdot \boldsymbol{u}_{ij}\right)\right)\right] \cdot [\boldsymbol{S}_i \times \boldsymbol{S}_j] \\ &= \sum_{<i,j>} \sum_{\mu,\nu} (u_{i\mu} - u_{j\mu}) T_{ij}^{\mu\nu} (\boldsymbol{S}_i \times \boldsymbol{S}_j)_{\nu}, \end{aligned} \tag{4.4}$$

where the magnon-phonon coupling matrix $T_{ij}^{\mu\nu}$ is given by

$$T_{ij}^{\mu\nu} = -\frac{D_{xy}^{\mathrm{nn}}(\boldsymbol{R}_{ij})}{|\boldsymbol{R}_{ij}|} \sum_{\xi=x,y,z} \varepsilon_{z\xi\nu} \left(\delta_{\mu\xi} - \hat{R}_{ij}^{\xi} \left(\hat{R}_{ij}^{\mu} - \frac{|\boldsymbol{R}_{ij}|}{D_{xy}^{\mathrm{nn}}(\boldsymbol{R}_{ij})} \frac{\partial D_{xy}^{\mathrm{nn}}(\boldsymbol{r}_{ij})}{\partial r_{ij}^{\mu}} \bigg|_{\boldsymbol{R}_{ij}} \right) \right),$$

and $\varepsilon_{z\xi\nu}$ is the Levi-Civita tensor. The matrix elements can be approximated further. We write the in-plane DM strength derivatives in cylindrical coordinates as

$$\nabla_{\boldsymbol{r}_{ij}} D_{xy}^{\mathrm{nn}}(\boldsymbol{r}_{ij})\big|_{\boldsymbol{R}_{ij}} = \frac{\partial D_{xy}^{\mathrm{nn}}(\boldsymbol{r}_{ij})}{\partial \rho_{ij}} \bigg|_{\boldsymbol{R}_{ij}} \hat{\boldsymbol{\rho}}_{ij} + \frac{\partial D_{xy}^{\mathrm{nn}}(\boldsymbol{r}_{ij})}{\rho_{ij} \partial \theta_{ij}} \bigg|_{\boldsymbol{R}_{ij}} \hat{\boldsymbol{\theta}}_{ij} + \frac{\partial D_{xy}^{\mathrm{nn}}(\boldsymbol{r}_{ij})}{\partial z_{ij}} \bigg|_{\boldsymbol{R}_{ij}} \hat{\boldsymbol{z}},$$

with $r_{ij}^{x} = \rho_{ij}\cos(\theta_{ij})$, $r_{ij}^{y} = \rho_{ij}\sin(\theta_{ij})$ and $z_{ij} = r_{ij}^{z}$. By neglecting the second term directed along $\hat{\boldsymbol{\theta}}_{ij}$, which is assumed to be small for tiny displacements [28], and using $\hat{\boldsymbol{\rho}}_{ij} \approx \hat{\boldsymbol{R}}_{ij}$ to lowest order in displacement, the approximation is

$$\left(\nabla_{\boldsymbol{r}_{ij}} D_{xy}^{\mathrm{nn}}(\boldsymbol{r}_{ij})\big|_{\boldsymbol{R}_{ij}} \right)_{\mu} \approx \frac{\partial D_{xy}^{\mathrm{nn}}(\boldsymbol{r}_{ij})}{\partial \rho_{ij}} \bigg|_{\boldsymbol{R}_{ij}} \hat{R}_{ij}^{\mu} + \frac{\partial D_{xy}^{\mathrm{nn}}(\boldsymbol{r}_{ij})}{\partial z_{ij}} \bigg|_{\boldsymbol{R}_{ij}} \hat{z}_{\mu}.$$

Using this expression, the coupling matrix elements are reduced to the form

$$T_{ij}^{\mu\nu} = -\frac{D_{xy}^{\mathrm{nn}}}{R_{ij}} \sum_{\xi=x,y,z} \varepsilon_{z\xi\nu} \left(\delta_{\mu\xi} - (1+d_R)\hat{R}_{ij}^{\xi}\hat{R}_{ij}^{\mu} - d_z \hat{R}_{ij}^{\xi}\hat{z}_{\mu} \right),$$

where $d_R = -(\partial D_{xy}^{\mathrm{nn}}(\boldsymbol{r}_{ij})/\partial\rho_{ij})(R_{ij}/D_{xy}^{\mathrm{nn}})$, $d_z = -(\partial D_{xy}^{\mathrm{nn}}(\boldsymbol{r}_{ij})/\partial z_{ij})(R_{ij}/D_{xy}^{\mathrm{nn}})$, $D_{xy}^{\mathrm{nn}} = D_{xy}^{\mathrm{nn}}(\boldsymbol{R}_{ij})$ and $R_{ij} = |\boldsymbol{R}_{ij}|$. The derivatives are evaluated at equilibrium position. Writing out the summation, the matrix elements that couple to in-plane ($\mu = x, y$) and out-of-plane ($\mu = z$) phonon modes are [18, 29]

$$\begin{aligned} (\mu = x,y):\ T_{ij}^{\mu\nu} &= \frac{D_{xy}^{\mathrm{nn}}}{R_{ij}} [\varepsilon_{z\nu x}(\delta_{\mu x} - (1+d_R)\hat{R}_{ij}^{x}\hat{R}_{ij}^{\mu}) + \varepsilon_{z\nu y}(\delta_{\mu y} - (1+d_R)\hat{R}_{ij}^{y}\hat{R}_{ij}^{\mu})], \\ (\mu = z):\ T_{ij}^{z\nu} &= -\frac{D_{xy}^{\mathrm{nn}} d_z}{R_{ij}} [\varepsilon_{z\nu x}\hat{R}_{ij}^{x} + \varepsilon_{z\nu y}\hat{R}_{ij}^{y}]. \end{aligned} \tag{4.5}$$

We notice that for $\mu = z$, the matrix elements are odd in $\hat{R}_{ij}$. Consequently, we have $T_{ji}^{z\nu} = -T_{ij}^{z\nu}$. This relationship implies that

$$\begin{aligned} (\mu = z):\ \mathcal{H}_{\mathrm{int}}^{D\parallel} &= \frac{1}{2} \sum_{<i,j>} \sum_{\nu} \left[(u_{iz} - u_{jz}) T_{ij}^{z\nu} (\boldsymbol{S}_i \times \boldsymbol{S}_j)_{\nu} + (u_{jz} - u_{iz}) T_{ji}^{z\nu} (\boldsymbol{S}_j \times \boldsymbol{S}_i)_{\nu} \right] \\ &= \frac{1}{2} \sum_{<i,j>} \sum_{\nu} (u_{iz} - u_{jz})(T_{ij}^{z\nu} + T_{ji}^{z\nu})(\boldsymbol{S}_i \times \boldsymbol{S}_j)_{\nu} = 0. \end{aligned}$$

As a result, we can infer that the in-plane DMI solely induces a higher-order coupling between magnons and out-of-plane phonon modes, without causing hybridization. This finding aligns with the outcomes reported in previous investigations [18, 26, 28]. On the other hand, alternative studies that do not rely on mirror symmetry breaking to achieve hybridization have found that magnons primarily couple to out-of-plane phonon modes in the case of a perpendicular magnetization alignment [27, 29]. In these studies, the magnetoelastic energy is derived from the continuum limit of the anisotropy energy density and is attributed to the local variation in anisotropy caused by atomic motion within the crystal [65]. Although there is a possibility of coupling to out-of-plane phonon modes, we will follow

the approach of Refs. [18, 26, 28] and ignore the coupling to out-of-plane phonon modes. Instead, we will rely on the derived expression.

We examine two scenarios where the magnetization is either perpendicular or parallel to the lattice plane, and analyze the coupling terms associated with both in-plane and out-of-plane DMI.

Perpendicular magnetization

With a perpendicular magnetization, the out-of-plane DMI part of the interacting Hamiltonian, equation (4.2), becomes

$$\mathcal{H}_{\text{int}}^{D\perp} = \sum_{<<i,j>>} \sum_{\mu} (\partial_{r_\mu} D_{\perp}^{\text{nnn}})(u_{i\mu} - u_{j\mu})(S_{iy}S_{jx} - S_{ix}S_{jy}),$$

with $\partial_{r_\mu} D_{\perp}^{\text{nnn}} = \left.\frac{\partial D_{\perp}^{\text{nnn}}(\boldsymbol{r}_{ij})}{\partial r_{ij}^{\mu}}\right|_{\boldsymbol{R}_{ij}}$. Because both S_x and S_y are linearly dependent on magnon operators, the lowest order terms involve cubic terms, which result in scattering. Therefore, in the case of perpendicular spin alignment, the out-of-plane DMI does not contribute to hybridization. Turning our attention to the in-plane DMI described in equation (4.4), we find that the interacting Hamiltonian contains the following quadratic terms

$$\mathcal{H}_{\text{int}}^{D||} = S \sum_{<i,j>} \sum_{\mu} (u_{i\mu} - u_{j\mu})[T_{ij}^{\mu x}(S_{iy} - S_{jy}) - T_{ij}^{\mu y}(S_{ix} - S_{jx})],$$

where we used $S_z = S$, assuming a ferromagnet. Thus, the in-plane DMI is a source for hybridization.

In-plane magnetization

Taking the magnetization axis to be along the x-axis, we set $S_x = S$ as a specific example. In this case, the contribution from the out-of-plane DMI to the interacting Hamiltonian is

$$\mathcal{H}_{\text{int}}^{D\perp} = S \sum_{<<i,j>>} \sum_{\mu} (\partial_{r_\mu} D_{\perp}^{\text{nnn}})(u_{i\mu} - u_{j\mu})(S_{iy} - S_{jy}).$$

Similarly, the interacting Hamiltonian is affected by the contribution from the in-plane DMI as follows

$$\mathcal{H}_{\text{int}}^{D||} = S \sum_{<i,j>} (u_{i\mu} - u_{j\mu}) T_{ij}^{\mu y}(S_{iz} - S_{jz}),$$

where we used that $T_{ij}^{\mu z} = 0$. Both the in-plane and out-of-plane DM vectors result in second-order contributions that can potentially lead to hybridization when the magnetization lies in the plane. However, it is generally observed that the out-of-plane DMI is insignificant compared to the in-plane component. This is primarily because the out-of-plane DMI is proportional to the derivative of the DMI strength, rendering its effect relatively negligible.

4.2. The Bogoliubov-de Gennes equation

The magnetic systems that were examined earlier utilized two methods to diagonalize the Hamiltonian: an unitary transformation for ferromagnetic systems and a Bogoliubov transformation for antiferromagnetic systems. Nonetheless, applying a direct Bogoliubov transformation for larger systems proves to be a laborious process. To address this issue, the Bogoliubov-de Gennes (BdG) equation is introduced in this section as a more convenient method for carrying out the Bogoliubov transformation in larger systems.

Let us consider a general quadratic Hamiltonian on the form

$$\mathcal{H} = \frac{1}{2}\sum_k \boldsymbol{X}_k^\dagger H(\boldsymbol{k}) \boldsymbol{X}_k,$$

where the basis consists of bosonic operators and $H(\boldsymbol{k})$ is a matrix. Assuming that we can diagonalize the Hamiltonian with a matrix V_k, it can be written as

$$\mathcal{H} = \frac{1}{2}\sum_k \boldsymbol{X}_k^\dagger H(\boldsymbol{k}) \boldsymbol{X}_k = \frac{1}{2}\sum_k (\boldsymbol{X}_k^\dagger (V_k^\dagger)^{-1})(V_k^\dagger H(\boldsymbol{k}) V_k)(V_k^{-1}\boldsymbol{X}_k) = \frac{1}{2}\sum_k \boldsymbol{X}_k'^\dagger \mathcal{E}_k \boldsymbol{X}_k',$$

where $\mathcal{E}_k = V_k^\dagger H(\boldsymbol{k}) V_k$ is a diagonal matrix containing the eigenvalues and $\boldsymbol{X}_k' = V_k^{-1}\boldsymbol{X}_k$ is the rotated basis. To ensure that the rotated basis is bosonic, a non-unitary transformation is typically necessary. By examining the commutation relation of the basis, we can determine the structure of the transformation matrix V_k. Specifically, the commutation relation of the basis satisfy the following condition [69]

$$[\boldsymbol{X}_k, \boldsymbol{X}_k^\dagger] = \boldsymbol{X}_k(\boldsymbol{X}_k^*)^T - (\boldsymbol{X}_k^* \boldsymbol{X}_k^T)^T \coloneqq \eta,$$

where $\boldsymbol{X}_k^*$ is the column vector of the Hermitian adjoint operators and η is a matrix composed of $c-$numbers (commuting real or complex numbers). By using $\boldsymbol{X}_k = V_k \boldsymbol{X}_k'$, it can be deduced that [69]

$$\begin{aligned}
\eta &= [V_k \boldsymbol{X}', \boldsymbol{X}'^\dagger V_k^\dagger] = V_k \boldsymbol{X}_k'(\boldsymbol{X}_k'^*)^T (V_k^*)^T - (V_k^* \boldsymbol{X}_k'^* \boldsymbol{X}_k'^T V_k^T)^T \\
&= V_k \boldsymbol{X}_k'(\boldsymbol{X}_k'^*)^T V_k^\dagger - V_k(\boldsymbol{X}_k'^* \boldsymbol{X}_k'^T)^T V_k^\dagger \\
&= V_k[\boldsymbol{X}_k', \boldsymbol{X}_k'^\dagger] V_k^\dagger = V_k \eta' V_k^\dagger,
\end{aligned}$$

where we used that the matrix V_k is also composed of $c-$numbers. In order for the rotated basis to fulfill the same bosonic commutation relation, it is necessary for η' to be equal to η, leading to the following relationships

$$\eta = V_k \eta V_k^\dagger \;\text{ and }\; V_k^{-1} = \eta V_k^\dagger \eta^{-1}.$$

The eigenvalues of the normal modes are then related to the Hamiltonian matrix via

$$H(\boldsymbol{k}) V_k = (V_k^\dagger)^{-1}\mathcal{E}_k = \eta^{-1} V_k \eta \mathcal{E}_k \implies \eta H(\boldsymbol{k}) V_k = V_k \eta \mathcal{E}_k.$$

In the case where η is a diagonal matrix, the equation can expressed in the form of an eigenvalue problem [69]

$$\eta H(\boldsymbol{k}) \boldsymbol{v}_{k,n} = \bar{\mathcal{E}}_{k,n} \boldsymbol{v}_{k,n}, \tag{4.6}$$

where $\boldsymbol{v}_{k,n}$ are the columns in V_k and $\bar{\mathcal{E}}_{k,n} = \eta_{nn}\mathcal{E}_{k,n}$. Solving this eigenvalue problem is a general procedure to find the energy spectrum while ensuring bosonic normal modes.

A typical BdG system consists of basis vectors on the form $\boldsymbol{X}_k = [\boldsymbol{\xi}_k^T, \boldsymbol{\xi}_{-k}^\dagger]^T$ with $\boldsymbol{\xi}_k^T = [\xi_{k,1}, \ldots, \xi_{k,N_d}]$, $\boldsymbol{\xi}_{-k}^\dagger = [\xi_{-k,1}^\dagger, \ldots, \xi_{-k,N_d}^\dagger]$ and each $\xi_{k,n}$ is a bosonic operator. The dimensions of $H(\boldsymbol{k})$ is then $2N_d \times 2N_d$. Similarly, we denote the rotated basis by $\boldsymbol{X}_k' = [\boldsymbol{\gamma}_k^T, \boldsymbol{\gamma}_{-k}^\dagger]^T$ with $\boldsymbol{\gamma}_k^T = [\gamma_{k,1}, \ldots, \gamma_{k,N_d}]$. In such a system, the diagonal matrix containing the eigenvalues is on the form

$$\mathcal{E}_k = \begin{bmatrix} \text{diag}(\mathcal{E}_{k,1}, \dots, \mathcal{E}_{k,N_d}) & 0 \\ 0 & \text{diag}(\mathcal{E}_{-k,1}, \dots, \mathcal{E}_{-k,N_d}) \end{bmatrix},$$

and the diagonal Hamiltonian can be written [70]

$$\mathcal{H} = \frac{1}{2} \sum_k \sum_n^{N_d} \left(\mathcal{E}_{k,n} \gamma_{k,n}^\dagger \gamma_{k,n} + \mathcal{E}_{-k,n} \gamma_{-k,n} \gamma_{-k,n}^\dagger \right) = \sum_k \sum_n^{N_d} \mathcal{E}_{k,n} (\gamma_{k,n}^\dagger \gamma_{k,n} + \frac{1}{2}).$$

The energy spectrum is comprised of the eigenvalues $\mathcal{E}_{k,n}$ for $n = 1, \dots, N_d$. With this particular basis, they satisfy the commutation relation

$$\eta = \sigma_3 \coloneqq \sigma_z \otimes I_{N_d \times N_d} = \begin{bmatrix} I & 0 \\ 0 & -I \end{bmatrix},$$

where each entry is a $N_d \times N_d$ matrix and σ_z is the third Pauli matrix. A matrix on this form is referred as a para-unit matrix and the matrix V_k leads to a para-unitary transformation. With the known form of η and $\mathcal{E}_k$, the eigenvalues of $\sigma_3 H(\boldsymbol{k})$ are

$$\sigma_3 \mathcal{E}_k = \begin{bmatrix} \text{diag}(\mathcal{E}_{k,1}, \dots, \mathcal{E}_{k,N_d}) & 0 \\ 0 & -\text{diag}(\mathcal{E}_{-k,1}, \dots, \mathcal{E}_{-k,N_d}) \end{bmatrix}.$$

The system produces two copies of the same eigenstates. In analogy to fermionic systems, we can denote the two sets as particle and hole states where the states $n = 1, \dots, N_d$ represents particles and the states $n = N_d + 1, \dots, 2N_d$ are holes. Retaining only the positive energies suffices as the negative ones are unnecessary. It is worth noting that the matrix $\sigma_3 H(\boldsymbol{k})$ is not necessarily Hermitian and its eigenvalues may not be real, but it has been proven that this is indeed the situation [69]. Furthermore, in order for $H(\boldsymbol{k})$ to be diagonalized with a para-unitary transformation, it must be a positive definite matrix, resulting in only positive eigenvalues [71].

The particle-hole symmetry of the BdG Hamiltonian leads to [70]

$$H(\boldsymbol{k}) = \sigma_1 H^T(-\boldsymbol{k}) \sigma_1, \quad \sigma_1 = \sigma_x \otimes I_{N_d \times N_d}, \tag{4.7}$$

where σ_x is the first Pauli matrix. By using this relation, the eigenvalue problem in equation (4.6) can be transformed to

$$\begin{aligned} \sigma_3 H(\boldsymbol{k}) \boldsymbol{v}_{k,n} = \bar{\mathcal{E}}_{k,n} \boldsymbol{v}_{k,n} \implies \sigma_3 \sigma_1 H^T(-\boldsymbol{k}) \sigma_1 \boldsymbol{v}_{k,n} = \bar{\mathcal{E}}_{k,n} \sigma_1 \sigma_1 \boldsymbol{v}_{k,n} \\ \implies \sigma_3 H(\boldsymbol{k}) \sigma_1 \boldsymbol{v}_{-k,n}^* = \sigma_3 \sigma_1 \sigma_3 \bar{\mathcal{E}}_{-k,n} \sigma_1 \sigma_1 \boldsymbol{v}_{-k,n}^* = -\bar{\mathcal{E}}_{-k,n} \sigma_1 \boldsymbol{v}_{-k,n}^*. \end{aligned}$$

Thus, if the Hamiltonian has an eigenvector $\boldsymbol{v}_{k,n}$ with eigenvalue $\bar{\mathcal{E}}_{k,n}$, then $\sigma_1 \boldsymbol{v}_{-k,n}^*$ is also an eigenvector of the same Hamiltonian matrix with eigenvalue $-\bar{\mathcal{E}}_{-k,n}$. By defining $\boldsymbol{v}_{n,+}(\boldsymbol{k}) = \boldsymbol{v}_{k,n}$ and $\boldsymbol{v}_{n,-}(\boldsymbol{k}) = \sigma_1 \boldsymbol{v}_{-k,n}^*$ for $n = 1, \dots, N_d$, the para-unitary matrix can be written on the form [72]

$$V_k = [\boldsymbol{v}_{1,+}(\boldsymbol{k}), \dots, \boldsymbol{v}_{N_d,+}(\boldsymbol{k}), \boldsymbol{v}_{1,-}(\boldsymbol{k}), \dots, \boldsymbol{v}_{N_d,-}(\boldsymbol{k})],$$

and the eigenvectors satisfy the para-orthogonality condition $\boldsymbol{v}_{n,\rho}^\dagger(\boldsymbol{k}) \sigma_3 \boldsymbol{v}_{n',\rho'}(\boldsymbol{k}) = \rho \delta_{nn'} \delta_{\rho\rho'}$. We should note that while solving the eigenvalue problem, there is no guarantee that the eigenvectors satisfy the para-orthogonality condition [19]. To address this, Colpa's method can be used [71]. This involves performing a Cholesky decomposition of the Hamiltonian matrix, $H = K^\dagger K$, which allows the definition of an unitary matrix U that diagonalizes $K \sigma_3 K^\dagger$ [19]

$$U^\dagger[K\sigma_3 K^\dagger]U = \bar{\mathcal{E}}.$$

The eigenvectors can then be defined as $V = K^{-1}U\sqrt{\mathcal{E}}$, where $\mathcal{E} = \sigma_3\bar{\mathcal{E}}$ is a diagonal matrix containing only positive energies.

4.3. Ferromagnetic square lattice

We consider a ferromagnetic square lattice with out-of-plane magnetization and imagine the mirror symmetry with respect to the lattice plane to be broken such that an in-plane DMI is present. Assuming that D_{xy}^{nn} is small enough to make the ground state a collinear ferromagnet, the condition $D_{xy}^{\mathrm{nn}} < \sqrt{JK_z}/2$ represents the upper limit in the absence of a magnetic field [18]. It can be shown that the in-plane DMI yields no contribution to the non-interacting magnon Hamiltonian as long as the spin alignment is perpendicular to the lattice plane [18, 28, 54]. Hence, we can safely add the in-plane DMI to the interacting Hamiltonian without altering the magnon dispersion. As demonstrated, the exchange term that results in coupling terms quadratic in bosonic operators, and therefore hybridization, is solely from the in-plane DMI in this perpendicular spin alignment. We consider only coupling to in-plane phonon modes as they provide the lowest order contribution. In particular, we use the obtained Taylor-expanded expression, equation (4.4), with the coupling matrix defined in equation (4.5). The calculation assumes that the values of D_{xy}^{nn} and d_R are uniform for all nearest neighbours.

The calculations are done in both the first and second quantized formalism. In the first quantized approach, the Hamiltonian is formulated using ion and spin displacements, and the system's energies are determined by applying the Heisenberg equation of motion. On the other hand, the second quantized method involves transforming the ion and spin displacements into magnons and phonons, and expressing the Hamiltonian in terms of creation and annihilation operators. The diagonalization of the Hamiltonian is achieved by solving the Bogoliubov-de Gennes equation.

4.3.1. First quantized approach

Phonon Hamiltonian

Before investigating the magnon-phonon interaction, we transform the phonon Hamiltonian, given by equation (2.1), into a more appropriate form. We introduce the dimensionless variables $\tilde{u}_{i\alpha\mu} = \sqrt{M_\alpha\Omega/\hbar}u_{i\alpha\mu}$ and $\tilde{p}_{i\alpha\mu} = \sqrt{1/M_\alpha\Omega\hbar}p_{i\alpha\mu}$, where Ω is an as-yet unspecified parameter in units of frequency. We also consider their Fourier components

$$\tilde{u}_{q\alpha\mu} = \frac{1}{\sqrt{N_{\mathrm{uc}}}}\sum_i \tilde{u}_{i\alpha\mu}\mathrm{e}^{-\mathrm{i}\boldsymbol{q}\cdot\boldsymbol{R}_{i\alpha}}, \quad \tilde{p}_{q\alpha\mu} = \frac{1}{\sqrt{N_{\mathrm{uc}}}}\sum_i \tilde{p}_{i\alpha\mu}\mathrm{e}^{-\mathrm{i}\boldsymbol{q}\cdot\boldsymbol{R}_{i\alpha}}. \tag{4.8}$$

The dimensionless displacement and momentum satisfy the commutation relation $[\tilde{u}_l, \tilde{p}_{l'}] = \mathrm{i}\delta_{l,l'}$. In terms of the dimensionless Fourier components, the phonon Hamiltonian is expressed as

$$\mathcal{H}_{\mathrm{ph}} = \frac{1}{2}\hbar\Omega\left(\sum_{q,\alpha}\tilde{\boldsymbol{p}}_{q,\alpha}^T\cdot\tilde{\boldsymbol{p}}_{-q,\alpha} + \sum_\beta \tilde{\boldsymbol{u}}_{-q,\alpha}^T\frac{D^{\alpha\beta}(\boldsymbol{q})}{\Omega^2}\tilde{\boldsymbol{u}}_{q,\beta}\right),$$

where $D^{\alpha\beta}(\boldsymbol{q})$ are $d\times d$ dynamical matrices between different lattice sites. Moreover, we let $\Omega = \sqrt{D_{\mu\nu}^{\alpha\beta}(\boldsymbol{\delta})}$ be a scaling parameter, for a particular configuration of indices that will be specified later on. This allows us to define the dimensionless dynamical matrix $\tilde{D}(\boldsymbol{q}) = D(\boldsymbol{q})/\Omega^2$, with the corresponding

dimensionless eigenvalues $\tilde{\omega}_{q,\lambda}^2$. The physical frequency is restored by multiplying with Ω, $\omega_{q,\lambda} = \Omega\tilde{\omega}_{q,\lambda}$. The phonon Hamiltonian can be written compactly as

$$\mathcal{H}_{\text{ph}} = \frac{1}{2}\sum_{q} \tilde{\boldsymbol{\phi}}_{\text{ph}}^T(-\boldsymbol{q}) H_{\text{ph}}(\boldsymbol{q}) \tilde{\boldsymbol{\phi}}_{\text{ph}}(\boldsymbol{q}), \tag{4.9}$$

in the basis $\tilde{\boldsymbol{\phi}}_{\text{ph}}(\boldsymbol{q}) = [\tilde{\boldsymbol{u}}_{q,\alpha_1}^T, \tilde{\boldsymbol{u}}_{q,\alpha_2}^T, \dots, \tilde{\boldsymbol{p}}_{-q,\alpha_1}^T, \tilde{\boldsymbol{p}}_{-q,\alpha_2}^T, \dots]^T$. The intention of this notation is for each component to be interpreted as a row vector, with its spatial components as individual elements. Moreover, we have

$$H_{\text{ph}}(\boldsymbol{q}) = \hbar\Omega \begin{bmatrix} \tilde{D}(\boldsymbol{q}) & 0 \\ 0 & I \end{bmatrix},$$

where each entry is a $dr \times dr$ matrix, r being the number of atoms in the unit cell. We want to express the phonon Hamiltonian in terms of its eigenmodes, where the Hamiltonian becomes diagonal. To achieve this, we introduce a rotated basis that diagonalizes the dynamical matrix. Denoting the first half of $\tilde{\boldsymbol{\phi}}_{\text{ph}}(\boldsymbol{q})$ as $\tilde{\boldsymbol{u}}_q$, the rotated basis is given by $\tilde{\boldsymbol{u}}'_q = U_{\text{ph}}^{-1}(\boldsymbol{q})\tilde{\boldsymbol{u}}_q$, where $U_{\text{ph}}(\boldsymbol{q}) = [\hat{\boldsymbol{e}}^1(\boldsymbol{q}), \dots, \hat{\boldsymbol{e}}^{dr}(\boldsymbol{q})]$ is an unitary matrix and $\hat{\boldsymbol{e}}^\lambda(\boldsymbol{q})$ represents the eigenvector to mode λ. The eigenvalues of the dimensionless dynamical are proportional to the square of the dimensionless frequency. To adjust for this, we factor out $\sqrt{\tilde{\omega}_{q,\lambda}}$ in the basis. Consequently, the basis that diagonalizes the dynamical matrix with eigenvalues proportional to the frequency is given by $\tilde{\boldsymbol{u}}'_q = \text{diag}(\sqrt{\tilde{\omega}_{q,\lambda}})U_{\text{ph}}^\dagger(\boldsymbol{q})\tilde{\boldsymbol{u}}_q$, with $\text{diag}(\sqrt{\tilde{\omega}_{q,\lambda}}) = \text{diag}(\sqrt{\tilde{\omega}_{q,1}}, \dots, \sqrt{\tilde{\omega}_{q,dr}})$ for shorthand notation. To maintain the commutation relation between the displacement and momentum, we define $\tilde{\boldsymbol{p}}'_q = \text{diag}(1/\sqrt{\tilde{\omega}_{q,\lambda}})U_{\text{ph}}^T(\boldsymbol{q})\tilde{\boldsymbol{p}}_q$ as the rotated momentum part of the basis. The commutation relation is calculated as

$$\begin{aligned}
[\tilde{u}'_{q,\lambda_m}, \tilde{p}'_{k,\lambda_n}] &= \sqrt{\frac{\tilde{\omega}_{q,\lambda_m}}{\tilde{\omega}_{k,\lambda_n}}}[\hat{\boldsymbol{e}}^{\lambda_m *}(\boldsymbol{q}) \cdot \tilde{\boldsymbol{u}}_q, \hat{\boldsymbol{e}}^{\lambda_n}(\boldsymbol{k}) \cdot \tilde{\boldsymbol{p}}_k] \\
&= \sqrt{\frac{\tilde{\omega}_{q,\lambda_m}}{\tilde{\omega}_{k,\lambda_n}}} \sum_{\substack{\alpha,\beta \\ \mu,\nu}} \hat{e}_{\alpha\mu}^{\lambda_m *}(\boldsymbol{q}) \hat{e}_{\beta\nu}^{\lambda_n}(\boldsymbol{k}) [\tilde{u}_{q\alpha\mu}, \tilde{p}_{k\beta\nu}] \\
&= \mathrm{i}\delta_{q,k}\sqrt{\frac{\tilde{\omega}_{q,\lambda_m}}{\tilde{\omega}_{q,\lambda_n}}} \sum_{\alpha,\mu} \hat{e}_{\alpha\mu}^{\lambda_m *}(\boldsymbol{q}) \hat{e}_{\alpha\mu}^{\lambda_n}(\boldsymbol{q}) = \mathrm{i}\delta_{q,k}\delta_{\lambda_m,\lambda_n},
\end{aligned}$$

where the orthonormality condition of the eigenvectors, equation (2.5), was used in the last equality. Since matrix satisfies $U_{\text{ph}}(-\boldsymbol{q}) = U_{\text{ph}}^*(\boldsymbol{q})$, the momentum part of the Hamiltonian transforms to

$$\tilde{\boldsymbol{p}}_q^T \cdot \tilde{\boldsymbol{p}}_{-q} = (U_{\text{ph}}^*(\boldsymbol{q})\text{diag}(\sqrt{\tilde{\omega}_{q,\lambda}})\tilde{\boldsymbol{p}}'_q)^T (U_{\text{ph}}(\boldsymbol{q})\text{diag}(\sqrt{\tilde{\omega}_{q,\lambda}})\tilde{\boldsymbol{p}}'_{-q}) = \text{diag}(\tilde{\omega}_{q,\lambda})\tilde{\boldsymbol{p}}_q'^T \cdot \tilde{\boldsymbol{p}}'_{-q}.$$

By the same approach, the displacement part transforms to

$$\begin{aligned}
\tilde{\boldsymbol{u}}_{-q}^T \tilde{D}(\boldsymbol{q}) \tilde{\boldsymbol{u}}_q &= (U_{\text{ph}}^*(\boldsymbol{q})\text{diag}(1/\sqrt{\tilde{\omega}_{q,\lambda}})\tilde{\boldsymbol{u}}'_{-q})^T \tilde{D}(\boldsymbol{q}) (U_{\text{ph}}(\boldsymbol{q})\text{diag}(1/\sqrt{\tilde{\omega}_{q,\lambda}})\tilde{\boldsymbol{u}}'_q) \\
&= \text{diag}(\tilde{\omega}_{q,\lambda})\tilde{\boldsymbol{u}}_{-q}'^T \cdot \tilde{\boldsymbol{u}}'_q,
\end{aligned}$$

where we used that $U_{\text{ph}}^\dagger(\boldsymbol{q})\tilde{D}(\boldsymbol{q})U_{\text{ph}}(\boldsymbol{q}) = \text{diag}(\tilde{\omega}_{q,\lambda}^2)$. The diagonal phonon Hamiltonian is then

$$\mathcal{H}_{\text{ph}} = \frac{1}{2}\sum_q \tilde{\boldsymbol{\phi}}_{\text{ph}}'^T(-\boldsymbol{q}) H'_{\text{ph}}(\boldsymbol{q}) \tilde{\boldsymbol{\phi}}'_{\text{ph}}(\boldsymbol{q}) = \frac{1}{2}\sum_q \tilde{\boldsymbol{\phi}}_{\text{ph}}'^\dagger(\boldsymbol{q}) H'_{\text{ph}}(\boldsymbol{q}) \tilde{\boldsymbol{\phi}}'_{\text{ph}}(\boldsymbol{q}),$$

$\tilde{\phi}'_{\mathrm{ph}}(\boldsymbol{q})$ is the rotated basis and

$$H'_{\mathrm{ph}}(\boldsymbol{q}) = \hbar\Omega \begin{bmatrix} \mathrm{diag}(\tilde{\omega}_{q,\lambda}) & 0 \\ 0 & \mathrm{diag}(\tilde{\omega}_{q,\lambda}) \end{bmatrix}.$$

This represents a general form of the phonon Hamiltonian. For a square lattice, the specific definitions of the eigenvectors and eigenvalues for various modes can be found in section 2.3.1, with $N_{\mathrm{uc}} = N$.

Interacting Hamiltonian

Expressing the spins as $\boldsymbol{S}_i = S\hat{\boldsymbol{z}} + \delta\boldsymbol{S}_i$, where $\delta\boldsymbol{S}_i$ lies in the plane, and considering only the quadratic terms, we can write the Taylor-expanded in-plane DMI as

$$\mathcal{H}_{\mathrm{int}} = S \sum_{<i,j>} \sum_{\mu} (u_{i\mu} - u_{j\mu}) \left[T^{\mu x}_{ij} (\delta S_{iy} - \delta S_{jy}) - T^{\mu y}_{ij} (\delta S_{ix} - \delta S_{jx}) \right],$$

for $\mu \in \{x, y\}$. To facilitate comparison, we examine the 'normalized' spin displacement $\delta\tilde{\boldsymbol{S}}_i = \delta\boldsymbol{S}_i/\sqrt{S}$. This allows us to directly correspond the result with those obtained in the second quantized formalism. Note the abuse of notation as the spin is already dimensionless. Furthermore, to prevent double counting, we utilize $\sum_{<i,j>} \to (1/2)\sum_{i,\delta}$, where i covers the entire lattice and δ represents the nearest neighbours. Expressing the interacting Hamiltonian in terms of the Fourier components

$$\delta\tilde{S}_{q\mu} = \frac{1}{\sqrt{SN}} \sum_i \delta S_{i\mu} \mathrm{e}^{-\mathrm{i}\boldsymbol{q}\cdot\boldsymbol{R}_i}, \quad \delta S_{i\mu} = \sqrt{\frac{S}{N}} \sum_q \delta\tilde{S}_{q\mu} \mathrm{e}^{\mathrm{i}\boldsymbol{q}\cdot\boldsymbol{R}_i},$$

and $\tilde{u}_{q\mu}$, defined in equation (4.8), it may be written as

$$\begin{aligned}
\mathcal{H}_{\mathrm{int}} =& \frac{S}{2N}\sqrt{\frac{\hbar S}{M\Omega}} \sum_{i,\delta} \sum_{\mu} \sum_{q,q'} \tilde{u}_{q'\mu} \mathrm{e}^{\mathrm{i}\boldsymbol{q}'\cdot\boldsymbol{R}_i} (1 - \mathrm{e}^{\mathrm{i}\boldsymbol{q}'\cdot\boldsymbol{\delta}}) \left[T^{\mu x}_{i,i+\delta} \delta\tilde{S}_{qy} \mathrm{e}^{\mathrm{i}\boldsymbol{q}\cdot\boldsymbol{R}_i} (1 - \mathrm{e}^{\mathrm{i}\boldsymbol{q}\cdot\boldsymbol{\delta}}) - T^{\mu y}_{i,i+\delta} \delta\tilde{S}_{qx} \mathrm{e}^{\mathrm{i}\boldsymbol{q}\cdot\boldsymbol{R}_i} (1 - \mathrm{e}^{\mathrm{i}\boldsymbol{q}\cdot\boldsymbol{\delta}}) \right] \\
=& S\sqrt{\frac{\hbar S}{M\Omega}} \sum_q \sum_{\delta,\mu} \tilde{u}_{-q\mu} (1 - \cos(\boldsymbol{q}\cdot\boldsymbol{\delta})) \left[T^{\mu x}_{\delta} \delta\tilde{S}_{qy} - T^{\mu y}_{\delta} \delta\tilde{S}_{qx} \right] \\
=& \sum_q \tilde{\boldsymbol{u}}^{\dagger}_q T_q \delta\tilde{\boldsymbol{S}}_q,
\end{aligned}$$

where $\tilde{\boldsymbol{u}}_q = [\tilde{u}_{qx}, \tilde{u}_{qy}]^T$, $\delta\tilde{\boldsymbol{S}}_q = (1/\sqrt{S})[\delta S_{qx}, \delta S_{qy}]^T$ and we used that $T^{\mu\nu}_{i,i+\delta} = T^{\mu\nu}_{\delta}$ as the matrix elements solely rely on the vectors connecting the nearest neighbours. Furthermore, T_q is a 2×2 matrix defined accordingly

$$T_q = S\sqrt{\frac{\hbar S}{M\Omega}} \sum_{\delta} \begin{bmatrix} -T^{xy}_{\delta} & T^{xx}_{\delta} \\ -T^{yy}_{\delta} & T^{yx}_{\delta} \end{bmatrix} (1 - \cos(\boldsymbol{q}\cdot\boldsymbol{\delta})).$$

Upon computation, we find that the matrix is diagonal with the following elements

$$\begin{aligned}
T^{xx}_q &= 2\zeta S\sqrt{S} D^{\mathrm{nn}}_{xy} \left(-d_R(1 - \cos(q_x a)) + 1 - \cos(q_y a) \right), \\
T^{yy}_q &= 2\zeta S\sqrt{S} D^{\mathrm{nn}}_{xy} \left(1 - \cos(q_x a) - d_R(1 - \cos(q_y a)) \right),
\end{aligned} \tag{4.10}$$

where $\zeta = (1/a)\sqrt{\hbar/M\Omega}$ is a dimensionless quantity proportional to the interaction strength. By expressing the displacement in terms of the normal modes $\tilde{\boldsymbol{u}}_q^\dagger = \tilde{\boldsymbol{u}}_q'^\dagger \mathrm{diag}(1/\sqrt{\tilde{\omega}_{q,\lambda}}) U_{\mathrm{ph}}^\dagger(\boldsymbol{q})$, the interacting Hamiltonian becomes

$$\mathcal{H}_{\mathrm{int}} = \sum_q \tilde{\boldsymbol{u}}_q'^\dagger T_q' \delta\tilde{\boldsymbol{S}}_q,$$

where the new rotated coupling matrix is $T_q' = \mathrm{diag}(1/\sqrt{\tilde{\omega}_{q,\lambda}}) U_{\mathrm{ph}}^\dagger(\boldsymbol{q}) T_q$. For shorthand notation, we denote the phonon modes by $\lambda = \{1,2\} = \{\mathrm{TA}, \mathrm{LA}\}$. The elements in the rotated coupling matrix are then

$$T_q' = \begin{bmatrix} \frac{(\mathcal{A}-\mathcal{C}-\mathcal{D})T_q^{xx}}{\sqrt{\tilde{\omega}_{q,1}}\sqrt{(\mathcal{A}-\mathcal{C}-\mathcal{D})^2+4\mathcal{B}^2}} & \frac{2\mathcal{B}T_q^{yy}}{\sqrt{\tilde{\omega}_{q,1}}\sqrt{(\mathcal{A}-\mathcal{C}-\mathcal{D})^2+4\mathcal{B}^2}} \\ \frac{(\mathcal{A}-\mathcal{C}+\mathcal{D})T_q^{xx}}{\sqrt{\tilde{\omega}_{q,2}}\sqrt{(\mathcal{A}-\mathcal{C}+\mathcal{D})^2+4\mathcal{B}^2}} & \frac{2\mathcal{B}T_q^{yy}}{\sqrt{\tilde{\omega}_{q,2}}\sqrt{(\mathcal{A}-\mathcal{C}+\mathcal{D})^2+4\mathcal{B}^2}} \end{bmatrix},$$

where the functions $\mathcal{A}, \mathcal{B}, \mathcal{C}$ and $\mathcal{D}$ are defined in section 2.3.1. By utilizing the fact that $\sum_q = \sum_{-q}$, the interacting Hamiltonian may be split up in the following way

$$\begin{aligned}\mathcal{H}_{\mathrm{int}} &= \frac{1}{2}\left(\sum_q \tilde{\boldsymbol{u}}_q'^\dagger T_q' \delta\tilde{\boldsymbol{S}}_q + \sum_{-q} \tilde{\boldsymbol{u}}_{-q}'^\dagger T_{-q}' \delta\tilde{\boldsymbol{S}}_{-q}\right) = \frac{1}{2}\sum_q \left(\tilde{\boldsymbol{u}}_q'^\dagger T_q' \delta\tilde{\boldsymbol{S}}_q + \tilde{\boldsymbol{u}}_{-q}'^\dagger T_{-q}' \delta\tilde{\boldsymbol{S}}_{-q}\right) \\ &= \frac{1}{2}\sum_q \left(\tilde{\boldsymbol{u}}_q'^\dagger T_q' \delta\tilde{\boldsymbol{S}}_q + \tilde{\boldsymbol{u}}_q'^T T_{-q}' \delta\tilde{\boldsymbol{S}}_q^*\right) = \frac{1}{2}\sum_q \left(\tilde{\boldsymbol{u}}_q'^\dagger T_q' \delta\tilde{\boldsymbol{S}}_q + \delta\tilde{\boldsymbol{S}}_q^\dagger T_q'^\dagger \tilde{\boldsymbol{u}}_q'\right),\end{aligned}$$

where we in the last equality took the transpose of the last term and also used that $T_{-q}'^T = T_q'^\dagger$.

Magnon Hamiltonian

The magnon Hamiltonian, equation (3.6), can be expressed in terms of $\delta\tilde{\boldsymbol{S}}_q$ by noticing that $\delta\tilde{S}_{qx} = (1/\sqrt{2})(a_q + a_{-q}^\dagger)$ and $\delta\tilde{S}_{qy} = -(\mathrm{i}/\sqrt{2})(a_q - a_{-q}^\dagger)$. The Hamiltonian is transformed to

$$\mathcal{H}_{\mathrm{m}} = \frac{1}{2}\sum_q \delta\tilde{\boldsymbol{S}}_q^\dagger H_{\mathrm{m}}(\boldsymbol{q}) \delta\tilde{\boldsymbol{S}}_q, \quad H_{\mathrm{m}}(\boldsymbol{q}) = E_q I_{2\times 2},$$

where E_q is the magnon dispersion.

Finding the energy bands

The total Hamiltonian, including the interacting part, can be written on the form

$$\begin{aligned}\mathcal{H} &= \frac{1}{2}\sum_q \left(\delta\tilde{\boldsymbol{S}}_q^\dagger H_{\mathrm{m}}(\boldsymbol{q}) \delta\tilde{\boldsymbol{S}}_q + \tilde{\boldsymbol{\phi}}_{\mathrm{ph}}'^\dagger(\boldsymbol{q}) H_{\mathrm{ph}}'(\boldsymbol{q}) \tilde{\boldsymbol{\phi}}_{\mathrm{ph}}'(\boldsymbol{q}) + \tilde{\boldsymbol{u}}_q'^\dagger T_q' \delta\tilde{\boldsymbol{S}}_q + \delta\tilde{\boldsymbol{S}}_q^\dagger T_q'^\dagger \tilde{\boldsymbol{u}}_q'\right) \\ &= \frac{1}{2}\sum_q \boldsymbol{\phi}_q^\dagger H_{\mathrm{me}}(\boldsymbol{q}) \boldsymbol{\phi}_q,\end{aligned}$$

in the basis $\boldsymbol{\phi}_q = [\delta\tilde{S}_{q,x}, \delta\tilde{S}_{q,y}, \tilde{u}_{q,1}', \tilde{u}_{q,2}', \tilde{p}_{-q,1}', \tilde{p}_{-q,2}']^T$. The magnetoelastic matrix $H_{\mathrm{me}}(\boldsymbol{q})$ is defined as

$$H_{\mathrm{me}}(\boldsymbol{q}) = \begin{bmatrix} H_{\mathrm{m}}(\boldsymbol{q}) & T_q'^\dagger \\ T_q' & H_{\mathrm{ph}}'(\boldsymbol{q}) \end{bmatrix}.$$

From the Heisenberg equation of motion, $\mathrm{i}\hbar\partial_t\boldsymbol{\phi}_q = [\boldsymbol{\phi}_q, \mathcal{H}]$, we obtain [18, 26]

$$\mathrm{i}\hbar\partial_t\boldsymbol{\phi}_q = \eta H_{\mathrm{me}}(\boldsymbol{q})\boldsymbol{\phi}_q,$$
$$\text{with } \eta = [\boldsymbol{\phi}_q, \boldsymbol{\phi}_q^\dagger] = \begin{bmatrix} -\sigma_y & 0_{2\times2} & 0_{2\times2} \\ 0_{2\times2} & 0_{2\times2} & \mathrm{i}I_{2\times2} \\ 0_{2\times2} & -\mathrm{i}I_{2\times2} & 0_{2\times2} \end{bmatrix},$$

and σ_y is the second Pauli matrix. Thus, the energy bands are obtained by diagonalizing the effective Hamiltonian matrix $\eta H_{\mathrm{me}}(\boldsymbol{q})$. The positive eigenvalues yield the energy spectrum while the negative ones are redundant. Finding the energies in this manner can be thought of as solving the generalized Bogoliubov-de Gennes equation [18].

4.3.2. Second quantized approach

From equations (2.9) and (3.6), the non-interacting part of the Hamiltonian in the second quantized formalism is

$$\begin{aligned}\mathcal{H}_0 &= \mathcal{H}_{\mathrm{ph}} + \mathcal{H}_{\mathrm{m}}, \\ \mathcal{H}_{\mathrm{ph}} &= \sum_{q,\lambda} \varepsilon_{q,\lambda} c_{q,\lambda}^\dagger c_{q,\lambda}, \\ \mathcal{H}_{\mathrm{m}} &= \sum_k E_k a_k^\dagger a_k.\end{aligned}$$

Here, $\{c_{q,\lambda}, c_{q,\lambda}^\dagger\}$ is the phonon annihilation and creation operator and $\varepsilon_{q,\lambda} = \hbar\omega_{q,\lambda}$ is the phonon energy in mode λ. Similarly, $\{a_k, a_k^\dagger\}$ denotes the magnon annihilation and creation operator. Employing the Holstein-Primakoff transformation, equation (3.2), and expressing the ionic displacement in terms of bosonic operators, equation (2.10), the quadratic terms in the interacting Hamiltonian described in equation (4.4) become

$$\begin{aligned}\mathcal{H}_{\mathrm{int}} &= -\frac{S}{2}\sqrt{\frac{S}{2}} \sum_{i,\delta}\sum_{\mu} (u_{i\mu} - u_{i+\delta,\mu}) \left[(T_\delta^{\mu y} + \mathrm{i}T_\delta^{\mu x})(a_i - a_{i+\delta}) + (T_\delta^{\mu y} - \mathrm{i}T_\delta^{\mu x})(a_i^\dagger - a_{i+\delta}^\dagger) \right] \\ &= -\frac{S}{4}\sqrt{\frac{\hbar S}{NM}} \sum_{q,\lambda}\sum_{i,\delta}\sum_{\mu} \frac{e_\mu^\lambda(\boldsymbol{q})}{\sqrt{\omega_{q,\lambda}}} (c_{q,\lambda} + c_{-q,\lambda}^\dagger) \mathrm{e}^{\mathrm{i}\boldsymbol{q}\cdot\boldsymbol{R}_i} \left(1 - \mathrm{e}^{\mathrm{i}\boldsymbol{q}\cdot\boldsymbol{\delta}}\right) \\ &\quad \times \left[(T_\delta^{\mu y} + \mathrm{i}T_\delta^{\mu x})(a_i - a_{i+\delta}) + (T_\delta^{\mu y} - \mathrm{i}T_\delta^{\mu x})(a_i^\dagger - a_{i+\delta}^\dagger) \right].\end{aligned}$$

Substituting for the magnon operators in reciprocal space, equation (3.4), the Hamiltonian transforms to

$$\begin{aligned}\mathcal{H}_{\mathrm{int}} &= -\frac{S}{4N}\sqrt{\frac{\hbar S}{M}} \sum_{q,q',\lambda}\sum_{i,\delta}\sum_{\mu} \frac{e_\mu^\lambda(\boldsymbol{q})}{\sqrt{\omega_{q,\lambda}}} (c_{q,\lambda} + c_{-q,\lambda}^\dagger) \mathrm{e}^{\mathrm{i}(\boldsymbol{q}-\boldsymbol{q}')\cdot\boldsymbol{R}_i} \left(1 - \mathrm{e}^{\mathrm{i}\boldsymbol{q}\cdot\boldsymbol{\delta}}\right) \\ &\quad \times (1 - \mathrm{e}^{-\mathrm{i}\boldsymbol{q}'\cdot\boldsymbol{\delta}}) \left[(T_\delta^{\mu y} + \mathrm{i}T_\delta^{\mu x}) a_{-q'} + (T_\delta^{\mu y} - \mathrm{i}T_\delta^{\mu x}) a_{q'}^\dagger \right] \\ &= -\frac{S}{2}\sqrt{\frac{\hbar S}{M}} \sum_{q,\lambda}\sum_{\delta,\mu} \frac{e_\mu^\lambda(\boldsymbol{q})}{\sqrt{\omega_{q,\lambda}}} (c_{q,\lambda} + c_{-q,\lambda}^\dagger) \left(1 - \cos(\boldsymbol{q}\cdot\boldsymbol{\delta})\right) \left[(T_\delta^{\mu y} + \mathrm{i}T_\delta^{\mu x}) a_{-q} + (T_\delta^{\mu y} - \mathrm{i}T_\delta^{\mu x}) a_q^\dagger \right] \\ &= \sum_{q,\lambda} \left[G_{q,\lambda}(c_{q,\lambda} + c_{-q,\lambda}^\dagger) a_{-q} + G_{q,\lambda}^*(c_{-q,\lambda} + c_{q,\lambda}^\dagger) a_{-q}^\dagger \right].\end{aligned}$$

Here we defined the coupling coefficients

$$\begin{aligned} G_{q,\lambda} &= -\frac{S}{2}\sqrt{\frac{\hbar S}{M\omega_{q,\lambda}}}\sum_{\delta,\mu} e_\mu^\lambda(\boldsymbol{q})(1-\cos(\boldsymbol{q}\cdot\boldsymbol{\delta}))(T_\delta^{\mu y}+\mathrm{i}T_\delta^{\mu x}) \\ &= \zeta S\sqrt{S}D_{xy}^{\mathrm{nn}}\frac{\boldsymbol{e}^\lambda(\boldsymbol{q})\cdot\boldsymbol{g}_q}{\sqrt{\tilde{\omega}_{q,\lambda}}}, \end{aligned}$$

and the elements in $\boldsymbol{g}_q$ are

$$\boldsymbol{g}_q = \begin{bmatrix} -d_R(1-\cos(q_x a)) + 1 - \cos(q_y a) \\ -\mathrm{i}(1-\cos(q_x a)) + \mathrm{i}d_R(1-\cos(q_y a)) \end{bmatrix}. \tag{4.11}$$

The total Hamiltonian can be written in matrix notation on the form

$$\mathcal{H} = \frac{1}{2}\sum_q \boldsymbol{\Psi}_q^\dagger H_{\mathrm{me}}(\boldsymbol{q})\boldsymbol{\Psi}_q,$$

with $\boldsymbol{\Psi}_q = [\boldsymbol{\psi}_q^T, \boldsymbol{\psi}_{-q}^\dagger]^T$ and $\boldsymbol{\psi}_q^T = [a_q, c_{q,1}, c_{q,2}]$. $H_{\mathrm{me}}(\boldsymbol{q})$ is a 6×6 Hermitian matrix with the elements

$$H_{\mathrm{me}}(\boldsymbol{q}) = \begin{bmatrix} E_q & G_{-q,1}^* & G_{-q,2}^* & 0 & G_{-q,1}^* & G_{-q,2}^* \\ G_{-q,1} & \varepsilon_{q,1} & 0 & G_{q,1}^* & 0 & 0 \\ G_{-q,2} & 0 & \varepsilon_{q,2} & G_{q,2}^* & 0 & 0 \\ 0 & G_{q,1} & G_{q,2} & E_q & G_{q,1} & G_{q,2} \\ G_{-q,1} & 0 & 0 & G_{q,1}^* & \varepsilon_{q,1} & 0 \\ G_{-q,2} & 0 & 0 & G_{q,2}^* & 0 & \varepsilon_{q,2} \end{bmatrix}.$$

The energy bands are obtained by solving the BdG equation, namely computing the eigenvalues of $\sigma_3 H_{\mathrm{me}}(\boldsymbol{q})$, where σ_3 is the para-unit matrix $\sigma_3 = \mathrm{diag}(1,1,1,-1,-1,-1)$. We keep only the positive eigenvalues.

4.3.3. Result

In an attempt to reproduce the results obtained in Ref. [18] where they considered coupling to in-plane phonon modes, we set the nonzero force coefficients in the phonon dispersion to $\rho_1 = \rho_2 = \gamma_1/8$ where $\gamma_1 = -|\gamma_1|$ and use the parameters $J = 2\,\mathrm{meV}$, $\hbar\Omega = 10\,\mathrm{meV}$ (with $\Omega = \sqrt{|\gamma_1|/M}$), $\Delta = 1\,\mathrm{meV}$ and $D_{xy}^{\mathrm{nn}} = 0.4\,\mathrm{meV}$. Since we are unable to determine the lattice constant used in Ref. [18], we set $\zeta = 0.1$ which is a commonly used value in materials [26]. Other parameters include $S = 3/2$ and $d_R = 0$. These values, except for the missing lattice constant, are typical values for atoms in 3d transition metals [18]. We choose not to display the out-of-plane phonon modes since they are unaffected by the interacting Hamiltonian.

We find the energy spectrum through numerical diagonalization and present the results in Figures 4.2a and 4.2b, which show the coupled magnon-phonon dispersion along the symmetry lines of the Brillouin zone, calculated with the first and second quantized approaches, respectively. Gap openings occur at avoided crossings between phonon and magnon branches where the hybridized magnon-polaron state is significant. This is demonstrated clearly in the inset figures. The wavefunction in these hybridized states is partially magnonic and partially phononic, and we illustrate this by assigning colors (red, blue, or yellow) to each mode based on the absolute value of the magnon part of the wavefunction, using a color scale from 0 to 1 where 1 means the wavefunction is completely magnonic, and thus red.

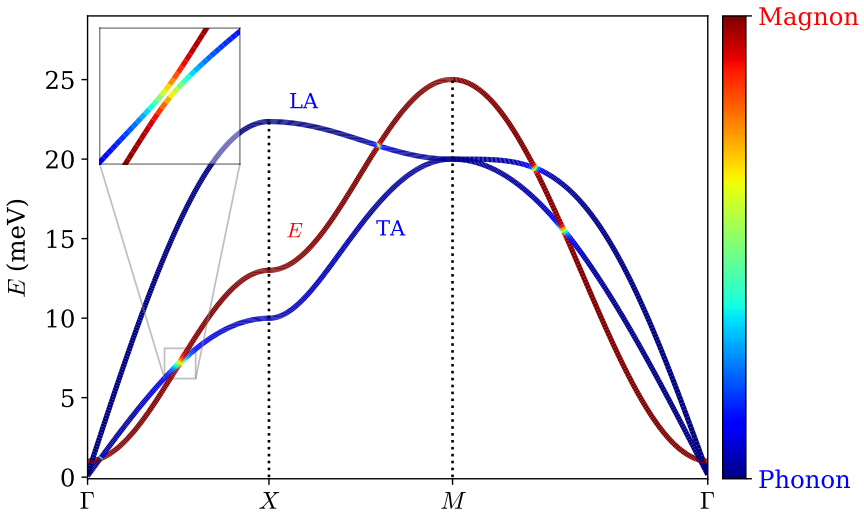

(a) First quantized formalism.

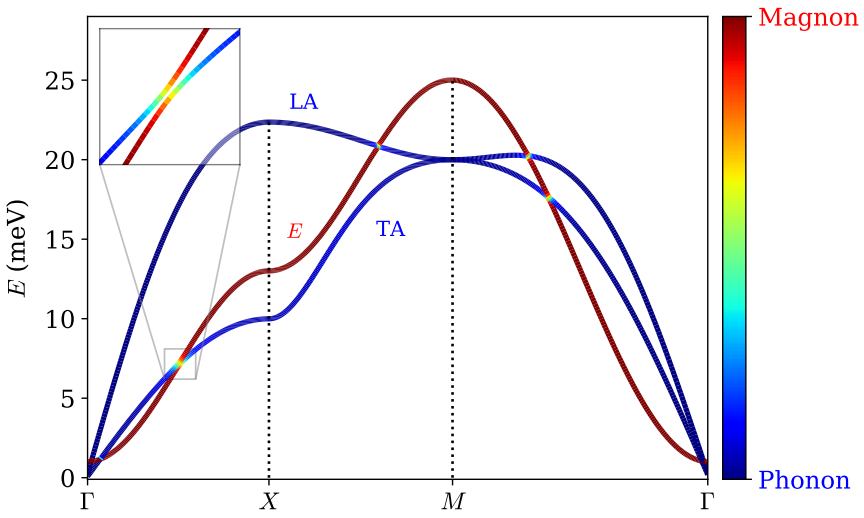

(b) Second quantized formalism.

Figure 4.2.: The figures show the magnetoelastic energy spectrum in a ferromagnetic square lattice found by calculating in the first and second quantized formalism. We only display the in-plane phonon branches as coupling to out-of-plane phonon modes are of higher order. The labels (LA,TA,E) correspond to the non-interacting system. The parameters are $J = 2$, $\hbar\Omega = 10$, $\Delta = 1$ and $D_{xy}^{\mathrm{nn}} = 0.4$, in units of meV. Moreover, $\zeta = 0.1$, $S = 3/2$ and $d_R = 0$.

Comparing the results obtained in our study to those in Ref. [18] is challenging to judge by just looking at the results. While the non-interacting magnon and phonon dispersions align, accurately determining the band gap size presents difficulties. It is likely that discrepancies arise from variations in the parameter ζ, which is proportional to the coupling strength. Additionally, we note a $\sqrt{2}$

discrepancy in the formulation of the coupling matrix elements, outlined in equation (4.10).

While lacking analytical proof, numerical comparisons between the first and second quantized approaches demonstrate a complete overlap in the obtained energy spectra. The results align precisely, accounting for numerical errors. This consistency holds true across various tested parameter configurations. The motivation behind selecting the 'normalized' spin as the basis in the first quantized method is its compatibility with the magnon operators. This choice ensures equal interaction strengths and facilitates direct comparisons. Similar considerations apply to the normal (rotated) ion displacement, which can be expressed as follows

$$\tilde{u}'_{q,\lambda} = \frac{1}{\sqrt{2}}(c_{q,\lambda} + c^\dagger_{-q,\lambda}).$$

An important observation is that the second quantized method offers greater ease and simplicity in its application. This is primarily due to the fact that the creation and annihilation operators correspond to excitations of the normal modes within the system, and they follow straightforward commutation relations.

4.4. Ferromagnetic honeycomb lattice

In this calculation, we study the magnon-phonon energy bands in a ferromagnetic honeycomb lattice. The lattice is made up of identical atoms and the magnetization is perpendicular to the lattice plane. We examine the bilinear terms in the Hamiltonian driven by the in-plane DMI, as defined in equation (4.4). The interacting Hamiltonian only accounts for nearest neighbour interactions between spin degrees of freedom and in-plane phonons, with the assumption of uniform values for D^{nn}_{xy} and d_R across all nearest neighbours. The calculation is carried out using both the first and second quantization methods.

4.4.1. First quantized approach

The phonon Hamiltonian is treated in a similar way as in section 4.3.1, where the in-plane eigenvalues and eigenvectors are defined in equations (2.21) and (2.23) respectively. Subsequently, the phonon eigenvectors are transformed to the Cartesian basis using equation (2.24).

Magnon Hamiltonian

The magnon Hamiltonian listed in equation (3.11) is on the form

$$\mathcal{H}_{\text{m}} = \sum_q \boldsymbol{\psi}^\dagger_{\text{m}}(\boldsymbol{q}) H_{\text{m}}(\boldsymbol{q}) \boldsymbol{\psi}_{\text{m}}(\boldsymbol{q}),$$

in the basis $\boldsymbol{\psi}_{\text{m}}(\boldsymbol{q}) = [a_q, b_q]^T$. We seek a Hamiltonian in the spin basis. By adding a hole space to the particle space, as done in [26], the Hamiltonian becomes

$$\begin{aligned}
\mathcal{H}_{\text{m}} =& \frac{1}{2}\sum_q \left(\boldsymbol{\psi}^\dagger_{\text{m}}(\boldsymbol{q}) H_{\text{m}}(\boldsymbol{q}) \boldsymbol{\psi}_{\text{m}}(\boldsymbol{q}) + \boldsymbol{\psi}^T_{\text{m}}(-\boldsymbol{q}) H^T_{\text{m}}(-\boldsymbol{q}) \boldsymbol{\psi}^*_{\text{m}}(-\boldsymbol{q})\right) \\
=& \frac{1}{2}\sum_q [a^\dagger_q, b^\dagger_q, a_{-q}, b_{-q}] \begin{bmatrix} H_{\text{m}}(\boldsymbol{q}) & 0 \\ 0 & H^T_{\text{m}}(-\boldsymbol{q}) \end{bmatrix} [a_q, b_q, a^\dagger_{-q}, b^\dagger_{-q}]^T \\
=& \frac{1}{2}\sum_q \delta\boldsymbol{S}^\dagger_q H'_{\text{m}}(\boldsymbol{q}) \delta\boldsymbol{S}_q,
\end{aligned}$$

where $\delta \boldsymbol{S}_q = \sqrt{S} P^\dagger [a_q, b_q, a^\dagger_{-q}, b^\dagger_{-q}]^T = [\delta S_{qAx}, \delta S_{qAy}, \delta S_{qBx}, \delta S_{qBy}]^T$ and we defined

$$H'_{\mathrm{m}}(\boldsymbol{q}) = \frac{1}{S} P^\dagger \begin{bmatrix} H_{\mathrm{m}}(\boldsymbol{q}) & 0 \\ 0 & H^T_{\mathrm{m}}(-\boldsymbol{q}) \end{bmatrix} P \text{ with } P = \frac{1}{\sqrt{2}} \begin{bmatrix} 1 & \mathrm{i} & 0 & 0 \\ 0 & 0 & 1 & \mathrm{i} \\ 1 & -\mathrm{i} & 0 & 0 \\ 0 & 0 & 1 & -\mathrm{i} \end{bmatrix}.$$

Interacting Hamiltonian

By decomposing the spin and the spin displacement as $\boldsymbol{S}_i = S\hat{\boldsymbol{z}} + \delta \boldsymbol{S}_i$ and splitting the summation into two separate summations over each sublattice, the interacting Hamiltonian can be expressed as

$$\begin{aligned} \mathcal{H}_{\mathrm{int}} = &\frac{S}{2} \sum_{\substack{i,\delta_A \\ i\in A}} \sum_{\mu} (u_{iA\mu} - u_{i+\delta_A,B\mu}) \left[T^{\mu x}_{\delta_A} (\delta S_{iAy} - \delta S_{i+\delta_A,By}) - T^{\mu y}_{\delta_A} (\delta S_{iAx} - \delta S_{i+\delta_A,Bx}) \right] \\ &+ \frac{S}{2} \sum_{\substack{i,\delta_B \\ i\in B}} \sum_{\mu} (u_{iB\mu} - u_{i+\delta_B,A\mu}) \left[T^{\mu x}_{\delta_B} (\delta S_{iBy} - \delta S_{i+\delta_B,Ay}) - T^{\mu y}_{\delta_B} (\delta S_{iBx} - \delta S_{i+\delta_B,Ax}) \right]. \end{aligned}$$

Due to the equality $T^{\mu\nu}_{\delta_A} = T^{\mu\nu}_{\delta_B}$, the contribution from each sublattice is identical. By substituting the Fourier-transformed displacements into the equation, with a normalization factor of $1/\sqrt{N_{\mathrm{uc}}} = \sqrt{2/N}$, we obtain

$$\begin{aligned} \mathcal{H}_{\mathrm{int}} =& S\sqrt{\frac{\hbar}{M\Omega}} \sum_q \sum_{\delta_A,\mu} (\tilde{u}_{-qA\mu} - \tilde{u}_{-qB\mu} \mathrm{e}^{-\mathrm{i}\boldsymbol{q}\cdot\boldsymbol{\delta}_A}) \left[T^{\mu x}_{\delta_A} (\delta S_{qAy} - \delta S_{qBy} \mathrm{e}^{\mathrm{i}\boldsymbol{q}\cdot\boldsymbol{\delta}_A}) \right. \\ &\left. - T^{\mu y}_{\delta_A} (\delta S_{qAx} - \delta S_{qBx} \mathrm{e}^{\mathrm{i}\boldsymbol{q}\cdot\boldsymbol{\delta}_A}) \right] \\ =& \sum_q \tilde{\boldsymbol{u}}_q H_c(\boldsymbol{q}) \delta \boldsymbol{S}_q, \end{aligned}$$

where $\tilde{\boldsymbol{u}}_q = [\tilde{u}_{qAx}, \tilde{u}_{qAy}, \tilde{u}_{qBx}, \tilde{u}_{qBy}]^T$. Moreover, $H_c(\boldsymbol{q})$ is a matrix on the form

$$H_c(\boldsymbol{q}) = \begin{bmatrix} T_{q=0} & -T_q \\ -T_{-q} & T_{q=0} \end{bmatrix},$$

with

$$T_q = S\sqrt{\frac{\hbar}{M\Omega}} \sum_{\delta_A} \begin{bmatrix} -T^{xy}_{\delta_A} & T^{xx}_{\delta_A} \\ -T^{yy}_{\delta_A} & T^{yx}_{\delta_A} \end{bmatrix} \mathrm{e}^{\mathrm{i}\boldsymbol{q}\cdot\boldsymbol{\delta}_A}.$$

The matrix elements are determined to be

$$T_q = \frac{1}{2} S D^{\mathrm{nn}}_{xy} \zeta \mathrm{e}^{-\frac{\mathrm{i}}{2\sqrt{3}} q_y a} \begin{bmatrix} (1-3d_R)\cos(\frac{1}{2}q_x a) + 2\mathrm{e}^{\mathrm{i}\frac{\sqrt{3}}{2} q_y a} & \mathrm{i}\sqrt{3}(1+d_R)\sin(\frac{1}{2}q_x a) \\ \mathrm{i}\sqrt{3}(1+d_R)\sin(\frac{1}{2}q_x a) & (3-d_R)\cos(\frac{1}{2}q_x a) - 2d_R \mathrm{e}^{\mathrm{i}\frac{\sqrt{3}}{2} q_y a} \end{bmatrix},$$

where we defined the dimensionless quantity $\zeta = (1/a_0)\sqrt{\hbar/M\Omega}$ with $a_0 = a/\sqrt{3}$ as the interatomic distance. We may split the summation into two terms in the following way

$$\mathcal{H}_{\text{int}} = \frac{1}{2}\sum_{q}\left(\tilde{\boldsymbol{u}}_q^\dagger H_c(\boldsymbol{q})\delta\boldsymbol{S}_q + \delta\boldsymbol{S}_q^\dagger H_c^\dagger(\boldsymbol{q})\tilde{\boldsymbol{u}}_q\right),$$

since the coupling matrix satisfies $H_c^T(-\boldsymbol{q}) = H_c^\dagger(\boldsymbol{q})$. By introducing the rotated ion displacement as the basis, the expression undergoes a transformation, resulting in

$$\mathcal{H}_{\text{int}} = \frac{1}{2}\sum_{q}\left(\tilde{\boldsymbol{u}}_q'^\dagger H_c'(\boldsymbol{q})\delta\boldsymbol{S}_q + \delta\boldsymbol{S}_q^\dagger H_c'^\dagger(\boldsymbol{q})\tilde{\boldsymbol{u}}_q'\right),$$

where the new coupling matrix is

$$H_c'(\boldsymbol{q}) = \text{diag}(1/\sqrt{\tilde{\omega}_{q,\lambda}})U_{\text{ph}}^\dagger(\boldsymbol{q})H_c(\boldsymbol{q}),\;\; U_{\text{ph}}(\boldsymbol{q}) = [\hat{\boldsymbol{e}}^{\text{TA}}(\boldsymbol{q}), \hat{\boldsymbol{e}}^{\text{LA}}(\boldsymbol{q}), \hat{\boldsymbol{e}}^{\text{TO}}(\boldsymbol{q}), \hat{\boldsymbol{e}}^{\text{LO}}(\boldsymbol{q})],$$

and each $\hat{\boldsymbol{e}}^\lambda(\boldsymbol{q})$ is written in terms of the $\tilde{\boldsymbol{u}}_q$ basis.

Finding the energy bands

Summing up all the terms, the total Hamiltonian is

$$\mathcal{H} = \frac{1}{2}\sum_q \boldsymbol{\phi}_q^\dagger H_{\text{me}}(\boldsymbol{q})\boldsymbol{\phi}_q,$$

$$H_{\text{me}}(\boldsymbol{q}) = \begin{bmatrix} H_{\text{m}}'(\boldsymbol{q}) & H_c'^\dagger(\boldsymbol{q}) & 0_{4\times4} \\ H_c'(\boldsymbol{q}) & \hbar\Omega\text{diag}(\tilde{\omega}_{q,\lambda}) & 0_{4\times4} \\ 0_{4\times4} & 0_{4\times4} & \hbar\Omega\text{diag}(\tilde{\omega}_{q,\lambda}) \end{bmatrix}, \quad \boldsymbol{\phi}_q = [\delta\boldsymbol{S}_q^T, \tilde{\boldsymbol{u}}_q'^T, \tilde{\boldsymbol{p}}'^T_{-q}]^T.$$

By using the Heisenberg equation of motion, the energy spectrum is found by diagonalizing $\eta H_{\text{me}}(\boldsymbol{q})$ where η is a matrix on the form

$$\eta = [\boldsymbol{\phi}_q, \boldsymbol{\phi}_q^\dagger] = \begin{bmatrix} \xi & 0_{4\times4} & 0_{4\times4} \\ 0_{4\times4} & 0_{4\times4} & \mathrm{i}I_{4\times4} \\ 0_{4\times4} & -\mathrm{i}I_{4\times4} & 0_{4\times4} \end{bmatrix}, \quad \xi = \begin{bmatrix} -S\sigma_y & 0 \\ 0 & -S\sigma_y \end{bmatrix}.$$

4.4.2. Second quantized approach

The non-interacting Hamiltonian is

$$\begin{aligned}
\mathcal{H}_0 &= \mathcal{H}_{\text{ph}} + \mathcal{H}_{\text{m}}, \\
\mathcal{H}_{\text{ph}} &= \sum_{q,\lambda}\varepsilon_{q,\lambda}c_{q,\lambda}^\dagger c_{q,\lambda}, \\
\mathcal{H}_{\text{m}} &= \sum_k\left(E_k^+\alpha_k^\dagger\alpha_k + E_k^-\beta_k^\dagger\beta_k\right),
\end{aligned}$$

where the magnon eigenmodes $\{\alpha_k, \beta_k\}$ and eigenfrequencies $E_k^\pm$ are defined in section 3.3.2. Regarding the interacting Hamiltonian, the contribution from each sublattice is similar, allowing us to perform the summation exclusively over sublattice A

$$\mathcal{H}_{\text{int}} = -S\sqrt{\frac{S}{2}}\sum_{\substack{i,\delta_A \\ i\in A}}\sum_\mu (u_{iA\mu} - u_{i+\delta_A,B\mu})\left[(T_{\delta_A}^{\mu y} + T_{\delta_A}^{\mu x})(a_i - b_{i+\delta_A}) + (T_{\delta_A}^{\mu y} - \mathrm{i}T_{\delta_A}^{\mu x})(a_i^\dagger - b_{i+\delta_A}^\dagger)\right].$$

By expressing the ionic and spin displacements in terms of bosonic operators in reciprocal space, the bilinear terms in the interacting Hamiltonian are

$$\mathcal{H}_{\text{int}} = -\frac{S}{2}\sqrt{\frac{\hbar S}{M}}\sum_{q,\lambda}\sum_{\delta_A,\mu}\frac{(c_{q,\lambda}+c^{\dagger}_{-q,\lambda})}{\sqrt{\omega_{q,\lambda}}}(\mathrm{e}^{\lambda}_{A\mu}(\boldsymbol{q})-\mathrm{e}^{\lambda}_{B\mu}(\boldsymbol{q})\mathrm{e}^{\mathrm{i}\boldsymbol{q}\cdot\boldsymbol{\delta}_A})$$
$$\times\left[(T^{\mu y}_{\delta_A}+\mathrm{i}T^{\mu x}_{\delta_A})(a_{-q}-b_{-q}\mathrm{e}^{-\mathrm{i}\boldsymbol{q}\cdot\boldsymbol{\delta}_A})+(T^{\mu y}_{\delta_A}-\mathrm{i}T^{\mu x}_{\delta_A})(a^{\dagger}_{q}-b^{\dagger}_{q}\mathrm{e}^{-\mathrm{i}\boldsymbol{q}\cdot\boldsymbol{\delta}_A})\right].$$

The expression can be written more concisely as

$$\mathcal{H}_{\text{int}} = \sum_{q,\lambda}\left[(c_{q,\lambda}+c^{\dagger}_{-q,\lambda})(G^{A}_{q,\lambda}a_{-q}+G^{B}_{q,\lambda}b_{-q})+(c^{\dagger}_{q,\lambda}+c_{-q,\lambda})(G^{A*}_{q,\lambda}a^{\dagger}_{-q}+G^{B*}_{q,\lambda}b^{\dagger}_{-q})\right],$$

where

$$G^{A}_{q,\lambda} = -\frac{S}{2}\sqrt{\frac{\hbar S}{M\omega_{q,\lambda}}}\sum_{\delta_A,\mu}(e^{\lambda}_{A\mu}(\boldsymbol{q})-e^{\lambda}_{B\mu}(\boldsymbol{q})\mathrm{e}^{\mathrm{i}\boldsymbol{q}\cdot\boldsymbol{\delta}_A})(T^{\mu y}_{\delta_A}+\mathrm{i}T^{\mu x}_{\delta_A}),$$
$$G^{B}_{q,\lambda} = -\frac{S}{2}\sqrt{\frac{\hbar S}{M\omega_{q,\lambda}}}\sum_{\delta_A,\mu}(e^{\lambda}_{B\mu}(\boldsymbol{q})-e^{\lambda}_{A\mu}(\boldsymbol{q})\mathrm{e}^{-\mathrm{i}\boldsymbol{q}\cdot\boldsymbol{\delta}_A})(T^{\mu y}_{\delta_A}+\mathrm{i}T^{\mu x}_{\delta_A}).$$

Upon computation, the coupling factors $G^{A(B)}_{q,\lambda}$ can be written as

$$\begin{aligned} G^{A}_{q,\lambda} &= \frac{1}{2}SD^{\text{nn}}_{xy}\zeta\sqrt{\frac{S}{\tilde{\omega}_{q,\lambda}}}\left(\boldsymbol{e}^{\lambda}_{A}(\boldsymbol{q})\cdot\boldsymbol{g}_{q=0}-\boldsymbol{e}^{\lambda}_{B}(\boldsymbol{q})\cdot\boldsymbol{g}_{q}\right),\\ G^{B}_{q,\lambda} &= \frac{1}{2}SD^{\text{nn}}_{xy}\zeta\sqrt{\frac{S}{\tilde{\omega}_{q,\lambda}}}\left(\boldsymbol{e}^{\lambda}_{B}(\boldsymbol{q})\cdot\boldsymbol{g}_{q=0}-\boldsymbol{e}^{\lambda}_{A}(\boldsymbol{q})\cdot\boldsymbol{g}_{-q}\right), \end{aligned} \tag{4.12}$$

with the new vector defined as

$$\boldsymbol{g}_{q} = \frac{1}{2}\mathrm{e}^{\frac{\mathrm{i}}{\sqrt{3}}q_y a}\begin{bmatrix} 2+\mathrm{e}^{-\mathrm{i}\frac{\sqrt{3}}{2}q_y a}\left((1-3d_R)\cos(\frac{1}{2}q_x a)+\sqrt{3}(1+d_R)\sin(\frac{1}{2}q_x a)\right)\\ 2\mathrm{i}d_R-\mathrm{i}\mathrm{e}^{-\mathrm{i}\frac{\sqrt{3}}{2}q_y a}((3-d_R)\cos(\frac{1}{2}q_x a)-\sqrt{3}(1+d_R)\sin(\frac{1}{2}q_x a))\end{bmatrix}.$$

By utilizing the magnon eigenmodes α_k and β_k, the interacting Hamiltonian can be transformed to the form

$$\mathcal{H}_{\text{int}} = \sum_{q,\lambda}\left[(c_{q,\lambda}+c^{\dagger}_{-q,\lambda})(G^{\alpha}_{q,\lambda}\alpha_{-q}+G^{\beta}_{q,\lambda}\beta_{-q})+(c^{\dagger}_{q,\lambda}+c_{-q,\lambda})(G^{\alpha*}_{q,\lambda}\alpha^{\dagger}_{-q}+G^{\beta*}_{q,\lambda}\beta^{\dagger}_{-q})\right],$$

with $G^{\alpha}_{q,\lambda}=[G^{A}_{q,\lambda},G^{B}_{q,\lambda}]^{T}\cdot\hat{\boldsymbol{e}}^{+}(-\boldsymbol{q})$ and $G^{\beta}_{q,\lambda}=[G^{A}_{q,\lambda},G^{B}_{q,\lambda}]^{T}\cdot\hat{\boldsymbol{e}}^{-}(-\boldsymbol{q})$. Note that $\hat{\boldsymbol{e}}^{\lambda}(\boldsymbol{q})$ are the phonon eigenvectors while $\hat{\boldsymbol{e}}^{\pm}(\boldsymbol{q})$ are the magnon eigenvectors. The four phonon branches are denoted by $\lambda=\{1,2,3,4\}$. In the basis $\boldsymbol{\Psi}_q=[\boldsymbol{\psi}^{T}_{q},\boldsymbol{\psi}^{\dagger}_{-q}]^{T}$, $\boldsymbol{\psi}^{T}_{q}=[\alpha_q,\beta_q,c_{q,1},c_{q,2},c_{q,3},c_{q,4}]$, the total Hamiltonian can be written like

$$\mathcal{H} = \frac{1}{2}\sum_{q}\boldsymbol{\Psi}^{\dagger}_{q}H_{\text{me}}(\boldsymbol{q})\boldsymbol{\Psi}_{q}. \tag{4.13}$$

The energy bands are obtained by diagonalizing $\sigma_3 H_{\text{me}}(\boldsymbol{q})$ where $H_{\text{me}}(\boldsymbol{q})$ is outlined in Appendix B.

4.4.3. Result

In Ref. [26], a calculation was previously done that focused on coupling with in-plane phonon modes. In our attempt to replicate the result, we select the following values for the nonzero force coefficients: $\gamma_2 = -|\gamma_2| = -\gamma_1$, $\rho_1 = \rho_2 = 0.08\gamma_2$, which result in the same in-plane phonon dispersion. Moreover, we set $J = 2\,\text{meV}$, $\hbar\Omega = 5\,\text{meV}$ (with $\Omega = \sqrt{2|\gamma_2|/M}$), $\Delta = 0\,\text{eV}$, $D_z^{\text{nnn}} = 0.1\,\text{meV}$ and $D_{xy}^{\text{nn}} = 0.5\,\text{meV}$.

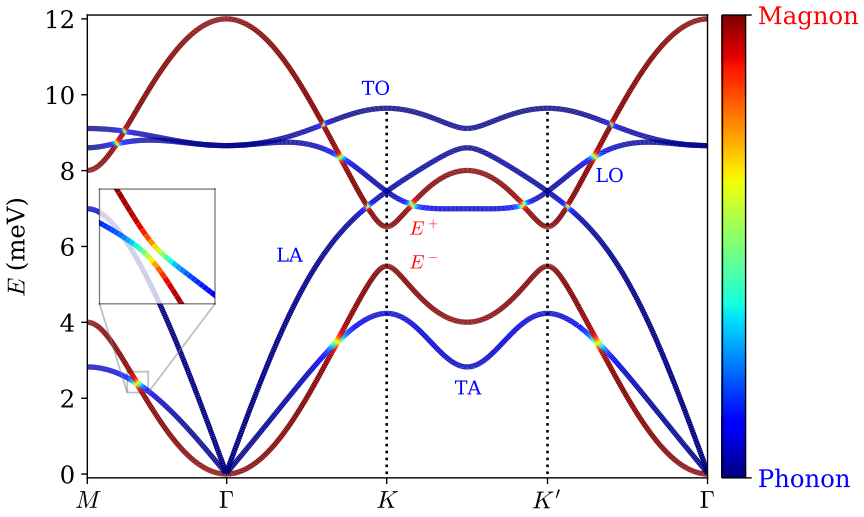

(a) First quantized formalism.

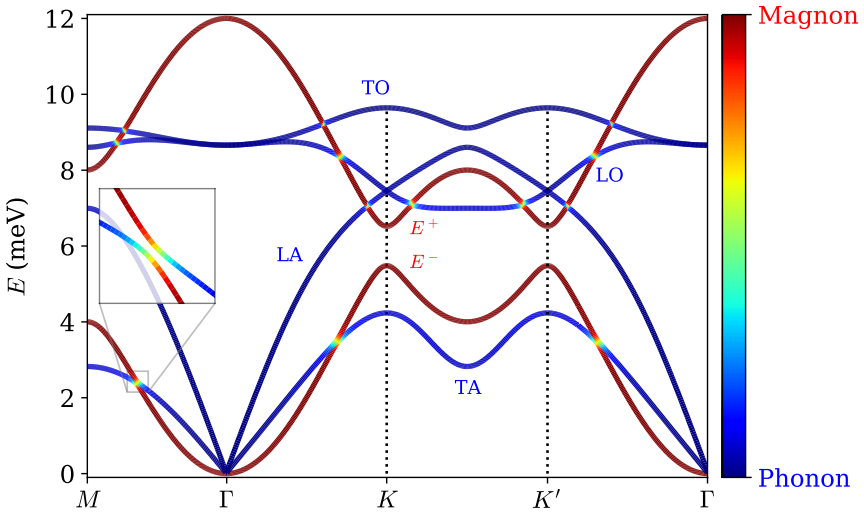

(b) Second quantized formalism.

Figure 4.3.: Dispersion curves for the coupled magnon-phonon systems in a ferromagnetic honeycomb lattice, calculated in the first and second quantized formalism. The labelling of the bands correspond to the non-interacting system. The parameters are $J = 2$, $\hbar\Omega = 5$, $\Delta = 0$, $D_z^{\text{nnn}} = 0.1$ and $D_{xy}^{\text{nn}} = 0.5$, in units of meV. Moreover, $S = 1$, $\zeta = 0.1$ and $d_R = 0$. The values of the in-plane force coefficients are given in the main text.

The dimensionless parameters are $S = 1$, $\zeta = 0.1$ and $d_R = 0$. It should be noted that these parameter values do not satisfy the condition $D_{xy}^{\mathrm{nn}} < \sqrt{JK_z}/2$, since we have assumed a zero magnon energy gap. However, we have chosen these values for the purpose of comparison.

Figure 4.3a and 4.3b display the energy spectrum of the hybrid magnon-phonon in a ferromagnetic honeycomb lattice along the symmetry lines in the Brillouin zone, calculated in the first and second quantized formalism, respectively. Like the ferromagnetic square lattice, magnons interact with phonons where their frequencies match and form anticrossing regions with the emergence of magnon-polaron states. The numerical dispersions obtained from the first and second quantization methods are in agreement, indicating complete overlap. This is achieved without introducing the normalized spin as the basis in the first quantized method since $S = 1$, making the basis and interaction strength equal for both methods.

When compared to the results from Ref. [26], the magnetoelastic modes appear to be similar but it is challenging to confirm if the band gaps are of exact size. Nevertheless, it can be concluded that the band gaps are of a comparable magnitude.

4.5. Antiferromagnetic lattices

We investigate the magnetoelastic energy spectrum in the antiferromagnetic (checkerboard-type) square and honeycomb lattice with an out-of-plane magnetization. The source of the coupling is the in-plane DMI, which is based on the same assumptions as in the calculation for the ferromagnetic square lattice (referred to in section 4.3). We utilize the second quantized formalism, which has been demonstrated to be effective and straightforward in previous sections, and consider only coupling to in-plane phonon modes as they constitute the lowest order contribution.

4.5.1. Square lattice

The non-interacting Hamiltonian is given by

$$\begin{aligned} \mathcal{H}_0 &= \mathcal{H}_{\mathrm{ph}} + \mathcal{H}_{\mathrm{m}}, \\ \mathcal{H}_{\mathrm{ph}} &= \sum_{q,\lambda} \varepsilon_{q,\lambda} c_{q,\lambda}^\dagger c_{q,\lambda}, \\ \mathcal{H}_{\mathrm{m}} &= \sum_k \left(E_k^+ \alpha_k^\dagger \alpha_k + E_k^- \beta_k^\dagger \beta_k \right), \end{aligned} \tag{4.14}$$

with the magnon energy bands and eigenmodes defined in section 3.4.1. To derive a suitable expression for the interacting Hamiltonian, we perform a Holstein-Primakoff transformation, equation (3.14), to obtain

$$\mathcal{H}_{\mathrm{int}} = S\sqrt{\frac{S}{2}} \sum_{\substack{i,\delta \\ i\in A}} \sum_{\mu} (u_{iA\mu} - u_{i+\delta,B\mu}) \left[(T_\delta^{\mu y} + \mathrm{i}T_\delta^{\mu x})(a_i + b_{i+\delta}^\dagger) + (T_\delta^{\mu y} - \mathrm{i}T_\delta^{\mu x})(a_i^\dagger + b_{i+\delta}) \right], \tag{4.15}$$

where the summation is performed over only one sublattice since the contribution from each sublattice is identical. In the case of a square lattice with a monoatomic crystal basis, we have $\boldsymbol{u}_{iA} = \boldsymbol{u}_{iB}$. Following similar calculations as before, we express the ionic displacement in terms of bosonic operators and Fourier transform the magnon operators using equation (3.15). This yields the following result

$$
\begin{aligned}
\mathcal{H}_{\text{int}} &= \frac{S}{2}\sqrt{\frac{\hbar S}{NM}}\sqrt{\frac{2}{N}}\sum_{q,q',\lambda}\sum_{\substack{i,\delta\\ i\in A}}\sum_{\mu}\frac{e_\mu^\lambda(\boldsymbol{q})}{\sqrt{\omega_{q,\lambda}}}(c_{q,\lambda}+c_{-q,\lambda}^\dagger)\mathrm{e}^{\mathrm{i}\boldsymbol{q}\cdot\boldsymbol{R}_{iA}}(1-\mathrm{e}^{\mathrm{i}\boldsymbol{q}\cdot\boldsymbol{\delta}}) \\
&\times \mathrm{e}^{-\mathrm{i}\boldsymbol{q}'\cdot\boldsymbol{R}_{iA}}\left[(T_\delta^{\mu y}+\mathrm{i}T_\delta^{\mu x})(a_{-q'}+b_{-q'}^\dagger\mathrm{e}^{-\mathrm{i}\boldsymbol{q}'\cdot\boldsymbol{\delta}})+(T_\delta^{\mu y}-\mathrm{i}T_\delta^{\mu x})(a_{q'}^\dagger+b_{q'}\mathrm{e}^{-\mathrm{i}\boldsymbol{q}'\cdot\boldsymbol{\delta}})\right] \\
&= \frac{S}{2}\sqrt{\frac{\hbar S}{2M}}\sum_{q,\lambda}\sum_{\delta,\mu}\frac{e_\mu^\lambda(\boldsymbol{q})}{\sqrt{\omega_{q,\lambda}}}(c_{q,\lambda}+c_{-q,\lambda}^\dagger)(1-\mathrm{e}^{\mathrm{i}\boldsymbol{q}\cdot\boldsymbol{\delta}}) \\
&\times \left[(T_\delta^{\mu y}+\mathrm{i}T_\delta^{\mu x})(a_{-q}+b_{-q}^\dagger\mathrm{e}^{-\mathrm{i}\boldsymbol{q}\cdot\boldsymbol{\delta}})+(T_\delta^{\mu y}-\mathrm{i}T_\delta^{\mu x})(a_q^\dagger+b_q\mathrm{e}^{-\mathrm{i}\boldsymbol{q}\cdot\boldsymbol{\delta}})\right] \\
&= \sum_{q,\lambda}\left[(c_{q,\lambda}+c_{-q,\lambda}^\dagger)G_{q,\lambda}(b_{-q}^\dagger-a_{-q})+(c_{-q,\lambda}+c_{q,\lambda}^\dagger)G_{q,\lambda}^*(b_{-q}-a_{-q}^\dagger)\right].
\end{aligned}
$$

The coupling coefficients are defined as

$$
G_{q,\lambda} = S\zeta D_{xy}^{\text{nn}}\sqrt{\frac{S}{2\tilde{\omega}_{q,\lambda}}}\hat{\boldsymbol{e}}^\lambda(\boldsymbol{q})\cdot\boldsymbol{g}_q,
$$

where $\boldsymbol{g}_q$ is outlined in equation (4.11). Inserting for the Bogoliubov transformed operators $\{\alpha_q,\beta_q\}$ obtained from equation (3.19), we obtain

$$
\mathcal{H}_{\text{int}} = \sum_{q,\lambda}\left[(c_{q,\lambda}+c_{-q,\lambda}^\dagger)G'_{q,\lambda}(\beta_{-q}^\dagger-\alpha_{-q})+(c_{-q,\lambda}+c_{q,\lambda}^\dagger)G'^*_{q,\lambda}(\beta_{-q}-\alpha_{-q}^\dagger)\right],
$$

with $G'_{q,\lambda}=G_{q,\lambda}(u_{-q}+v_{-q})$. In the basis $\boldsymbol{\Psi}_q=[\boldsymbol{\psi}_q^T,\boldsymbol{\psi}_{-q}^\dagger]^T$, $\boldsymbol{\psi}_q^T=[\alpha_q,\beta_q^\dagger,c_{q,1},c_{q,2}]$, where $\lambda=\{1,2\}=\{\text{TA},\text{LA}\}$, the Hamiltonian is

$$
\mathcal{H}=\frac{1}{2}\sum_q\boldsymbol{\Psi}_q^\dagger H_{\text{me}}(\boldsymbol{q})\boldsymbol{\Psi}_q,
$$

with

$$
H_{\text{me}}(\boldsymbol{q})=\begin{bmatrix}
E_q^+ & 0 & -G'^*_{-q,1} & -G'^*_{-q,2} & 0 & 0 & -G'^*_{-q,1} & -G'^*_{-q,2}\\
0 & E_q^- & G'^*_{-q,1} & G'^*_{-q,2} & 0 & 0 & G'^*_{-q,1} & G'^*_{-q,2}\\
-G'_{-q,1} & G'_{-q,1} & \varepsilon_{q,1} & 0 & -G'^*_{q,1} & G'^*_{q,1} & 0 & 0\\
-G'_{-q,2} & G'_{-q,2} & 0 & \varepsilon_{q,2} & -G'^*_{q,2} & G'^*_{q,2} & 0 & 0\\
0 & 0 & -G'_{q,1} & -G'_{q,2} & E_q^+ & 0 & -G'_{q,1} & -G'_{q,2}\\
0 & 0 & G'_{q,1} & G'_{q,2} & 0 & E_q^- & G'_{q,1} & G'_{q,2}\\
-G'_{-q,1} & G'_{-q,1} & 0 & 0 & -G'^*_{q,1} & G'^*_{q,1} & \varepsilon_{q,1} & 0\\
-G'_{-q,2} & G'_{-q,2} & 0 & 0 & -G'^*_{q,2} & G'^*_{q,2} & 0 & \varepsilon_{q,2}
\end{bmatrix}.
$$

The energy spectrum is found by diagonalizing $\eta H_{\text{me}}(\boldsymbol{q})$ where η is on the form

$$
\eta=\operatorname{diag}(1,-1,1,1,-1,1,-1,-1). \tag{4.16}
$$

We utilize the same parameters as those used for the ferromagnetic square lattice: $J=-2\,\text{meV}$, $K_z=0.5\,\text{meV}$, $\hbar\Omega=10\,\text{meV}$ (with $\Omega=\sqrt{|\gamma_1|/M}$), $D_{xy}^{\text{nn}}=0.4\,\text{meV}$, $\zeta=0.1$, $d_R=0$ and $S=3/2$. Additionally, the nonzero force coefficients are $\rho_1=\rho_2=\gamma_1/8$, $\gamma_z=\gamma_1/10$.

The results are shown in Figure 4.4, which displays the magnetoelastic energy spectrum in the presence

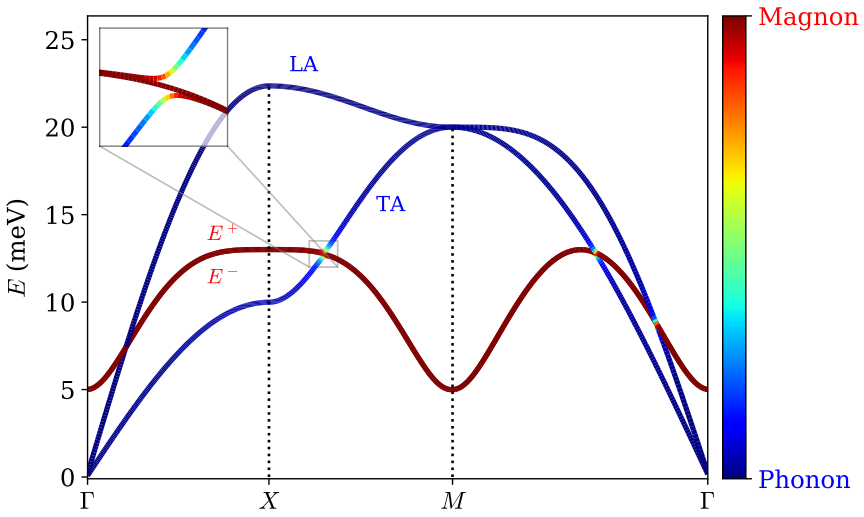

(a) $h = 0.0\,\text{meV}$.

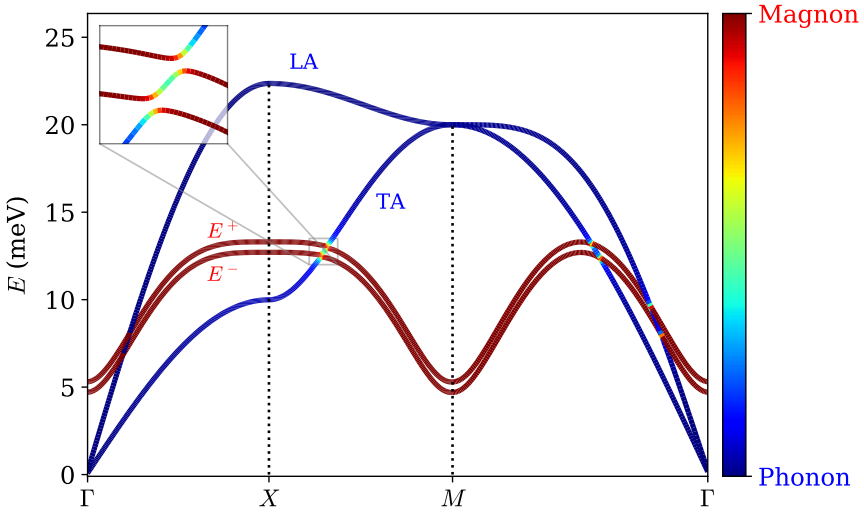

(b) $h = 0.3\,\text{meV}$.

Figure 4.4.: The figures show the magnetoelastic energy spectrum in an antiferromagnetic square lattice in the absence, Figure 4.4a, and presence, Figure 4.4b, of a magnetic field. The labelling of the bands correspond to the non-interacting system. The parameters are $J = -2$, $K_z = 0.5$, $\hbar\Omega = 10$ and $D_{xy}^{\text{nn}} = 0.4$, in units of meV. The dimensionless parameters are $\zeta = 0.1$, $d_R = 0$ and $S = 3/2$.

and absence of a magnetic field. In the presence of a magnetic field, when the magnon modes are nondegenerate, they both couple to acoustic phonons at their respective anticrossings. However, in the absence of an external field, only a single magnon mode couples to the phonon branch, as seen in the inset of Figure 4.4a. This breaks the degeneracy as the hybridized magnon-polaron state forms from the coupling of a single magnon and a single phonon. The additional degenerate mode is therefore

unaffected. If the parameters are adjusted so that the avoided crossings occurs at the M-point, where the LA and TA modes coincide, both magnon branches are impacted by the interaction since they effectively anticross two phonon branches.

4.5.2. Honeycomb lattice

The non-interacting Hamiltonian is given by equation (4.14), which incorporates the magnon energy bands and eigenmodes $\{\alpha_k, \beta_k\}$ as defined in section 3.4.2. On the other hand, the interacting Hamiltonian, described in equation (4.15), takes into account the distinct displacements, $\boldsymbol{u}_{iA}$ and $\boldsymbol{u}_{iB}$, associated with different sublattices. By substituting the phonon creation and annihilation operators, along with the Fourier-transformed magnon operators, the expression can be written as

$$\begin{aligned}\mathcal{H}_{\text{int}} &= \frac{S}{2}\sqrt{\frac{\hbar S}{M}}\sum_{q,\lambda}\sum_{\delta_A,\mu}\frac{(c_{q,\lambda}+c^\dagger_{-q,\lambda})}{\sqrt{\omega_{q,\lambda}}}(e^\lambda_{A\mu}(\boldsymbol{q}) - e^\lambda_{B\mu}(\boldsymbol{q})\mathrm{e}^{\mathrm{i}\boldsymbol{q}\cdot\boldsymbol{\delta}_A}) \\ &\times\left[(T^{\mu y}_{\delta_A}+\mathrm{i}T^{\mu x}_{\delta_A})(a_{-q}+b^\dagger_{-q}\mathrm{e}^{-\mathrm{i}\boldsymbol{q}\cdot\boldsymbol{\delta}_A}) + (T^{\mu y}_{\delta_A}-\mathrm{i}T^{\mu x}_{\delta_A})(a^\dagger_q+b_q\mathrm{e}^{-\mathrm{i}\boldsymbol{q}\cdot\boldsymbol{\delta}_A})\right] \\ &= \sum_{q,\lambda}\left[(c_{q,\lambda}+c^\dagger_{-q,\lambda})(G^B_{q,\lambda}b^\dagger_{-q} - G^A_{q,\lambda}a_{-q}) + (c_{-q,\lambda}+c^\dagger_{q,\lambda})(G^{B*}_{q,\lambda}b_{-q} - G^{A*}_{q,\lambda}a^\dagger_{-q})\right],\end{aligned}$$

with the coupling factors $G^{A(B)}_{q,\lambda}$ defined in equation (4.12). When expressed in terms of the magnon eigenmodes, the expression transforms to

$$\mathcal{H}_{\text{int}} = \sum_{q,\lambda}\left[(c_{q,\lambda}+c^\dagger_{-q,\lambda})(G^\beta_{q,\lambda}\beta^\dagger_{-q} + G^\alpha_{q,\lambda}\alpha_{-q}) + (c_{-q,\lambda}+c^\dagger_{q,\lambda})(G^{\beta*}_{q,\lambda}\beta_{-q} + G^{\alpha*}_{q,\lambda}\alpha^\dagger_{-q})\right],$$

where $G^\alpha_{q,\lambda} = -u^*_{-q}G^A_{q,\lambda} - v_{-q}G^B_{q,\lambda}$ and $G^\beta_{q,\lambda} = v^*_{-q}G^A_{q,\lambda} + u_{-q}G^B_{q,\lambda}$. In the basis $\boldsymbol{\Psi}_q = [\boldsymbol{\psi}^T_q, \boldsymbol{\psi}^\dagger_{-q}]^T$, $\boldsymbol{\psi}^T_q = [\alpha_q, \beta^\dagger_q, c_{q,1}, c_{q,2}, c_{q,3}, c_{q,4}]$, the Hamiltonian is

$$\mathcal{H} = \frac{1}{2}\sum_q \boldsymbol{\Psi}^\dagger_q H_{\text{me}}(\boldsymbol{q})\boldsymbol{\Psi}_q. \tag{4.17}$$

$H_{\text{me}}(\boldsymbol{q})$ is a matrix outlined in Appendix B and the eigenvalues are obtained by diagonalizing $\eta H_{\text{me}}(\boldsymbol{q})$ where $\eta = \text{diag}(1,-1,1,1,1,1,-1,1,-1,-1,-1,-1)$. When using this matrix, we would obtain E^-_{-q} instead of E^-_q because we only consider the positive energies. However, this does not affect the dispersion as long as $D^{\text{nnn}}_z = 0$, forming reciprocal bands. With the given values $J = -2\,\text{meV}$, $K_z = 0.5\,\text{meV}$, $h = 0.3\,\text{meV}$, $\hbar\Omega = 7\,\text{meV}$ ($\Omega = \sqrt{2|\gamma_2|/M}$), $D^{\text{nnn}}_z = 0\,\text{meV}$, $D^{\text{nn}}_{xy} = 0.2\,\text{meV}$, $\zeta = 0.5$, $d_R = 0$ and assuming $S = 3/2$, the calculated hybridized magnon-phonon energy spectrum is presented Figure 4.5. The phonon dispersion is set with $\gamma_2 = -|\gamma_2| = -\gamma_1$, $\rho_1 = \rho_2 = \gamma_2/392$. The parameters are similar to the parameters used in a previous study of coupling between magnons and in-plane phonons (Ref. [28]). Note that the lattice constant was not provided in the reference, so we chose $\zeta = 0.5$ to ensure that the resulting band gaps fit well.

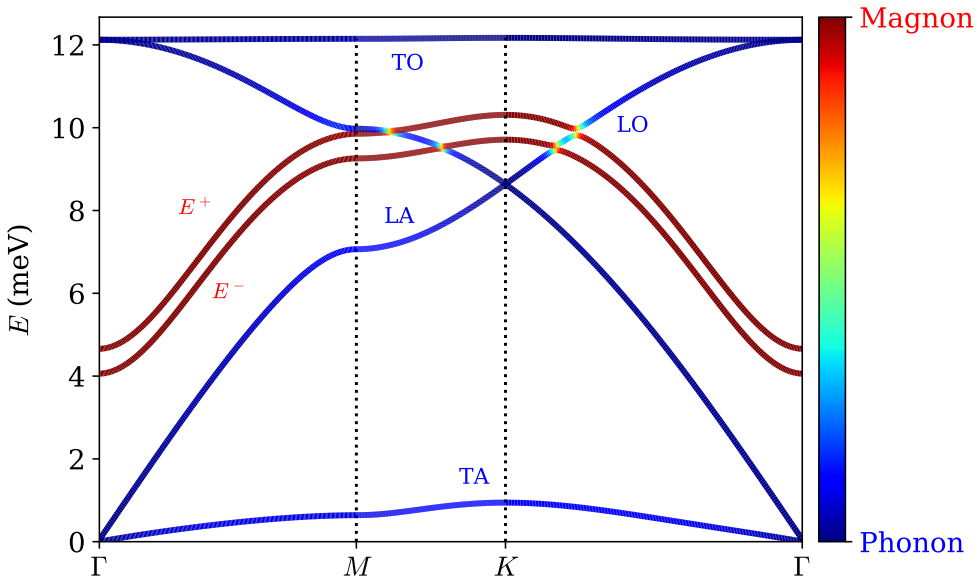

Figure 4.5.: Dispersion curves for coupled magnon-phonon excitations in an antiferromagnetic honeycomb lattice. The labels correspond to the non-interacting bands. The parameters are $J = -2$, $K_z = 0.5$, $h = 0.3$, $\hbar\Omega = 7$, $D_z^{\mathrm{nnn}} = 0$ and $D_{xy}^{\mathrm{nn}} = 0.2$, in units of meV, and $\zeta = 0.5$, $d_R = 0$ and $S = 3/2$.

Part II.

Topological Analysis of Magnon-Phonon Coupling on Ferromagnetic Honeycomb Layer with Arbitrary Magnetization Direction

CHAPTER 5

Topological band theory

Topological band theory is a branch of condensed matter physics that aims to explain various physical phenomena in solid-state materials by analyzing the topology of their band structure and classifying materials based on their physical properties. Topological insulators are a well-known example of such materials, where the bulk is insulating, while the edge states are robust conducting modes protected from external perturbations [15, 73]. In topological band theory, the Berry curvature plays a crucial role as it characterizes the geometry of the space of Bloch states across the Brillouin zone [60]. Functioning as a gauge field, it unveils the material's energy band topology and contributes intrinsically to various transport phenomena, including the quantum Hall effect and the intrinsic anomalous Hall effect in electronic systems [74]. Similarly, analogous transport phenomena can also be observed in bosonic systems. For instance, the magnon-mediated thermal Hall effect, which was initially detected in the insulating pyrochlore ferromagnet $Lu_2V_2O_7$, exemplifies this phenomenon [60].

This chapter provides a concise introduction to topological band theory, highlighting key concepts such as the Chern number and transport properties that are closely associated with topological systems. Additionally, the chapter offers a brief overview of the computation of Berry curvature in Bogoliubov-de Gennes systems. In order to gain a deeper understanding of how these transport phenomena emerge in condensed matter physics, we begin by explaining the Berry phase and see how it is related to the Berry curvature and the Chern number.

5.1. The relation between Berry phase, Berry curvature and the Chern number

In 1984, Berry proposed that under an adiabatic evolution of a quantum system, the quantum state may acquire a phase that is gauge-invariant and hence observable in physical systems [75]. This phase is known as the Berry phase and is an important quantity in topological band theory. To understand its origin, consider a system with a Hamiltonian that is dependent on a set of parameters $\boldsymbol{l}$, implicitly time-dependent. Now, imagine that we vary the system from $t = 0$ to $t = T$ such that the parameters make a closed curve $\mathcal{C}$ in parameter space. The phase acquired traversing this path, not including the well-known dynamical phase factor $\exp(-\mathrm{i}Et/\hbar)$, is known as the Berry phase (or geometrical phase) and takes the form [74, 75]

$$\gamma_n = \mathrm{i} \oint_{\mathcal{C}} \langle n(\boldsymbol{l})| \nabla_{\boldsymbol{l}} |n(\boldsymbol{l})\rangle \cdot \mathrm{d}\boldsymbol{l}.$$

$|n(\boldsymbol{l})\rangle$ are the instantaneous eigenstates of the Hamiltonian with energies $E_n(\boldsymbol{l})$. Assuming the parameter space is three-dimensional, Stoke's theorem can be applied to convert the path integral to a surface integral [74, 75]

$$\gamma_n = \int_{\mathcal{S}} \mathrm{d}\boldsymbol{S} \cdot \boldsymbol{\mathcal{F}}_n(\boldsymbol{l}),$$

where $\boldsymbol{\mathcal{F}}_n(\boldsymbol{l}) = \nabla_{\boldsymbol{l}} \times \mathrm{i} \langle n(\boldsymbol{l})| \nabla_{\boldsymbol{l}} |n(\boldsymbol{l})\rangle = \mathrm{i} \langle \nabla_{\boldsymbol{l}} n(\boldsymbol{l})| \times |\nabla_{\boldsymbol{l}} n(\boldsymbol{l})\rangle$ is the Berry curvature and the integral is taken over a surface that encloses the curve $\mathcal{C}$. By drawing an analogy, the Berry phase can be understood as the Aharanov-Bohm phase experienced by a charged particle moving along a loop with

magnetic flux, while the Berry curvature can be compared to the magnetic field [74]. To show that the Berry curvature is gauge-invariant, and hence also the Berry phase, the gauge transformation $|n(\boldsymbol{l})\rangle \to \mathrm{e}^{\mathrm{i}\phi(\boldsymbol{l})}\,|n(\boldsymbol{l})\rangle$ induces the change $\langle n(\boldsymbol{l})|\,\nabla_{\boldsymbol{l}}\,|n(\boldsymbol{l})\rangle \to \langle n(\boldsymbol{l})|\,\nabla_{\boldsymbol{l}}\,|n(\boldsymbol{l})\rangle + \mathrm{i}\nabla\phi(\boldsymbol{l})$, and since $\nabla_{\boldsymbol{l}} \times \nabla_{\boldsymbol{l}}\phi(\boldsymbol{l}) = 0$, the Berry curvature remains unchanged [75]. The Berry phase is only nonzero as long as the path $\mathcal{C}$ is closed. For an open path, one can always choose a gauge such that the Berry phase cancels [74]. Unlike the Berry phase, the Berry curvature is a local property that characterizes the geometric features of the parameter space. Therefore, it can be considered a more fundamental quantity than the Berry phase [74].

As one traverses the closed path $\mathcal{C}$, the Berry phase undergoes a change represented by $\phi(\boldsymbol{l}(t = 0)) - \phi(\boldsymbol{l}(t = T))$ due to the gauge transformation. In order for the eigenstates to remain single-valued functions, $|n(\boldsymbol{l}(t = 0))\rangle = |n(\boldsymbol{l}(t = T))\rangle$, which also applies for the gauge-transformed eigenstates, the acquired Berry phase resulting from the gauge transformation, $\phi(\boldsymbol{l}(t = 0)) - \phi(\boldsymbol{l}(t = T))$, must equal $2\pi m$, where m is an integer [74]. This observation signifies that the Berry phase is equal to a multiple of 2π in any gauge, as it is gauge-invariant. Extending this principle to a surface integral, the integrated Berry curvature over a closed manifold is quantized in units of 2π [74]. This quantized number is referred to as the Chern number. In reciprocal space, for nondegenerate volume bands, it is possible to assign a Chern number C_n to each band by [15, 72]

$$C_n = \frac{1}{2\pi}\int_{\mathrm{BZ}} \mathrm{d}\boldsymbol{k}^2 \mathcal{F}_n(\boldsymbol{k}),$$
$$\text{where}\;\; \mathcal{F}_n(\boldsymbol{k}) = \mathrm{i}\left(\langle \partial_x n(\boldsymbol{k})|\,\partial_y n(\boldsymbol{k})\rangle - \langle \partial_y n(\boldsymbol{k})|\,\partial_x n(\boldsymbol{k})\rangle\right),$$

$\partial_\mu = \partial/(\partial k_\mu)$ is the partial derivative and the integration is performed over the first Brillouin zone. If a band has a nonzero Chern number, it is classified as a Chern band and is regarded as possessing nontrivial topological properties [47]. The Chern number is zero only if a well-defined choice of gauge exists for the wavefunctions across the entire Brillouin zone [76]. If not, the Brillouin zone can be dissected into patches with unique gauges to make the wavefunctions well-defined, and the Chern number becomes related to the winding number of the gauge transformation on the boundary between the patches [76]. Since the Chern number is an integer, it is a topological invariant that cannot change continuously. However, if the system's adiabatic evolution leads to gap closing and reopening between adjacent bands, the adiabatic theorem no longer holds and the Chern number may change [15, 74].

The Chern number is a powerful tool for characterizing topological properties of two-dimensional gapped Hamiltonians with a broken time-reversal symmetry [47]. However, and as we mentioned earlier, the *effective* time-reversal symmetry may be preserved in certain cases, resulting in gapless bands that are still topologically nontrivial. Apart from the Chern number, there are many more topological invariants that can be used. For instance, if the time-reversal symmetry is preserved, a Z_2 index can be defined as the topological invariant [15, 47, 60]. This index determines the parity between the Chern numbers of the degenerate bands with different spin-polarization in the absence of spin-orbit coupling [60].

The principle of the bulk-edge correspondence is a fundamental concept in topological band theory. When a finite sample has a topologically nontrivial bulk and a topologically trivial exterior, the bands must intersect at the edge of the sample [47]. As a result, edge states emerge, which are found between the gapped bulk bands and typically have a gapless Dirac cone-dispersion [47, 73]. One noteworthy characteristic of these edge states is their persistence in remaining gapless even under moderate variations in the parameters of the sample, making them regarded as robust modes that are protected by the topology of the bulk states [15, 60].

5.2. Berry curvature in Bogoliubov-de Gennes systems

Given the para-unitary nature of eigenvectors in Bogoliubov-de Gennes systems, it becomes necessary to adjust the definition of the Berry curvature. The revised expression takes the following form [26, 70]

$$\mathcal{F}_n(\boldsymbol{k}) = \mathrm{i}\varepsilon_{\mu\nu}\left[\sigma_3(\partial_\mu V_k^\dagger)\sigma_3(\partial_\nu V_k)\right]_{nn}, \tag{5.1}$$

where $\varepsilon_{\mu\nu}$ represents the Levi-Civita tensor in two dimensions, with an implicit summation over the spatial indices μ and ν. The matrices V_k and σ_3 are known from section 4.2. We notice that the expression is gauge-dependent, which can pose challenges in numerical computations. We will in the following address this problem by transforming this into a new expression. In the case of a standard Bogoliubov-de Gennes Hamiltonian, the eigenvalue problem can be formulated as

$$\sigma_3 H(\boldsymbol{k}) V_k = V_k \sigma_3 \mathcal{E}_k, \quad \text{with} \quad V_k \sigma_3 V_k^\dagger = \sigma_3,$$

By differentiating this equation with respect to the momentum, we obtain

$$\begin{aligned} &\sigma_3(\partial_\mu H(\boldsymbol{k}))V_k + \sigma_3 H(\boldsymbol{k})(\partial_\mu V_k) = (\partial_\mu V_k)\sigma_3\mathcal{E}_k + V_k\sigma_3(\partial_\mu\mathcal{E}_k) \\ \implies\ &\sigma_3 V_k^\dagger(\partial_\mu H(\boldsymbol{k}))V_k = V_k^{-1}(\partial_\mu V_k)\sigma_3\mathcal{E}_k - \sigma_3 V_k^\dagger H(\boldsymbol{k})(\partial_\mu V_k), \end{aligned}$$

where we only consider the off-diagonal elements. We multiplied the equation with V_k^{-1} from the left and used that $V_k^{-1}\sigma_3 = \sigma_3 V_k^\dagger$. Furthermore, by considering the eigenvalue problem, we can derive the useful relationship $\sigma_3 V_k^\dagger H(\boldsymbol{k}) = \sigma_3\mathcal{E}_k V_k^{-1}$. Introducing $\bar{\mathcal{E}}_k = \sigma_3\mathcal{E}_k$ as the diagonal matrix with elements $\bar{\mathcal{E}}_{k,n}$, we can express the matrix elements of the equation as

$$\begin{aligned} \left(\sigma_3 V_k^\dagger(\partial_\mu H(\boldsymbol{k}))V_k\right)_{mn} =& \sum_{l,s}\left[\left(V_k^{-1}\right)_{ml}(\partial_\mu V_k)_{ls}\,\delta_{sn}\left(\bar{\mathcal{E}}_k\right)_{s,n} - \delta_{ml}\left(\bar{\mathcal{E}}_k\right)_{ml}\left(V_k^{-1}\right)_{ls}(\partial_\mu V_k)_{sn}\right] \\ =& (\bar{\mathcal{E}}_{k,n} - \bar{\mathcal{E}}_{k,m})\sum_l\left(V_k^{-1}\right)_{ml}(\partial_\mu V_k)_{ln} \\ \implies\ \left(V_k^{-1}(\partial_\mu V_k)\right)_{mn} =& \frac{\left(\sigma_3 V_k^\dagger(\partial_\mu H(\boldsymbol{k}))V_k\right)_{mn}}{(\bar{\mathcal{E}}_{k,n} - \bar{\mathcal{E}}_{k,m})}, \quad m \neq n. \end{aligned} \tag{5.2}$$

Using a similar approach, we can determine a relationship for the complex conjugate of that expression, given by

$$\left((\partial_\mu V_k^\dagger)(V_k^\dagger)^{-1}\right)_{mn} = \frac{\left(V_k^\dagger(\partial_\mu H(\boldsymbol{k}))V_k\sigma_3\right)_{mn}}{(\bar{\mathcal{E}}_{k,m} - \bar{\mathcal{E}}_{k,n})}, \quad m \neq n. \tag{5.3}$$

The expression for the Berry curvature, as given in equation (5.1), can be expanded into the following form

$$\begin{aligned} \mathcal{F}_n(\boldsymbol{k}) &= \mathrm{i}\varepsilon_{\mu\nu}\left[\sigma_3(\partial_\mu V_k^\dagger)(V_k^\dagger)^{-1}V_k^\dagger\sigma_3 V_k V_k^{-1}(\partial_\nu V_k)\right]_{nn} \\ &= \mathrm{i}\varepsilon_{\mu\nu}\left[\sigma_3(\partial_\mu V_k^\dagger)(V_k^\dagger)^{-1}\sigma_3 V_k^{-1}(\partial_\nu V_k)\right]_{nn} \\ &= \mathrm{i}\varepsilon_{\mu\nu}\sum_{m\neq n}\rho_n\left((\partial_\mu V_k^\dagger)(V_k^\dagger)^{-1}\right)_{nm}\rho_m\left(V_k^{-1}(\partial_\nu V_k)\right)_{mn}, \end{aligned}$$

where $\rho_n \coloneqq (\sigma_3)_{nn} = 1$ when band n is in the particle space and $\rho_n = -1$ when the band is in the hole space. The term $m = n$ has been excluded from the summation, as it has been demonstrated that the diagonal terms do not contribute to the Berry curvature [19]. By substituting the derived expressions from equations (5.2) and (5.3), we obtain the following result [26]

$$\begin{aligned}\mathcal{F}_n(\boldsymbol{k}) &= \mathrm{i}\varepsilon_{\mu\nu} \sum_{\substack{m=1 \\ m\neq n}}^{2N_d} \frac{\rho_n \left(V_k^\dagger(\partial_\mu H(\boldsymbol{k}))V_k\right)_{nm} \rho_m \left(V_k^\dagger(\partial_\nu H(\boldsymbol{k})V_k)\right)_{mn}}{(\bar{\mathcal{E}}_{k,n} - \bar{\mathcal{E}}_{k,m})^2} \\ &= \mathrm{i}\varepsilon_{\mu\nu} \sum_{\substack{m=1 \\ m\neq n}}^{2N_d} \frac{\rho_n\rho_m}{(\bar{\mathcal{E}}_{k,n} - \bar{\mathcal{E}}_{k,m})^2} \langle n_k| \partial_\mu H(\boldsymbol{k}) |m_k\rangle \langle m_k| \partial_\nu H(\boldsymbol{k}) |n_k\rangle ,\end{aligned} \tag{5.4}$$

where N_d is the number of particle states in the system. It is worth noting that the resulting expression is gauge-independent, making it suitable for numerical computations. It becomes apparent that the Berry curvature remains well-defined only when the bands are isolated. Additionally, we observe that the Berry curvature captures the complete energy spectrum of the system, and it is not possible to have a finite Berry curvature for a Hamiltonian associated with a single band. Based on this expression, we can deduce the following properties of the Berry curvature [70]

$$\begin{aligned}&\text{(i)} \quad \sum_{n=1}^{2N_d} \mathcal{F}_n(\boldsymbol{k}) = 0, \\ &\text{(ii)} \quad \mathcal{F}_n(\boldsymbol{k}) = -\mathcal{F}_{n+N_d}(-\boldsymbol{k}) \ \text{ for } \ n = 1, \dots, N_d.\end{aligned}$$

The first relation becomes evident upon summation, while the second expression establishes a connection between the Berry curvature in the particle and hole space. To demonstrate the second relation, we utilize the eigenvectors $\boldsymbol{v}_{n,+}(\boldsymbol{k})$ for the particle states and $\boldsymbol{v}_{n,-}(\boldsymbol{k})$ for the hole states, which are related by $\boldsymbol{v}_{n,-}(\boldsymbol{k}) = \sigma_1 \boldsymbol{v}^*_{n,+}(-\boldsymbol{k})$ [72]. In terms of these eigenvectors, the Berry curvature $\mathcal{F}_{n,\rho_n}(\boldsymbol{k})$ for the (n, ρ_n) band can be expressed as

$$\begin{aligned}\mathcal{F}_{n,\rho_n}(\boldsymbol{k}) =& \mathrm{i}\varepsilon_{\mu\nu} \sum_{\substack{m,\rho_m \\ (m,\rho_m)\neq(n,\rho_n)}} \frac{\rho_n\rho_m}{(\mathcal{E}_{k,n,\rho_n} - \mathcal{E}_{k,m,\rho_m})^2} \left[\boldsymbol{v}^\dagger_{n,\rho_n}(\boldsymbol{k})(\partial_\mu H(\boldsymbol{k}))\boldsymbol{v}_{m,\rho_m}(\boldsymbol{k})\boldsymbol{v}^\dagger_{m,\rho_m}(\boldsymbol{k})(\partial_\nu H(\boldsymbol{k}))\boldsymbol{v}_{n,\rho_n}(\boldsymbol{k})\right] \\ =& -\mathrm{i}\varepsilon_{\mu\nu} \sum_{\substack{m,\rho_m \\ (m,\rho_m)\neq(n,\rho_n)}} \frac{\rho_n\rho_m}{(\mathcal{E}_{k,n,\rho_n} - \mathcal{E}_{k,m,\rho_m})^2} \Big[\boldsymbol{v}^\dagger_{n,\bar{\rho}_n}(-\boldsymbol{k})(\partial_\mu H(-\boldsymbol{k}))\boldsymbol{v}_{m,\bar{\rho}_m}(-\boldsymbol{k}) \\ &\qquad \times \boldsymbol{v}^\dagger_{m,\bar{\rho}_m}(-\boldsymbol{k})(\partial_\nu H(-\boldsymbol{k}))\boldsymbol{v}_{n,\bar{\rho}_n}(-\boldsymbol{k})\Big] ,\end{aligned}$$

where $m \in \{1, \dots, N_d\}$ and $\rho_m \in \{-1, +1\}$. We utilized the particle-hole symmetry of the Hamiltonian from equation (4.7), and we defined $\bar{\rho}_n = -\rho_n$. Moreover, we use the notation $\mathcal{E}_{k,n,+} = \mathcal{E}_{k,n}$ and $\mathcal{E}_{k,n,-} = -\mathcal{E}_{-k,n}$, such that the eigenvalues of the bands are related by $\mathcal{E}_{k,n,\rho_n} = -\mathcal{E}_{-k,n,\bar{\rho}_n}$. By using that $\rho_n\rho_m = \bar{\rho}_n\bar{\rho}_m$, in addition to switching indices $\bar{\rho}_m \to \rho_m$, we obtain

$$\begin{aligned}\mathcal{F}_{n,\rho_n}(-\boldsymbol{k}) =& -\mathrm{i}\varepsilon_{\mu\nu} \sum_{\substack{m,\rho_m \\ (m,\rho_m)\neq(n,\rho_n)}} \frac{\bar{\rho}_n\rho_m}{(\mathcal{E}_{k,n,\bar{\rho}_n} - \mathcal{E}_{k,m,\rho_m})^2} \left[\boldsymbol{v}^\dagger_{n,\bar{\rho}_n}(\boldsymbol{k})(\partial_\mu H(\boldsymbol{k}))\boldsymbol{v}_{m,\rho_m}(\boldsymbol{k})\boldsymbol{v}^\dagger_{m,\rho_m}(\boldsymbol{k})(\partial_\nu H(\boldsymbol{k}))\boldsymbol{v}_{n,\bar{\rho}_n}(\boldsymbol{k})\right] \\ =& -\mathcal{F}_{n,\bar{\rho}_n}(\boldsymbol{k}),\end{aligned}$$

where we also used that $(\mathcal{E}_{-k,n,\rho_n} - \mathcal{E}_{-k,m,\bar{\rho}_m})^2 = (\mathcal{E}_{k,n,\bar{\rho}_n} - \mathcal{E}_{k,m,\rho_m})^2$. Thus, if band n corresponds to a particle band, then $\mathcal{F}_n(\boldsymbol{k}) = -\mathcal{F}_{n+N_d}(-\boldsymbol{k})$.

Like the properties exhibited by the Berry curvature in Bogoliubov-de Gennes systems, the Chern number also follows a summation rule. Specifically, when summing the Chern numbers across all particle bands or all hole bands, the result reduces to zero [70]. The summation rule can be expressed as follows

$$\sum_{n=1}^{N_d} C_n = 0, \quad \text{and} \quad \sum_{n=N_d}^{2N_d} C_n = 0.$$

5.3. Transport properties related to the Berry curvature

Topological electronic systems can exhibit transport phenomena such as the quantum Hall effect, and potentially, the anomalous Hall effect. The Hall effect is a well-known phenomenon in conductors where an external magnetic field applied perpendicularly to the electric current deflects the charge carriers from their straight paths, causing them to accumulate at one end of the material and produce a transverse voltage. The quantum Hall effect is a quantized version of this phenomenon, where the Hall conductivity is proportional to the Chern number [74]. Similarly, the anomalous Hall effect's conductivity is proportional to the Berry curvature, but it does not require a nonzero Chern number for a nonvanishing conductivity.

In bosonic systems, where the transport properties concerns neutral quasiparticles such as magnons and phonons, the experienced Lorentz force which produces the anomalous velocity comes from the Berry curvature in momentum space [47]. This effect is exemplified by the Dzyaloshinskii-Moriya interaction in magnetic systems, where the canting of neighbouring spins yields a spin chirality that results in a geometrical phase for propagating magnons [60]. The Berry curvature can also originate from dipolar interaction, magnon-magnon interaction or noncollinear and noncoplanar magnetic textures [15, 60, 70]. Applying a thermal gradient to such a system, a transverse magnon current emerges, producing a heat current since magnons are neutral particles. This phenomenon is called the magnon-mediated thermal Hall effect, and a similar effect can be observed for phonons [60]. Moreover, topological magnonic systems can display the spin Nernst effect, where the longitudinal temperature gradient generates a transverse spin current [57]. Both the spin Nernst coefficient and the thermal Hall conductivity are directly related to the Berry curvature. However, while the spin Nernst effect is expected to occur in all systems with nonvanishing Berry curvature, the thermal Hall effect requires a broken effective time-reversal symmetry [60].

In topological magnon insulators[1], the thermal Hall effect can be attributed to the magnon edge current [15, 77]. When a thermal gradient is applied, the heat current flowing through the two opposite edges of the insulator shows a difference in contribution, resulting in a finite thermal Hall current. This phenomenon has been extensively studied due to its importance in understanding the topological properties of magnetic materials. It is important to note that both the thermal Hall effect and spin Nernst effect are geometric properties rather than topological properties of the system, as they rely on the local Berry curvature in momentum space [60]. Indeed, the magnon Hall effect has been observed in a cubic magnet with topologically trivial characteristics [27]. However, although the

[1] In contrast to "true" insulators, topological magnon insulators involve the participation of all magnon bands, including both bulk and edge states, in transport properties. However, the dominant contribution to transport comes from the edge states [15].

presence of such Hall effects does not guarantee the existence of magnon band topology, it is expected to be present in nondegenerate Chern bands and can serve as an indicator of nontrivial topology [47]. Furthermore, similar anomalous Hall effects has been observed in other topological systems, such as topological superconductors and Weyl semimetals, indicating its relevance across various fields of physics [73, 78].

The thermal Hall conductivity κ_{xy} is a quantity that relates the transverse heat current to the applied temperature gradient. Mathematically, this relation can be expressed as $J_x^Q = \kappa_{xy}(-\nabla T)_y$, where T denotes temperature and J_x^Q refers to the transverse heat current [26, 54]. The theoretical derivation of this conductivity in electronic systems is typically accomplished using linear response theory by introducing a fictitious gravitational field that exerts a force on the wave packet [77]. A similar method can be used for magnons, where two significant contributions are identified. The first component is a deviation of the particle density operator from equilibrium as calculated using the Kubo formula [17], while the second component is associated with the orbital motion of magnons [70, 77]. The complete derivation is beyond the scope of this thesis, therefore, we present only the final result. The thermal Hall conductivity in a bosonic system can be expressed as follows [70]

$$\kappa_{xy} = -\frac{k_B^2 T}{\hbar \mathcal{A}} \sum_{k} \sum_{n=1}^{N_d} \left(c_2[g_{\mathrm{BE}}(\mathcal{E}_{k,n})] - \frac{\pi^2}{3} \right) \mathcal{F}_n(\boldsymbol{k}), \tag{5.5}$$

where k_B is the Boltzmann constant, $\mathcal{A}$ is the area of the system and $g_{\mathrm{BE}}(\mathcal{E}_{k,n})$ is the Bose-Einstein distribution, given by

$$g_{\mathrm{BE}}(\mathcal{E}_{k,n}) = \frac{1}{\mathrm{e}^{\mathcal{E}_{k,n}/k_B T} - 1}.$$

Furthermore, the function $c_2(x)$ is defined as

$$c_2(x) = (1+x)\left(\ln \frac{1+x}{x}\right)^2 - (\ln x)^2 - 2\mathrm{Li}_2(-x),$$

where $\mathrm{Li}_2(x)$ is the polylogarithm function of second order. The function $c_2[g_{\mathrm{BE}}(\mathcal{E}_{k,n})]$ has its maximum value of $\pi^2/3$ at zero energy and is a monotonically decreasing function where it approaches zero in the limit $\mathcal{E}_{k,n} \to \infty$ [70]. It is important to highlight that the summation is confined to the particle bands of the BdG Hamiltonian. When summing over the first Brillouin zone, the last term in the parentheses is directly related to the summation of the Chern numbers of all particle bands. However, as demonstrated in the previous section, we established that this term evaluates to zero and can thus be disregarded in the calculations.

Similarly, the spin Nernst coefficient α_{xy} relates the spin current density to the applied temperature gradient through the equation $J_x^S = \alpha_{xy}(-\nabla T)_y$. To derive an expression for this coefficient, we introduce the spin Berry curvature, which is associated with the spin current operator defined as $\boldsymbol{j}^S = \frac{1}{4}(\boldsymbol{u}\sigma_3\mathcal{S} + \mathcal{S}\sigma_3\boldsymbol{u})$, where $\boldsymbol{u} = \hbar^{-1}\partial_{\boldsymbol{k}} H(\boldsymbol{k})$ is the velocity operator. Additionally, $\mathcal{S}$ is the spin excitation operator, which takes the form of a diagonal matrix with values ± 1 for the elements corresponding to magnon excitations. Specifically, if a magnon excitation is associated with a spin aligned parallel to the magnetization axis, we insert -1, while for an anti-parallel spin alignment, we use $+1$. The spin Berry curvature is defined as follows [79, 80]

$$\left[\mathcal{F}_n^S(\boldsymbol{k})\right]_{\mu\nu} = 2\mathrm{i}\hbar^2 \sum_{\substack{m=1 \\ m\neq n}}^{2N_d} \frac{\rho_n \rho_m}{(\bar{\mathcal{E}}_{k,n} - \bar{\mathcal{E}}_{k,m})^2} \left\langle n_k \right| j_\mu^S \left| m_k \right\rangle \left\langle m_k \right| u_\nu \left| n_k \right\rangle. \tag{5.6}$$

With this expression at hand, the spin Nernst coefficient, obtained through linear response theory, is given by [54, 79, 80]

$$\alpha_{xy} = -\frac{2k_B}{\mathcal{A}} \sum_{k} \sum_{n=1}^{N_d} c_1[g_{\mathrm{BE}}(\mathcal{E}_{k,n})] \left[\mathcal{F}_n^S(\boldsymbol{k})\right]_{xy}, \tag{5.7}$$

where

$$c_1(x) = (1+x)\ln(1+x) - x\ln(x).$$

Similar to the behaviour of $c_2(x)$, the function $c_1(x)$ demonstrates a monotonically decreasing nature that converges to zero as $\mathcal{E}_{k,n}$ approaches infinity. Moreover, the spin Berry curvature follows the same summation rule as the conventional Berry curvature, where the total sum of the Berry curvatures across all bands is zero. We can also establish a relationship between the spin Berry curvature of the particle and hole states with the following expression $\left[\mathcal{F}_n^S(\boldsymbol{k})\right]_{\mu\nu} = \left[\mathcal{F}_{n+N_d}^S(-\boldsymbol{k})\right]_{\mu\nu}$ [79].

CHAPTER 6

Modifying the magnon dispersion

Within this chapter, we build on the work in Chapter 3 where we studied the magnon dispersion in various lattices with both ferro- and antiferromagnetic ordering. However, in the present chapter, we narrow our focus to the honeycomb lattice with ferromagnetic ordering and extend our model to include additional features. Specifically, we investigate the impact on the magnon dispersion and the magnon-phonon coupling, which we cover in Chapter 7, when the magnetization direction deviates from the out-of-plane alignment. Furthermore, we utilize a magnon Hamiltonian that includes the biquadratic Heisenberg exchange term and a general form of the nearest and next-nearest neighbour DMI. Towards the end of the chapter, we compare the dispersion of magnons in the presence of either DMI or Kitaev interactions. Both interactions have the potential to give rise to topological magnons, and we examine the differences in the magnon energy spectra resulting from each interaction.

We aim to investigate the magnon-phonon coupling in a general honeycomb lattice. However, our magnon Hamiltonian is based on CrI_3, a vdW magnet with ferromagnetic ordering perpendicular to the lattice plane and a Curie temperature of $T_c = 45$K in the 2D-limit [81]. The Cr^{3+} ions are arranged in a 2D honeycomb network with six I^- ions in an edge-sharing octahedral environment [81]. The interaction between the crystal field and the iodine ions leads to a total spin of $S = 3/2$ with quenched orbital momentum ($L = 0$) [13, 81]. Ferromagnetic ordering is achieved through superexhange paths via the iodine atoms. Despite the weak spin-orbit coupling of chromium ions, the magnetic anisotropy is significant due to the strong spin-orbit coupling of the heavier iodine atoms, which ensures thermal stability [13].

6.1. Biquadratic exchange

Apart from the (bilinear) Heisenberg exchange interaction, there exist higher-order terms, like the biquadratic exchange interaction, that can have an impact on the magnon Hamiltonian. The presence of these additional terms arises from the intricate interplay between superexchange processes involving nonmagnetic atoms and Coulomb repulsion between neighbouring magnetic sites. These interactions can significantly influence the overall energy of the system and can be effectively incorporated by introducing the biquadratic exchange interaction [82]. Biquadratic exchange has a strong impact in materials where the exchange is weak, such as several 2D magnets that have been discovered so far [82].

To accurately depict the magnon energy spectrum in CrI_3, we incorporate the biquadratic exchange interaction between nearest neighbours into the magnon Hamiltonian. The term can be expressed as follows [82]

$$\mathcal{H}_{\mathrm{bq}} = -\sum_{<i,j>} \Lambda_{ij} (\boldsymbol{S}_i \cdot \boldsymbol{S}_j)^2,$$

with $\Lambda_{ij} = \Lambda$ for all pairs of nearest neighbours. In the following, we will examine the impact of the biquadratic exchange on the magnon dispersion and assess whether it can result in linear magnetoelastic coupling terms.

6.1.1. Effect of biquadratic exchange on magnon dispersion

By splitting the honeycomb lattice into two distinct sublattices, labeled as A and B, the biquadratic exchange interaction can be expressed as follows

$$\mathcal{H}_{\text{bq}} = -\Lambda \sum_{\substack{i,\delta_A \\ i\in A}} (\boldsymbol{S}_{iA} \cdot \boldsymbol{S}_{i+\delta_A,B})^2.$$

To facilitate comparison, we will investigate both ferromagnetic and antiferromagnetic ordering.

Ferromagnetic ordering

For a ferromagnet, the biquadratic exchange can be described using the Holstein-Primakoff transformation for spins ordered in a ferromagnetic manner, resulting in

$$\mathcal{H}_{\text{bq}} = -\Lambda \sum_{\substack{i,\delta_A \\ i\in A}} (S^2 - Sa_i^\dagger a_i - Sb_{i+\delta_A}^\dagger b_{i+\delta_A} + Sa_i^\dagger b_{i+\delta_A} + Sb_{i+\delta_A}^\dagger a_i)^2.$$

After evaluating the product and rearranging the terms into normal order, similar to what was done for the anisotropy term, the resulting expression becomes

$$\mathcal{H}_{\text{bq}} = -\Lambda \sum_{\substack{i,\delta_A \\ i\in A}} \left[S^4 - 2S^2(S-1)(a_i^\dagger a_i + b_{i+\delta_A}^\dagger b_{i+\delta_A} - a_i^\dagger b_{i+\delta_A} - b_{i+\delta_A}^\dagger a_i) \right],$$

to second order in bosonic operators. The magnon Hamiltonian's complete Heisenberg exchange part is obtained by combining the bilinear exchange and dropping the zeroth order term, expressed as

$$\mathcal{H}_{\text{Heis}} = \mathcal{H}_{\text{bl}} + \mathcal{H}_{\text{bq}} = (J + 2\Lambda S(S-1))S \sum_{\substack{i,\delta_A \\ i\in A}} (a_i^\dagger a_i + b_{i+\delta_A}^\dagger b_{i+\delta_A} - a_i^\dagger b_{i+\delta_A} - b_{i+\delta_A}^\dagger a_i).$$

The biquadratic exchange leads to a shift in the effective exchange coupling coefficient. Defining $\tilde{J} = J + 2\Lambda S(S-1)$ as the effective exchange coupling coefficient, the magnon dispersion in the honeycomb lattice is on the form described in equation (3.12) with $J \to \tilde{J}$. Neglecting the normal ordering procedure for the fourth-order terms, the result would have been $\tilde{J} = J + 2\Lambda S^2$ [82, 83].

Antiferromagnetic ordering

By employing the Holstein-Primakoff transformation for antialigned spins, the biquadratic exchange is transformed to

$$\mathcal{H}_{\text{bq}} = -\Lambda \sum_{\substack{i,\delta_A \\ i\in A}} (-S^2 + Sa_i^\dagger a_i + Sb_{i+\delta_A}^\dagger b_{i+\delta_A} + Sa_i^\dagger b_{i+\delta_A}^\dagger + Sa_i b_{i+\delta_A})^2,$$

which after rearranging the terms according to their normal order and keeping only the second-order terms yields

$$\mathcal{H}_{\text{bq}} = 2\Lambda S^2(S-1) \sum_{\substack{i,\delta_A \\ i\in A}} (a_i^\dagger a_i + b_{i+\delta_A}^\dagger b_{i+\delta_A} + a_i^\dagger b_{i+\delta_A}^\dagger + a_i b_{i+\delta_A}),$$

where we also removed the zeroth order terms. By comparing with the bilinear exchange part of the magnon Hamiltonian (equation (3.16)), the inclusion of a biquadratic exchange leads to the effective exchange coupling coefficient $\mathcal{J} = J - 2\Lambda S(S-1)$. This is in accordance with Ref. [83], neglecting

the normal ordering procedure of the fourth order terms. By assuming the biquadratic exchange does not alter the sign of the effective exchange coupling coefficient, such that $\mathcal{J}$ is a negative number, the magnon dispersion in the honeycomb lattice is given by equation (3.25) with $J \to \mathcal{J}$.

6.1.2. Taylor expansion of the biquadratic exchange coupling coefficient

Similar to the bilinear exchange coupling coefficient, the biquadratic exchange coupling coefficient is in general a function of the ionic coordinates. A Taylor expansion around the equilibrium position yields

$$\Lambda(\boldsymbol{r}_{ij}) = \Lambda(\boldsymbol{R}_{ij}) + (\nabla_{\boldsymbol{r}_{ij}} \Lambda(\boldsymbol{r}_{ij})\Big|_{\boldsymbol{R}_{ij}}) \cdot \boldsymbol{u}_{ij}.$$

Thus, the magnon-phonon coupling terms arising from the biquadratic exchange can be expressed as follows

$$\mathcal{H}_{\text{int}}^{\text{bq}} = -\sum_{<i,j>} \sum_{\mu} \frac{\partial \Lambda(\boldsymbol{r}_{ij})}{\partial r_{ij}^{\mu}}\bigg|_{\boldsymbol{R}_{ij}} (u_{i\mu} - u_{j\mu})(\boldsymbol{S}_i \cdot \boldsymbol{S}_j)^2.$$

Like the coupling terms obtained by expanding the bilinear exchange coupling coefficient, the dot product couples spins with the same spatial component to each other, resulting in terms of first, third, or higher order. This relationship holds when considering collinear spin ordering within the Holstein-Primakoff framework.

6.2. Computing magnon dispersion with arbitrary magnetization direction

Up to this point, the magnetization direction of the investigated two-dimensional magnetic systems has been exclusively perpendicular to the plane of the lattice. In this section, we aim to investigate the implications of ferromagnetic ordering of spins in an arbitrary direction. Our assumption is that a strong magnetic field aligns the spins with the field in the classical ground state, and that the spin direction can be modified by altering the field direction. Specifically, we analyze a ferromagnetic honeycomb lattice governed by a Hamiltonian on the following form

$$\mathcal{H} = -J \sum_{<i,j>} \boldsymbol{S}_i \cdot \boldsymbol{S}_j - \Lambda \sum_{<i,j>} (\boldsymbol{S}_i \cdot \boldsymbol{S}_j)^2 - \sum_i \boldsymbol{S}_i \cdot \boldsymbol{h} - K_z \sum_i S_{iz}^2 - \sum_{i,j} \boldsymbol{D}_{ij} \cdot [\boldsymbol{S}_i \times \boldsymbol{S}_j]. \tag{6.1}$$

The system possesses an easy-axis single ion anisotropy, and the DMI is expressed in a general form. As mentioned earlier in equation (4.1), the out-of-plane next-nearest neighbour DMI is intrinsic and stems from the locally asymmetric path to the next-nearest neighbours. On the other hand, the in-plane nearest neighbour DMI arises from the loss of mirror symmetry with respect to the lattice plane and can be induced by different factors like a surrounding substrate or an electric field [11, 26]. However, when the mirror symmetry is broken, both the next-nearest and nearest neighbour DM vector can deviate from their perpendicular and in-plane orientations, respectively [11, 84]. We consider two scenarios for the next-nearest neighbour DM vector; a tilted out-of-plane DM vector with arbitrary directions for the in-plane components, or a vector where the in-plane components are directed towards the next-nearest neighbours. The latter is the proposed format of the DM vector in CrI_3 [11]. We utilize the following expressions

$$\begin{aligned}
\boldsymbol{D}_{ij}^{\text{nnn},t} &= \nu_{ij}(D_x^{\text{nnn}}\hat{\boldsymbol{x}} + D_y^{\text{nnn}}\hat{\boldsymbol{y}} + D_z^{\text{nnn}}\hat{\boldsymbol{z}}), \\
\boldsymbol{D}_{ij}^{\text{nnn},r} &= -\eta_{ij} D_{xy}^{\text{nnn}} \hat{\boldsymbol{R}}_{ij} + \nu_{ij} D_z^{\text{nnn}} \hat{\boldsymbol{z}},
\end{aligned}$$

where $\eta_{ij} = +1(-1)$ for bonds between the $A(B)$ sublattice and ν_{ij} is the Haldane sign. Additionally, we modify the previously used expression for the nearest neighbour DMI by adding an out-of-plane component, resulting in the DM vector taking the form of [11]

$$\boldsymbol{D}_{ij}^{\mathrm{nn}} = D_{xy}^{\mathrm{nn}}(\hat{\boldsymbol{z}} \times \hat{\boldsymbol{R}}_{ij}) + D_z^{\mathrm{nn}}\hat{\boldsymbol{z}}.$$

The objective of this section is to examine the magnon dispersion for each of the DM-vectors and distinguish their dissimilarities. A significant emphasis is placed on identifying the presence of a band gap and observing how it varies with alterations in the magnetization direction. Before proceeding with the calculations, we shortly investigate the symmetry of the proposed expressions for the DM vectors.

6.2.1. Symmetry analysis of the DM vectors

The presence of Dirac cones in the magnon energy spectrum is conditional on the existence of effective time-reversal symmetry in the system. One possible method to achieve this symmetry is by combining a rotation in spin space with time-reversal symmetry [16]. A spin rotation should restore the initial spin texture, as the time-reversal symmetry operator corresponds to a spin-flip. However, the Hamiltonian must remain unchanged for this transformation to be an effective time-reversal symmetry. The spin rotation is represented by $\mathcal{R}(\boldsymbol{n}, \pi)$ and causes a π spin rotation around an axis $\boldsymbol{n}$, which is perpendicular to the magnetization direction. When we consider the out-of-plane next-nearest neighbour DMI with a magnetization normal to the lattice plane, the rotation $\mathcal{R}(x, \pi)$ results in $\boldsymbol{S}_i \to (S_{ix}, -S_{iy}, -S_{iz})$ such that the term $D_z^{\mathrm{nnn}}(S_{ix}S_{jy} - S_{iy}S_{jx})$ reverses its sign. However, for a magnetization in the plane, the spin rotation is around the $z-$axis, which leaves the term unchanged [16]. As a result, we expect to see gap openings as long as the magnetization has out-of-plane components.

The two expressions for the next-nearest neighbour DM vectors have different in-plane components. If the in-plane components point toward the next-nearest neighbours, the vector has the same symmetries as the neighbouring vectors, including reflection, inversion and rotational symmetry. This symmetry preserves the effective time-reversal symmetry. For instance, consider the magnetization along the $x-$axis, and let's apply the rotation $\mathcal{R}(z, \pi)$. This rotation changes the sign of the in-plane DMI terms. However, as the transformation $\hat{\boldsymbol{R}}_{ij} \to -\hat{\boldsymbol{R}}_{ij}$ maps the in-plane DM vectors in $\boldsymbol{D}_{ij}^{\mathrm{nnn},r}$ onto itself, the DMI terms are left unchanged under a spin rotation. This is not the case for the other next-nearest neighbour DM vector, and we should expect a gap opening.

When considering the in-plane part of the nearest neighbour DM vector, the combined symmetry of $C_{2,z}$ rotation and time-reversal symmetry forms an effective time-reversal symmetry when the magnetization lies in the plane [16]. The $C_{2,z}$ transformation involves rotating the space and spins around the $z-$axis, with the center of mass of the hexagon acting as the center of rotation. However, in the case of out-of-plane magnetization, the systems does not possess effective time-reversal symmetry since there is no in-plane axis about which the spins can be rotated without altering the DMI terms [16]. Therefore, the existence of nonzero out-of-plane components in the magnetization is anticipated to cause gap openings as a consequence of the nearest neighbour DMI.

6.2.2. Next-nearest neighbour DMI

To find the magnon dispersion for an arbitrary direction of the spins, it is convenient to change the frame of reference to $\{\hat{\boldsymbol{e}}_1, \hat{\boldsymbol{e}}_2, \hat{\boldsymbol{e}}_3\}$, where each $\hat{\boldsymbol{e}}_i$ is a unit vector. The new frame of reference is defined such that $\hat{\boldsymbol{e}}_3$ is aligned with the magnetic field, and hence the magnetization direction. It is related to the lab-frame via a rotation on the form [13]

$$\hat{\boldsymbol{e}}_1 = O\hat{\boldsymbol{x}},\ \ \hat{\boldsymbol{e}}_2 = O\hat{\boldsymbol{y}},\ \ \hat{\boldsymbol{e}}_3 = O\hat{\boldsymbol{z}},$$

where $O = O_z(\phi)O_y(\theta)O_x(\vartheta)$ is the rotation matrix and

$$O_z(\phi) = \begin{bmatrix} \cos(\phi) & -\sin(\phi) & 0 \\ \sin(\phi) & \cos(\phi) & 0 \\ 0 & 0 & 1 \end{bmatrix},\ O_y(\theta) = \begin{bmatrix} \cos(\theta) & 0 & \sin(\theta) \\ 0 & 1 & 0 \\ -\sin(\theta) & 0 & \cos(\theta) \end{bmatrix},$$
$$O_x(\vartheta) = \begin{bmatrix} 1 & 0 & 0 \\ 0 & \cos(\vartheta) & -\sin(\vartheta) \\ 0 & \sin(\vartheta) & \cos(\vartheta) \end{bmatrix}.$$

Denoting $\boldsymbol{S}_i'$ as the spins in the new frame of reference, they are related to the ones in the lab-frame by $\boldsymbol{S}_i' = O^T\boldsymbol{S}_i$, where

$$O = \begin{bmatrix} O_{x1} & O_{x2} & O_{x3} \\ O_{y1} & O_{y2} & O_{y3} \\ O_{z1} & O_{z2} & O_{z3} \end{bmatrix}$$
$$= \begin{bmatrix} \cos(\theta)\cos(\phi) & \sin(\theta)\cos(\phi)\sin(\vartheta) - \sin(\phi)\cos(\vartheta) & \sin(\theta)\cos(\phi)\cos(\vartheta) + \sin(\phi)\sin(\vartheta) \\ \cos(\theta)\sin(\phi) & \sin(\theta)\sin(\phi)\sin(\vartheta) + \cos(\phi)\cos(\vartheta) & \sin(\theta)\sin(\phi)\cos(\vartheta) - \cos(\phi)\sin(\vartheta) \\ -\sin(\theta) & \cos(\theta)\sin(\vartheta) & \cos(\theta)\cos(\vartheta) \end{bmatrix}.$$

The rotation matrix is an orthogonal matrix satisfying $O^TO = I$. For the spins in the new frame of reference, the Holstein-Primakoff transformation can be written like

$$\begin{aligned} S_{iA1}' =& \sqrt{\frac{S}{2}}(a_i + a_i^\dagger), \\ S_{iA2}' =& -\mathrm{i}\sqrt{\frac{S}{2}}(a_i - a_i^\dagger), \\ S_{iA3}' =& S - a_i^\dagger a_i, \end{aligned} \tag{6.2}$$

and similarly for the spins at sublattice B.

As the transformation to the new reference frame is independent of the lattice sites, the bilinear and biquadratic Heisenberg exchange terms are not affected by the spin rotation. This can be demonstrated by

$$\boldsymbol{S}_i \cdot \boldsymbol{S}_j = \boldsymbol{S}_i^T\boldsymbol{S}_j = \boldsymbol{S}_i'^T O^T O\boldsymbol{S}_j' = \boldsymbol{S}_i' \cdot \boldsymbol{S}_j'.$$

Likewise, the Zeeman term remains unaffected as the spins align with the magnetic field. However, the anisotropy interaction is influenced by the new spin direction. To second order, the anisotropy term can be expressed as

$$\begin{aligned}\mathcal{H}_{\text{ani}} =& -K_z \sum_{\substack{i \\ i\in A}} (O\boldsymbol{S}'_{iA})_z^2 \\ =& -K_z \sum_{\substack{i \\ i\in A}} \Bigg[S^2 O_{z3}^2 + \frac{S}{2}(O_{z1}^2 + O_{z2}^2) + S\sqrt{\frac{S}{2}} O_{z3}(O_{z1} - \mathrm{i}O_{z2}) a_i + \text{h.c} \\ & - \left((2S-1)O_{z3}^2 - S(O_{z1}^2 + O_{z2}^2) \right) a_i^\dagger a_i + \frac{S}{2} Q_z a_i a_i + \text{h.c} \Bigg],\end{aligned}$$

where

$$Q_z = (O_{z1} - \mathrm{i}O_{z2})^2.$$

The notation h.c denotes the Hermitian conjugate of the previous term and the summation over sublattice B is similar with $a_i \to b_i$. Note that there are terms with single magnon operators. These linear terms contribute to the magnon dispersion only at the $\Gamma-$point, and can therefore be disregarded [13]. In addition, we omit the ground state energy, the zeroth order terms, by changing the reference energy. In terms of the Fourier-transformed operators, the anisotropy term is on the form

$$\mathcal{H}_{\text{ani}} = K_z \sum_k \left[\left((2S-1)O_{z3}^2 - S(O_{z1}^2 + O_{z2}^2) \right) (a_k^\dagger a_k + b_k^\dagger b_k) - \frac{S}{2} Q_z (a_k a_{-k} + b_k b_{-k}) + \text{h.c} \right].$$

For the Dzyaloshinskii-Moriya interaction, we let $\boldsymbol{D}_{ij}^{\text{nnn}} \in \{\boldsymbol{D}_{ij}^{\text{nnn},t}, \boldsymbol{D}_{ij}^{\text{nnn},r}\}$ be any of the two types of next-nearest neighbour DM vectors. To bring the vector into the frame of reference, it can be rotated by

$$\boldsymbol{D}_{ij}^{\text{nnn}\prime} = O^T \boldsymbol{D}_{ij}^{\text{nnn}} = \begin{bmatrix} D_{ij,1}^{\text{nnn}\prime} \\ D_{ij,2}^{\text{nnn}\prime} \\ D_{ij,3}^{\text{nnn}\prime} \end{bmatrix},$$

such that the DMI term can be written as [13]

$$\begin{aligned}\mathcal{H}_{\text{DMI,nnn}} =& -\sum_{<<i,j>>} \boldsymbol{D}_{ij}^{\text{nnn}} \cdot [\boldsymbol{S}_i \times \boldsymbol{S}_j] = -\sum_{<<i,j>>} (\boldsymbol{D}_{ij}^{\text{nnn}})^T O O^T [\boldsymbol{S}_i \times \boldsymbol{S}_j] \\ =& -\sum_{<<i,j>>} \boldsymbol{D}_{ij}^{\text{nnn}\prime} \cdot [\boldsymbol{S}'_i \times \boldsymbol{S}'_j].\end{aligned} \tag{6.3}$$

By substituting the magnon operators, the summation over sublattice A becomes

$$\mathcal{H}_{\text{DMI,nnn}} = \sum_{\substack{<<i,j>> \\ i\in A}} \left[S\sqrt{\frac{S}{2}} (D_{ij,2}^{\text{nnn}\prime} + \mathrm{i}D_{ij,1}^{\text{nnn}\prime})(a_i - a_j) + \text{h.c} + \mathrm{i}S D_{ij,3}^{\text{nnn}\prime} (a_i^\dagger a_j - a_j^\dagger a_i) \right].$$

The first term, which involves single magnon operators, sums to zero. This can be demonstrated by taking into account the antisymmetric nature of the DM vector $\boldsymbol{D}_{ij}^{\text{nnn}} = -\boldsymbol{D}_{ji}^{\text{nnn}}$, which also holds true for the rotated vector, and results in the following

$$\sum_{\substack{<<i,j>>\\ i\in A}} (D^{\mathrm{nnn}\prime}_{ij,2} + \mathrm{i}D^{\mathrm{nnn}\prime}_{ij,1})(a_i - a_j) = \sum_{\substack{<<i,j>>\\ i\in A}} 2a_i(D^{\mathrm{nnn}\prime}_{ij,2} + \mathrm{i}D^{\mathrm{nnn}\prime}_{ij,1})$$
$$= \sum_{i\in A} a_i \sum_{\tau_A} (D^{\mathrm{nnn}\,\prime}_{\tau_A,2} + \mathrm{i}D^{\mathrm{nnn}\,\prime}_{\tau_A,1}),$$

where $\boldsymbol{\tau}_A = -\boldsymbol{R}_{ij}$ is the vector to the next-nearest neighbours. As $\boldsymbol{\tau}_A$ consists of a collection of symmetric vectors, such as $\boldsymbol{\tau}_1^A = -\boldsymbol{\tau}_4^A$, the summation over the neighbouring vectors result in the cancellation of all terms. Thus, only the quadratic terms remain. The summation over both sublattices can be expressed as

$$\begin{aligned}
\mathcal{H}_{\mathrm{DMI,nnn}} =& \frac{\mathrm{i}}{2}S\sum_{\substack{i,\tau_A\\ i\in A}} D^{\mathrm{nnn}\,\prime}_{\tau_A,3}(a_i^\dagger a_{i+\tau_A} - a_{i+\tau_A}^\dagger a_i) + \frac{\mathrm{i}}{2}S\sum_{\substack{i,\tau_B\\ i\in B}} D^{\mathrm{nnn}\,\prime}_{\tau_B,3}(b_i^\dagger b_{i+\tau_B} - b_{i+\tau_B}^\dagger b_i)\\
=& -S\sum_k\sum_{\tau_A} D^{\mathrm{nnn}\,\prime}_{\tau_A,3}\sin(\boldsymbol{k}\cdot\boldsymbol{\tau}_A)a_k^\dagger a_k - S\sum_k\sum_{\tau_B} D^{\mathrm{nnn}\,\prime}_{\tau_B,3}\sin(\boldsymbol{k}\cdot\boldsymbol{\tau}_B)b_k^\dagger b_k\\
=& S\sum_k D_k^{\mathrm{nnn}}(a_k^\dagger a_k - b_k^\dagger b_k),
\end{aligned}$$

where we defined $D_k^{\mathrm{nnn}} = -\sum_{\tau_A} D^{\mathrm{nnn}\,\prime}_{\tau_A,3}\sin(\boldsymbol{k}\cdot\boldsymbol{\tau}_A)$. Separating between the two expressions for the DM vectors, the rotated components $D^{\mathrm{nnn}\,\prime}_{\tau_A,3}$ are

$$\begin{aligned}
D^{\mathrm{nnn},t\prime}_{\tau_A,3} &= \nu_{\tau_A}(O_{x3}D_x^{\mathrm{nnn}} + O_{y3}D_y^{\mathrm{nnn}} + O_{z3}D_z^{\mathrm{nnn}}),\\
D^{\mathrm{nnn},r\prime}_{\tau_A,3} &= O_{x3}D_{xy}^{\mathrm{nnn}}\hat{\tau}_{Ax} + O_{y3}D_{xy}^{\mathrm{nnn}}\hat{\tau}_{Ay} + \nu_{\tau_A}O_{z3}D_z^{\mathrm{nnn}},
\end{aligned}$$

and the function D_k^{nnn} for each type is

$$\begin{aligned}
D_k^{\mathrm{nnn},t} =& -2(O_{x3}D_x^{\mathrm{nnn}} + O_{y3}D_y^{\mathrm{nnn}} + O_{z3}D_z^{\mathrm{nnn}})(\sin(k_xa) - 2\sin(\frac{1}{2}k_xa)\cos(\frac{\sqrt{3}}{2}k_ya)),\\
D_k^{\mathrm{nnn},r} =& -2\sin(k_xa)(O_{x3}D_{xy}^{\mathrm{nnn}} + O_{z3}D_z^{\mathrm{nnn}}) - 2\sin(\frac{1}{2}k_xa)\cos(\frac{\sqrt{3}}{2}k_ya)(O_{x3}D_{xy}^{\mathrm{nnn}} - 2O_{z3}D_z^{\mathrm{nnn}})\\
&- 2\sqrt{3}\cos(\frac{1}{2}k_xa)\sin(\frac{\sqrt{3}}{2}k_ya)O_{y3}D_{xy}^{\mathrm{nnn}}.
\end{aligned}$$

Since the out-of-plane components of the DM vectors are identical, the contribution from D_z^{nnn} is the same in both cases. By combining all the terms, the total Hamiltonian is

$$\mathcal{H} = \sum_k \left[t_k^A a_k^\dagger a_k + t_k^B b_k^\dagger b_k - t_k a_k^\dagger b_k - t_k^* b_k^\dagger a_k - \frac{1}{2}SK_zQ_z(a_ka_{-k} + b_kb_{-k}) - \frac{1}{2}SK_zQ_z^*(a_k^\dagger a_{-k}^\dagger + b_k^\dagger b_{-k}^\dagger)\right], \tag{6.4}$$

with the new coefficients defined as

$$\begin{aligned}
t_k^A &= 3\tilde{J}S + \Delta' + SD_k^{\mathrm{nnn}}, & t_k^B &= 3\tilde{J}S + \Delta' - SD_k^{\mathrm{nnn}},\\
t_k &= \tilde{J}Sf_{\delta_A}(\boldsymbol{k}), & \Delta' &= h + \left((2S-1)O_{z3}^2 - S(O_{z1}^2 + O_{z2}^2)\right)K_z,
\end{aligned}$$

$\tilde{J} = J + 2\Lambda S(S-1)$, $D_k^{\mathrm{nnn}} \in \{D_k^{\mathrm{nnn},t}, D_k^{\mathrm{nnn},r}\}$ and $f_{\delta_A}(\boldsymbol{k})$ is the structure factor. The Hamiltonian can be represented in matrix form as follows

$$\mathcal{H} = \frac{1}{2}\sum_k \boldsymbol{\psi}_{\mathrm{m}}^\dagger(\boldsymbol{k}) H_{\mathrm{m}}(\boldsymbol{k}) \boldsymbol{\psi}_{\mathrm{m}}(\boldsymbol{k}),$$

where $\boldsymbol{\psi}_{\mathrm{m}}(\boldsymbol{k}) = [a_k, b_k, a_{-k}^\dagger, b_{-k}^\dagger]$ and

$$H_{\mathrm{m}}(\boldsymbol{k}) = \begin{bmatrix} t_k^A & -t_k & -SK_zQ_z^* & 0 \\ -t_k^* & t_k^B & 0 & -SK_zQ_z^* \\ -SK_zQ_z & 0 & t_{-k}^A & -t_{-k}^* \\ 0 & -SK_zQ_z & -t_{-k} & t_{-k}^B \end{bmatrix}, \tag{6.5}$$

As usual, we obtain the eigenvalues by diagonalizing $\sigma_3 H_{\mathrm{m}}(\boldsymbol{k})$. By using that $t_{-k}^A = t_k^B$ and $t_{-k} = t_k^*$, the positive eigenvalues are

$$E_k^{\pm} = \Big((3\tilde{J}S + \Delta')^2 + S^2(D_k^{\mathrm{nnn}})^2 + \tilde{J}^2S^2|f_{\delta_A}(\boldsymbol{k})|^2 - S^2K_z^2|Q_z|^2 \\ \pm 2S\sqrt{(D_k^{\mathrm{nnn}})^2((3\tilde{J}S+\Delta')^2 - S^2K_z^2|Q_z|^2) + \tilde{J}^2|f_{\delta_A}(\boldsymbol{k})|^2(3\tilde{J}S+\Delta')^2}\Big)^{1/2}.$$

The magnetic field strength must meet certain requirements to yield positive eigenvalues, which depend on the orientation of the spins. When the spins are aligned perpendicular to the plane, there is no constraint, however, for spins lying in the plane, the Zeeman energy h must be greater than $2SK_z$. This requirement holds for all rotation angles since the competing anisotropy term is largest for the in-plane spin alignment. The obtained expression for the magnon dispersion is general and holds for an arbitrary spin direction. For the sake of simplicity, let's consider the case where $\vartheta = 0$. In this scenario, the newly defined variables simplifies to

$$|Q_z| = \sin^2(\theta), \quad \Delta' = h + ((2S-1)\cos^2(\theta) - S\sin^2(\theta))K_z \\ O_{x3} = \sin(\theta)\cos(\phi), \quad O_{y3} = \sin(\theta)\sin(\phi), \quad O_{z3} = \cos(\theta).$$

It is evident that the contribution of each component of the DM vector to the dispersion is determined by its projection onto the spins, which is expressed by O_{x3}, O_{y3} and O_{z3}. When the spins are parallel to the plane ($\theta = \pi/2$), only the in-plane components of the DM vector affect the dispersion, whereas if the spins are tilted from the plane and the in-plane components are zero, the dispersion is affected only by the projection of the out-of-plane component, $\cos(\theta)D_z^{\mathrm{nnn}}$. The next step is to explore the impact of the two different next-nearest neighbour DM vectors on the magnon dispersion.

DM vector tilted along the x-axis

With the obtained expression for $D_k^{\mathrm{nnn},t}$, we expand around the $\Gamma-$point and find a quadratic dispersion on the form

$$E_k^- \approx \sqrt{\Delta'^2 - S^2K_z^2|Q_z|^2} + \frac{1}{4}\frac{\tilde{J}S\Delta'}{\sqrt{\Delta'^2 - S^2K_z^2|Q_z|^2}}(ka)^2.$$

The relationship between the magnon energy gap (Δ) and the angles can be described as follows when $\vartheta = 0$

$$\Delta = \sqrt{\Delta'^2 - S^2 K_z^2 |Q_z|^2}$$
$$= \left(h^2 - 2hSK_z + 2K_z \cos^2(\theta)((3S-1)h - S(2S-1)K_z) + \cos^4(\theta)(2S-1)(4S-1)K_z^2\right)^{1/2},$$

where it is easily seen that $h > 2SK_z$ for $\theta = \pi/2$. Furthermore, the band gap that opens up at the K-point is given by

$$\Delta_K = E^+_{k=K} - E^-_{k=K} = 2S|D^{\mathrm{nnn},t}_{k=K}| = 6\sqrt{3}|O_{x3}D^{\mathrm{nnn}}_x + O_{y3}D^{\mathrm{nnn}}_y + O_{z3}D^{\mathrm{nnn}}_z|. \tag{6.6}$$

The contribution to the band gap comes from the projection of both the in-plane and out-of-plane components of the DM vector onto the spins, indicating that a band gap is expected for any spin orientation in the plane, provided that the DM vector has an in-plane component along the same axis. To illustrate this further, Figures 6.1a, 6.1b, 6.1c and 6.1d demonstrate the magnon dispersion

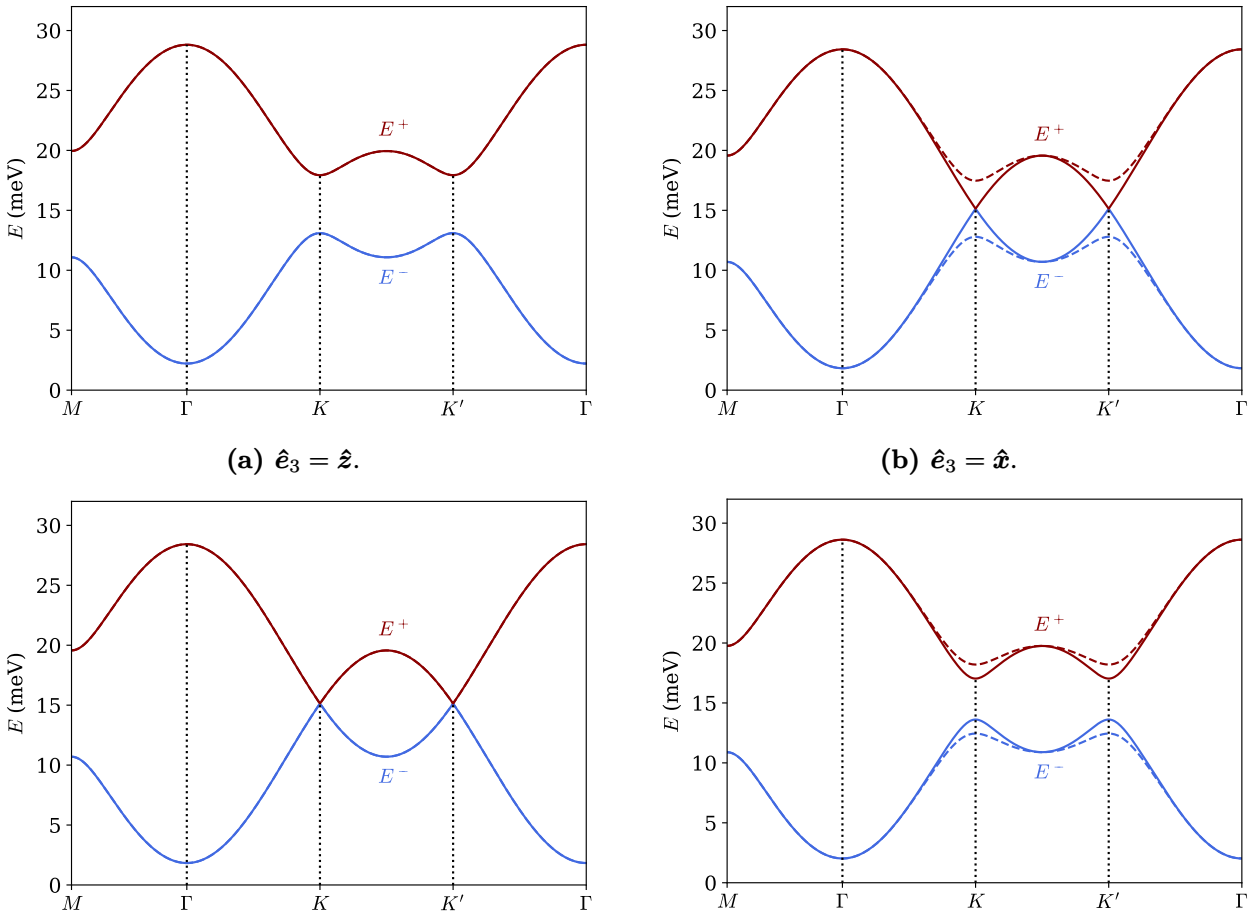

(a) $\hat{\boldsymbol{e}}_3 = \hat{\boldsymbol{z}}$. **(b)** $\hat{\boldsymbol{e}}_3 = \hat{\boldsymbol{x}}$.

(c) $\hat{\boldsymbol{e}}_3 = \hat{\boldsymbol{y}}$. **(d)** $\hat{\boldsymbol{e}}_3 = (1/2)[1, 1, \sqrt{2}]^T$.

Figure 6.1.: The figures display the magnon dispersion in a ferromagnetic honeycomb lattice for different orientations of the magnetization, $\hat{\boldsymbol{e}}_3$. The calculations are done with a NNN DM vector, $\boldsymbol{D}^{\mathrm{nnn},t}_{ij}$, that is perpendicular to the plane $[D^{\mathrm{nnn}}_x, D^{\mathrm{nnn}}_y, D^{\mathrm{nnn}}_z] = [0.0, 0.0, 0.31]$meV (solid lines) and tilted $[0.3, 0.0, 0.31]$meV (dashed lines). Other parameters include $\tilde{J} = 2.955$ meV, $K_z = 0.109$ meV, $h = 2$meV and $S = 3/2$.

for various spin directions $\hat{\boldsymbol{e}}_3$, and in each of these figures, the effects of the in-plane portion of the DM vector are clarified by computing the dispersion with a perpendicular next-nearest neighbour DM vector, and a DM vector that is tilted towards the $x-$axis. Our analysis employ specific parameters for the magnon dispersion in CrI_3 that have been measured or calculated, including $\tilde{J} = 2.955\text{meV}$, $K_z = 0.109\text{meV}$, $D_z^{\text{nnn}} = 0.31\text{meV}$ and $S = 3/2$ [82]. Moreover, we choose the remaining values as $h = 2\text{meV}$ and $D_x^{\text{nnn}} = 0.3\text{meV}$. In the perpendicular spin alignment, we obtain the dispersion found in section 3.3.2 since the in-plane DM components yield no contribution. When comparing the band gap of spin alignments along $\hat{\boldsymbol{x}}$ and $\hat{\boldsymbol{y}}$, the gap closes for $\hat{\boldsymbol{y}}$ because they are orthogonal to the DM vector, but opens along $\hat{\boldsymbol{x}}$ because D_x^{nnn} is nonzero. If $\hat{\boldsymbol{e}}_3 = (1/2)[1, 1, \sqrt{2}]^T$, a DM vector tilted along the $x-$axis increase the band gap due to the in-plane DM vector component. However, if $D_x^{\text{nnn}} < 0$ with the same magnetization direction, a tilted DM vector results in a smaller band gap due to the negative contribution. By integrating the Berry curvature, which is computed using equation (5.4), across the Brillouin zone, we determine the Chern numbers associated with the topologically nontrivial magnon bands. Specifically, we find that the lower band possesses a Chern number of $C = +1$, while

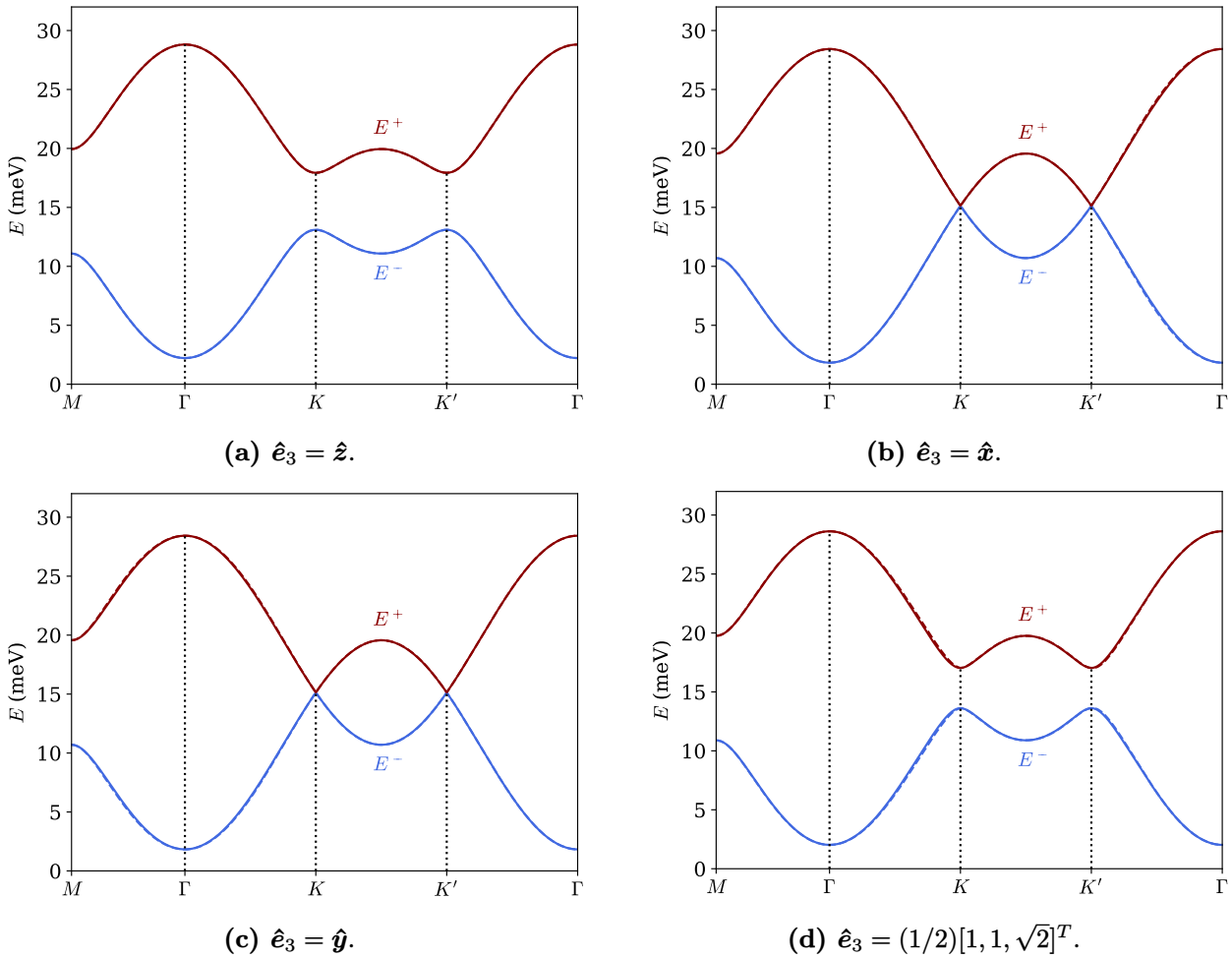

(a) $\hat{\boldsymbol{e}}_3 = \hat{\boldsymbol{z}}$.

(b) $\hat{\boldsymbol{e}}_3 = \hat{\boldsymbol{x}}$.

(c) $\hat{\boldsymbol{e}}_3 = \hat{\boldsymbol{y}}$.

(d) $\hat{\boldsymbol{e}}_3 = (1/2)[1, 1, \sqrt{2}]^T$.

Figure 6.2.: The figures display the magnon dispersion in a ferromagnetic honeycomb lattice for different orientations of the magnetization, $\hat{\boldsymbol{e}}_3$. The calculations are done with a NNN DM vector, $\boldsymbol{D}_{ij}^{\text{nnn},r}$, that is perpendicular to the plane $(D_{xy}^{\text{nnn}}, D_z^{\text{nnn}}) = (0.0, 0.31)\text{meV}$ (solid lines) and tilted $(D_{xy}^{\text{nnn}}, D_z^{\text{nnn}}) = (0.3, 0.31)\text{meV}$ (dashed lines) along the next-nearest neighbouring vectors. The remaining parameters consist of $\tilde{J} = 2.955\,\text{meV}$, $K_z = 0.109\,\text{meV}$, $h = 2\text{meV}$ and $S = 3/2$.

the upper band has a Chern number of $C = -1$, when the magnetization has a positive out-of-plane component. However, when the magnetization is tilted below the plane without any in-plane DM components, the bands touch and reopen, resulting in a phase transition where the Chern numbers of the bands interchange. A similar phenomenon occurs in the presence of D_x^{nnn}, but the angle at which the bands touch depends on the angle ϕ. In the $xz-$plane where $\phi = 0$, this angle is given by $\theta = \tan^{-1}(-D_z^{\text{nnn}}/D_x^{\text{nnn}})$.

At a constant magnetic field strength, the magnon energy gap gradually reduces as the spin alignment tilts towards the plane. This is because the anisotropy term favours a perpendicular alignment, so exciting magnons, which are deviations from the ferromagnetic ground state, requires less energy when the spins are in the plane.

DM vector directed along the next-nearest neighbours

The effect of the function $D_k^{\text{nnn},r}$ on the dispersion is more complex compared to a DM vector tilted along the $x-$axis, and it is not easy to understand its impact intuitively. Expanding the function around the $\Gamma-$point, we obtain

$$D_k^{\text{nnn},r} \approx -3D_{xy}^{\text{nnn}}(O_{x3}k_x + O_{y3}k_y),$$

suggesting that the DMI has no effect on the magnon energy gap, but has a stronger influence on the dispersion in the long wavelength limit compared to $D_k^{\text{nnn},t}$. The band gap at the symmetry point K is found to be

$$\Delta_K = 6\sqrt{3}|O_{z3}D_z^{\text{nnn}}|,$$

implying that the in-plane components have no effect on the band gap. This is in contrast to the other choice of DM vector, as stated in equation (6.6), and is in alignment with the observations done in the symmetry analysis.

The magnon dispersion for different spin directions is depicted in Figures 6.2a, 6.2b, 6.2c and 6.2d,

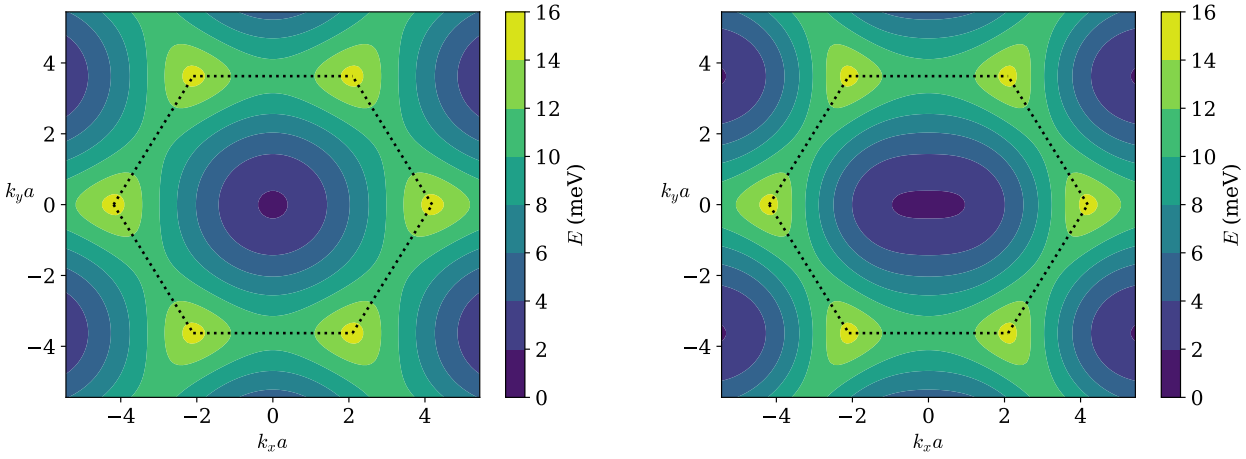

(a) $D_{xy}^{\text{nnn}} = 0.0$meV. **(b)** $D_{xy}^{\text{nnn}} = 1.2$meV.

Figure 6.3.: Contour plots of the lower magnon band for the case studied in Figure 6.2b, where the magnetization is directed along the $x-$axis. Figure a) and b) display the dispersion in the absence and presence of an in-plane next-nearest neighbour DMI, respectively.

using $\boldsymbol{D}_{ij}^{\text{nnn},r}$ as the DM vector. We examine the influence of in-plane components by displaying the dispersion using two DM vectors: $(D_{xy}^{\text{nnn}}, D_z^{\text{nnn}}) = (0.0, 0.31)\text{meV}$ and $(D_{xy}^{\text{nnn}}, D_z^{\text{nnn}}) = (0.3, 0.31)\text{meV}$. The other parameters remain the same. The in-plane component of the DM vector has a relatively small impact on the magnon dispersion, causing only a slight deviation from the perpendicular DM vector along the symmetry lines and leaving the magnon energy gap and band gap unaffected. However, we do observe that the in-plane component of the DM vector introduces an asymmetry in the magnon dispersion when the magnetization has in-plane components. This asymmetry becomes apparent in the differences observed along the symmetry lines $\Gamma \to K$ and $\Gamma \to K'$. More specifically, the presence of the in-plane component disturbs the rotational symmetry of the magnon dispersion, resulting in contour plots that display a more elongated shape. Figure 6.3 provides a clear illustration of this effect by comparing the cases with and without an in-plane next-nearest neighbour DM vector when the magnetization is directed along the x-axis. Additionally, it is important to note that the bands retain their reciprocal nature even when there is an in-plane next-nearest neighbour DMI present.

As the in-plane part of $\boldsymbol{D}_{ij}^{\text{nnn},r}$ does not create a band gap, the magnon bands are topologically trivial when the magnetization lies within the plane. Furthermore, when the magnetization is tilted away from the plane and D_z^{nnn} is nonzero, the in-plane components do not affect the Chern numbers. Therefore, we still observe $C = 1$ for the E_k^- branch and $C = -1$ for the E_k^+ branch when the magnetization has a positive out-of-plane component.

6.2.3. Nearest neighbour DMI

We are going to calculate the nearest neighbour DMI contribution for an arbitrary spin direction. As shown in equation (6.3), the DMI term retains the same form in the new frame of reference. We rotate the DM vector to

$$\boldsymbol{D}_{ij}^{\text{nn}\prime} = O^T \boldsymbol{D}_{ij}^{\text{nn}} = \begin{bmatrix} D_{ij,1}^{\text{nn}\ \prime} \\ D_{ij,2}^{\text{nn}\ \prime} \\ D_{ij,3}^{\text{nn}\ \prime} \end{bmatrix},$$

and employ the Holstein-Primakoff such that the nearest neighbour DMI contribution becomes

$$\begin{aligned} \mathcal{H}_{\text{DMI,nn}} = &\sum_{\substack{<<i,j>> \\ i\in A}} \left[S\sqrt{\frac{S}{2}}(D_{ij,2}^{\text{nn}\ \prime} + \mathrm{i}D_{ij,1}^{\text{nn}\ \prime})(a_i - b_{i+\delta_A}) + \text{h.c} + \mathrm{i}SD_{ij,3}^{\text{nn}\ \prime}(a_i^\dagger b_{i+\delta_A} - b_{i+\delta_A}^\dagger a_i) \right] \\ &+ A \leftrightarrow B. \end{aligned}$$

After discarding the terms of first order, we are left with

$$\begin{aligned} \mathcal{H}_{\text{DMI,nn}} =& \frac{\mathrm{i}}{2} S \sum_{\substack{i,\delta_A \\ i\in A}} D_{\delta_A,3}^{\text{nn}\ \prime}(a_i^\dagger b_{i+\delta_A} - b_{i+\delta_A}^\dagger a_i) + \frac{\mathrm{i}}{2} S \sum_{\substack{i,\delta_B \\ i\in B}} D_{\delta_B,3}^{\text{nn}\ \prime}(b_i^\dagger a_{i+\delta_B} - a_{i+\delta_B}^\dagger b_i) \\ =& \frac{\mathrm{i}}{2} S \sum_{k,\delta_A} \left[(D_{\delta_A,3}^{\text{nn}\ \prime} - D_{-\delta_A,3}^{\text{nn}\ \prime}) \mathrm{e}^{\mathrm{i}\boldsymbol{k}\cdot\boldsymbol{\delta}_A} a_k^\dagger b_k - (D_{\delta_A,3}^{\text{nn}\ \prime} - D_{-\delta_A,3}^{\text{nn}\ \prime}) \mathrm{e}^{-\mathrm{i}\boldsymbol{k}\cdot\boldsymbol{\delta}_A} b_k^\dagger a_k \right] \\ =& S \sum_k \left[D_k^{\text{nn}} a_k^\dagger b_k + D_k^{\text{nn}*} b_k^\dagger a_k \right], \end{aligned}$$

where we used that $\boldsymbol{\delta}_i^A = -\boldsymbol{\delta}_i^B$ for $i = 1, 2, 3$. Furthermore, we have introduced the function D_k^{nn}, which, upon evaluation, is on the following form

$$
\begin{aligned}
D_k^{\mathrm{nn}} =& \frac{\mathrm{i}}{2}\sum_{\delta_A}(D_{\delta_A,3}^{\mathrm{nn}\,\prime} - D_{-\delta_A,3}^{\mathrm{nn}\,\prime})\mathrm{e}^{\mathrm{i}\boldsymbol{k}\cdot\boldsymbol{\delta}_A} \\
=& \mathrm{i}D_{xy}^{\mathrm{nn}}\sum_{\delta_A}(O_{x3}\hat{\delta}_{Ay} - O_{y3}\hat{\delta}_{Ax})\mathrm{e}^{\mathrm{i}\boldsymbol{k}\cdot\boldsymbol{\delta}_A} \\
=& \mathrm{i}D_{xy}^{\mathrm{nn}}\left[O_{x3}\mathrm{e}^{\frac{\mathrm{i}}{\sqrt{3}}k_y a} - (\sqrt{3}\mathrm{i}\sin(\frac{1}{2}k_x a)O_{y3} + \cos(\frac{1}{2}k_x a)O_{x3})\mathrm{e}^{-\mathrm{i}\frac{k_y a}{2\sqrt{3}}}\right].
\end{aligned}
$$

It is important to mention that the out-of-plane component of the DM vector is canceled out and does not affect the dispersion. However, it can still play a role in magnon-phonon coupling. By expanding the definition of t_k to $t_k = \tilde{J}Sf_{\delta_A}(\boldsymbol{k}) - SD_k^{\mathrm{nn}}$, the energy spectrum is obtained by computing the eigenvalues of $\sigma_3 H_{\mathrm{m}}(\boldsymbol{k})$, as given in equation (6.5). Numerical methods are employed to find the eigenvalues due to the fourth order equation that arises. Additionally, it should be noted that t_k now satisfies $t_{-k}^* = \tilde{J}Sf_{\delta_A}(\boldsymbol{k}) + SD_k^{\mathrm{nn}} \neq t_k$.

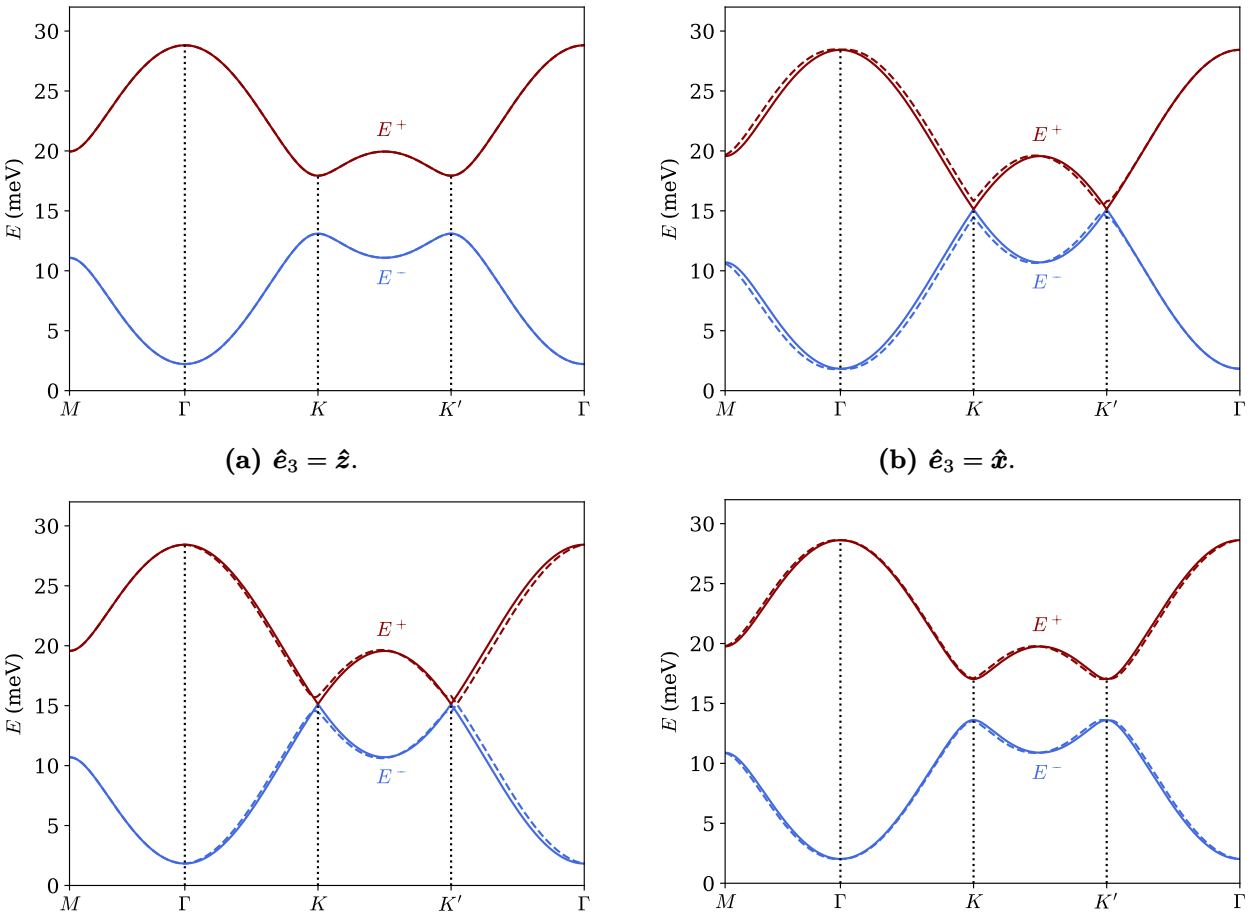

(a) $\hat{\boldsymbol{e}}_3 = \hat{\boldsymbol{z}}$. **(b)** $\hat{\boldsymbol{e}}_3 = \hat{\boldsymbol{x}}$.

(c) $\hat{\boldsymbol{e}}_3 = \hat{\boldsymbol{y}}$. **(d)** $\hat{\boldsymbol{e}}_3 = (1/2)[1, 1, \sqrt{2}]^T$.

Figure 6.4.: The figures display the magnon dispersion in a ferromagnetic honeycomb lattice for different orientations of the magnetization, $\hat{\boldsymbol{e}}_3$. The calculations are done without (solid lines) and with (dashed lines), a nearest neighbour DMI of magnitude $D_{xy}^{\mathrm{nn}} = 0.3\mathrm{meV}$. Other parameters include $\tilde{J} = 2.955\,\mathrm{meV}$, $K_z = 0.109\,\mathrm{meV}$, $h = 2\mathrm{meV}$, $S = 3/2$, and we also include a perpendicular NNN DMI with the strength $D_z^{\mathrm{nnn}} = 0.31\mathrm{meV}$.

Similar to the previous cases, we present the magnon dispersion for different spin directions and compare the outcomes. Figures 6.4a, 6.4b, 6.4c and 6.4d display the dispersions for each spin orientation with and without a nearest neighbour DMI of magnitude $D_{xy}^{\text{nn}} = 0.3\text{meV}$. We use similar parameters as earlier where we also include the intrinsic out-of-plane next-nearest neighbour DMI, $D_z^{\text{nnn}} = 0.31\text{meV}$. When the magnetization is perpendicular to the plane, the nearest neighbour DMI has no effect on the dispersion, as shown in Figure 6.4a. However, for magnetizations that are not perpendicular to the plane, a gap appears at the symmetry points K and K', and the branches exhibit nonreciprocal behaviour. To observe how the asymmetry arises in the dispersion, it is useful to examine the dispersion across the entire Brillouin zone. We consider the lower band and present contour plots of the dispersion. Without the nearest neighbour DMI, the dispersion is independent of the spin orientation in the plane, as illustrated in Figure 6.5a. Figures 6.5b and 6.5c depict the dispersion when the spins are oriented along $\hat{\boldsymbol{x}}$ and $\hat{\boldsymbol{y}}$, respectively, with $D_{xy}^{\text{nn}} = 0.3\text{meV}$. It is evident that the presence of nearest

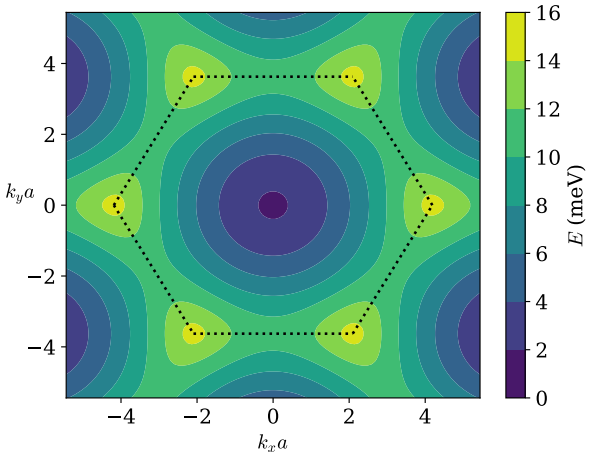

(a) $D_{xy}^{\text{nn}} = 0.0\text{meV}$ and $\hat{\boldsymbol{e}}_3 = \hat{\boldsymbol{x}}$.

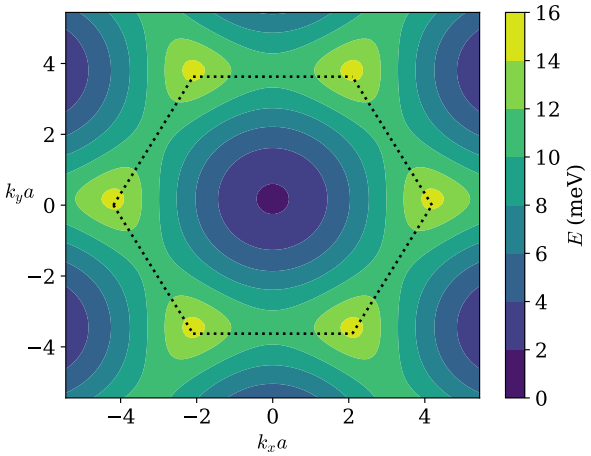

(b) $D_{xy}^{\text{nn}} = 0.3\text{meV}$ and $\hat{\boldsymbol{e}}_3 = \hat{\boldsymbol{x}}$.

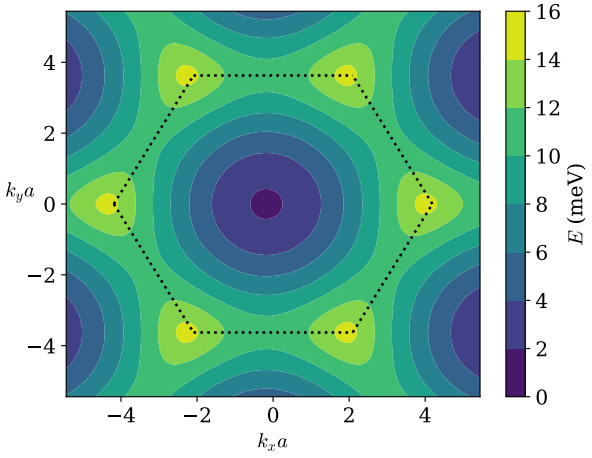

(c) $D_{xy}^{\text{nn}} = 0.3\text{meV}$ and $\hat{\boldsymbol{e}}_3 = \hat{\boldsymbol{y}}$.

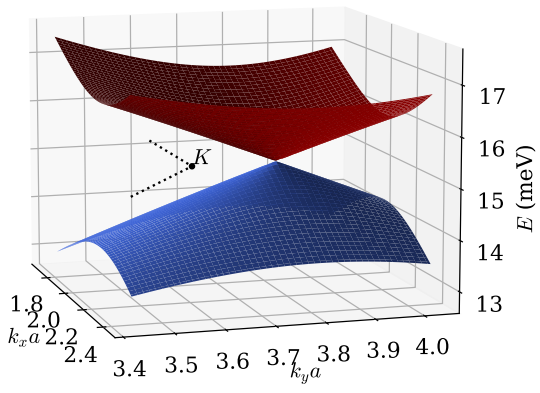

(d) $D_{xy}^{\text{nn}} = 0.3\text{meV}$ and $\hat{\boldsymbol{e}}_3 = \hat{\boldsymbol{x}}$.

Figure 6.5.: Contour plots in Figure a)-c) show the dispersion of the lower band $E_{\boldsymbol{k}}^{-}$ across the Brillouin zone with varying magnetization directions $\hat{\boldsymbol{e}}_3$ and D_{xy}^{nn} values. Figure d) displays a 3D-plot of the two bands around the $K-$point in the presence of nearest neighbour DMI. We have excluded the next-nearest neighbour DMI from the analysis and the remaining parameters are: $\tilde{J} = 2.955\,\text{meV}$, $K_z = 0.109\,\text{meV}$, $h = 2\text{meV}$ and $S = 3/2$.

neighbour DMI causes a shift in the energy spectrum within the Brillouin zone. The direction of the shift depends on the magnetization direction. For a magnetization along $\hat{\boldsymbol{x}}$ and $D_{xy}^{\mathrm{nn}} > 0$, the shift is towards $+\hat{\boldsymbol{k}}_y$, while for a magnetization along $\hat{\boldsymbol{y}}$, the shift is towards $-\hat{\boldsymbol{k}}_x$. This shift accounts for the asymmetry in the magnon dispersion along the symmetry lines of the Brillouin zone.

According to the argument that the nearest neighbour DMI only causes a shift in the dispersion, the band gap is expected to disappear in the absence of a perpendicular next-nearest neighbour DMI or when the magnetization is solely in the lattice plane. This is shown in Figure 6.5d, which uses the same parameters as in Figure 6.5b, where the Dirac point is shifted from the K symmetry point. Hence, in this scenario, the presence of a gap at the K and K' points does not necessarily indicate the existence of topologically gapped bands. This finding contradicts the previous symmetry analysis, where a band gap due to the nearest neighbour DMI was expected as long as the magnetization had out-of-plane components. The reason for this discrepancy is that the breaking of effective time-reversal symmetry is not evident in the harmonic theory and only becomes apparent when we include the third-order terms and renormalize the magnon energy spectrum [16]. Conversely, when there is a perpendicular next-nearest neighbour DMI present and the magnetization is tilted away from the plane to create a band gap, the energy spectrum shift does not impact the Chern numbers of the bands.

6.3. Comparison between Dzyaloshinskii-Moriya and Kitaev interactions

The band gap observed in the magnon dispersion can be generated not only by the Dzyaloshinskii-Moriya interaction but also by other exchange interactions, such as Kitaev interactions or off-diagonal symmetric exchange [47, 85]. Kitaev interactions are naturally found in two-dimensional honeycomb lattices with edge-sharing octahedrally coordinated transition metals, such as in CrI_3. In these materials, the Kitaev interaction arises due to the strong spin-orbit coupling of the heavy ligands, which results in competing pathways for the exchange coupling [86]. However, determining the underlying interaction in a material can be challenging. For example, in CrI_3, some reports suggest that the Kitaev interaction generates the band gap [86], while other suggests that the DMI is responsible for producing the Dirac gaps [13]. The objective of this section is to calculate the magnon dispersion in a ferromagnetic honeycomb lattice for an arbitrary magnetization direction, including Kitaev interactions, and see how the gap opening emerges. Lastly, we perform a brief comparison to the case where DMI is present.

We apply a strong external magnetic field to align the ground state spin direction with the direction of the magnetic field. We follow the previously outlined methodology in section 6.2.2. By including the Heisenberg exchange interaction, together with the Kitaev interaction, the Hamiltonian can be expressed as follows [87]

$$\mathcal{H} = -\sum_{<i,j>\in\gamma} \tilde{\boldsymbol{S}}_i^T H_{K,\gamma} \tilde{\boldsymbol{S}}_j,$$

$$H_{K,\xi} = \begin{bmatrix} J+K & 0 & 0 \\ 0 & J & 0 \\ 0 & 0 & J \end{bmatrix}, \quad H_{K,\eta} = \begin{bmatrix} J & 0 & 0 \\ 0 & J+K & 0 \\ 0 & 0 & J \end{bmatrix}, \quad H_{K,\zeta} = \begin{bmatrix} J & 0 & 0 \\ 0 & J & 0 \\ 0 & 0 & J+K \end{bmatrix},$$

with K as the Kitaev interaction strength. The notation $< i,j >\in \gamma$ symbolizes the nearest neighbouring bonds between sublattice A and B, and the spins are written in the local Kitaev frame $\{\hat{\boldsymbol{\xi}}, \hat{\boldsymbol{\eta}}, \hat{\boldsymbol{\zeta}}\}$. The neighbouring bonds are denoted by $\gamma \in \{\xi, \eta, \zeta\}$, which corresponds to the previously used notation $\{\delta_2^A, \delta_3^A, \delta_1^A\}$, respectively. Taking CrI_3 as an example, each Cr-Cr bond has an associated Kitaev

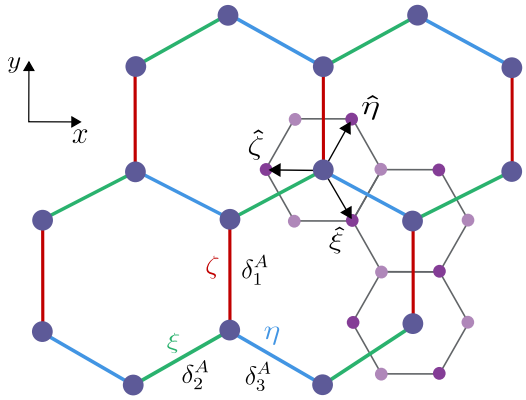

Figure 6.6.: Illustration of a honeycomb network where the magnetic ions are in a edge-sharing octahedral environment, as shown for three ions on the right hand side. Using CrI_3 as an illustration, the blue circles are Cr^{3+} ions, the dark purple are I^- ions above the plane while the light purple are I^- below the plane. The Kitaev axes $\{\hat{\boldsymbol{\xi}}, \hat{\boldsymbol{\eta}}, \hat{\boldsymbol{\zeta}}\}$ are shown with arrows, directed towards the I^- ions above the plane. The neighbouring Cr-Cr bonds $\{\xi, \eta, \zeta\}$, marked with green, blue and red respectively are shown together with the previously used notation $\{\delta_1^A, \delta_2^A, \delta_3^A\}$ for the same bonds. The illustration is inspired by Ref. [86].

axis directed towards the intermediate I^- ion, based on the direction of the super-exchange path. The geometry of the system is further explained in Figure 6.6. The position of these Kitaev axes relative to the Cartesian (crystallographic) axes is given by [87]

$$\hat{\boldsymbol{\xi}} = [\frac{1}{\sqrt{6}}, -\frac{1}{\sqrt{2}}, \frac{1}{\sqrt{3}}]^T, \quad \hat{\boldsymbol{\eta}} = [\frac{1}{\sqrt{6}}, \frac{1}{\sqrt{2}}, \frac{1}{\sqrt{3}}]^T, \quad \hat{\boldsymbol{\zeta}} = [-\frac{\sqrt{6}}{3}, 0, \frac{1}{\sqrt{3}}]^T,$$

suggesting that the spins in the Cartesian frame are related to the spins in the Kitaev frame via $\tilde{\boldsymbol{S}}_i = U_K \boldsymbol{S}_i$, where U_K is an orthogonal matrix containing $\hat{\boldsymbol{\xi}}$, $\hat{\boldsymbol{\eta}}$ and $\hat{\boldsymbol{\zeta}}$ as rows. By performing this transformation, we obtain the following expression for the Hamiltonian

$$\mathcal{H} = -\sum_{<i,j>\in\gamma} \boldsymbol{S}_i^T H_{C,\gamma} \boldsymbol{S}_j,$$

with $H_{C,\gamma} = U_K^T H_{K,\gamma} U_K$. Computing the matrices for each bond, the summation may be written compactly as [88]

$$\mathcal{H} = -J' \sum_{<i,j>\in\gamma} \boldsymbol{S}_i \cdot \boldsymbol{S}_j + \frac{1}{3} K \sum_{<i,j>\in\gamma} \boldsymbol{S}_i^T W^\gamma \boldsymbol{S}_j,$$

$$W^\gamma = \begin{bmatrix} -c_{\phi_\gamma} & s_{\phi_\gamma} & \sqrt{2}c_{\phi_\gamma} \\ s_{\phi_\gamma} & c_{\phi_\gamma} & \sqrt{2}s_{\phi_\gamma} \\ \sqrt{2}c_{\phi_\gamma} & \sqrt{2}s_{\phi_\gamma} & 0 \end{bmatrix},$$

where $J' = J + \frac{1}{3}K$, $c_{\phi_\gamma} = \cos(\phi_\gamma)$, $s_{\phi_\gamma} = \sin(\phi_\gamma)$ and $\phi_\gamma = 0, 2\pi/3, 4\pi/3$ for $\gamma = \zeta, \xi, \eta$ bonds respectively. The first term represents a scaling of the isotropic Heisenberg exchange coupling coefficient, while the second term introduces anisotropic contributions. The first term was treated in section 6.2.2, so we will further investigate the last term. We remember that the spins are rotated according to the direction of the magnetic field, and that the transformation to this basis is done via $\boldsymbol{S}_i = O\boldsymbol{S}'_i$. The matrix multiplication in the second term can then be expressed as $\boldsymbol{S'}_i^T M^\gamma \boldsymbol{S'}_j$, where $M^\gamma = O^T W^\gamma O$. We notice that the summation over each sublattice is identical because both

spins on sublattice A and B are projected onto the same Kitaev axis. Therefore, we only need to sum over sublattice A to simplify the calculations. By using the Holstein-Primakoff transformation and retaining only second-order terms, the resulting expression is as follows

$$\mathcal{H}_K = \frac{1}{3}KS \sum_{\substack{<i,j>\in\gamma \\ i\in A}} \left[-M_{33}^{\gamma}(a_i^{\dagger}a_i + b_j^{\dagger}b_j) + \frac{1}{2}M_{+}^{\gamma}a_i^{\dagger}b_j + \text{h.c} + \frac{1}{2}M_{-}^{\gamma}a_i b_j + \text{h.c} \right],$$

where

$$\begin{aligned} M_{\pm}^{\gamma} &= M_{11}^{\gamma} \pm M_{22}^{\gamma} - \mathrm{i}(M_{12}^{\gamma} \mp M_{21}^{\gamma}), \\ \implies M_{+}^{\gamma} &= c_{\phi_\gamma}(\Gamma_{yy} - \Gamma_{xx} + 2\sqrt{2}\Gamma_{xz}) + 2s_{\phi_\gamma}(\Gamma_{xy} + \sqrt{2}\Gamma_{yz}), \\ \implies M_{-}^{\gamma} &= c_{\phi_\gamma}(O_y^2 - O_x^2 + 2\sqrt{2}O_xO_z) + 2s_{\phi_\gamma}(O_xO_y + \sqrt{2}O_yO_z). \end{aligned}$$

We defined the quantities $\Gamma_{\mu\nu} = O_{\mu 1}O_{\nu 1} + O_{\mu 2}O_{\nu 2}$ and $O_\mu = O_{\mu 1} - \mathrm{i}O_{\mu 2}$ for shorthand notation. By inserting the Fourier-transformed magnon operators, we obtain

$$\mathcal{H}_K = \frac{1}{3}KS \sum_{k} \sum_{\{\delta_A,\gamma\}} \left[-M_{33}^{\gamma}(a_k^{\dagger}a_k + b_k^{\dagger}b_k) + \frac{1}{2}M_{+}^{\gamma}\mathrm{e}^{\mathrm{i}\boldsymbol{k}\cdot\boldsymbol{\delta}_A}a_k^{\dagger}b_k + \text{h.c} + \frac{1}{2}M_{-}^{\gamma}\mathrm{e}^{-\mathrm{i}\boldsymbol{k}\cdot\boldsymbol{\delta}_A}a_k b_{-k} + \text{h.c} \right],$$

where $\{\delta_A, \gamma\}$ denotes a summation over the neighbouring bonds with the corresponding Kitaev axes. If we incorporate this term into the total Hamiltonian where we include the Heisenberg exchange interactions (both linear and biquadratic), the single-ion anisotropy and the Zeeman term, as in equation (6.4) without the DMI, the total Hamiltonian may be written

$$\begin{aligned} \mathcal{H} = \sum_k \Big[& t_0(a_k^{\dagger}a_k + b_k^{\dagger}b_k) - \tilde{t}_k a_k^{\dagger}b_k - \tilde{t}_k^{*}b_k^{\dagger}a_k - \frac{1}{2}SK_zQ_z(a_k a_{-k} + b_k b_{-k}) \\ & - \frac{1}{2}SK_zQ_z^{*}(a_k^{\dagger}a_{-k}^{\dagger} + b_k^{\dagger}b_{-k}^{\dagger}) + d_k a_k b_{-k} + d_k^{*}a_k^{\dagger}b_{-k}^{\dagger} \Big]. \end{aligned}$$

The newly defined coefficients are given by

$$\begin{aligned} t_0 = 3J'S + \Delta' - \frac{1}{3}KS \sum_{\{\delta_A,\gamma\}} M_{33}^{\gamma}, \quad \tilde{t}_k = J'Sf_{\delta_A}(\boldsymbol{k}) - \frac{1}{6}KS \sum_{\{\delta_A,\gamma\}} M_{+}^{\gamma}\mathrm{e}^{\mathrm{i}\boldsymbol{k}\cdot\boldsymbol{\delta}_A}, \\ d_k = \frac{1}{6}KS \sum_{\{\delta_A,\gamma\}} M_{-}^{\gamma}\mathrm{e}^{-\mathrm{i}\boldsymbol{k}\cdot\boldsymbol{\delta}_A}, \end{aligned}$$

with $J' = J + 2\Lambda S(S-1) + K/3$. This expression for the Hamiltonian aligns with the findings in Ref. [86] for spin ordering in the out-of-plane direction. By summing over the nearest neighbours, we obtain the following coefficients

$$
\begin{aligned}
t_0 =& 3J'S + \Delta', \\
\tilde{t}_k =& J'Sf_{\delta_A}(\boldsymbol{k}) - \frac{KS}{6}\Big[(\Gamma_{yy} - \Gamma_{xx} + 2\sqrt{2}\Gamma_{xz})\mathrm{e}^{\mathrm{i}\frac{k_y a}{\sqrt{3}}} - \mathrm{e}^{-\mathrm{i}\frac{k_y a}{2\sqrt{3}}}\Big((\Gamma_{yy} - \Gamma_{xx} + 2\sqrt{2}\Gamma_{xz})\cos(\frac{1}{2}k_x a) \\
&+ \mathrm{i}2\sqrt{3}(\Gamma_{xy} + \sqrt{2}\Gamma_{yz})\sin(\frac{1}{2}k_x a)\Big)\Big], \\
d_k =& \frac{KS}{6}\Big[(O_y^2 - O_x^2 + 2\sqrt{2}O_x O_z)\mathrm{e}^{-\mathrm{i}\frac{k_y a}{\sqrt{3}}} - \mathrm{e}^{\mathrm{i}\frac{k_y a}{2\sqrt{3}}}\Big((O_y^2 - O_x^2 + 2\sqrt{2}O_x O_z)\cos(\frac{1}{2}k_x a) \\
&- \mathrm{i}2\sqrt{3}(O_x O_y + \sqrt{2}O_y O_z)\sin(\frac{1}{2}k_x a)\Big)\Big].
\end{aligned}
$$

By using that $\tilde{t}_{-k} = \tilde{t}_k^*$, we can write the Hamiltonian in matrix notation on the form

$$
\mathcal{H} = \frac{1}{2}\sum_k \boldsymbol{\psi}_{\mathrm{m}}^\dagger(\boldsymbol{k}) H_{\mathrm{m,Kit}}(\boldsymbol{k}) \boldsymbol{\psi}_{\mathrm{m}}(\boldsymbol{k}), \quad \boldsymbol{\psi}_{\mathrm{m}}(\boldsymbol{k}) = [a_k, b_k, a_{-k}^\dagger, b_{-k}^\dagger]^T,
$$

$$
H_{\mathrm{m,Kit}}(\boldsymbol{k}) = \begin{bmatrix} t_0 & -\tilde{t}_k & -SK_z Q_z^* & d_k^* \\ -\tilde{t}_k^* & t_0 & d_{-k}^* & -SK_z Q_z * \\ -SK_z Q_z & d_{-k} & t_0 & -\tilde{t}_k \\ d_k & -SK_z Q_z & -\tilde{t}_k^* & t_0 \end{bmatrix}.
$$

Solving the BdG system by computing the eigenvalues of $\sigma_3 H_{\mathrm{m,Kit}}(\boldsymbol{k})$, the positive eigenvalues are

$$
E_k^{\pm} = \frac{1}{\sqrt{2}}\left(-\tilde{A}_k \pm \sqrt{\tilde{A}_k^2 - 4\tilde{B}_k}\right)^{\frac{1}{2}},
$$

with the helping variables defined as

$$
\begin{aligned}
\tilde{A}_k =& -2t_0^2 - 2|\tilde{t}_k|^2 + 2S^2K_z^2|Q_z|^2 + |d_k|^2 + |d_{-k}|^2, \\
\tilde{B}_k =& (t_0^2 - |\tilde{t}_k|^2)^2 + S^2K_z^2|Q_z|^2(S^2K_z^2|Q_z|^2 - 2t_0^2 - 2|\tilde{t}_k|^2) - t_0^2(|d_k|^2 + |d_{-k}|^2) + |d_k|^2|d_{-k}|^2 \\
&+ 4t_0 SK_z \operatorname{Re}\left(\tilde{t}_k Q_z d_{-k}^* + \tilde{t}_k Q_z^* d_k\right) - 2\operatorname{Re}\left(\tilde{t}_k^2 d_k d_{-k}^*\right) - 2S^2K_z^2 \operatorname{Re}\left(Q_z^2 d_k^* d_{-k}^*\right).
\end{aligned}
$$

Figure 6.7a, 6.7c and 6.7e display the magnon dispersion along the symmetry lines of the Brillouin zone for the $\hat{\boldsymbol{x}}$, $\hat{\boldsymbol{y}}$ and $\hat{\boldsymbol{z}}$ magnetization directions. The parameters used in this analysis are taken from Ref. [86], specifically $J = 0.2$meV and $K = 5.2$meV which corresponds to the dispersion in bulk CrI_3. This results in an effective exchange coupling coefficient of $J' = J + K/3 = 1.94$meV. To facilitate comparison, we present the dispersion with and without Kitaev interaction, using the same effective exchange coupling coefficient. Other parameters utilized are $h = 2$meV, $K_z = 0.109$meV and $S = 3/2$. Moreover, Figure 6.7b, 6.7d and 6.7f show contour plots of the lower band E_k^- in the presence of Kitaev interactions for the respective magnetization directions. It should be noted that the strength of the Kitaev interaction remains a topic of debate, with some studies suggesting a value 25 times larger than J, while others propose a relative strength of 0.4 [88]. Additionally, the relative sign of the Kitaev interaction may change accordingly [11].

Figure 6.7e demonstrates that a gap opens up in the magnon dispersion when the magnetization is ordered out of the lattice plane and the Kitaev interaction is activated. In contrast, when the magnetization lies in the plane, it remains unclear if the band gaps close due to a shift of the extreme points away from the K and K' symmetry points. Thus, there may be gap closings that are not

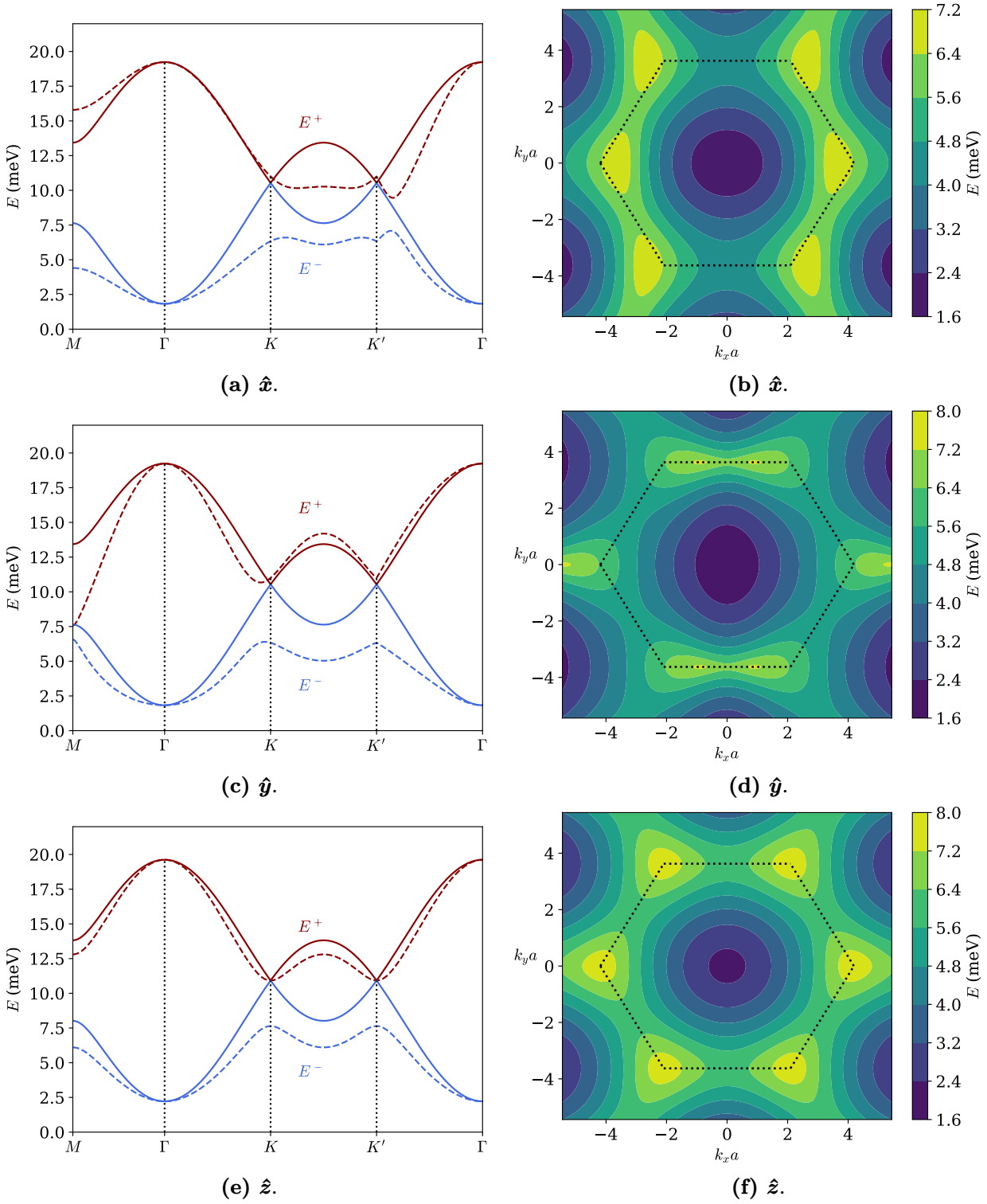

(a) $\hat{x}$. (b) $\hat{x}$. (c) $\hat{y}$. (d) $\hat{y}$. (e) $\hat{z}$. (f) $\hat{z}$.

Figure 6.7.: The figures in the left column display the magnon dispersion in a ferromagnetic honeycomb lattice for different magnetization orientations. The solid (dashed) lines indicate the dispersion without (with) Kitaev interactions, with a magnitude of $K = 5.2$meV. Both types of dispersion use the same effective exchange coupling coefficient, $J' = J + K/3 = 1.94$meV. The remaining parameters are $K_z = 0.109\,$meV, $h = 2$meV and $S = 3/2$. The right column depicts contour plots of the lower band, $E_{\boldsymbol{k}}^{-}$, using the same parameters, including Kitaev interaction.

apparent in the figures. A similar shift of the extreme points was observed in the presence of a nearest neighbour DMI. When comparing this shift to the one induced by the DMI, we observe that the latter results in a complete displacement of the entire energy spectrum in a particular direction, while the Kitaev interaction exhibits a more intricate characteristic with elongated contour plots that vary in size for magnetizations along the $\hat{\boldsymbol{x}}$ and $\hat{\boldsymbol{y}}$ directions. This elongated shape leads to a disruption of the rotational symmetry in the dispersion.

To examine the relationship between the gap and magnetization direction more closely, we investigate various planes and observe how the gap evolves with the tilting angle. Specifically, we consider four scenarios: tilting in the xz- and yz-plane as θ varies, in addition to magnetization directions in the $xy-$plane and the plane where $\theta = \pi/4$ as ϕ varies. We consider angles within the range $[0, \pi]$, and for each angle, we calculate the displacement of the extreme point from the K-point and determine the corresponding gap size. The results of this analysis are presented in Figure 6.8, where we also compare them to the case when the DMI is included. We employ two parameter sets: $J = 0.2$meV (without biquadratic exchange) and $K = 5.2$meV for the Kitaev case, and $\tilde{J} = 2.955$meV, $D_z^{\text{nnn}} = 0.31$meV and $D_{xy}^{\text{nn}} = 0.3$meV in the DMI case. The remaining parameters are left unchanged.

In the presence of the DMI, the size of the gap reaches its maximum when the magnetization is perpendicular to the lattice plane. As the magnetization tilts away from the perpendicular direction, the gap gradually decreases following a cosine function until it closes completely for parallel alignment with the lattice plane. This behaviour is observed in both the xz- and yz-plane. The shift is most significant when $\theta = \pi/2$ because the projection of the in-plane nearest neighbour DM vector onto the magnetization is largest at this angle. When examining the $xy-$plane and the plane where $\theta = \pi/4$ with a varying azimuthal angle ϕ, we observe an isotropic behaviour of the DMI-induced gap and shift. In these cases, both the displacement and the size of the gap remain independent of the angle ϕ.

In the case of Kitaev interactions, the gap closure occurs for two intermediate angles within the xz-plane, while in the yz-plane, it closes for three angles, including $\theta = \pi/2$. This implies that unlike DMI, the gap does not necessarily close for a magnetization lying in the plane. Comparing the gap sizes between $D_z^{\text{nnn}} = 0.31$meV and $K = 5.2$meV, we observe that the gap size increases more rapidly with DMI. Additionally, for the Kitaev interaction, there are noticeable differences when comparing the shift and gap size between the $xz-$ and $yz-$planes, where symmetric curves around $\theta = \pi/2$ is observed only in the $yz-$plane. This anisotropic behaviour is further illustrated when varying ϕ in the planes where $\theta = \pi/2$ and $\theta = \pi/4$. For magnetization directions in the plane, we observe gap closure when the magnetization aligns along both the neighbouring bonds associated with sublattices A and B. This explains why the gap closes for a magnetizations in the $\hat{\boldsymbol{y}}$ direction but not in the $\hat{\boldsymbol{x}}$ direction.

Based on this analysis, we can infer that in the presence of DMI, the band gap tends to close uniformly as the magnetization is tilted towards the plane, regardless of the in-plane magnetization components. However, in the presence of Kitaev interactions, a strong dependence on the in-plane magnetization components is expected. It is also important to note that in the absence of mirror symmetry breaking, where D_{xy}^{nn} is zero, the influence of the magnetization direction on the magnon dispersion is primarily limited to the vicinity of the K and K' symmetry points when an out-of-plane next-nearest neighbour DMI is present. In contrast, the impact of the magnetization direction extends beyond these points in the presence of Kitaev interactions. These observations are consistent with a study mentioned in Ref. [13], where the magnon dispersion in CrI_3 was measured using inelastic neutron scattering for both in-plane and out-of-plane magnetization directions.

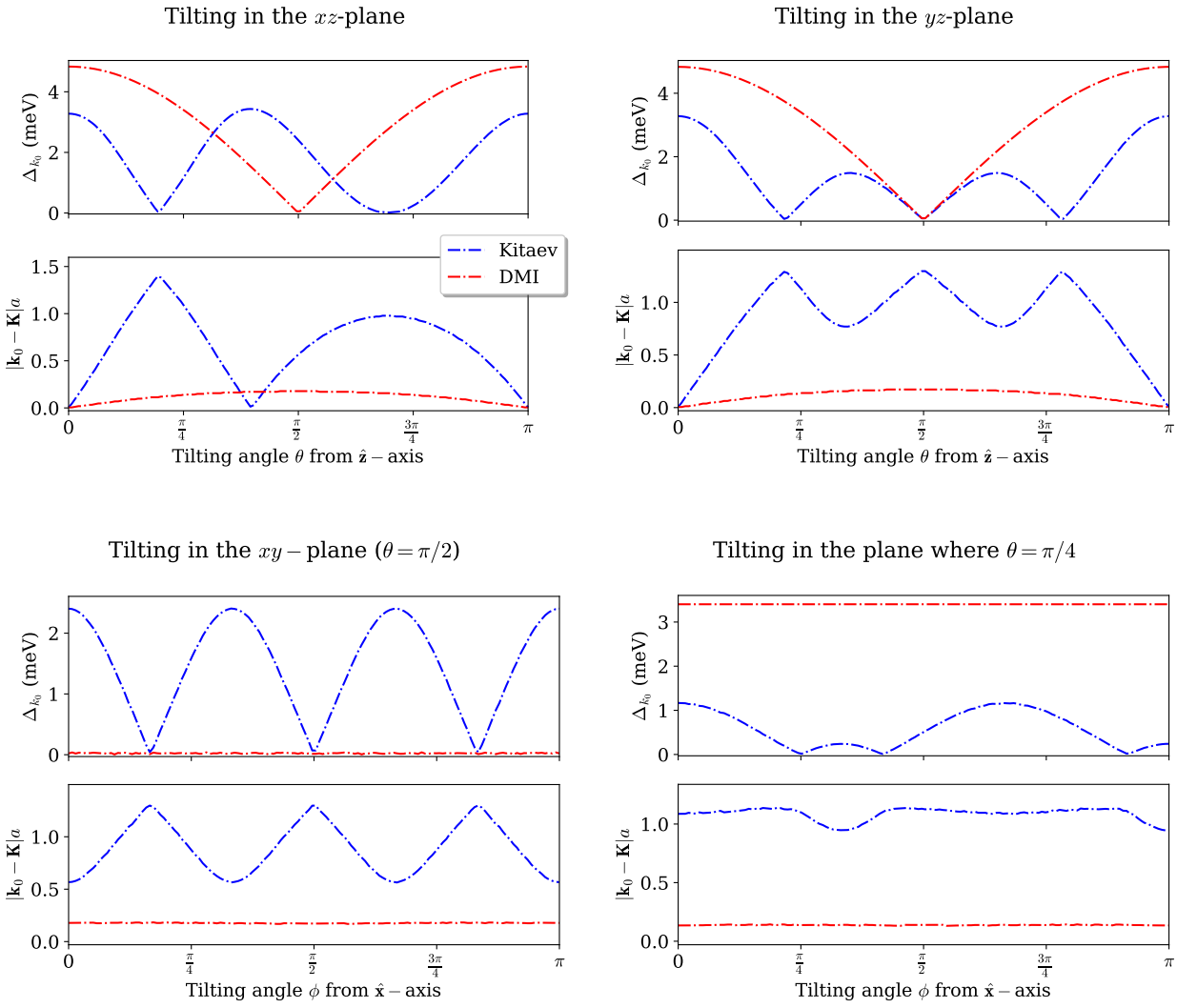

Figure 6.8.: The figures illustrate two quantities: the band gap ($\Delta_{\boldsymbol{k}_0}$) at the extreme points of the magnon dispersion, represented by $\boldsymbol{k}_0$ (maximum for the lower band and minimum for the upper band), and the displacement of these extreme points from the $K-$point ($|\boldsymbol{k}_0 - \boldsymbol{K}|a$). We examine four scenarios: varying the angle θ in the $xz-$ and $yz-$planes, and varying ϕ in the $xy-$plane and the plane where $\theta = \pi/4$. Each figure compares the effects of Kitaev interactions ($J = 0.2$meV and $K = 5.2$meV without considering biquadratic exchange) and DMI ($\tilde{J} = 2.955$meV, $D_z^{\text{nnn}} = 0.31$meV and $D_{xy}^{\text{nn}} = 0.3$meV). The other parameters are held constant for both cases, with $h = 2$meV, $K_z = 0.109$meV and $S = 3/2$.

CHAPTER 7

Hybridization in FM honeycomb layer with arbitrary magnetization direction

In this chapter, our goal is to analyze the magnetoelastic energy spectrum arising from bilinear coupling in a ferromagnetic honeycomb lattice, considering different magnetization directions. Building upon the spin-rotation techniques utilized in Chapter 6 to obtain the magnon dispersion for a general form of the Dzyaloshinskii-Moriya interaction, our calculations in this chapter bear similarities to those presented in Chapter 4. Furthermore, we will compute the Chern numbers of the magnon-polaron bands and compare them with those of the non-interacting system, in addition to investigate the Hall response to a temperature gradient.

7.1. Derivation of the magnetoelastic energy

The objective of this section is to derive the interacting Hamiltonian that arises from lattice vibrations in a ferromagnet. We employ a microscopic approach by conducting a Taylor expansion of the magnetic exchange interactions that depend on the lattice sites. We will not consider Kitaev interactions and solely focus on DMI, as previous chapters have shown, can generate bilinear coupling terms in the interacting Hamiltonian for collinear spin ordering. In addition, an anisotropy-based contribution to the magnetoelastic energy is included, as discussed in section 4.1.2. In section 6.2, two types of next-nearest neighbour DM vectors were introduced: one with arbitrary direction for the in-plane components, $\boldsymbol{D}_{ij}^{\mathrm{nnn},t}$, and the other with in-plane components directed along the next-nearest neighbours, $\boldsymbol{D}_{ij}^{\mathrm{nnn},r}$. It has been found that only the latter generates the lowest order of coupling terms, and therefore, will be used in the following analysis.

Contribution from the NNN DMI

We expressed the next-nearest neighbour DM vector in the following form

$$\boldsymbol{D}^{\mathrm{nnn},r}(\boldsymbol{r}_{ij}) = -\eta_{ij} D_{xy}^{\mathrm{nnn}}(\boldsymbol{r}_{ij})\hat{\boldsymbol{r}}_{ij} + \nu_{ij} D_{z}^{\mathrm{nnn}}(\boldsymbol{r}_{ij})\hat{\boldsymbol{z}}.$$

By Taylor expanding the interaction strengths $D_{xy}^{\mathrm{nnn}}(\boldsymbol{r}_{ij})$, $D_{z}^{\mathrm{nnn}}(\boldsymbol{r}_{ij})$ and the unit vector $\hat{\boldsymbol{r}}_{ij}$ around the equilibrium position $\boldsymbol{R}_{ij}$, the vector can be expressed as a first-order approximation in terms of the ionic displacement as

$$\begin{aligned}
\boldsymbol{D}^{\mathrm{nnn},r}(\boldsymbol{r}_{ij}) \approx & \boldsymbol{D}^{\mathrm{nnn},r}(\boldsymbol{R}_{ij}) - \eta_{ij}\frac{D_{xy}^{\mathrm{nnn}}(\boldsymbol{R}_{ij})}{|\boldsymbol{R}_{ij}|}\left(\boldsymbol{u}_{ij} - (\hat{\boldsymbol{R}}_{ij}\cdot\boldsymbol{u}_{ij})\hat{\boldsymbol{R}}_{ij}\right) \\
& - \eta_{ij}\left(\nabla_{\boldsymbol{r}_{ij}} D_{xy}^{\mathrm{nnn}}(\boldsymbol{r}_{ij})\Big|_{\boldsymbol{R}_{ij}}\cdot\boldsymbol{u}_{ij}\right)\hat{\boldsymbol{R}}_{ij} + \nu_{ij}\left(\nabla_{\boldsymbol{r}_{ij}} D_{z}^{\mathrm{nnn}}(\boldsymbol{r}_{ij})\Big|_{\boldsymbol{R}_{ij}}\cdot\boldsymbol{u}_{ij}\right)\hat{\boldsymbol{z}} \\
\approx & \boldsymbol{D}^{\mathrm{nnn},r}(\boldsymbol{R}_{ij}) - \eta_{ij}\frac{D_{xy}^{\mathrm{nnn}}(\boldsymbol{R}_{ij})}{|\boldsymbol{R}_{ij}|}\left(\boldsymbol{u}_{ij} - (\hat{\boldsymbol{R}}_{ij}\cdot\boldsymbol{u}_{ij})\hat{\boldsymbol{R}}_{ij}\right),
\end{aligned}$$

where we only keep the dominant terms, assuming the derivatives make negligible contributions. This is the reason why we have chosen to use this type of DM vector instead of $\boldsymbol{D}_{ij}^{\mathrm{nnn},t}$, where all the

first-order terms in the ionic displacement involve derivatives. The last term makes a contribution to the interacting Hamiltonian, given by

$$\mathcal{H}_{\text{int}}^{\text{D,nnn}} = \sum_{<<i,j>>} \sum_{\mu,\nu} (u_{i\mu} - u_{j\mu}) \eta_{ij} \frac{D_{xy}^{\text{nnn}}}{R_{ij}} \left(\delta_{\mu\nu} - \hat{R}_{ij}^{\mu} \hat{R}_{ij}^{\nu} \right) (\boldsymbol{S}_i \times \boldsymbol{S}_j)_{\nu},$$

with $R_{ij} = |\boldsymbol{R}_{ij}|$ and $D_{xy}^{\text{nnn}} = D_{xy}^{\text{nnn}}(\boldsymbol{R}_{ij})$. By performing a rotation $(\boldsymbol{S}_i \times \boldsymbol{S}_j)_{\nu} = (O(\boldsymbol{S}_i' \times \boldsymbol{S}_j'))_{\nu}$, the spins can be expressed in terms of the reference frame consisting of $\{\hat{\boldsymbol{e}}_{\boldsymbol{1}}, \hat{\boldsymbol{e}}_2, \hat{\boldsymbol{e}}_3\}$, where $\hat{\boldsymbol{e}}_3$ aligns with the magnetic field direction. This allows us to represent the Hamiltonian in a concise form as follows

$$\mathcal{H}_{\text{int}}^{\text{D,nnn}} = \sum_{<<i,j>>} \sum_{\mu,\nu} (u_{i\mu} - u_{j\mu}) F_{ij}^{\mu\nu} (\boldsymbol{S}_i' \times \boldsymbol{S}_j')_{\nu},$$

where $\mu \in \{x, y, x\}$, $\nu \in \{1, 2, 3\}$ and the coupling matrix is defined by

$$F_{ij}^{\mu\nu} = \sum_{\xi=x,y,z} \eta_{ij} \frac{D_{xy}^{\text{nnn}}}{R_{ij}} \left(\delta_{\mu\xi} - \hat{R}_{ij}^{\mu} \hat{R}_{ij}^{\xi} \right) O_{\xi\nu}.$$

Writing out the summation, the coupling to in-plane ($\mu = x, y$) and out-of-plane ($\mu = z$) phonon modes can be separated as

$$\begin{aligned}
(\mu = x, y): \quad F_{ij}^{\mu\nu} =& \eta_{ij} \frac{D_{xy}^{\text{nnn}}}{R_{ij}} \left[(\delta_{\mu x} - \hat{R}_{ij}^{\mu} \hat{R}_{ij}^{x}) O_{x\nu} + (\delta_{\mu y} - \hat{R}_{ij}^{\mu} \hat{R}_{ij}^{y}) O_{y\nu}) \right], \\
(\mu = z): \quad F_{ij}^{z\nu} =& \eta_{ij} \frac{D_{xy}^{\text{nnn}}}{R_{ij}} O_{z\nu}.
\end{aligned}$$

Contribution from the NN DMI

The nearest neighbour DM vector is on the form

$$\boldsymbol{D}_{ij}^{\text{nn}} = D_{xy}^{\text{nn}} (\hat{\boldsymbol{z}} \times \hat{\boldsymbol{R}}_{ij}) + D_z^{\text{nn}} \hat{\boldsymbol{z}}.$$

Section 4.1.2 carefully addressed the in-plane aspect of the nearest neighbour DMI. However, we redo the calculations for the updated nearest neighbour DM vector to ensure all aspects are considered. By performing a Taylor expansion, the DM vector's lowest order contributions are

$$\begin{aligned}
\boldsymbol{D}^{\text{nn}}(\boldsymbol{r}_{ij}) \approx& \boldsymbol{D}^{\text{nn}}(\boldsymbol{R}_{ij}) + \frac{D_{xy}^{\text{nn}}}{R_{ij}} \left(\hat{\boldsymbol{z}} \times (\boldsymbol{u}_{ij} - (\hat{\boldsymbol{R}}_{ij} \cdot \boldsymbol{u}_{ij}) \hat{\boldsymbol{R}}_{ij}) \right) \\
&+ \left(\nabla_{\boldsymbol{r}_{ij}} D_{xy}^{\text{nn}}(\boldsymbol{r}_{ij}) \Big|_{\boldsymbol{R}_{ij}} \cdot \boldsymbol{u}_{ij} \right) (\hat{\boldsymbol{z}} \times \hat{\boldsymbol{R}}_{ij}) + \left(\nabla_{\boldsymbol{r}_{ij}} D_z^{\text{nn}}(\boldsymbol{r}_{ij}) \Big|_{\boldsymbol{R}_{ij}} \cdot \boldsymbol{u}_{ij} \right) \hat{\boldsymbol{z}} \\
\approx& \boldsymbol{D}^{\text{nn}}(\boldsymbol{R}_{ij}) + \frac{D_{xy}^{\text{nn}}}{R_{ij}} \left(\hat{\boldsymbol{z}} \times (\boldsymbol{u}_{ij} - (\hat{\boldsymbol{R}}_{ij} \cdot \boldsymbol{u}_{ij}) \hat{\boldsymbol{R}}_{ij}) \right),
\end{aligned}$$

with $D_{xy}^{\text{nn}} = D_{xy}^{\text{nn}}(\boldsymbol{R}_{ij})$ and we ignore the terms containing derivatives. The second term yields an additional contribution to the interacting Hamiltonian, which may be written concisely as

$$\mathcal{H}_{\text{int}}^{\text{D,nn}} = \sum_{<i,j>} \sum_{\mu,\nu} (u_{i\mu} - u_{j\mu}) T_{ij}^{\mu\nu} (\boldsymbol{S}_i' \times \boldsymbol{S}_j')_{\nu},$$

for $\mu \in \{x, y, x\}$, $\nu \in \{1, 2, 3\}$ and the nearest neighbour coupling matrix is defined by

$$T_{ij}^{\mu\nu} = -\sum_{\substack{\xi,\gamma \\ \in\{x,y,z\}}} \frac{D_{xy}^{\mathrm{nn}}}{R_{ij}} \varepsilon_{z\gamma\xi} \left(\delta_{\mu\gamma} - \hat{R}_{ij}^{\mu}\hat{R}_{ij}^{\gamma}\right) O_{\xi\nu},$$

where $\varepsilon_{z\gamma\xi}$ is the Levi-Civita tensor. If we explicitly express the summation, the interacting Hamiltonian's lowest order contribution does not result in coupling with out-of-plane phonon modes, as previously stated in section 4.1.2. However, the coupling with in-plane phonon modes takes the following form

$$(\mu = x, y): \quad T_{ij}^{\mu\nu} = -\frac{D_{xy}^{\mathrm{nn}}}{R_{ij}} \left[(\delta_{\mu x} - \hat{R}_{ij}^{\mu}\hat{R}_{ij}^{x})O_{y\nu} - (\delta_{\mu y} - \hat{R}_{ij}^{\mu}\hat{R}_{ij}^{y})O_{x\nu}\right].$$

Contribution from anisotropy

The magnetoelastic energy caused by crystalline anisotropy occurs because the movement of atoms results in a local alteration of crystal axes, which in turn affects the crystalline anisotropy and becomes linked to spins. As crystalline anisotropy is a feature of all solids, this form of magnetoelastic coupling should also exist. The derivation of the contribution to the interacting Hamiltonian takes its starting point from the anisotropy energy density h^{ani} in an untrained cubic crystal. Expanding the energy density in terms of the strains, the magnetoelastic energy density is on the form [29, 65, 67]

$$h_{\mathrm{me}}^{\mathrm{ani}} = b_1(\hat{m}_x^2 e_{xx} + \hat{m}_y^2 e_{yy} + \hat{m}_z^2 e_{zz}) + 2b_2(\hat{m}_x\hat{m}_y e_{xy} + \hat{m}_y\hat{m}_z e_{yz} + \hat{m}_x\hat{m}_z e_{zx}),$$

where $e_{\mu\nu} = \frac{1}{2}\left(\partial_\nu u_\mu + \partial_\mu u_\nu\right)$ are the strains and $\partial_\nu u_\mu = \frac{\partial u_\mu}{\partial r_\nu}$. The magnetoelastic coupling constants are denoted by b_1 and b_2, while the directional cosines of the magnetization are represented by $(\hat{m}_x, \hat{m}_y, \hat{m}_z)$. Additionally, in the continuum limit, $\boldsymbol{u}(\boldsymbol{r})$ signifies the displacement. Since we look at a two-dimensional system, we can neglect the derivative of the displacement with respect to z [29]. By rotating the Cartesian magnetization components to the new frame of reference and neglecting higher order contributions, we obtain

$$\begin{aligned} h_{\mathrm{me}}^{\mathrm{ani}} =& 2b_1\left[\partial_x u_x(\Gamma_1^{xx}\hat{m}_1' + \Gamma_2^{xx}\hat{m}_2') + \partial_y u_y(\Gamma_1^{yy}\hat{m}_1' + \Gamma_2^{yy}\hat{m}_2')\right] \\ &+2b_2\left[(\partial_y u_x + \partial_x u_y)(\Gamma_1^{xy}\hat{m}_1' + \Gamma_2^{xy}\hat{m}_2') + \partial_x u_z(\Gamma_1^{xz}\hat{m}_1' + \Gamma_2^{xz}\hat{m}_2')\right. \\ &\left.+\partial_y u_z(\Gamma_1^{yz}\hat{m}_1' + \Gamma_2^{yz}\hat{m}_2')\right], \end{aligned}$$

where $\Gamma_\nu^{\mu\mu'} = (1/2)(O_{\mu\nu}O_{\mu'3} + O_{\mu 3}O_{\mu'\nu})$ and we utilized $\hat{m}_3' \approx 1$. In order to use this expression in a discrete lattice, we approximate the strain tensor with the discrete strain tensor [63]

$$\tilde{e}_{ij}^{\mu\nu} = \frac{1}{2}\frac{1}{|\boldsymbol{R}_i - \boldsymbol{R}_j|^2}\left[(R_{i\nu} - R_{j\nu})(u_{i\mu} - u_{j\mu}) + (R_{i\mu} - R_{j\mu})(u_{i\nu} - u_{j\nu})\right],$$

which is proportional to the strain tensor in the long wavelength limit. By using $\hat{m}_\mu' = S_{i\mu}'/S^2$ and summing over the nearest neighbours, the magnetoelastic energy becomes

$$\begin{aligned} \mathcal{H}_{\mathrm{int}}^{\mathrm{ani}} =& \frac{1}{a_0^2}\sum_{<i,j>}\left[\kappa_1\left(R_{ij}^x u_{ij}^x(\Gamma_1^{xx}S_{i1}' + \Gamma_2^{xx}S_{i2}') + R_{ij}^y u_{ij}^y(\Gamma_1^{yy}S_{i1}' + \Gamma_2^{yy}S_{i2}')\right)\right. \\ &+\kappa_2\left((R_{ij}^y u_{ij}^x + R_{ij}^x u_{ij}^y)(\Gamma_1^{xy}S_{i1}' + \Gamma_2^{xy}S_{i2}') + R_{ij}^x u_{ij}^z(\Gamma_1^{xz}S_{i1}' + \Gamma_2^{xz}S_{i2}')\right) \\ &\left.R_{ij}^y u_{ij}^z(\Gamma_1^{yz}S_{i1}' + \Gamma_2^{y2}S_{i2}')\right)\Big] \\ =& \sum_{<i,j>}\sum_{\mu\nu}(u_{i\mu} - u_{j\mu})K_{ij}^{\mu\nu}S_{i\nu}', \end{aligned}$$

for $\mu \in \{x, y, z\}$ and $\nu \in \{1, 2\}$. The interaction strengths κ_1 and κ_2 have been defined, with each being proportional to b_1 and b_2, respectively, and expressed in units of energy. The coupling matrix is defined as follows

$$K_{ij} = \frac{1}{a_0^2} \begin{bmatrix} \kappa_1 R_{ij}^x \Gamma_1^{xx} + \kappa_2 R_{ij}^y \Gamma_1^{xy} & \kappa_1 R_{ij}^x \Gamma_2^{xx} + \kappa_2 R_{ij}^y \Gamma_2^{xy} \\ \kappa_1 R_{ij}^y \Gamma_1^{yy} + \kappa_2 R_{ij}^x \Gamma_1^{xy} & \kappa_1 R_{ij}^y \Gamma_2^{yy} + \kappa_2 R_{ij}^x \Gamma_2^{xy} \\ \kappa_2 (R_{ij}^x \Gamma_1^{xz} + R_{ij}^y \Gamma_1^{yz}) & \kappa_2 (R_{ij}^x \Gamma_2^{xz} + R_{ij}^y \Gamma_2^{yz}) \end{bmatrix}.$$

When considering a magnetization perpendicular to the plane, the expression simplifies to

$$(\text{magnetization} \perp \text{plane}): \quad \mathcal{H}_{\text{int}}^{\text{ani}} = \frac{\kappa_2}{2a_0} \sum_{<i,j>} (u_{iz} - u_{jz})(\hat{\boldsymbol{R}}_{ij} \cdot \boldsymbol{S}_i),$$

which bears resemblance to the utilized expression in Ref. [27]. In contrast to the DMI, which solely interacts with in-plane phonon modes when the magnetization is perpendicular to the plane, the anisotropy induces a coupling that is limited to out-of-plane phonon modes for the same magnetization direction. Similarly, a magnetization aligned with the $\hat{\boldsymbol{x}}$ direction generates the following interacting Hamiltonian

$$(\text{magnetization} \parallel \hat{\boldsymbol{x}}): \quad \mathcal{H}_{\text{int}}^{\text{ani}} = \frac{\kappa_2}{2a_0} \sum_{<i,j>} \left((u_{ij}^x \hat{R}_{ij}^y + u_{ij}^y \hat{R}_{ij}^x) S_{iy} + u_{ij}^z \hat{R}_{ij}^x S_{iz} \right).$$

It is important to observe that in order for κ_1 to have an impact on the dispersion, the orientation of the magnetization must not be parallel to any of the Cartesian axes in the coordinate system. This is connected to the fact that the derivation begins with the anisotropy energy density specific to a cubic lattice.

The interacting Hamiltonian

The total interacting Hamiltonian is then

$$\mathcal{H}_{\text{int}} = \overbrace{\sum_{<i,j>} \sum_{\mu,\nu} (u_{i\mu} - u_{j\mu}) T_{ij}^{\mu\nu} (\boldsymbol{S}_i' \times \boldsymbol{S}_j')_\nu}^{\mathcal{H}_{\text{int}}^{\text{D,nn}}} + \overbrace{\sum_{<<i,j>>} \sum_{\mu,\nu} (u_{i\mu} - u_{j\mu}) F_{ij}^{\mu\nu} (\boldsymbol{S}_i' \times \boldsymbol{S}_j')_\nu}^{\mathcal{H}_{\text{int}}^{\text{D,nnn}}} + \underbrace{\sum_{<i,j>} \sum_{\mu\nu} (u_{i\mu} - u_{j\mu}) K_{ij}^{\mu\nu} S_{i\nu}'}_{\mathcal{H}_{\text{int}}^{\text{ani}}}.$$

By neglecting the terms that contain derivatives, only the planar components D_{xy}^{nn} and D_{xy}^{nnn}, along with κ_1 and κ_2, play a role in the hybridization and establish the extent of the coupling.

7.2. Calculation of magnon-phonon energy spectrum

Two methods are employed to derive the magnetoelastic energy spectrum. The first method involves the use of the second quantization formalism, where the basis is constructed using magnon and phonon bosonic operators. In the second approach, the phonon Hamiltonian is expressed in a non-diagonalized form, and the magnetoelastic Hamiltonian is formulated using the magnon bosonic operators and the phonon BdG field. Although the two methods produce the same energy spectrum, the latter method is better suited for numerical computations of the Berry curvature [19].

7.2.1. Second quantized approach

The Hamiltonian for the non-interacting energy of phonons and magnons in the honeycomb ferromagnet can be expressed as follows

$$\begin{aligned}\mathcal{H}_0 &= \mathcal{H}_{\mathrm{ph}} + \mathcal{H}_{\mathrm{m}},\\ \mathcal{H}_{\mathrm{ph}} &= \sum_{q,\lambda} \varepsilon_{q,\lambda} c^\dagger_{q,\lambda} c_{q,\lambda},\\ \mathcal{H}_{\mathrm{m}} &= \frac{1}{2}\sum_{k} \boldsymbol{\psi}^\dagger_{\mathrm{m}}(\boldsymbol{k}) H_{\mathrm{m}}(\boldsymbol{k}) \boldsymbol{\psi}_{\mathrm{m}}(\boldsymbol{k}),\end{aligned}$$

where $\varepsilon_{q,\lambda} = \hbar\omega_{q,\lambda} = \hbar\Omega\tilde{\omega}_{q,\lambda}$ is the phonon energy in mode λ, and $\Omega = \sqrt{\Phi^{\alpha\beta}_{\mu\nu}/M}$ for a yet to be specified force coefficient. The magnon basis vector is on the form $\boldsymbol{\psi}_{\mathrm{m}}(\boldsymbol{k}) = [a_k, b_k, a^\dagger_{-k}, b^\dagger_{-k}]^T$, and $H_{\mathrm{m}}(\boldsymbol{k})$ is described in equation (6.5). To account for interactions, it is necessary to derive a more applicable expression for the interacting Hamiltonian. Since we are examining a ferromagnetic system, we can make the following approximations $S'_{i3} \approx S$ and $S'_{j3} \approx S$, such that

$$\begin{aligned}\mathcal{H}_{\mathrm{int}} = S &\sum_{<i,j>}\sum_{\mu}(u_{i\mu} - u_{j\mu})\left[T^{\mu 1}_{ij}(S'_{i2} - S'_{j2}) - T^{\mu 2}_{ij}(S'_{i1} - S'_{j1})\right]\\ + S &\sum_{<<i,j>>}\sum_{\mu}(u_{i\mu} - u_{j\mu})\left[F^{\mu 1}_{ij}(S'_{i2} - S'_{j2}) - F^{\mu 2}_{ij}(S'_{i1} - S'_{j1})\right]\\ + &\sum_{<i,j>}\sum_{\mu}(u_{i\mu} - u_{j\mu})\left[K^{\mu 1}_{ij} S'_{i1} + K^{\mu 2}_{ij} S'_{i2}\right],\end{aligned}$$

to second order in bosonic operators. By considering the first term, we utilize the Holstein-Primakoff transformation given by equation (6.2), to obtain the following

$$\begin{aligned}\mathcal{H}^{\mathrm{D,nn}}_{\mathrm{int}} =& \frac{S}{2}\sqrt{\frac{S}{2}}\sum_{\substack{i,\delta_A\\ i\in A}}\sum_{\mu}(u_{iA\mu} - u_{i+\delta_A,B\mu})\left[T^{\mu}_{\delta_A}(b_{i+\delta_A} - a_i) + T^{\mu *}_{\delta_A}(b^\dagger_{i+\delta_A} - a^\dagger_i)\right]\\ &+ \frac{S}{2}\sqrt{\frac{S}{2}}\sum_{\substack{i,\delta_B\\ i\in B}}\sum_{\mu}(u_{iB\mu} - u_{i+\delta_B,A\mu})\left[T^{\mu}_{\delta_B}(a_{i+\delta_B} - b_i) + T^{\mu *}_{\delta_B}(a^\dagger_{i+\delta_B} - b^\dagger_i)\right],\end{aligned}$$

where we defined $T^{\mu}_{\delta_{A(B)}} = T^{\mu 2}_{\delta_{A(B)}} + \mathrm{i}T^{\mu 1}_{\delta_{A(B)}}$ for shorthand notation. By expressing the ionic displacement in terms of bosonic operators using equation (2.10), and substituting for the Fourier-transformed magnon operators, it results in

$$\mathcal{H}^{\mathrm{D,nn}}_{\mathrm{int}} = \sum_{q,\lambda}\left[(c_{q,\lambda} + c^\dagger_{-q,\lambda})(T^{A}_{q,\lambda} a_{-q} + T^{B}_{q,\lambda} b_{-q}) + (c_{-q,\lambda} + c^\dagger_{q,\lambda})(T^{A*}_{q,\lambda} a^\dagger_{-q} + T^{B*}_{q,\lambda} b^\dagger_{-q})\right],$$

where the coupling coefficients are defined by

$$T^{A(B)}_{q,\lambda} = -\frac{S}{2}\sqrt{\frac{\hbar S}{M\omega_{q,\lambda}}}\sum_{\delta_{A(B)},\mu}\left(e^{\lambda}_{A(B),\mu}(\boldsymbol{q}) - e^{\lambda}_{B(A),\mu}(\boldsymbol{q})\mathrm{e}^{\mathrm{i}\boldsymbol{q}\cdot\boldsymbol{\delta}_{A(B)}}\right)T^{\mu}_{\delta_{A(B)}}.$$

The coefficients can be written more compactly as

$$
\begin{aligned}
T^{A}_{q,\lambda} =& \frac{1}{2} S\zeta D^{\mathrm{nn}}_{xy} \sqrt{\frac{S}{\tilde{\omega}_{q,\lambda}}} \left(\boldsymbol{e}^{\lambda}_{A}(\boldsymbol{q}) \cdot \boldsymbol{g}^{\mathrm{nn}}_{q=0} - \boldsymbol{e}^{\lambda}_{B}(\boldsymbol{q}) \cdot \boldsymbol{g}^{\mathrm{nn}}_{q} \right), \\
T^{B}_{q,\lambda} =& \frac{1}{2} S\zeta D^{\mathrm{nn}}_{xy} \sqrt{\frac{S}{\tilde{\omega}_{q,\lambda}}} \left(\boldsymbol{e}^{\lambda}_{B}(\boldsymbol{q}) \cdot \boldsymbol{g}^{\mathrm{nn}}_{q=0} - \boldsymbol{e}^{\lambda}_{A}(\boldsymbol{q}) \cdot \boldsymbol{g}^{\mathrm{nn}}_{-q} \right),
\end{aligned}
$$

with $\zeta = (1/a_0)\sqrt{\hbar/M\Omega}$, and the elements in $\boldsymbol{g}^{\mathrm{nn}}_{q}$ are

$$
\begin{aligned}
g^{\mathrm{nn}}_{qx} =& \mathrm{e}^{\frac{\mathrm{i}}{\sqrt{3}} q_y a} O_y + \frac{1}{2} \mathrm{e}^{-\mathrm{i}\frac{q_y a}{2\sqrt{3}}} \left(\cos(\frac{1}{2} q_x a) O_y - \mathrm{i}\sqrt{3} \sin(\frac{1}{2} q_x a) O_x \right), \\
g^{\mathrm{nn}}_{qy} =& -\frac{1}{2} \mathrm{e}^{-\mathrm{i}\frac{q_y a}{2\sqrt{3}}} \left(3\cos(\frac{1}{2} q_x a) O_x - \mathrm{i}\sqrt{3} \sin(\frac{1}{2} q_x a) O_y \right), \\
g^{\mathrm{nn}}_{qz} =& 0,
\end{aligned}
$$

where we also defined $O_\mu = O_{\mu 2} + \mathrm{i} O_{\mu 1}$.

Similarly, the second term in the interacting Hamiltonian can be split up in the following way

$$
\begin{aligned}
\mathcal{H}^{\mathrm{D,nnn}}_{\mathrm{int}} =& \frac{S}{2}\sqrt{\frac{S}{2}} \sum_{\substack{i,\tau_A \\ i\in A}} \sum_{\mu} (u_{iA\mu} - u_{i+\tau_A, A\mu}) \left[F^{\mu}_{\tau_A} (a_{i+\tau_A} - a_i) + F^{\mu *}_{\tau_A} (a^{\dagger}_{i+\tau_A} - a^{\dagger}_{i}) \right] \\
&+ \frac{S}{2}\sqrt{\frac{S}{2}} \sum_{\substack{i,\tau_B \\ i\in B}} \sum_{\mu} (u_{iB\mu} - u_{i+\tau_B, B\mu}) \left[F^{\mu}_{\tau_B} (b_{i+\tau_B} - b_i) + F^{\mu *}_{\tau_B} (b^{\dagger}_{i+\tau_B} - b^{\dagger}_{i}) \right],
\end{aligned}
$$

with $F^{\mu}_{\tau_{A(B)}} = F^{\mu 2}_{\tau_{A(B)}} + \mathrm{i} F^{\mu 1}_{\tau_{A(B)}}$. Proceeding, we have

$$
\begin{aligned}
\mathcal{H}^{\mathrm{D,nnn}}_{\mathrm{int}} =& -\frac{S}{2}\sqrt{\frac{\hbar S}{M}} \sum_{q,\lambda} \sum_{\tau_A,\mu} \frac{(c_{q,\lambda} + c^{\dagger}_{-q,\lambda})}{\sqrt{\omega_{q,\lambda}}} e^{\lambda}_{A\mu}(\boldsymbol{q}) (1 - \cos(\boldsymbol{q}\cdot\boldsymbol{\tau}_A)) \left[F^{\mu}_{\tau_A} a_{-q} + F^{\mu *}_{\tau_A} a^{\dagger}_{q} \right] \\
&- \frac{S}{2}\sqrt{\frac{\hbar S}{M}} \sum_{q,\lambda} \sum_{\tau_B,\mu} \frac{(c_{q,\lambda} + c^{\dagger}_{-q,\lambda})}{\sqrt{\omega_{q,\lambda}}} e^{\lambda}_{B\mu}(\boldsymbol{q}) (1 - \cos(\boldsymbol{q}\cdot\boldsymbol{\tau}_B)) \left[F^{\mu}_{\tau_B} b_{-q} + F^{\mu *}_{\tau_B} b^{\dagger}_{q} \right] \\
=& \sum_{q,\lambda} \left[(c_{q,\lambda} + c^{\dagger}_{-q,\lambda})(F^{A}_{q,\lambda} a_{-q} + F^{B}_{q,\lambda} b_{-q}) + (c_{-q,\lambda} + c^{\dagger}_{q,\lambda})(F^{A*}_{q,\lambda} a^{\dagger}_{-q} + F^{B*}_{q,\lambda} b^{\dagger}_{-q}) \right],
\end{aligned}
$$

where the coefficients are given by

$$
F^{A(B)}_{q,\lambda} = -\frac{S}{2}\sqrt{\frac{\hbar S}{M\omega_{q,\lambda}}} \sum_{\tau_{A(B)},\mu} e^{\lambda}_{A(B),\mu}(\boldsymbol{q}) (1 - \cos(\boldsymbol{q}\cdot\boldsymbol{\tau}_{A(B)})) F^{\mu}_{\tau_{A(B)}}.
$$

Computing the summation over the second nearest neighbours, the coupling coefficients may be written as

$$
\begin{aligned}
F^{A}_{q,\lambda} =& -\frac{1}{2} S\zeta D^{\mathrm{nnn}}_{xy} \sqrt{\frac{S}{3\tilde{\omega}_{q,\lambda}}} \boldsymbol{e}^{\lambda}_{A}(\boldsymbol{q}) \cdot \boldsymbol{g}^{\mathrm{nnn}}_{q}, \\
F^{B}_{q,\lambda} =& \frac{1}{2} S\zeta D^{\mathrm{nnn}}_{xy} \sqrt{\frac{S}{3\tilde{\omega}_{q,\lambda}}} \boldsymbol{e}^{\lambda}_{B}(\boldsymbol{q}) \cdot \boldsymbol{g}^{\mathrm{nnn}}_{q},
\end{aligned}
$$

with

$$
\begin{aligned}
g_{qx}^{\mathrm{nnn}} =& 3O_x\left(1-\cos(\frac{1}{2}q_xa)\cos(\frac{\sqrt{3}}{2}q_ya)\right)-\sqrt{3}O_y\sin(\frac{1}{2}q_xa)\sin(\frac{\sqrt{3}}{2}q_ya),\\
g_{qy}^{\mathrm{nnn}} =& O_y\left(3-2\cos(q_xa)-\cos(\frac{1}{2}q_xa)\cos(\frac{\sqrt{3}}{2}q_ya)\right)\\
&-\sqrt{3}O_x\sin(\frac{1}{2}q_xa)\sin(\frac{\sqrt{3}}{2}q_ya),\\
g_{qz}^{\mathrm{nnn}} =& 2O_z\left(3-\cos(q_xa)-2\cos(\frac{1}{2}q_xa)\cos(\frac{\sqrt{3}}{2}q_ya)\right).
\end{aligned}
$$

The third term in the interacting Hamiltonian, stemming from the anisotropy, can be expressed as

$$
\begin{aligned}
\mathcal{H}_{\mathrm{int}}^{\mathrm{ani}} =& \frac{1}{2}\sqrt{\frac{S}{2}}\sum_{\substack{i,\delta_A\\ i\in A}}\sum_{\mu}(u_{iA\mu}-u_{i+\delta_A,B\mu})\left[(K_{\delta_A}^{\mu 1}-\mathrm{i}K_{\delta_A}^{\mu 2})a_i+(K_{\delta_A}^{\mu 1}+\mathrm{i}K_{\delta_A}^{\mu 2})a_i^\dagger\right]\\
&+\frac{1}{2}\sqrt{\frac{S}{2}}\sum_{\substack{i,\delta_B\\ i\in B}}\sum_{\mu}(u_{iB\mu}-u_{i+\delta_B,A\mu})\left[(K_{\delta_B}^{\mu 1}-\mathrm{i}K_{\delta_B}^{\mu 2})b_i+(K_{\delta_B}^{\mu 1}+\mathrm{i}K_{\delta_B}^{\mu 2})b_i^\dagger\right]\\
=&\sum_{q,\lambda}\left[(c_{q,\lambda}+c_{-q,\lambda}^\dagger)(K_{q,\lambda}^{A}a_{-q}+K_{q,\lambda}^{B}b_{-q})+(c_{-q,\lambda}+c_{q,\lambda}^\dagger)(K_{q,\lambda}^{A*}a_{-q}^\dagger+K_{q,\lambda}^{B*}b_{-q}^\dagger)\right],
\end{aligned}
$$

where

$$
K_{q,\lambda}^{A(B)}=\frac{1}{4}\sqrt{\frac{\hbar S}{M\omega_{q,\lambda}}}\sum_{\delta_{A(B)},\mu}\left(e_{A(B)\mu}^{\lambda}(\boldsymbol{q})-e_{B(A)\mu}^{\lambda}(\boldsymbol{q})\mathrm{e}^{\mathrm{i}\boldsymbol{q}\cdot\boldsymbol{\delta}_{A(B)}}\right)(K_{\delta_{A(B)}}^{\mu 1}-\mathrm{i}K_{\delta_{A(B)}}^{\mu 2}).
$$

In a more concise format, the coefficients are on the form

$$
\begin{aligned}
K_{q,\lambda}^{A} =& -\frac{1}{4}\zeta\sqrt{\frac{S}{\tilde{\omega}_{q,\lambda}}}\boldsymbol{e}_B^{\lambda}(\boldsymbol{q})\cdot\boldsymbol{g}_q^{\mathrm{ani}},\\
K_{q,\lambda}^{B} =& \frac{1}{4}\zeta\sqrt{\frac{S}{\tilde{\omega}_{q,\lambda}}}\boldsymbol{e}_A^{\lambda}(\boldsymbol{q})\cdot\boldsymbol{g}_{-q}^{\mathrm{ani}},
\end{aligned}
$$

with the vector defined as

$$
\begin{aligned}
g_{qx}^{\mathrm{ani}} =& -\kappa_2\Gamma^{xy}\mathrm{e}^{\frac{\mathrm{i}}{\sqrt{3}}q_ya}+\mathrm{e}^{-\mathrm{i}\frac{q_ya}{2\sqrt{3}}}(\kappa_2\Gamma^{xy}\cos(\frac{1}{2}q_xa)-\mathrm{i}\sqrt{3}\kappa_1\Gamma^{xx}\sin(\frac{1}{2}q_xa)),\\
g_{qy}^{\mathrm{ani}} =& -\kappa_1\Gamma^{yy}\mathrm{e}^{\frac{\mathrm{i}}{\sqrt{3}}q_ya}+\mathrm{e}^{-\mathrm{i}\frac{q_ya}{2\sqrt{3}}}(\kappa_1\Gamma^{yy}\cos(\frac{1}{2}q_xa)-\mathrm{i}\sqrt{3}\kappa_2\Gamma^{xy}\sin(\frac{1}{2}q_xa)),\\
g_{qz}^{\mathrm{ani}} =& -\kappa_2\Gamma^{yz}\mathrm{e}^{\frac{\mathrm{i}}{\sqrt{3}}q_ya}+\kappa_2\mathrm{e}^{-\mathrm{i}\frac{q_ya}{2\sqrt{3}}}(\Gamma^{yz}\cos(\frac{1}{2}q_xa)-\mathrm{i}\sqrt{3}\Gamma^{xz}\sin(\frac{1}{2}q_xa)),
\end{aligned}
$$

and $\Gamma^{\mu\mu'}=\Gamma_1^{\mu\mu'}-\mathrm{i}\Gamma_2^{\mu\mu'}$.

By summing up the contributions from the three terms, we obtain the following interacting Hamiltonian

$$\mathcal{H}_{\text{int}} = \sum_{q,\lambda} \left[(c_{q,\lambda} + c^{\dagger}_{-q,\lambda})(G^{A}_{q,\lambda} a_{-q} + G^{B}_{q,\lambda} b_{-q}) + (c_{-q,\lambda} + c^{\dagger}_{q,\lambda})(G^{A*}_{q,\lambda} a^{\dagger}_{-q} + G^{B*}_{q,\lambda} b^{\dagger}_{-q}) \right],$$

with $G^{A(B)}_{q,\lambda} = T^{A(B)}_{q,\lambda} + F^{A(B)}_{q,\lambda} + K^{A(B)}_{q,\lambda}$. The total magnetoelastic Hamiltonian in the second quantized (sq) formalism can then be written as

$$\mathcal{H} = \frac{1}{2} \sum_{q} \boldsymbol{\Psi}^{\dagger}_{q} H^{\text{sq}}_{\text{me}}(\boldsymbol{q}) \boldsymbol{\Psi}_{q}, \tag{7.1}$$

in the basis $\boldsymbol{\Psi}_q = [\boldsymbol{\psi}^T_q, \boldsymbol{\psi}^{\dagger}_{-q}]^T$, $\boldsymbol{\psi}^T_q = [a_q, b_q, c_{q,1}, c_{q,2}, c_{q,3}, c_{q,4}, c_{q,5}, c_{q,6}]$ and the 16×16 matrix $H^{\text{sq}}_{\text{me}}(\boldsymbol{q})$ is listed in Appendix B. The eigenvalues are obtained numerically by diagonalizing $\sigma_3 H^{\text{sq}}_{\text{me}}(\boldsymbol{q})$.

7.2.2. Method using non-diagonalized form of the phonon Hamiltonian

From equation (4.9), the phonon Hamiltonian is given by

$$\mathcal{H}_{\text{ph}} = \frac{1}{2} \sum_{q} \tilde{\boldsymbol{\phi}}^{\dagger}_{\text{ph}}(\boldsymbol{q}) H_{\text{ph}}(\boldsymbol{q}) \tilde{\boldsymbol{\phi}}_{\text{ph}}(\boldsymbol{q}), \;\; H_{\text{ph}}(\boldsymbol{q}) = \hbar\Omega \begin{bmatrix} \tilde{D}(\boldsymbol{q}) & 0 \\ 0 & I_{\text{ph}} \end{bmatrix}, \;\; \tilde{\boldsymbol{\phi}}_{\text{ph}}(\boldsymbol{q}) = [\tilde{\boldsymbol{u}}^T_{q,A}, \tilde{\boldsymbol{u}}^T_{q,B}, \tilde{\boldsymbol{p}}^T_{-q,A}, \tilde{\boldsymbol{p}}^T_{-q,B}]^T,$$

where $\tilde{\boldsymbol{u}}^T_{q,\alpha} = [\tilde{u}_{q\alpha x}, \tilde{u}_{q\alpha y}, \tilde{u}_{q\alpha z}]$ denotes the dimensionless displacement of the ions at sublattice $\alpha = A, B$ while $\tilde{\boldsymbol{p}}_{-q,\alpha}$ is the dimensionless momentum, and $I_{\text{ph}} = I_{6\times 6}$. The derivation of the interacting Hamiltonian follows a similar approach as in the previous section, so we present the final result as follows. The interacting Hamiltonian, which couples the displacement to the magnonic Holstein-Primakoff operators, can be expressed as

$$\mathcal{H}_{\text{int}} = \sum_{q} \tilde{\boldsymbol{u}}^{\dagger}_{q} H_c(\boldsymbol{q}) \boldsymbol{\psi}_{\text{m}}(\boldsymbol{q}), \;\; \tilde{\boldsymbol{u}}_q = [\tilde{\boldsymbol{u}}^T_{qA}, \tilde{\boldsymbol{u}}^T_{qB}]^T, \;\; \boldsymbol{\psi}_{\text{m}}(\boldsymbol{q}) = [a_q, b_q, a^{\dagger}_{-q}, b^{\dagger}_{-q}]^T,$$

$$H_c(\boldsymbol{q}) = \zeta \sqrt{\frac{S}{2}} \begin{bmatrix} -\boldsymbol{d}^{\text{nn}}_{q=0} - \boldsymbol{d}^{\text{nnn}}_{q} & \boldsymbol{d}^{\text{nn}}_{q} + \boldsymbol{d}^{\text{ani}}_{q} & -\boldsymbol{d}^{\text{nn}^*}_{q=0} - \boldsymbol{d}^{\text{nnn}^*}_{q} & \boldsymbol{d}^{\text{nn}^*}_{-q} + \boldsymbol{d}^{\text{ani}^*}_{-q} \\ \boldsymbol{d}^{\text{nn}}_{-q} - \boldsymbol{d}^{\text{ani}}_{-q} & -\boldsymbol{d}^{\text{nn}}_{q=0} + \boldsymbol{d}^{\text{nnn}}_{q} & \boldsymbol{d}^{\text{nn}^*}_{q} - \boldsymbol{d}^{\text{ani}^*}_{q} & -\boldsymbol{d}^{\text{nn}^*}_{q=0} + \boldsymbol{d}^{\text{nnn}^*}_{q} \end{bmatrix},$$

where each element in the matrix is a 3×1 column vector. In order to define the vectors $\boldsymbol{d}_q$, we introduce the helping functions

$$f_q(s_1, s_2, s_3) = s_1 \mathrm{e}^{\mathrm{i}\frac{q_y a}{\sqrt{3}}} + s_2 \mathrm{e}^{-\mathrm{i}(\frac{q_x a}{2} + \frac{q_y a}{2\sqrt{3}})} + s_3 \mathrm{e}^{\mathrm{i}(\frac{q_x a}{2} - \frac{q_y a}{2\sqrt{3}})},$$

$$h_q(s_1, s_2, s_3) = s_1(1 - \cos(q_x a)) + s_2(1 - \cos(\frac{1}{2} q_x a + \frac{\sqrt{3}}{2} q_y a)) + s_3(1 - \cos(\frac{1}{2} q_x a - \frac{\sqrt{3}}{2} q_y a)),$$

which corresponds to a summation over the first and second nearest neighbours, respectively. The $\boldsymbol{d}_q$ vectors corresponding to the nearest neighbour DMI, the anisotropy, and the next-nearest neighbour DMI are given by the following expressions

$$
\begin{aligned}
\boldsymbol{d}_q^{\mathrm{nn}} &= -SD_{xy}^{\mathrm{nn}}\begin{bmatrix} f_q(O_y, \frac{1}{4}(O_y+\sqrt{3}O_x), \frac{1}{4}(O_y-\sqrt{3}O_x)) \\ f_q(0, -\frac{1}{4}(3O_x+\sqrt{3}O_y), -\frac{1}{4}(3O_x-\sqrt{3}O_y)) \\ 0 \end{bmatrix}, \\
\boldsymbol{d}_q^{\mathrm{ani}} &= \frac{1}{2}\begin{bmatrix} f_q(-\kappa_2\Gamma^{xy}, \frac{1}{2}(\kappa_2\Gamma^{xy}+\sqrt{3}\kappa_1\Gamma^{xx}), \frac{1}{2}(\kappa_2\Gamma^{xy}-\sqrt{3}\kappa_1\Gamma^{xx})) \\ f_q(-\kappa_1\Gamma^{yy}, \frac{1}{2}(\kappa_1\Gamma^{yy}+\sqrt{3}\kappa_2\Gamma^{xy}), \frac{1}{2}(\kappa_1\Gamma^{yy}-\sqrt{3}\kappa_2\Gamma^{xy})) \\ f_q(-\kappa_2\Gamma^{yz}, \frac{1}{2}\kappa_2(\Gamma^{yz}+\sqrt{3}\Gamma^{xz}), \frac{1}{2}\kappa_2(\Gamma^{yz}-\sqrt{3}\Gamma^{xz})) \end{bmatrix}, \\
\boldsymbol{d}_q^{\mathrm{nnn}} &= \frac{SD_{xy}^{\mathrm{nnn}}}{\sqrt{3}}\begin{bmatrix} h_q(0, \frac{1}{2}(3O_x-\sqrt{3}O_y), \frac{1}{2}(3O_x+\sqrt{3}O_y)) \\ h_q(2O_y, \frac{1}{2}(O_y-\sqrt{3}O_x), \frac{1}{2}(O_y+\sqrt{3}O_x)) \\ 2h_q(O_z, O_z, O_z) \end{bmatrix}.
\end{aligned}
\tag{7.2}
$$

Thus, in the basis $\bar{\boldsymbol{\phi}}_q = [\boldsymbol{\psi}_{\mathrm{m}}^T, \tilde{\boldsymbol{u}}_q^T, \tilde{\boldsymbol{p}}_{-q}^T]^T$, the magnetoelastic Hamiltonian becomes

$$
\mathcal{H} = \frac{1}{2}\sum_q \bar{\boldsymbol{\phi}}_q^\dagger H_{\mathrm{me}}(\boldsymbol{q})\bar{\boldsymbol{\phi}}_q, \quad H_{\mathrm{me}}(\boldsymbol{q}) = \begin{bmatrix} H_{\mathrm{m}}(\boldsymbol{q}) & H_{\mathrm{c}}^\dagger(\boldsymbol{q}) & 0_{4\times 6} \\ H_{\mathrm{c}}(\boldsymbol{q}) & \hbar\Omega\tilde{D}(\boldsymbol{q}) & 0_{6\times 6} \\ 0_{6\times 4} & 0_{6\times 6} & \hbar\Omega I_{\mathrm{ph}} \end{bmatrix}.
$$

This Hamiltonian matrix is not a bosonic BdG Hamiltonian since the basis operators do not obey the bosonic commutation relation. However, this can be adjusted by introducing the phonon BdG field [19]

$$
\boldsymbol{v}_q = \frac{1}{\sqrt{2}}(\tilde{\boldsymbol{p}}_{-q} - \mathrm{i}\tilde{\boldsymbol{u}}_q), \quad \boldsymbol{v}_{-q}^\dagger = \frac{1}{\sqrt{2}}(\tilde{\boldsymbol{p}}_{-q} + \mathrm{i}\tilde{\boldsymbol{u}}_q).
$$

By defining $\boldsymbol{v'}_{q,+} = \boldsymbol{v}_q$ and $\boldsymbol{v'}_{q,-} = \boldsymbol{v}_{-q}^\dagger$, we see that the operators satisfy the typical BdG commutation relation $[\boldsymbol{v'}_{q,\rho}, \boldsymbol{v'}_{q,\rho'}^\dagger] = \rho\delta_{\rho,\rho'}I_{\mathrm{ph}}$. Furthermore, we sort the basis into particle and hole spaces with the matrix P. Finally, we obtain

$$
\begin{gathered}
\mathcal{H} = \frac{1}{2}\sum_q \boldsymbol{\phi}_q^\dagger H_{\mathrm{me}}^{\mathrm{nd}}(\boldsymbol{q})\boldsymbol{\phi}_q, \quad \boldsymbol{\phi}_q = [a_q, b_q, \boldsymbol{v'}_{q,+}^T, a_{-q}^\dagger, b_{-q}^\dagger, \boldsymbol{v'}_{q,-}^T]^T, \\
H_{\mathrm{me}}^{\mathrm{nd}}(\boldsymbol{q}) = PLH_{\mathrm{me}}(\boldsymbol{q})L^\dagger P^\dagger, \\
L = \begin{bmatrix} I_{2\mathrm{m}} & 0 & 0 \\ 0 & -\frac{\mathrm{i}}{\sqrt{2}}I_{\mathrm{ph}} & \frac{1}{\sqrt{2}}I_{\mathrm{ph}} \\ 0 & \frac{\mathrm{i}}{\sqrt{2}}I_{\mathrm{ph}} & \frac{1}{\sqrt{2}}I_{\mathrm{ph}} \end{bmatrix}, \quad P = \begin{bmatrix} I_{\mathrm{m}} & & & \\ & & I_{\mathrm{ph}} & \\ & I_{\mathrm{m}} & & \\ & & & I_{\mathrm{ph}} \end{bmatrix},
\end{gathered}
$$

$I_{\mathrm{m}} = I_{2\times 2}$, $I_{2\mathrm{m}} = I_{4\times 4}$ and $H_{\mathrm{me}}^{\mathrm{nd}}(\boldsymbol{q})$ is the magnetoelastic Hamiltonian matrix in the non-diagonalized (nd) phonon basis. The eigenvalues are obtained by diagonalizing $\sigma_3 H_{\mathrm{me}}^{\mathrm{nd}}(\boldsymbol{q})$.

7.3. The magnetoelastic energy spectrum

Our analysis uses the following parameter values for the magnon dispersion: $\tilde{J} = 2.955\mathrm{meV}$, $S = 3/2$, $K_z = 0.109\mathrm{meV}$ and $D_z^{\mathrm{nnn}} = 0.31\mathrm{meV}$, which have shown good agreement with experimental results in CrI_3 [82]. We also establish $h = 4.5\mathrm{meV}$ as the strength of the Zeeman term. The strength of the coupling is determined by the planar components of the nearest and next-nearest neighbour DM vector

and is dependent on the degree of symmetry breaking present in the system. The coupling associated with the anisotropy is exclusively determined by the phenomenological parameter κ_2, as we limit our investigation to magnetization directions parallel to the Cartesian axes. Our toy model uses the values $D_{xy}^{\mathrm{nn}} = 0.2\mathrm{meV}$, $D_{xy}^{\mathrm{nnn}} = 0.3\mathrm{meV}$ and $\kappa_2 = 1\mathrm{meV}$. As the Cr atoms in CrI_3 form a honeycomb lattice, we use the same relative relationship between the force coefficients as for the dispersion in graphene, listed in equation (2.25), and set the scaling parameter to $\hbar\Omega = 10\mathrm{meV}$ (with $\Omega = \sqrt{|\gamma_2|/M}$). We chose this value to match the energies of the optical branches with the high-frequency branches reported in Refs. [81, 89], which calculated the phonon dispersion in CrI_3 using first-principles calculations. However, it is crucial to note that our phonon dispersion is distinct from that of CrI_3 because we neglect the iodine atoms and assume a perfect honeycomb lattice in our calculation. The dimensionless constant ζ that is proportional to the coupling terms has the magnitude $\zeta = 0.023$, considering the mass $M = 51.996\mathrm{u}$ of the Cr atoms and a lattice constant of $a = 6.687\text{Å}$ [81]. This constant induces a relatively weak coupling. Nevertheless, to observe gap openings, we use a higher value of $\zeta = 0.2$. Despite the gap's size, the topological properties should remain unaffected, as long as there is a gap opening.

To examine the impacts of the various coupling terms, we calculate and present the dispersion with either D_{xy}^{nnn}, D_{xy}^{nn} or κ_2 being nonzero, as well as the case where all parameters are nonzero. We display the dispersions in Figures 7.1 and 7.2, where each figure illustrates the dispersion with the magnetization along $\hat{\boldsymbol{x}}$, $\hat{\boldsymbol{y}}$ and $\hat{\boldsymbol{z}}$. Consistent with previous findings, we find that the magnon and phonon bands exhibit anticrossing regions where their frequencies match. Notably, differences are observed when either D_{xy}^{nn} or D_{xy}^{nnn} is nonzero. In the former case, there is no coupling to out-of-plane phonon modes for any magnetization direction to lowest order, while in the latter case, there is coupling to out-of-plane phonon modes as long as the magnetization has in-plane components. These distinctions may not be clearly visible in the figures due to the intersection of the ZO branch with the lower magnon branch where the TA phonon mode also hybridizes with the same magnon branch. However, it can be viewed along the line $M \to \Gamma$. Both the nearest neighbour and next-nearest neighbour planar DM components induce hybridization between in-plane phonons and magnons in all investigated magnetization directions. Additionally, the D_{xy}^{nnn} generates a more significant hybridization compared to D_{xy}^{nn} in most cases, particularly among the TA branch when the magnetization is out-of-plane. It is important to note that even if there are no apparent indications of hybridization, particularly near the Γ-point, there may still be subtle gap openings that are not readily observable. In the presence of a nonzero κ_2, the dispersion reveals that the most profound hybridization occurs among the TA branch when the magnetization lies in the plane, while the coupling to out-of-plane phonon modes is weak in all examined magnetization directions. Furthermore, it is evident that the anisotropy-based coupling exhibits stronger hybridization with in-plane phonon modes near the $\Gamma-$point compared to the DMI. It should be emphasized that these observations are not universally applicable, as they depend on the specific parameters for the phonon and magnon dispersions.

In the presence of in-plane DMI, the bare magnon dispersion becomes asymmetric when the magnetization lies in the plane. This asymmetry was previously observed in Chapter 6, where the dispersion displayed different characteristics along the symmetry lines $\Gamma \to K$ and $\Gamma \to K'$. As a result, the hybridization pattern also exhibits the same asymmetry, as evident from the figures. A similar effect is observed when κ_2 serves as the source for hybridization. While the bands exhibit asymmetry, it is only in the presence of a nonzero D_{xy}^{nn} that the bands become nonreciprocal. It is important to note that this asymmetry disappears when the magnetization is oriented out of the plane.

In addition to the avoided crossings between magnon and phonon branches, we also observe a nondegeneracy of the interacting phonon branches at the K and K' symmetry points. This gap arises due to the breaking of inversion symmetry caused by the interactions between magnons and phonons [28].

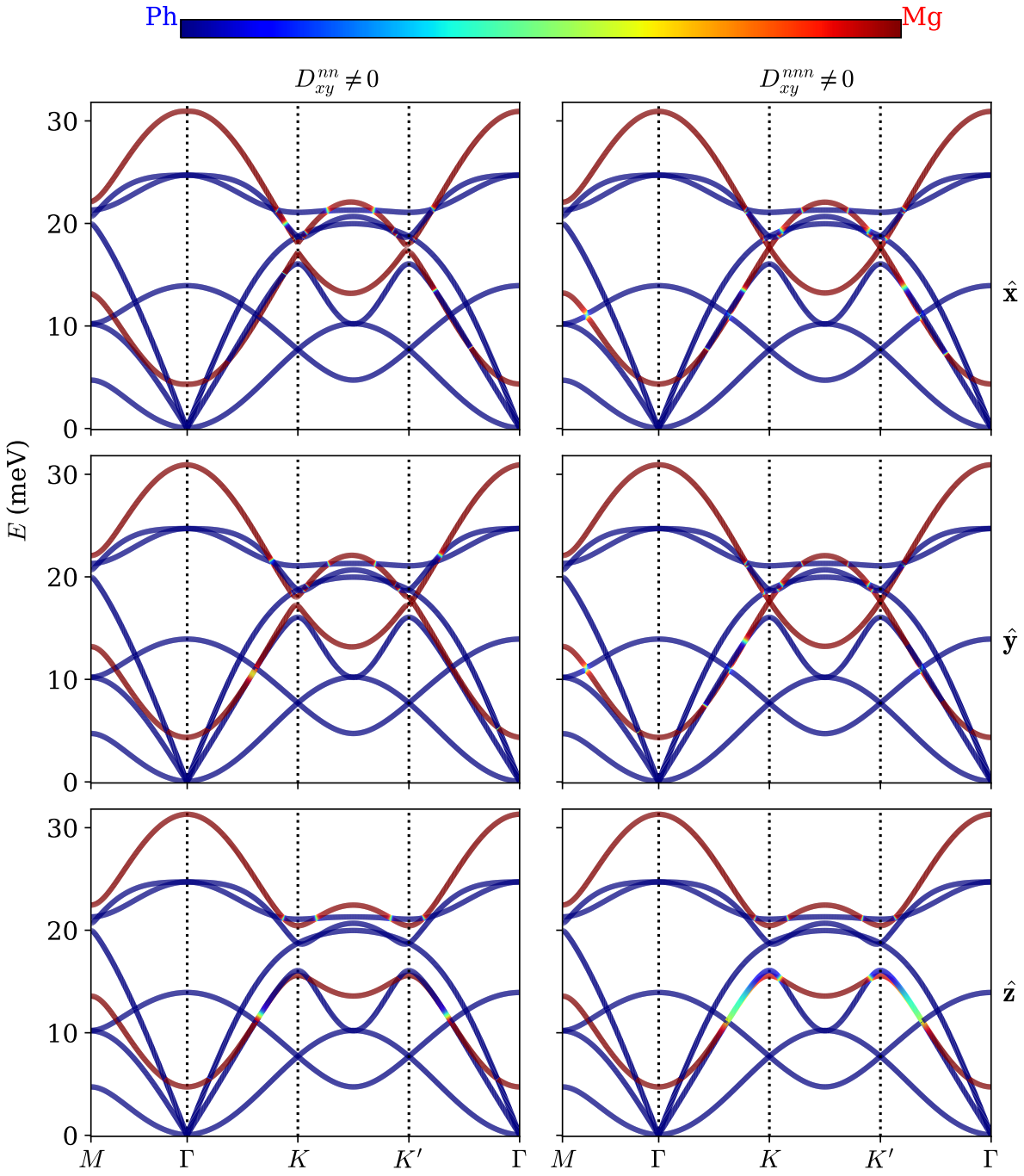

Figure 7.1.: The figures in columns show the dispersion curves for magnon-phonon excitations in a ferromagnetic honeycomb lattice, with magnetization directions $\hat{\boldsymbol{x}}$, $\hat{\boldsymbol{y}}$ and $\hat{\boldsymbol{z}}$. In the left column, the dispersion is shown with a nonzero nearest neighbour planar DM-vector component of $D_{xy}^{\mathrm{nn}} = 0.2\mathrm{meV}$, while in the the right column, it is shown with $D_{xy}^{\mathrm{nnn}} = 0.3\mathrm{meV}$. The values of the other parameters are: $\tilde{J} = 2.955$, $K_z = 0.109$, $h = 4.5$, $\hbar\Omega = 10$, $D_z^{\mathrm{nnn}} = 0.31$, in units of meV, and $\zeta = 0.2$, $S = 3/2$. The force coefficients used have the same relative relationship as those listed in equation (2.14), resulting in a phonon dispersion similar to that in graphene.

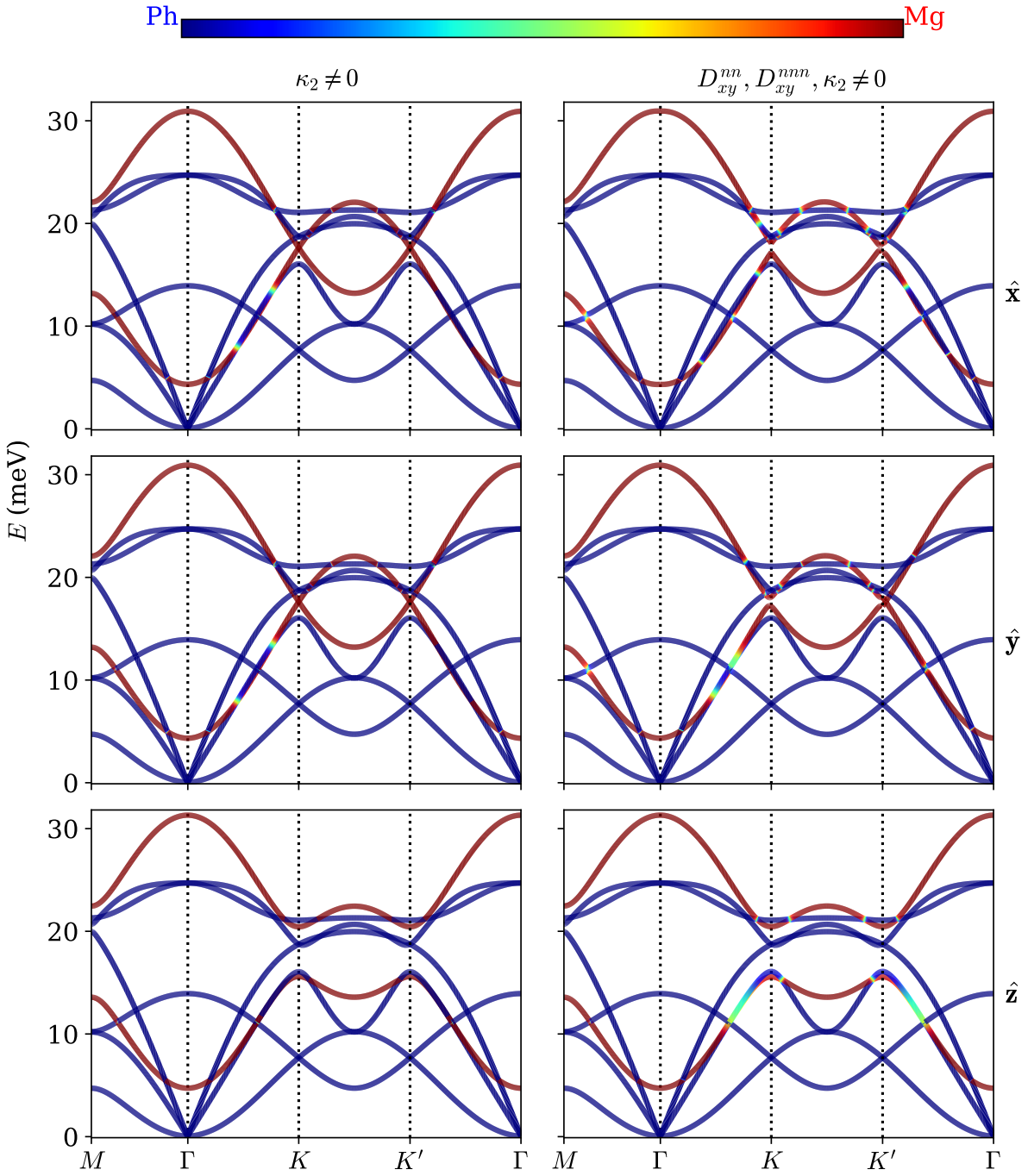

Figure 7.2.: The magnetoelastic energy spectrum is displayed for a ferromagnetic honeycomb lattice with magnetization orientations $\hat{\boldsymbol{x}}$, $\hat{\boldsymbol{y}}$ and $\hat{\boldsymbol{z}}$. The left column illustrates the dispersion with $\kappa_2 =$ 1meV as the sole source of coupling, while the right column includes $D_{xy}^{\text{nn}} = 0.2$meV, $D_{xy}^{\text{nnn}} = 0.3$meV and $\kappa_2 = 1$meV. Other parameters include $\tilde{J} = 2.955$, $K_z = 0.109$, $h = 4.5$, $\hbar\Omega = 10$, $D_z^{\text{nnn}} = 0.31$, in units of meV, and $\zeta = 0.2$, $S = 3/2$. The force coefficients have the same relative relationship as listed in equation (2.14) and yields a phonon dispersion like that in graphene.

However, the size of these gaps are too small to be visually distinguishable in the presented figures. The presence of such a gap between the phonon branches can suggest the existence of chiral phonons, which are phonons with circular polarization and exhibit opposite chirality at different valleys (K and K') [90]. Chiral phonons can possess phonon angular momentum and may exhibit a valley phonon Hall effect. However, our investigation does not delve further into this aspect. A similar gap opening is observed among the magnon bands when the magnetization lies in the plane.

While not explicitly shown in this section, we can confirm that both the second quantized method and the non-diagonalized phonon Hamiltonian approach yield consistent results, indicating complete overlap of the energy bands. However, a difference is observed at the symmetry points K and K' when using the analytically obtained phonon eigenvectors (as given by equations (2.20) and (2.23)) compared to the numerical calculation of the eigenvectors. The reason for this difference is that the analytical expression is not well-defined at these points.

7.4. Computing the Chern numbers

As demonstrated in Chapter 6, the intrinsic out-of-plane next-nearest neighbour DMI yields topological magnons characterized by Chern numbers $C = \pm 1$, provided that the magnetization has nonzero out-of-plane components. In contrast, the in-plane components of $\boldsymbol{D}_{ij}^{\mathrm{nn}}$ and $\boldsymbol{D}_{ij}^{\mathrm{nnn},r}$ do not introduce gap openings in the magnon dispersion. However, when considering the lowest order interactions between magnons and phonons, the topological properties are modified. This is because the presence of anticrossing regions between the magnon and phonon bands, along with gap openings between phonon-phonon and magnon-magnon branches, can generate localized regions of Berry curvature. These Berry curvature hot-spots have an impact on the Chern numbers.

The Chern numbers are calculated numerically by integrating the Berry curvature, equation (5.4), across the Brillouin zone. We utilize the non-diagonalized form of the phonon Hamiltonian, $H_{\mathrm{me}}^{\mathrm{nd}}(\boldsymbol{q})$, and compute the derivatives of the Hamiltonian matrix using numerical methods, specifically employing a second-order finite difference scheme. To ease the computations, we use a numerical Brillouin zone that takes the shape of a rectangle with four corners: (0,0), $(0, 4\pi/\sqrt{3}a)$, $(2\pi/a, 2\pi/\sqrt{3}a)$ and $(2\pi/a, 6\pi/\sqrt{3}a)$. The corners are located at the $\Gamma-$points of four neighbouring Wigner-Seitz unit cells. For each point in the numerical Brillouin zone, we determine the eigenvalues and eigenvectors using Colpa's method. However, the output of the numerical diagonalization procedure is sorted according to energy and not according to the band to which it belongs.

To address this challenge, we adopt a simplified approach by studying two separate isolated systems: in-plane phonon modes + magnons and out-of-plane phonon modes + magnons. By doing so, the interacting bands are naturally arranged in order of energy, thanks to the emergence of gap openings. While this approach does not provide accurate Chern numbers for the entire system, it allows us to observe intriguing characteristics. It is worth mentioning that this choice of approach was made after extensive efforts to properly sort the bands, which proved challenging due to unforeseen numerical complexities.

In addition to avoiding the complexities of a complicated sorting algorithm, we address the issue of intersections between in-plane and out-of-plane phonon branches by splitting the entire system into two subsystems. These intersections pose challenges when computing Berry curvature, as the expression is only well-defined for isolated bands. However, even in the out-of-plane phonon modes + magnons system, we still encounter singularities. This is due to the extremely small magnon-magnon

	$\hat{\boldsymbol{x}}$	$\hat{\boldsymbol{y}}$	$\hat{\boldsymbol{z}}$
Non-interacting	[0, 0, 0, 0, 0, 0, 0, 0]	[0, 0, 0, 0, 0, 0, 0, 0]	[0, 0, 0, 1, 0, 0, 0, -1]

(a) Non-interacting bands, labeled by [ZA, TA, LA, E_k^-, ZO, LO, TO, E_k^+].

	$\hat{\boldsymbol{x}}$	$\hat{\boldsymbol{y}}$	$\hat{\boldsymbol{z}}$
D_{xy}^{nn}	×	×	×
D_{xy}^{nnn}	[0, 0, 0, 0]	[0, 0, 0, 0]	×
κ_2	BC= 0	BC= 0	[0, -2, 3, -1]
$D_{xy}^{\mathrm{nn}}, D_{xy}^{\mathrm{nnn}}, \kappa_2$	[0, 0, 0, 0]	[0, 0, 0, 0]	[0, -2, 3, -1]

(b) Out-of-plane phonon modes + magnons. The labelling of the bands correspond to [ZA, E_k^-, ZO, E_k^+] around the $\Gamma-$point.

	$\hat{\boldsymbol{x}}$	$\hat{\boldsymbol{y}}$	$\hat{\boldsymbol{z}}$
D_{xy}^{nn}	BC= 0	BC= 0	[0, 0, -1, 3, -3, 1]
D_{xy}^{nnn}	[0, -1, 1, 3, -2, -1]	[0, 0, 0, 0, 0, 0]	[0, 3, -4, 2, -2, 1]
κ_2	BC= 0	BC= 0	×
$D_{xy}^{\mathrm{nn}}, D_{xy}^{\mathrm{nnn}}, \kappa_2$	[0, 1, 0, -2, 2, -1]	[0, 0, 0, 0, 0, 0]	[0, 0, -1, 0, 0, 1]

(c) In-plane phonon modes + magnons. The labelling of the bands correspond to [TA, LA, E_k^-, LO, TO, E_k^+] around the $\Gamma-$point.

Table 7.1.: Chern numbers for the particle bands with varying magnetization directions and nonzero coupling parameters, computed by diagonalizing $H_{\mathrm{me}}^{\mathrm{nd}}(\boldsymbol{q})$. Table 7.1a correspond to the non-interacting system while table 7.1b and 7.1c display the Chern numbers for the isolated systems out-of-plane phonons + magnons and in-plane phonons + magnons, respectively. Notice that we only display the Chern numbers when there is observed nonvanishing Berry curvature between interacting bands. For the cases where there is no magnon-phonon interaction (represented by ×), we refer to Table 7.1a for the Chern numbers. Moreover, in the cases with vanishing Berry curvature (represented by BC= 0), all Chern numbers are zero. We utilize the same parameters as in Figure 7.1 and 7.2.

and phonon-phonon band gaps that appear at the K and K' symmetry points, with a magnitude of $\sim 10^{-7}$meV. Although these points are not true singularities, they can cause numerical difficulties in calculations. To address this problem, we simply exclude these points from the summation whenever singularities arise.

To obtain accurate Chern numbers, a high grid resolution is required, which is defined as $(N_r \times N_r)$ grid points in the numerical Brillouin zone. This is crucial due to the presence of extremely small band gap openings, necessitating high precision. To address this challenge, we calculate the Chern numbers several times using increasing resolutions and observe convergence towards integer values, which are the expected results. Generally, a resolution of around $N_r = 1200$ is sufficient, although certain cases may demand a higher resolution, approximately $N_r = 3500$. In situations where computational efficiency is necessary, we artificially enhance the interaction strength ζ to achieve faster convergence, while maintaining the same values for the coupling parameters D_{xy}^{nn}, D_{xy}^{nnn} and κ_2.

Table 7.1b and 7.1c present the calculated Chern numbers for the interacting systems of out-of-plane phonons + magnons and in-plane phonons + magnons, respectively. Each table element correspond to a specific combination of magnetization direction ($\hat{\boldsymbol{x}}$, $\hat{\boldsymbol{y}}$ or $\hat{\boldsymbol{z}}$) and nonzero coupling parameters (D_{xy}^{nn}, D_{xy}^{nnn}, κ_2 or all combined). We utilize the same parameters for the magnon and phonon dispersion as in the previous section. Comparing with the non-interacting system (Table 7.1a), we observe that the interaction between magnons and phonons induces topological bands in the presence of a perpendicular magnetization or when the magnetization is aligned along the $x-$axis with a nonzero D_{xy}^{nnn} coupling parameter.

For the out-of-plane spin alignment, certain out-of-plane phonon modes exhibit topological properties solely in the presence of anisotropy-based coupling. In the isolated system of out-of-plane phonons + magnons, the acoustic out-of-plane phonon mode possesses a Chern number of zero, as it does not undergo anticrossings with any of the magnon branches. Similarly, the E_k^+ branch remains unaffected by the interaction and maintains a Chern number of $C = -1$. However, the ZO and E_k^- branches form anticrossing regions, leading to a redistribution of Berry curvature and thereby altering their respective Chern numbers.

Conversely, some in-plane phonon modes exhibit topological behaviour exclusively in the presence of in-plane DMI for a magnetization perpendicular to the plane. However, not all bands exhibit topological properties, as some experience multiple anticrossing regions that effectively cancel out the Berry curvature. Moreover, it is worth mentioning that certain bands, even without anticrossing regions, still possess a nonzero Chern number. This is attributed to the gap openings between phonon-phonon branches, which generate Berry curvature. The LO phonon branch serves as an example of such a case. In the isolated system of in-plane phonons + magnons with the same magnetization direction, we observe a difference in the Chern numbers between the cases where the nearest neighbour and next-nearest neighbour DMI is nonzero. Although phonon and magnon bands form anticrossing regions at the same locations, the wavefunctions are modified, resulting in different contributions to the Berry curvature and consequently the Chern numbers. Moreover, when both the nearest neighbour and next-nearest neighbour planar DM components are nonzero, the resulting Chern numbers are further modified. Additionally, our investigations reveal that by varying the relative strength of D_{xy}^{nn} and D_{xy}^{nnn}, we observe corresponding changes in the Chern numbers as the dominant interaction changes accordingly.

In cases where κ_2 or D_{xy}^{nn} is nonzero and the magnetization lies in the plane, we find a vanishing Berry curvature. Although the system exhibits interactions and anticrossing regions between magnon and phonon branches, the resulting wavefunctions possesses topologically trivial properties, resulting in Chern numbers of zero. However, perturbing the magnetization to have nonzero out-of-plane components, Berry curvature appears at the avoided crossings and the bands are of topological nature.

This pattern does not hold true when D_{xy}^{nnn} is the coupling source, generating Berry curvature at the anticrossing regions in all examined magnetization directions. However, even in this scenario, the Chern numbers remain zero when the magnetization lies in the plane for the out-of-plane phonons + magnons system, or when the magnetization is oriented along the $y-$axis for the in-plane phonons + magnons system. This cancellation of Chern numbers arises from the balanced distribution of Berry curvature, effectively canceling out the net contribution when integrated over the Brillouin zone. By perturbing the magnetization direction away from the $y-$axis for the in-plane phonons + magnons system, we break the symmetry of the Berry curvature distribution, resulting in nonzero Chern numbers. However, for the out-of-plane phonons + magnons system, achieving topological

bands requires tilting the magnetization away from the lattice plane. Furthermore, we observe different Chern numbers for the in-plane phonons + magnons system when the magnetization is along the $x-$axis, comparing the case where solely D_{xy}^{nnn} is nonzero and the case where D_{xy}^{nn}, D_{xy}^{nnn} and κ_2 are all nonzero. One would expect identical Chern numbers since the next-nearest neighbour DMI is the only coupling parameter contributing to the Berry curvature. However, the nearest neighbour in-plane DMI induces a shift in the magnon dispersion, causing the anticrossings to occur at different locations, thereby resulting in different Chern numbers.

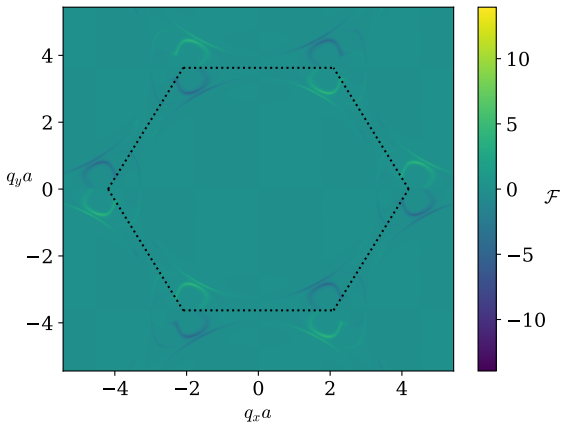

(a) Berry curvature calculated using $H_{\mathrm{me}}^{\mathrm{nd}}(\boldsymbol{q})$.

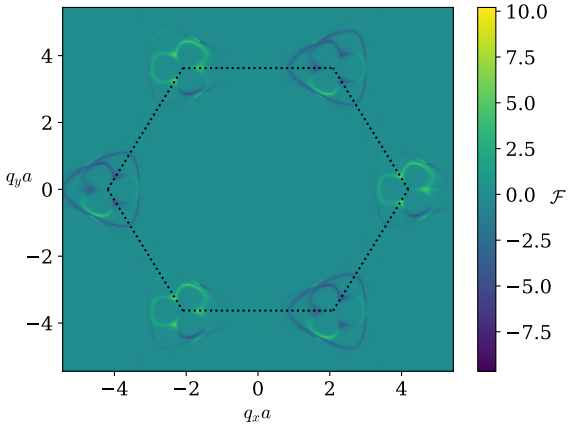

(b) Berry curvature calculated using $H_{\mathrm{me}}^{\mathrm{sq}}(\boldsymbol{q})$ and analytical phonon eigenvectors.

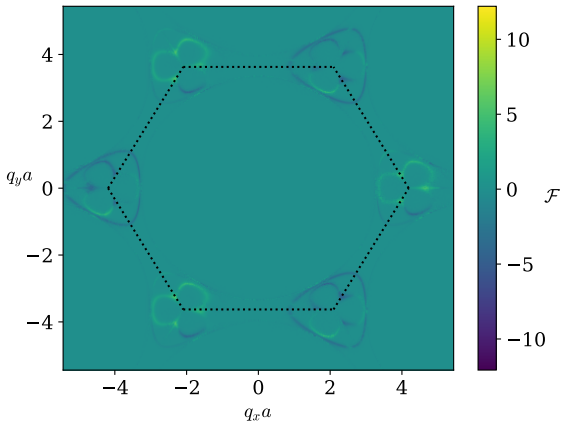

(c) Berry curvature calculated using $H_{\mathrm{me}}^{\mathrm{sq}}(\boldsymbol{q})$ and numerical phonon eigenvectors.

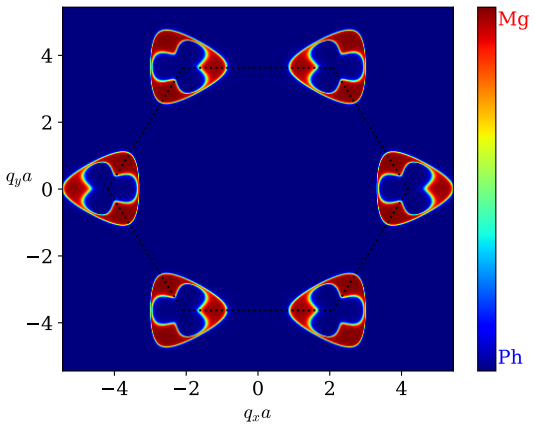

(d) Magnon and phonon part of the wavefunction.

Figure 7.3.: Figure a) to c) show the Berry curvature obtained through different computational methods. Specifically, we present the Berry curvature distribution across the Brillouin zone for the fifth band, which corresponds to the TO phonon branch near the $\Gamma-$point, in the system composed of in-plane phonons + magnons. The hybridization is solely influenced by $D_{xy}^{\mathrm{nnn}} = 0.3\mathrm{meV}$, with $\zeta = 0.2$, and a magnetization oriented along the $y-$axis. The Berry curvature is expressed in terms of the function $\mathrm{sgn}(\mathcal{F}(\boldsymbol{q}))\ln(1+\mathcal{F}(\boldsymbol{q}))$. Additionally, panel d) indicates regions where the magnon or phonon part of the wavefunction is dominant. The remaining parameters are consistent with those employed in section 7.3, namely $\tilde{J} = 2.955\,\mathrm{meV}$, $S = 3/2$, $K_z = 0.109\,\mathrm{meV}$, $h = 4.5\mathrm{meV}$ and $\hbar\Omega = 10\mathrm{meV}$.

7.4.1. Comparison using $H^{\mathsf{sq}}_{\mathsf{me}}(\boldsymbol{q})$ and $H^{\mathsf{nd}}_{\mathsf{me}}(\boldsymbol{q})$

The Chern numbers were calculated using $H^{\mathrm{nd}}_{\mathrm{me}}(\boldsymbol{q})$ due to the limitations of the second quantized approach in numerical calculations, which relies on smooth phonon eigenvectors. Ref [19] highlights the challenge of obtaining smoothly defined numerical phonon eigenvectors, rendering the Hamiltonian matrix $H^{\mathrm{sq}}_{\mathrm{me}}(\boldsymbol{q})$ problematic. The analytical expression for phonon eigenvectors also encounters difficulties across the Brillouin zone, leading to different results. To demonstrate this, Figure 7.3 presents contour plots of the Berry curvature obtained with $H^{\mathrm{nd}}_{\mathrm{me}}(\boldsymbol{q})$ and $H^{\mathrm{sq}}_{\mathrm{me}}(\boldsymbol{q})$ using both numerical and analytical phonon eigenvectors. Specifically, the Berry curvature for the fifth band in the isolated in-plane phonon modes + magnons system is presented, with a planar next-nearest neighbour DM vector component and a magnetization along the $y-$axis. Notably, Figure 7.3c reveals discontinuities in the Berry curvature when using numerical phonon eigenvectors, forming a dotted pattern. While the use of analytical phonon eigenvectors reduces the degree of discontinuity, discrepancies persist when compared to the non-diagonalized form of the phonon Hamiltonian. These observations are consistent with the discrepancies observed in the magnetoelastic energy spectrum, which arise from the lack of well-defined analytical expressions for the phonon eigenvectors at certain locations in the Brillouin zone.

Figure 7.3d illustrates the regions where the wavefunction exhibits characteristics resembling either magnons or phonons for the same interacting band. In this configuration, where the magnetization lies in the plane and the bare magnon bands possess topologically trivial properties, the emergence of Berry curvature is solely attributed to the interaction between magnons and phonons. When comparing this figure with the contour plot of the Berry curvature, we observe that Berry curvature hot-spots precisely arise at the locations of the hybridization rings. Furthermore, we notice the presence of additional Berry curvature lines that are not associated with the hybridization rings. These lines emerge as a result of the gap openings between phonon-phonon branches.

For this particular band, as well as for all bands when the magnetization is aligned in the $\hat{\boldsymbol{y}}$ direction and a nonzero next-nearest neighbour planar DM vector is considered, the corresponding Chern number is zero. This occurs due to the balanced distribution of Berry curvature, which, when summed over the Brillouin zone, results in a vanishing overall effect. By further analysing the symmetry, we observe that the Berry curvature satisfies

$$(\boldsymbol{m} \,||\, \hat{\boldsymbol{y}}): \quad \mathcal{F}_n(q_x, q_y) = -\mathcal{F}_n(-q_x, q_y), \text{ and } \mathcal{F}_n(q_x, q_y) = -\mathcal{F}_n(q_x, -q_y).$$

This symmetry of the Berry curvature is demonstrated in Figure 7.3a, serving as a compelling example of how bands can possess finite Berry curvature despite being topologically trivial.

7.5. Transport properties

In experimental settings, transport properties in materials can be measured to probe the presence of finite Berry curvature and characterize the materials accordingly [29, 47]. In magnonic systems, two notable transport phenomena associated with Berry curvature are the thermal Hall effect and the spin Nernst effect. While the observation of these transport effects does not definitively prove the existence of a topological system, they are typically associated with bands that possess nonzero Chern numbers, thus serving as an indication of a topological system. In this section, our main focus is on calculating the thermal Hall conductivity and the spin Nernst coefficient which arise from the Berry curvature in momentum space within the interacting magnon-phonon system.

7.5.1. Thermal Hall conductivity

The thermal Hall conductivity, κ_{xy}, is calculated using equation (5.5), where the Berry curvature is obtained from $H_{\mathrm{me}}^{\mathrm{nd}}(\boldsymbol{q})$. To evaluate the summation over $\boldsymbol{q}$ in momentum space, we convert the expression into an integral with the following relation [16]

$$\frac{1}{\mathcal{A}}\sum_{q} \rightarrow \int_{\mathrm{BZ}} \frac{\mathrm{d}^2 q}{(2\pi)^2}.$$

In our calculation, we consider the entire system of both phonon and magnon bands, and there is no need to sort the bands since we sum over the Berry curvature of all particle bands at each point in the numerical Brillouin zone. However, we observe that the full system exhibits additional singularities caused by the intersection of in-plane and out-of-plane phonon branches. To avoid these singularities, we only include bands in the summation that have a gap to adjacent bands larger than a threshold value of approximately 10^{-4}meV. We have validated the effectiveness of this approach by comparing the thermal Hall conductivity computed in the full system using the threshold value to the case of an in-plane phonons + magnons system, where only in-plane phonons interact with magnons. Furthermore, we find that the non-interacting case, consisting solely of topological magnons, agrees completely with the full system when using this threshold value.

To provide a simplified explanation of how conductivity arises, we examine a specific point in momentum space where a gap forms between two branches. At this point, the Berry curvature for the lower and upper bands exhibits equal magnitudes but opposite signs. For instance, let's assume the lower band has a positive Berry curvature while the upper band has a negative Berry curvature. In this case, the contribution to the thermal Hall conductivity at this particular point is proportional to

$$\left(c_2[g_{\mathrm{BE}}(\mathcal{E}_{q,2})] - c_2[g_{\mathrm{BE}}(\mathcal{E}_{q,1})]\right)|\mathcal{F}_q|, \tag{7.3}$$

where $\mathcal{E}_{q,1}$ represents the lower branch, while $\mathcal{E}_{q,2}$ represents the upper branch, and $|\mathcal{F}_q|$ represents their mutual Berry curvature magnitude. We notice that the thermal Hall conductivity depends on both the size of the band gap and the magnitude of the Berry curvature (which is also indirectly influenced by the energy gap), and is expected to rise as the band gap expands. Additionally, as $c_2[g_{\mathrm{BE}}(\mathcal{E}_{q,n})]$ decreases with increasing energy, we observe that $c_2[g_{\mathrm{BE}}(\mathcal{E}_{q,2})]$ is smaller than $c_2[g_{\mathrm{BE}}(\mathcal{E}_{q,1})]$, resulting in a negative contribution to the conductivity. Conversely, if the upper band demonstrates positive Berry curvature, it contributes positively to the conductivity.

To compare the thermal Hall conductivity for different magnetization directions, we focus on the case where the next-nearest neighbour DMI is nonzero, as the other coupling sources (anisotropy-based coupling and nearest neighbour DMI) do not generate any Berry curvature when the magnetization lies in the plane, resulting in a trivial case with no thermal Hall conductivity. Specifically, we use the same parameters for the magnon and phonon dispersion as described in section 7.3, with $D_{xy}^{\mathrm{nnn}} = 0.3$meV and $\zeta = 0.2$. Figure 7.4 presents the thermal Hall conductivity resulting from the interaction between magnons and phonons, plotted as a function of temperature for magnetization directions along $\hat{\boldsymbol{x}}$, $\hat{\boldsymbol{y}}$ and $\hat{\boldsymbol{z}}$. It is important to note that when the magnetization is perpendicular to the plane, resulting in topological magnons, we subtract the conductivity originating from the non-interacting system to focus solely on the contributions arising from magnon-phonon interactions. The thermal Hall conductivity, measured in SI units, is on the order of 10^{-13}W/K, which is comparable to previous studies [18, 28]. Moreover, we observe a notable increase in positive conductivity for a magnetization perpendicular to the plane in comparison to in-plane magnetization directions at higher temperatures. This distinction can primarily be attributed to the disparities in magnon dispersion between in-plane and out-of-plane magnetization directions. Additionally, in the perpendicular alignment, spin interactions are

exclusively hybridized with in-plane phonon modes. Interestingly, we have discovered that by tuning the strength of D_z^{nnn} in the perpendicular magnetization direction, new anticrossing regions emerge, leading to significant fluctuations in the conductivity. This highlights the sensitivity of the conductivity to the parameters that govern the magnon dispersion.

The thermal Hall conductivity exhibits varying signs for both the $\hat{\boldsymbol{x}}$ and $\hat{\boldsymbol{z}}$ magnetization directions. At low temperatures, only the interaction between the LA phonon branch and the lower magnon band becomes thermally significant. In this regime, the lower band acquires a positive Berry curvature, while the upper band possesses negative Berry curvature, leading to a negative conductivity. However, as the temperature rises, additional band gaps become thermally activated, causing a change in sign.

The conductivity is negligibly small, approximately 10^{-16}W/K, when the magnetization is aligned along the $y-$axis compared to other magnetization directions. However, after conducting several tests with different grid resolutions, we have observed that this value is not numerically stable. The conductivity alternates around zero due to the lack of symmetry in grid points around the hybridization rings, resulting in nonzero values. Nevertheless, the true value, which is challenging to obtain numerically, is expected to be zero. This expectation arises from the complete balance in the distribution of Berry curvature. Specifically, for each band gap that contributes to the conductivity according to equation (7.3), there exists a corresponding band gap elsewhere in the Brillouin zone where the bands exhibit opposite Berry curvature, leading to a negative contribution. Consequently, the net conductivity should be zero. This finding strengthens the idea that a nonzero conductivity can serve as an indicator of a topological system.

Moving forward, it is interesting to compare the different parameters D_{xy}^{nn}, D_{xy}^{nnn} and κ_2 as sources for

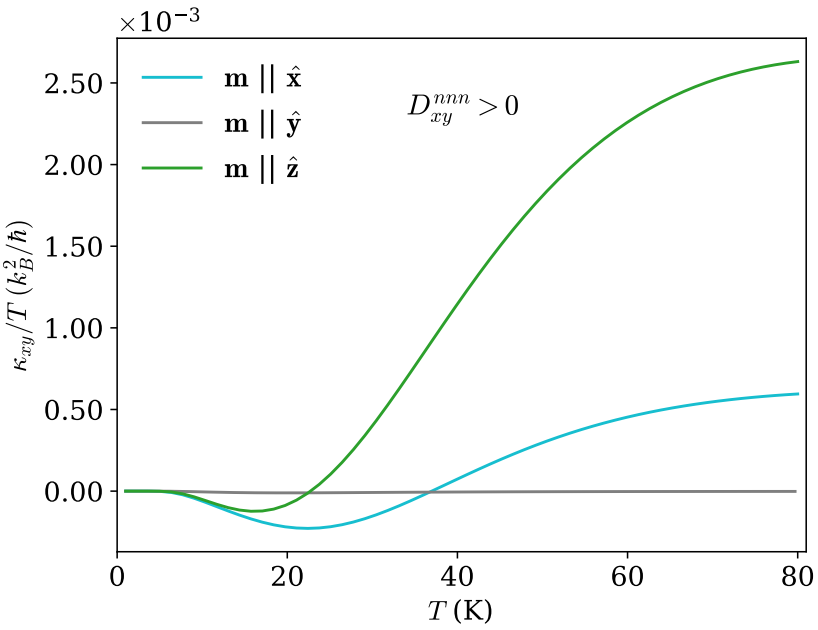

Figure 7.4.: The thermal Hall conductivity that arises solely from interactions between magnons and phonons are presented as a function of temperature. The interaction is solely driven by $D_{xy}^{\text{nnn}} = 0.3$meV, and we compare the conductivity generated in the magnetization directions $\hat{\boldsymbol{x}}$, $\hat{\boldsymbol{y}}$ and $\hat{\boldsymbol{z}}$. Furthermore, we utilize $\zeta = 0.2$ while the remaining parameters for the magnon and phonon dispersion are alike the ones used in Figure 7.1 and 7.2.

hybridization and their impact on the thermal Hall effect. To facilitate this comparison, we consider the out-of-plane magnetization direction and use the same effective interaction strength in all cases. The effective interaction strengths are defined as the prefactors in front of the vectors in equation (7.2). By setting these strengths equal, we obtain the following relationships: $D_{xy}^{\mathrm{nnn}} = \sqrt{3} D_{xy}^{\mathrm{nn}}$ and $D_{xy}^{\mathrm{nnn}} = \kappa_2 / 2\sqrt{3}$, with $S = 3/2$. Using the value $D_{xy}^{\mathrm{nnn}} = 0.3\mathrm{meV}$, we find that $D_{xy}^{\mathrm{nn}} = 0.173\mathrm{meV}$ and $\kappa_2 = 1.04\mathrm{meV}$ approximately satisfy the requirements. Employing these values, we calculate the thermal Hall conductivity, which is presented in Figure 7.5a. Additionally, we include the case without magnon-phonon interactions, where only the topological magnons contribute to the conductivity. We observe a significant conductivity magnitude in all scenarios, on the order of $10^{-11}\mathrm{W/K}$, which is comparable to the findings in Ref. [26] where they used a lower value for D_z^{nnn}. However, it is worth noting that the interactions have only a minor effect on the conductivity, primarily due to the relatively low interaction strength compared to the magnon energy. By using $\bar{D}_{xy}^{\mathrm{nnn}} = \zeta S D_{xy}^{\mathrm{nnn}} \sqrt{S/6}$ as the effective interaction strength, the relative strength is approximately given by $\bar{D}_{xy}^{\mathrm{nnn}} / \tilde{J} S \approx 0.01$.

Upon examining Figure 7.5b, which displays the contribution to the conductivity arising solely from magnon-phonon interactions in the perpendicular magnetization direction, a significant difference between the DMI and anisotropy contributions become apparent. Unlike the DMI, the anisotropy contribution exhibits nonzero values at low temperatures. One possible explanation for this disparity is the emergence of a slightly negative Berry curvature in the ZA phonon branch around the Γ-points in the presence of a nonzero κ_2. This negative curvature contributes to a positive conductivity. Interestingly, this effect diminishes as the ZA branch scales linearly, highlighting its unique behaviour in two-dimensional materials. However, the underlying reason for the existence of this nonzero Berry curvature near the Brillouin center remains unclear.

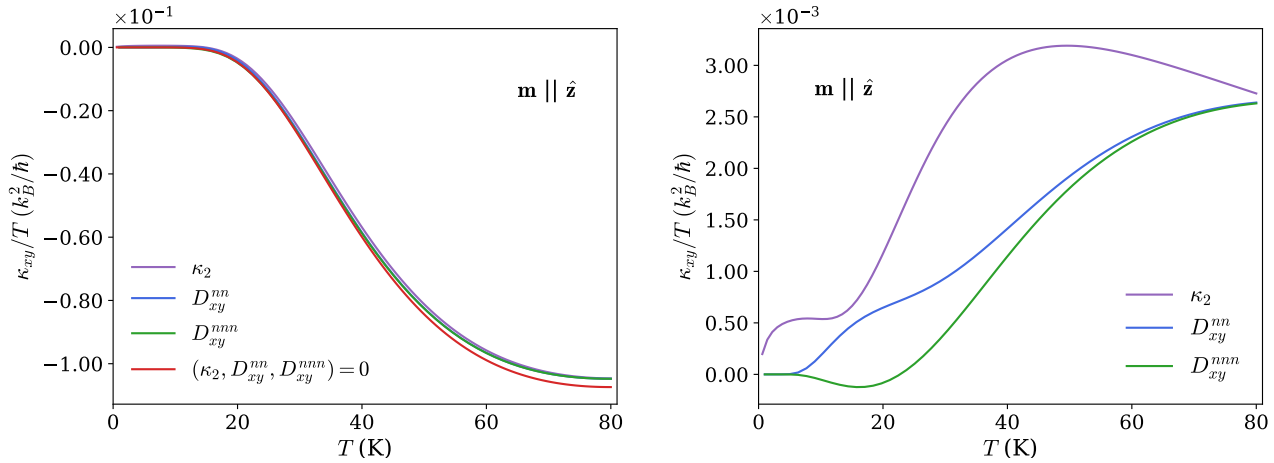

Figure 7.5.: The thermal Hall conductivity is plotted as a function of temperature when the magnetization is perpendicular to the plane. Three cases are considered: κ_2, D_{xy}^{nn} and D_{xy}^{nnn} representing the nonzero coupling parameter, with values of 1.04meV, 0.173meV and 0.3meV respectively. In Figure a), the effects of the interaction are compared to the non-interacting system, while Figure b) specifically shows the conductivity resulting solely from magnon-phonon interactions. The same parameters for the magnon and phonon dispersion as in section 7.3 are used, with $\zeta = 0.2$.

7.5.2. Spin Nernst coefficient

By utilizing equation (5.7), we calculate the spin Nernst coefficient, α_{xy}. The spin excitation operator, $\mathcal{S}$, takes the form of a diagonal matrix in which the elements associated with magnon operators possess a value of -1, while the remaining elements are zero. Following a similar approach as the analysis of the thermal Hall conductivity, we investigate two different scenarios. Firstly, we consider a nonzero D_{xy}^{nnn} with different magnetization directions, focusing on the contribution arising from magnon-phonon interactions. Secondly, we examine the case of a magnetization perpendicular to the plane with varying coupling parameters κ_2, D_{xy}^{nn} and D_{xy}^{nnn}, in addition to the non-interacting case where all coupling parameters are zero. The results are presented in Figure 7.6a and 7.6b, respectively.

When comparing the contribution of magnon-phonon interactions to the spin Nernst coefficient in the presence of a nonzero D_{xy}^{nnn}, we observe a nonvanishing spin Nernst coefficient for all examined magnetization directions. The magnitude of the coefficient is similar in all cases, but the sign varies. A positive coefficient is observed when the magnetization is oriented along $\hat{\boldsymbol{y}}$, while negative contributions are observed for the directions $\hat{\boldsymbol{x}}$ and $\hat{\boldsymbol{z}}$. In contrast to the thermal Hall conductivity shown in Figure 7.4, the spin Nernst coefficient does not change sign when increasing the temperature. This difference can be attributed to the distinct distribution of the conventional Berry curvature and the spin Berry curvature. Furthermore, we find that the magnitude of the spin Nernst coefficient resulting from magnon-phonon interactions is an order of magnitude lower compared to the results reported in Ref. [54], where magnon-phonon interactions in a honeycomb ferrimagnet were studied, and two orders of magnitude lower than in a bilayer antiferromagnet [80].

Interestingly, even in cases where the bands exhibit topologically trivial behaviour (such as when the magnetization aligns with $\hat{\boldsymbol{y}}$), we still observe a nonvanishing spin Nernst coefficient. The nonvanishing spin current arises from the spin Berry curvature, which, unlike the conventional Berry curvature, is not directly linked to the Chern number [80]. In contrast, the thermal Hall conductivity remains zero, indicating that the system exhibits a spin current while the heat current vanishes. Consequently, there must exist a counteracting phonon current that opposes and cancels out the spin current. Systems exhibiting these characteristics are highly intriguing in the field of magnon spintronics [57].

When considering a magnetization direction perpendicular to the plane, the inclusion of either coupling parameter in the magnon-phonon interaction leads to a modest renormalization of the spin Nernst coefficient. This can be attributed to the relatively weak interaction strength compared to the energy of the magnons, as discussed earlier. By further breaking the mirror symmetry and increasing the strength of the in-plane DMI, a more pronounced renormalization effect is anticipated. However, it is important to note that in this study, we employed an artificially large value for ζ, which suggests that weaker renormalization effects would be expected in practical measurements. Our findings reveal that the magnitude of the spin Nernst coefficient, in the absence of magnon-phonon interactions, is consistent with previous studies conducted in various systems. For example, comparable magnitudes have been observed in studies involving a kagome lattice ferromagnet with DMI [91] or a noncollinear antiferromagnet [79].

The expression for the spin Nernst coefficient employed in this study is derived from linear response theory. Alternatively, a semiclassical approach can be utilized to derive a similar expression. However, it should be noted that the semiclassical approach is not suitable for situations where spin is not conserved, such as in the presence of magnon-phonon interactions. In Appendix C, we present the results obtained using the semiclassical approach, along with a discussion on the numerical convergence challenges associated with this method.

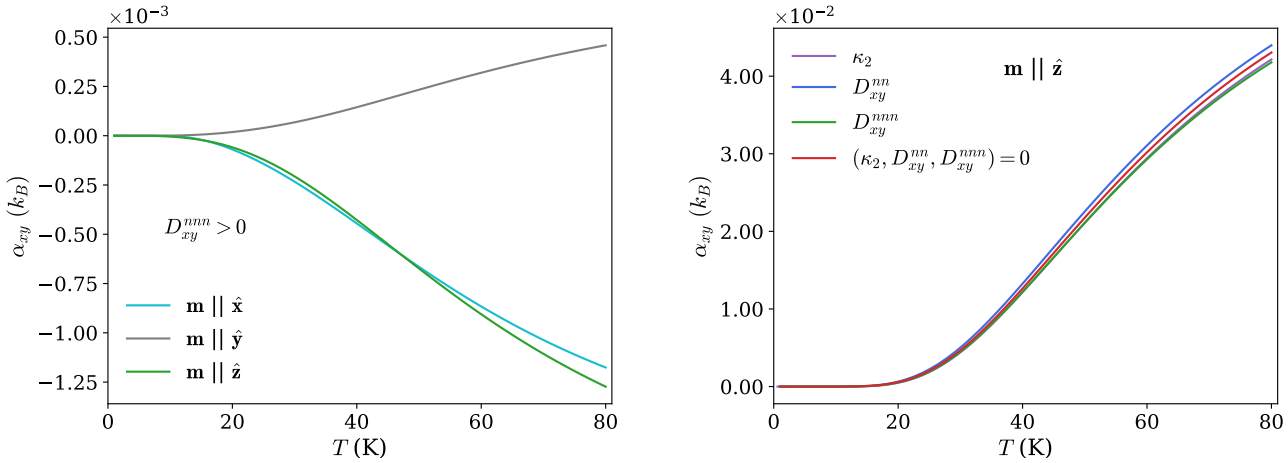

Figure 7.6.: Spin Nernst coefficient as a function of temperature. In panel a), we showcase the magnon-phonon interaction contribution to the coefficient due to an in-plane next-nearest neighbour DMI, and compare with different magnetization directions $\hat{\boldsymbol{x}}$, $\hat{\boldsymbol{y}}$ and $\hat{\boldsymbol{z}}$. In panel b), the coefficient is displayed when the magnetization is perpendicular to the plane and we consider the cases where either κ_2, D_{xy}^{nn} or D_{xy}^{nnn} has nonzero values, in addition to the scenario where all are zero which corresponds to the non-interacting system. We utilize the values $\kappa_2 = 1.04\mathrm{meV}$, $D_{xy}^{\mathrm{nn}} = 0.173\mathrm{meV}$, $D_{xy}^{\mathrm{nnn}} = 0.3\mathrm{meV}$, $\zeta = 0.2$ and the remaining parameters for the magnon and phonon dispersion are alike the ones used in section 7.3.

CHAPTER 8

Conclusion and Outlook

In this thesis, we have established the necessary theoretical framework for investigating the hybridization of magnons and phonons in a ferromagnetic honeycomb layer with adjustable magnetization direction via an external magnetic field. By considering symmetry constraints, we determined the phonon dispersion up to third neighbour interactions, resulting in a phonon spectrum that accurately matches the experimentally observed dispersion in graphene. This includes the presence of out-of-plane phonon modes with quadratic scaling. Additionally, we accounted for mirror symmetry breaking with respect to the lattice plane and utilized a generalized form of the Dzyaloshinskii-Moriya vector to derive the magnon dispersion. Utilizing literature values representing the magnon dispersion in CrI_3 and matching the phonon spectrum with the high-frequency branches found in the same material, we computed the magnetoelastic energy spectrum, taking into account the lowest order contributions to the interacting Hamiltonian. Notably, the calculations specifically accounted for three sources of hybridization: nearest neighbour and next-nearest neighbour in-plane Dzyaloshinskii-Moriya interaction, as well as magnetic anisotropy.

The obtained results demonstrate the emergence of a hybridized magnon-polaron state at the regions of anticrossing between magnon and phonon branches. It is revealed that these regions exhibit the generation of Berry curvature when the magnetization possesses nonzero out-of-plane components. Moreover, even in cases where the magnetization lies within the plane, the presence of a next-nearest neighbour planar DM vector induces Berry curvature in these regions. Furthermore, we witness the emergence of band gaps between both phonon-phonon and magnon-magnon branches, attributed to the inversion symmetry breaking caused by magnon-phonon interactions. These gap openings contribute to the generation of Berry curvature, thereby influencing the Chern numbers. By conducting a topological analysis of the magnon-polaron bands, it is concluded that the interaction between magnons and phonons enhances the pre-existing topology by assigning nonzero Chern numbers to multiple initial phonon branches. Additionally, the in-plane next-nearest neighbour DMI can induce topological bands from initially uncoupled trivial bands when the magnetization lies within the plane.

The findings indicate that when the magnetization is perpendicular to the lattice plane, magnon-phonon interactions cause a renormalization of the thermal Hall conductivity and spin Nernst coefficient. However, this renormalization effect is relatively weak and challenging to distinguish from uncertainties originating from the parameters of the magnetoelastic Hamiltonian. Moreover, the extent of renormalization is highly sensitive to variations in the magnon and phonon dispersions. As a result, experimental verification of such coupling may present difficulties when considering this magnetization direction. On the other hand, when the magnetization lies in the plane and uncoupled magnons do not exhibit a Hall response to an applied temperature gradient, we observed a nonvanishing thermal Hall conductivity and spin Nernst coefficient due to the presence of an in-plane next-nearest neighbour Dzyaloshinskii-Moriya interaction. This distinct feature, unlike other sources of hybridization, serves as a valuable tool for identifying the presence of such magnon-phonon interactions in a material. Of particular interest is the situation where the magnetization is aligned along the $y-$axis, as it gives rise to a scenario where a spin current is opposed by a phonon current, resulting in the cancellation of the transverse thermal flow in the system. The discoveries made in this thesis are anticipated to offer valuable insights into the topological aspects of magnon-phonon interactions and hold promise

for potential applications in the field of spin caloritronics.

To conduct a more comprehensive study of our model, several interesting avenues can be explored. Firstly, it would be intriguing to investigate whether the phonons exhibit chiral properties at the gap openings of K and K' points, similar to what has been observed in analogous antiferromagnetic systems. Such chiral phonons could potentially enable applications in valley Hall effects [28]. Additionally, exploring the formation of magnon-polarons in a finite ribbon geometry would be valuable. Comparing the effects of different magnetization directions becomes particularly intriguing in systems with armchair edges, as the presence of edge phonons may play a significant role [27]. Furthermore, while the spin Nernst current does not guarantee edge spin accumulation due to the spin non-conserving nature emerging from the magnon-phonon interactions, it would be informative to calculate the spin density to verify this aspect [54]. Spin accumulation serves as a measurable quantity in experiments and can provide evidence for the existence of magnon-phonon interactions. Although the main focus of this study was on responses to an applied temperature gradient, it is worth noting that magnons can also generate a spin current in the presence of a magnetic field gradient, known as the spin Hall effect of magnons [16, 92]. Conducting a similar calculation of the spin Hall conductivity would be intriguing.

As part of future research directions, we suggest investigating analogous antiferromagnetic systems that demonstrate similar types of magnon-phonon interactions and exploring their behaviour under varying magnetization directions. Recent studies have demonstrated the tunability of transport properties in such systems through the application of an external magnetic field [28, 54, 80], which makes them particularly interesting for spintronics applications. In antiferromagnets, the presence of an external field can lead to the splitting of degenerate magnon bands, and the magnitude of the field determines the size of the magnon band gap. Additionally, we propose investigating magnon-phonon interactions arising from other important magnetic exchange interactions, such as the Kitaev interaction. By conducting a comparative analysis of magnetoelastic modes and transport properties, considering magnon-phonon interactions arising from both the Dzyaloshinskii-Moriya interaction and the Kitaev interaction, novel experimental approaches may be discovered to determine the dominant interaction in the material.

APPENDIX A

Calculation of phonon dispersion with a spring force model

The spring force model considers the directional forces between adjacent ions, similar to how a spring connects the ions. Ions that are equidistant from each other are assigned the same spring constant. Specifically, the nearest neighbours are assigned the spring constant C_1, while the next-nearest neighbours are assigned C_2, and so on. The relationship between the in-plane force coefficients and the spring constants is given by [31]

$$\Phi_{\mu\nu}^{\alpha\beta}(\boldsymbol{\Delta}) = -C^{\alpha\beta}(\boldsymbol{\Delta})\hat{\boldsymbol{\Delta}}_\mu\hat{\boldsymbol{\Delta}}_\nu, \tag{A.1}$$

where $\hat{\boldsymbol{\Delta}}_\mu = \boldsymbol{\Delta}_\mu/|\boldsymbol{\Delta}|$ is the μ-component of the unit vector to one of the neighbours.

A.1. Square lattice

The phonon dispersion in a monoatomic square lattice is calculated by considering interactions up to the next-nearest neighbours. In this case, the (α, β) indices become irrelevant. The lattice is situated in the $xy-$plane, and the ions can move in three dimensions. The vectors connecting neighbouring ions are described in equation (2.13). The presence of $z \to -z$ mirror symmetry allows us to distinguish between the in-plane and out-of-plane modes [39].

In-plane modes

The nonzero in-plane force coefficients, computed with the above-mentioned equation (A.1), are given by

$$\begin{aligned}
&\Phi_{xx}(\boldsymbol{\delta}_{1,3}) = \Phi_{yy}(\boldsymbol{\delta}_{2,4}) = -C_1,\\
&\Phi_{xx}(\boldsymbol{\tau}_{1,2,3,4}) = \Phi_{yy}(\boldsymbol{\tau}_{1,2,3,4}) = \Phi_{xy}(\boldsymbol{\tau}_{1,3}) = \Phi_{yx}(\boldsymbol{\tau}_{1,3}) = -\frac{C_2}{2},\\
&\Phi_{xy}(\boldsymbol{\tau}_{2,4}) = \Phi_{yx}(\boldsymbol{\tau}_{2,4}) = \frac{C_2}{2},
\end{aligned}$$

and the nonzero self-force coefficients, found from the stability condition (2.12), are

$$\begin{aligned}
\Phi_{xx}(0) &= 2(C_1 + C_2),\\
\Phi_{yy}(0) &= 2(C_1 + C_2).
\end{aligned}$$

We compute the matrix elements of the dynamical matrix $D(\boldsymbol{q})$ with equation (2.11), and obtain

$$\begin{aligned}
D_{xx}(\boldsymbol{q}) =& \frac{2C_1}{M}(1 - \cos(q_x a)) + \frac{2C_2}{M}(1 - \cos(q_x a)\cos(q_y a)),\\
D_{xy}(\boldsymbol{q}) =& D_{yx}(\boldsymbol{q}) = \frac{2C_2}{M}\sin(q_x a)\sin(q_y a),\\
D_{yy}(\boldsymbol{q}) =& \frac{2C_1}{M}(1 - \cos(q_y a)) + \frac{2C_2}{M}(1 - \cos(q_x a)\cos(q_y a)).
\end{aligned}$$

Thus, the eigenvalues of the in-plane phonon branches are as follows

$$\omega_{\mathrm{TA}}^2 = \frac{D_{xx}+D_{yy}}{2} - \sqrt{\left(\frac{D_{xx}-D_{yy}}{2}\right)^2 + (D_{xy})^2},$$
$$\omega_{\mathrm{LA}}^2 = \frac{D_{xx}+D_{yy}}{2} + \sqrt{\left(\frac{D_{xx}-D_{yy}}{2}\right)^2 + (D_{xy})^2}.$$

Out-of-plane modes

Considering that equation (A.1) is applicable only to the in-plane force coefficients, we represent the force coefficients for the first and second nearest neighbours in the out-of-plane direction as $-C_1^z$ and $-C_2^z$, respectively. Consequently, the mode corresponding to the out-of-plane motion is expressed as

$$\begin{aligned}\omega_{\mathrm{ZA}}^2 &= D_{zz}(\boldsymbol{q}) \\ &= \frac{2C_1^z}{M}(2-\cos(q_x a)-\cos(q_y a)) + \frac{4C_2^z}{M}(1-\cos(q_x a)\cos(q_y a)).\end{aligned}$$

The dispersion

The more general method used in section 2.3.1 reduce to the spring force model if $C_1 = -\gamma_1$, $C_2 = -2\rho_1 = -2\rho_2$, $C_1^z = -\gamma_z$, $C_2^z = -\rho_z$ and all other force coefficients are set equal to zero. Figure A.1 shows the phonon dispersion obtained with the spring force model in a square lattice along the

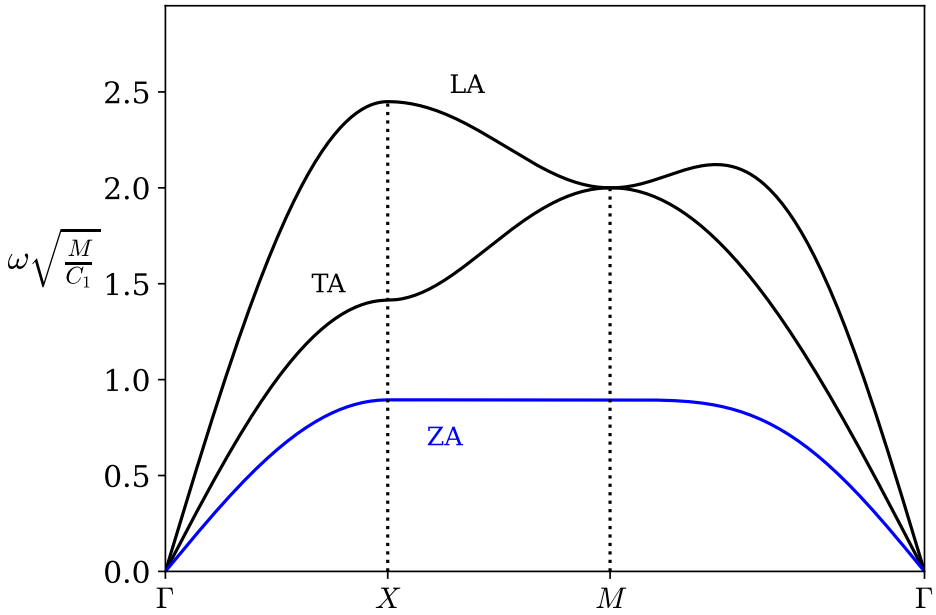

Figure A.1.: The three acoustic branches of the phonon dispersion in a square lattice, longitudinal (LA), transverse (TA) and out-of-plane (ZA), are shown along the symmetry lines of the Brillouin zone. The frequency is given in units of $\sqrt{C_1/M}$, with the following values for the spring constants $C_2/C_1 = 1/2$, $C_1^z/C_1 = 1/10$ and $C_2^z/C_1 = 1/20$.

symmetry lines of the Brillouin zone. The dispersion is shown in unit of $\sqrt{C_1/M}$ and the values of the spring constants are $C_2/C_1 = 1/2$, $C_1^z/C_1 = 1/10$ and $C_2^z/C_1 = 1/20$, using the same values as in equation (2.14).

A.2. Honeycomb lattice

By employing the spring force model and taking into account interactions up to second nearest neighbours, we calculate the phonon dispersion in a honeycomb lattice consisting of two sublattices (A and B) with identical ions. The vectors connecting to the first and second nearest neighbours are listed in equation (2.15).

In-plane modes

By decomposing the in-plane force coefficients to spring constants with relation (A.1), the nonzero force coefficients based on sublattice A are given by

$$
\begin{aligned}
&\Phi_{xx}^{AB}(\boldsymbol{\delta}_{2,3}^A) = -\frac{3}{4}C_1, && \Phi_{xy}^{AB}(\boldsymbol{\delta}_2^A) = \Phi_{yx}^{AB}(\boldsymbol{\delta}_2^A) = -\frac{\sqrt{3}}{4}C_1,\\
&\Phi_{yy}^{AB}(\boldsymbol{\delta}_{2,3}^A) = -\frac{1}{4}C_1, && \Phi_{xy}^{AB}(\boldsymbol{\delta}_3^A) = \Phi_{yx}^{AB}(\boldsymbol{\delta}_3^A) = \frac{\sqrt{3}}{4}C_1,\\
&\Phi_{yy}^{AB}(\boldsymbol{\delta}_1^A) = -C_1, && \Phi_{xx}^{AA}(\boldsymbol{\tau}_{1,4}^A) = -C_2,\\
&\Phi_{xx}^{AA}(\boldsymbol{\tau}_{2,3,5,6}^A) = -\frac{1}{4}C_2, && \Phi_{xy}^{AA}(\boldsymbol{\tau}_{3,6}^A) = \Phi_{yx}^{AA}(\boldsymbol{\tau}_{3,6}^A) = \frac{\sqrt{3}}{4}C_2,\\
&\Phi_{yy}^{AA}(\boldsymbol{\tau}_{2,3,5,6}^A) = -\frac{3}{4}C_2, && \Phi_{xy}^{AA}(\boldsymbol{\tau}_{2,5}^A) = \Phi_{yx}^{AA}(\boldsymbol{\tau}_{2,5}^A) = -\frac{\sqrt{3}}{4}C_2,
\end{aligned}
$$

and the nonzero self-force coefficients computed with the stability condition are

$$
\Phi_{xx}^{AA}(0) = \Phi_{yy}^{AA}(0) = \frac{3}{2}C_1 + 3C_2.
$$

The matrix elements in $D^{AA}(\boldsymbol{q})$ and $D^{AB}(\boldsymbol{q})$ can be expressed as

$$
\begin{aligned}
D_{xx}^{AA}(\boldsymbol{q}) &= \frac{3C_1}{2M} + \frac{C_2}{M}(3 - 2\cos(q_x a) - \cos(\frac{1}{2}q_x a)\cos(\frac{\sqrt{3}}{2}q_y a)) && \equiv \mathcal{A},\\
D_{yy}^{AA}(\boldsymbol{q}) &= \frac{3C_1}{2M} + \frac{3C_2}{M}(1 - \cos(\frac{1}{2}q_x a)\cos(\frac{\sqrt{3}}{2}q_y a)) && \equiv \mathcal{B},\\
D_{xy}^{AA}(\boldsymbol{q}) &= D_{yx}^{AA}(\boldsymbol{q}) = \frac{\sqrt{3}C_2}{M}\sin(\frac{1}{2}q_x a)\sin(\frac{\sqrt{3}}{2}q_y a) && \equiv \mathcal{C},\\
D_{xx}^{AB}(\boldsymbol{q}) &= -\frac{3C_1}{2M}\mathrm{e}^{-\mathrm{i}\frac{q_y a}{2\sqrt{3}}}\cos(\frac{1}{2}q_x a) && \equiv \mathcal{D},\\
D_{xy}^{AB}(\boldsymbol{q}) &= D_{yx}^{AB}(\boldsymbol{q}) = \mathrm{i}\frac{\sqrt{3}C_1}{2M}\mathrm{e}^{-\mathrm{i}\frac{q_y a}{2\sqrt{3}}}\sin(\frac{1}{2}q_x a) && \equiv \mathcal{E},\\
D_{yy}^{AB}(\boldsymbol{q}) &= -\frac{C_1}{M}\mathrm{e}^{\mathrm{i}\frac{q_y a}{\sqrt{3}}}\left(1 + \frac{1}{2}\mathrm{e}^{-\mathrm{i}\frac{\sqrt{3}q_y a}{2}}\cos(\frac{1}{2}q_x a)\right) && \equiv \mathcal{F}.
\end{aligned}
$$

Moreover, $D^{BB}(\boldsymbol{q}) = D^{AA}(\boldsymbol{q})$ due to the sublattice symmetry and the $D^{BA}(\boldsymbol{q})$ matrix is determined by setting $\boldsymbol{\Delta} \to -\boldsymbol{\Delta}$ in the $D^{AB}(\boldsymbol{q})$ matrix. This amounts to a complex conjugation. Thus, the determinant that needs to be solved takes the following form

$$\det\begin{pmatrix} \mathcal{A}-\omega^2 & \mathcal{C} & \mathcal{D} & \mathcal{E} \\ \mathcal{C} & \mathcal{B}-\omega^2 & \mathcal{E} & \mathcal{F} \\ \mathcal{D}^* & \mathcal{E}^* & \mathcal{A}-\omega^2 & \mathcal{C} \\ \mathcal{E}^* & \mathcal{F}^* & \mathcal{C} & \mathcal{B}-\omega^2 \end{pmatrix} = 0,$$

and the characteristic polynomial may be written

$$\lambda^4 + A\lambda^3 + B\lambda^2 + C\lambda + D = 0, \quad \lambda = \omega^2.$$

The coefficients are related to the matrix elements from the following formulas

$$\begin{aligned}
A =& -2(\mathcal{A}+\mathcal{B}),\\
B =& \mathcal{A}^2 + 4\mathcal{A}\mathcal{B} + \mathcal{B}^2 - 2\mathcal{C}^2 - |\mathcal{F}|^2 - |\mathcal{D}|^2 - 2|\mathcal{E}|^2,\\
C =& 2\left[(\mathcal{A}+\mathcal{B})(\mathcal{C}^2+|\mathcal{E}|^2) + \mathcal{A}(|\mathcal{F}|^2-\mathcal{B}^2) + \mathcal{B}(|\mathcal{D}|^2-\mathcal{A}^2) - \mathcal{C}(\mathcal{E}\mathcal{D}^* + \mathcal{D}\mathcal{E}^* + \mathcal{F}\mathcal{E}^* + \mathcal{E}\mathcal{F}^*)\right],\\
D =& \mathcal{A}^2(\mathcal{B}^2-|\mathcal{F}|^2) + 2\mathcal{A}\mathcal{C}(\mathcal{F}\mathcal{E}^* + \mathcal{E}\mathcal{F}^* - \mathcal{B}\mathcal{C}) + 2\mathcal{B}\mathcal{C}(\mathcal{E}\mathcal{D}^* + \mathcal{D}\mathcal{E}^*) - \mathcal{B}^2|\mathcal{D}|^2 + \mathcal{C}^4 -\\
& \mathcal{C}^2(\mathcal{F}\mathcal{D}^* + \mathcal{D}\mathcal{F}^* + 2|\mathcal{E}|^2) - 2\mathcal{A}\mathcal{B}|\mathcal{E}|^2 - \mathcal{E}^2\mathcal{D}^*\mathcal{F}^* - \mathcal{D}\mathcal{F}(\mathcal{E}^*)^2 + |\mathcal{D}|^2|\mathcal{F}|^2 + |\mathcal{E}|^4.
\end{aligned}$$

The solutions to the fourth-order equation are expressed as

$$\begin{aligned}
\omega^2_{\mathrm{LA}} &= -\frac{A}{4} - \zeta + \frac{1}{2}\sqrt{-4\zeta^2 - 2p_1 + \frac{p_2}{\zeta}}, \quad \omega^2_{\mathrm{TA}} = -\frac{A}{4} - \zeta - \frac{1}{2}\sqrt{-4\zeta^2 - 2p_1 + \frac{p_2}{\zeta}},\\
\omega^2_{\mathrm{TO}} &= -\frac{A}{4} + \zeta + \frac{1}{2}\sqrt{-4\zeta^2 - 2p_1 - \frac{p_2}{\zeta}}, \quad \omega^2_{\mathrm{LO}} = -\frac{A}{4} + \zeta - \frac{1}{2}\sqrt{-4\zeta^2 - 2p_1 - \frac{p_2}{\zeta}},
\end{aligned}$$

where the helping variables are defined in equation (2.22).

Out-of-plane modes

We denote the out-of-plane force coefficients for the first and second nearest neighbours by $-C_1^z$ and $-C_2^z$. The matrix elements of $D_{\text{out-of-plane}}(\boldsymbol{q})$ are

$$\begin{aligned}
D^{AA}_{zz}(\boldsymbol{q}) &= D^{BB}_{zz}(\boldsymbol{q}) = \frac{1}{M}\left[3C_1^z + 2C_2^z(3 - \cos(q_x a) - 2\cos(\frac{1}{2}q_x a)\cos(\frac{\sqrt{3}}{2}q_y a))\right],\\
D^{AB}_{zz}(\boldsymbol{q}) &= D^{BA*}_{zz}(\boldsymbol{q}) = -\frac{C_1^z}{M}\mathrm{e}^{\mathrm{i}\frac{q_y a}{\sqrt{3}}}(1 + 2\cos(\frac{1}{2}q_x a)\mathrm{e}^{-\mathrm{i}\frac{\sqrt{3}q_y a}{2}}),
\end{aligned}$$

which yields the following eigenvalues

$$\omega_{\mathrm{ZO}} = \sqrt{D^{AA}_{zz} + |D^{AB}_{zz}|}, \quad \omega_{\mathrm{ZA}} = \sqrt{D^{AA}_{zz} - |D^{AB}_{zz}|}.$$

The dispersion

The more general method derived in section 2.3.2 reduce to the spring force model when $C_1 = 4\gamma_1 = -4\gamma_2$, $C_2 = -4\rho_1 = -4\rho_2$, $C_1^z = -\gamma_z$, $C_2^z = -\rho_z$ and the remaining force coefficients are zero. Figure A.2 shows the phonon dispersion in a honeycomb lattice along the symmetry lines of the Brillouin zone, obtained with the spring force model. The dispersion is shown in units of $\sqrt{C_1/M}$, with the following values for the spring constants $C_2/C_1 = 0.40$, $C_1^z/C_1 = 0.35$ and $C_2^z/C_1 = -0.04$.

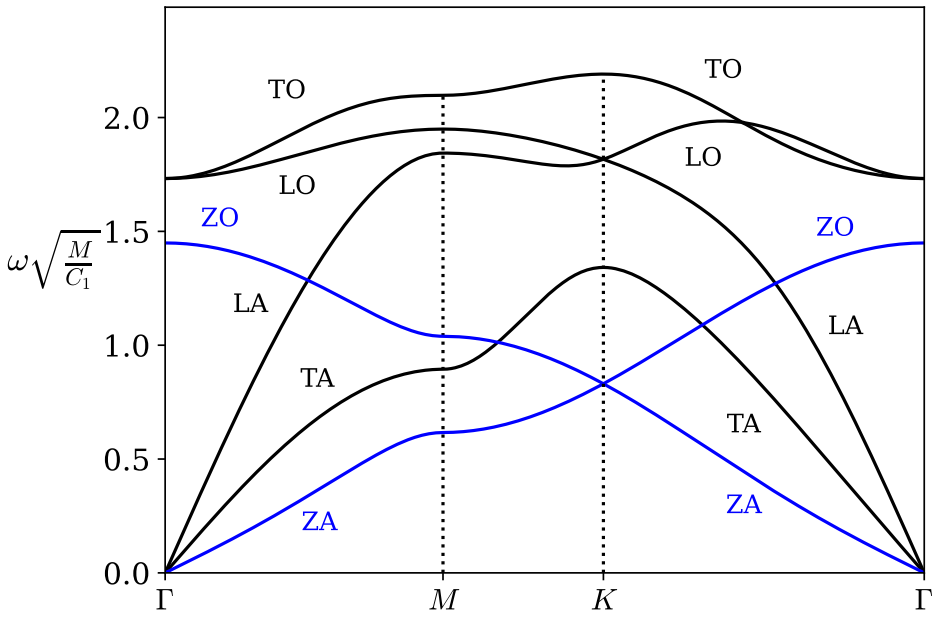

Figure A.2.: The six branches of the phonon dispersion in graphene are shown along the symmetry lines of the Brillouin zone. The six branches are longitudinal acoustic (optical) [LA (LO)], transverse acoustic (optical) [TA (TO)] and out-of-plane acoustic (optical) [ZA (ZO)]. The frequency is in units of $\sqrt{C_1/M}$, with $C_2/C_1 = 0.40$, $C_1^z/C_1 = 0.35$ and $C_2^z/C_1 = -0.04$.

APPENDIX B

The magnetoelastic Hamiltonian for the honeycomb lattice

Perpendicular magnetization

The Hamiltonian matrix $H_{\mathrm{me}}(\boldsymbol{q})$ for the magnon-phonon system in a honeycomb lattice, considering ferromagnetic (equation (4.13)) and antiferromagnetic (equation (4.17)) ordering with spins oriented perpendicular to the lattice plane, can be expressed in a similar form. However, the magnon energy spectrum $E_q^{\pm}$ and the coupling coefficients $G_{q,\lambda}^{\alpha(\beta)}$ have different definitions. The matrix takes the following structure

$$
H_{\mathrm{me}}(\boldsymbol{q}) = \begin{bmatrix}
E_q^+ & 0 & G_{-q,1}^{\alpha*} & G_{-q,2}^{\alpha*} & G_{-q,3}^{\alpha*} & G_{-q,4}^{\alpha*} \\
0 & E_q^- & G_{-q,1}^{\beta*} & G_{-q,2}^{\beta*} & G_{-q,3}^{\beta*} & G_{-q,4}^{\beta*} \\
G_{-q,1}^{\alpha} & G_{-q,1}^{\beta} & \varepsilon_{q,1} & 0 & 0 & 0 \\
G_{-q,2}^{\alpha} & G_{-q,2}^{\beta} & 0 & \varepsilon_{q,2} & 0 & 0 \\
G_{-q,3}^{\alpha} & G_{-q,3}^{\beta} & 0 & 0 & \varepsilon_{q,3} & 0 \\
G_{-q,4}^{\alpha} & G_{-q,4}^{\beta} & 0 & 0 & 0 & \varepsilon_{q,4} \\
0 & 0 & G_{q,1}^{\alpha} & G_{q,2}^{\alpha} & G_{q,3}^{\alpha} & G_{q,4}^{\alpha} \\
0 & 0 & G_{q,1}^{\beta} & G_{q,2}^{\beta} & G_{q,3}^{\beta} & G_{q,4}^{\beta} \\
G_{-q,1}^{\alpha} & G_{-q,1}^{\beta} & 0 & 0 & 0 & 0 \\
G_{-q,2}^{\alpha} & G_{-q,2}^{\beta} & 0 & 0 & 0 & 0 \\
G_{-q,3}^{\alpha} & G_{-q,3}^{\beta} & 0 & 0 & 0 & 0 \\
G_{-q,4}^{\alpha} & G_{-q,4}^{\beta} & 0 & 0 & 0 & 0
\end{bmatrix}
\begin{bmatrix}
0 & 0 & G_{-q,1}^{\alpha*} & G_{-q,2}^{\alpha*} & G_{-q,3}^{\alpha*} & G_{-q,4}^{\alpha*} \\
0 & 0 & G_{-q,1}^{\beta*} & G_{-q,2}^{\beta*} & G_{-q,3}^{\beta*} & G_{-q,4}^{\beta*} \\
G_{q,1}^{\alpha*} & G_{q,1}^{\beta*} & 0 & 0 & 0 & 0 \\
G_{q,2}^{\alpha*} & G_{q,2}^{\beta*} & 0 & 0 & 0 & 0 \\
G_{q,3}^{\alpha*} & G_{q,3}^{\beta*} & 0 & 0 & 0 & 0 \\
G_{q,4}^{\alpha*} & G_{q,4}^{\beta*} & 0 & 0 & 0 & 0 \\
E_{-q}^+ & 0 & G_{q,1}^{\alpha} & G_{q,2}^{\alpha} & G_{q,3}^{\alpha} & G_{q,4}^{\alpha} \\
0 & E_{-q}^- & G_{q,1}^{\beta} & G_{q,2}^{\beta} & G_{q,3}^{\beta} & G_{q,4}^{\beta} \\
G_{q,1}^{\alpha*} & G_{q,1}^{\beta*} & \varepsilon_{q,1} & 0 & 0 & 0 \\
G_{q,2}^{\alpha*} & G_{q,2}^{\beta*} & 0 & \varepsilon_{q,2} & 0 & 0 \\
G_{q,3}^{\alpha*} & G_{q,3}^{\beta*} & 0 & 0 & \varepsilon_{q,3} & 0 \\
G_{q,4}^{\alpha*} & G_{q,4}^{\beta*} & 0 & 0 & 0 & \varepsilon_{q,4}
\end{bmatrix}.
$$

Arbitrary magnetization direction

The matrix $H^{\mathrm{sq}}_{\mathrm{me}}(\boldsymbol{q})$ in the magnetoelastic Hamiltonian for the honeycomb lattice with ferromagnetic order and arbitrary magnetization direction, computed using the second quantized formalism as described in equation (7.1), has the following form

$$
H^{\mathrm{sq}}_{\mathrm{me}}(\boldsymbol{q}) = \begin{bmatrix}
t_q^A & -t_q & G^{A*}_{-q,1} & G^{A*}_{-q,2} & G^{A*}_{-q,3} & G^{A*}_{-q,4} & G^{A*}_{-q,5} & G^{A*}_{-q,6} \\
-t_q^* & t_q^B & G^{B*}_{-q,1} & G^{B*}_{-q,2} & G^{B*}_{-q,3} & G^{B*}_{-q,4} & G^{B*}_{-q,5} & G^{B*}_{-q,6} \\
G^A_{-q,1} & G^B_{-q,1} & \varepsilon_{q,1} & 0 & 0 & 0 & 0 & 0 \\
G^A_{-q,2} & G^B_{-q,2} & 0 & \varepsilon_{q,2} & 0 & 0 & 0 & 0 \\
G^A_{-q,3} & G^B_{-q,3} & 0 & 0 & \varepsilon_{q,3} & 0 & 0 & 0 \\
G^A_{-q,4} & G^B_{-q,4} & 0 & 0 & 0 & \varepsilon_{q,4} & 0 & 0 \\
G^A_{-q,5} & G^B_{-q,5} & 0 & 0 & 0 & 0 & \varepsilon_{q,5} & 0 \\
G^A_{-q,6} & G^B_{-q,6} & 0 & 0 & 0 & 0 & 0 & \varepsilon_{q,6} \\
-SK_zQ_z & 0 & G^A_{q,1} & G^A_{q,2} & G^A_{q,3} & G^A_{q,4} & G^A_{q,5} & G^A_{q,6} \\
0 & -SK_zQ_z & G^B_{q,1} & G^B_{q,2} & G^B_{q,3} & G^B_{q,4} & G^B_{q,5} & G^B_{q,6} \\
G^A_{-q,1} & G^B_{-q,1} & 0 & 0 & 0 & 0 & 0 & 0 \\
G^A_{-q,2} & G^B_{-q,2} & 0 & 0 & 0 & 0 & 0 & 0 \\
G^A_{-q,3} & G^B_{-q,3} & 0 & 0 & 0 & 0 & 0 & 0 \\
G^A_{-q,4} & G^B_{-q,4} & 0 & 0 & 0 & 0 & 0 & 0 \\
G^A_{-q,5} & G^B_{-q,5} & 0 & 0 & 0 & 0 & 0 & 0 \\
G^A_{-q,6} & G^B_{-q,6} & 0 & 0 & 0 & 0 & 0 & 0 \\
-SK_zQ_z^* & 0 & G^{A*}_{-q,1} & G^{A*}_{-q,2} & G^{A*}_{-q,3} & G^{A*}_{-q,4} & G^{A*}_{-q,5} & G^{A*}_{-q,6} \\
0 & -SK_zQ_z^* & G^{B*}_{-q,1} & G^{B*}_{-q,2} & G^{B*}_{-q,3} & G^{B*}_{-q,4} & G^{B*}_{-q,5} & G^{B*}_{-q,6} \\
G^{A*}_{q,1} & G^{B*}_{q,1} & 0 & 0 & 0 & 0 & 0 & 0 \\
G^{A*}_{q,2} & G^{B*}_{q,2} & 0 & 0 & 0 & 0 & 0 & 0 \\
G^{A*}_{q,3} & G^{B*}_{q,3} & 0 & 0 & 0 & 0 & 0 & 0 \\
G^{A*}_{q,4} & G^{B*}_{q,4} & 0 & 0 & 0 & 0 & 0 & 0 \\
G^{A*}_{q,5} & G^{B*}_{q,5} & 0 & 0 & 0 & 0 & 0 & 0 \\
G^{A*}_{q,6} & G^{B*}_{q,6} & 0 & 0 & 0 & 0 & 0 & 0 \\
t_q^B & -t_{-q}^* & G^A_{q,1} & G^A_{q,2} & G^A_{q,3} & G^A_{q,4} & G^A_{q,5} & G^A_{q,6} \\
-t_{-q} & t_q^A & G^B_{q,1} & G^B_{q,2} & G^B_{q,3} & G^B_{q,4} & G^B_{q,5} & G^B_{q,6} \\
G^{A*}_{q,1} & G^{B*}_{q,1} & \varepsilon_{q,1} & 0 & 0 & 0 & 0 & 0 \\
G^{A*}_{q,2} & G^{B*}_{q,2} & 0 & \varepsilon_{q,2} & 0 & 0 & 0 & 0 \\
G^{A*}_{q,3} & G^{B*}_{q,3} & 0 & 0 & \varepsilon_{q,3} & 0 & 0 & 0 \\
G^{A*}_{q,4} & G^{B*}_{q,4} & 0 & 0 & 0 & \varepsilon_{q,4} & 0 & 0 \\
G^{A*}_{q,5} & G^{B*}_{q,5} & 0 & 0 & 0 & 0 & \varepsilon_{q,5} & 0 \\
G^{A*}_{q,6} & G^{B*}_{q,6} & 0 & 0 & 0 & 0 & 0 & \varepsilon_{q,6}
\end{bmatrix}.
$$

APPENDIX C

Semiclassical calculation of spin Nernst coefficient

Following Ref. [54], the spin Nernst coefficient can be obtained through a semiclassical calculation using the following expression

$$\alpha_{xy} = -\frac{k_B}{\mathcal{A}} \sum_{k} \sum_{n=1}^{N_d} \langle \mathcal{S} \rangle_{k,n} \, c_1[g_{\mathrm{BE}}(\mathcal{E}_{k,n})] \mathcal{F}_n(\boldsymbol{k}),$$

where $\langle \mathcal{S} \rangle_{k,n} = \langle n_k | \, \mathcal{S} \, | n_k \rangle$ represents the spin expectation value of the nth band at a specific $\boldsymbol{k}$. In cases where spin is conserved, this expression coincides with the one derived from linear response theory (equation (5.7)). To demonstrate the connection between this expression and a purely magnonic system, we can simplify it by considering a ferromagnetic lattice where each magnon excitation corresponds to a spin expectation value of -1. In this case, the expression reduces to the following form [91]

$$\alpha_{xy} = \frac{k_B}{\mathcal{A}} \sum_{k} \sum_{n=1}^{N_d} c_1[g_{\mathrm{BE}}(\mathcal{E}_{k,n})] \mathcal{F}_n(\boldsymbol{k}).$$

In order to compare the spin Nernst coefficient obtained through the semiclassical approach and linear response theory, we analyze its temperature dependence for the same scenarios discussed in section 7.5.2, as shown in Figure C.1. Notably, significant differences are observed when considering nonzero values for D_{xy}^{nnn} with magnetization directions along $\hat{\boldsymbol{y}}$ and $\hat{\boldsymbol{z}}$. Additionally, when the magnetization is

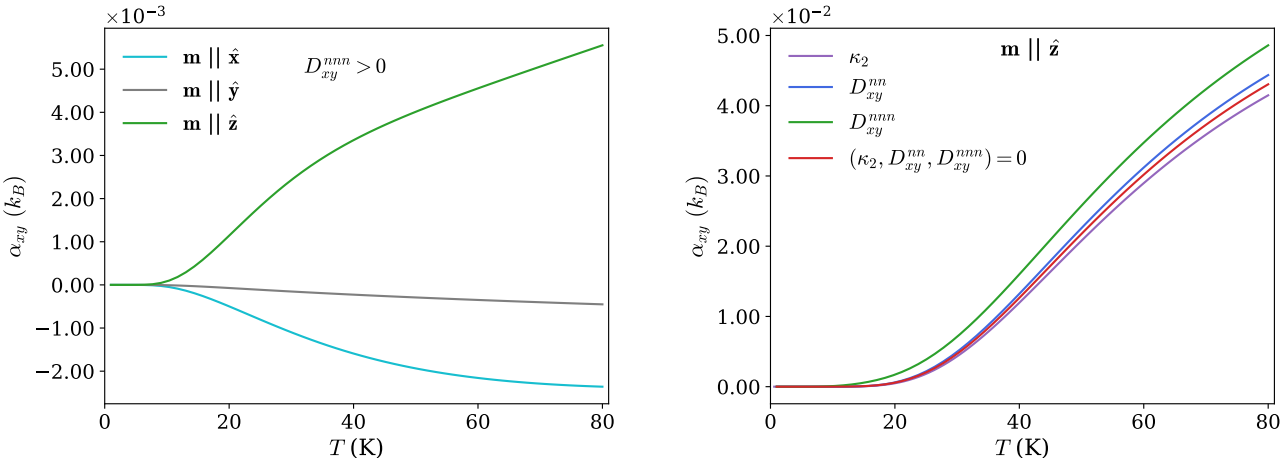

Figure C.1.: Spin Nernst coefficient as a function of temperature, calculated with the semiclassical approach. The figure on the left display the magnon-phonon interaction contribution to the coefficient due to an in-plane next-nearest neighbour DMI, and we compare with different magnetization directions $\hat{\boldsymbol{x}}$, $\hat{\boldsymbol{y}}$ and $\hat{\boldsymbol{z}}$. The figure on the right shows the coefficient when the magnetization is perpendicular to the plane and we consider the scenarios where either κ_2, D_{xy}^{nn} or D_{xy}^{nnn} is nonzero, in addition to the case where all are zero which corresponds to the non-interacting system. We use the following values: $\kappa_2 = 1.04\mathrm{meV}$, $D_{xy}^{\mathrm{nn}} = 0.173\mathrm{meV}$, $D_{xy}^{\mathrm{nnn}} = 0.3\mathrm{meV}$, $\zeta = 0.2$ while the remaining parameters for the magnon and phonon dispersion are consistent with those used in section 7.3.

out of the plane, the semiclassical approach yields a considerably larger magnitude for the coefficient. As for the other cases examined, such as nonzero values of κ_2 or D_{xy}^{nn} for the out-of-plane magnetization direction, the two approaches yield approximately similar results.

To further investigate the significant discrepancy observed when D_{xy}^{nnn} is nonzero and the magnetization is aligned with the $z-$axis, we perform a convergence test by calculating the coefficient using both the semiclassical approach and linear response theory. We consider various resolutions ($N_r \times N_r$) in the Brillouin zone and compare the results, as shown in Figure C.2. The findings reveal that the semiclassical approach yields numerically unstable results, exhibiting substantial variations depending on the grid resolution. Consequently, we deem these results unreliable. We attribute this instability to the combined distribution of $\langle \mathcal{S}^z \rangle_{k,n} \mathcal{F}_n(\boldsymbol{k})$ near the anticrossing regions, where the spin expectation value undergoes a gradual transition as the bands transition between phonon and magnon states. As the band gaps diminish, giving rise to a large Berry curvature and a more abrupt transition in the spin expectation value, the outcome becomes highly sensitive to the resolution. In contrast, the spin Nernst coefficient obtained from linear response theory demonstrates numerically stable results. It is evident that a resolution of $N_r = 1400$ is sufficient to obtain reliable outcomes.

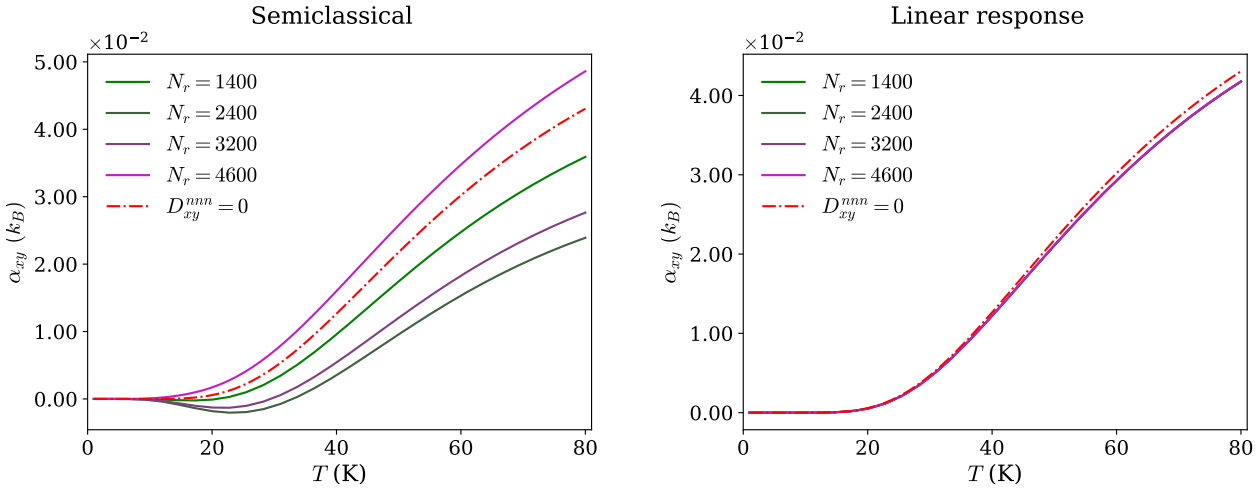

Figure C.2.: The figures show the Spin Nernst coefficient calculated using the semiclassical approach (left) and the linear response theory (right) for different grid resolutions ($N_r \times N_r$) in the numerical Brillouin zone. We specifically focus on a scenario with a magnetization out of the lattice plane, considering $D_{xy}^{\mathrm{nnn}} = 0.3\mathrm{meV}$ and $\zeta = 0.2$. The remaining parameters for the magnon and phonon dispersion are alike the ones used in section 7.3. Additionally, we include the spin Nernst coefficient obtained in the non-interacting case where $D_{xy}^{\mathrm{nnn}} = 0.0\mathrm{meV}$.

Bibliography

[1] A. D. Zdetsis and C. S. Wang. "Lattice dynamics of Ge and Si using the Born-von Karman model". In: *Phys. Rev. B* 19 (6 Mar. 1979), pp. 2999–3003. DOI: 10.1103/PhysRevB.19.2999.

[2] J.M. Ziman. *Electrons and Phonons: The theory of Transport Phenomena in Solids*. Ed. by N.F. Mott, E.C. Bullard, and D.H. Wilkinson. The international series of monographs on physics. Oxford University Press, 1960, pp. 1–49.

[3] Charles Kittel. *Introduction to Solid State Physics*. Ed. by Stuart Johnson. 8. John Wiley & Sons, Inc, 2005, pp. 95–97, 107–126, 299, 302–308, 323–352, 420–422, 474–475. ISBN: 0-471-41526-X.

[4] Neil W. Ashcroft and N. David Mermin. *Solid State Physics*. Ed. by Dorothy Garbose Crane. Harcourt College Publishers, 1976, pp. 135–137, 425–426, 672–681, 705–722. ISBN: 0-03-083993-9.

[5] K. S. Novoselov et al. "Electric Field Effect in Atomically Thin Carbon Films". In: *Science* 306.5696 (Oct. 2004), pp. 666–669. DOI: 10.1126/science.1102896.

[6] Aleksandr Rodin et al. "Collective excitations in 2D materials". In: *Nature Reviews Physics* 2.10 (Oct. 2020), pp. 524–537. ISSN: 2522-5820. DOI: 10.1038/s42254-020-0214-4.

[7] I. O. Raikov et al. "A theory of flexural modes in graphene". In: *Journal of Physics: Conference Series* 1695.1 (Dec. 2020), p. 012179. DOI: 10.1088/1742-6596/1695/1/012179.

[8] N. D. Mermin and H. Wagner. "Absence of Ferromagnetism or Antiferromagnetism in One- or Two-Dimensional Isotropic Heisenberg Models". In: *Phys. Rev. Lett.* 17 (22 Nov. 1966), pp. 1133–1136. DOI: 10.1103/PhysRevLett.17.1133.

[9] Kenneth S. Burch, David Mandrus, and Je-Geun Park. "Magnetism in two-dimensional van der Waals materials". In: *Nature* 563.7729 (Nov. 2018), pp. 47–52. DOI: 10.1038/s41586-018-0631.

[10] Bevin Huang et al. "Layer-dependent ferromagnetism in a van der Waals crystal down to the monolayer limit". In: *Nature* 546.7657 (June 2017), pp. 270–273. ISSN: 1476-4687. DOI: 10.1038/nature22391.

[11] R. Jaeschke-Ubiergo, E. Suárez Morell, and A. S. Nunez. "Theory of magnetism in the van der Waals magnet CrI_3". In: *Phys. Rev. B* 103 (17 May 2021), p. 174410. DOI: 10.1103/PhysRevB.103.174410.

[12] Juan M. Losada, Arne Brataas, and Alireza Qaiumzadeh. "Ultrafast control of spin interactions in honeycomb antiferromagnetic insulators". In: *Phys. Rev. B* 100 (6 Aug. 2019), p. 060410. DOI: 10.1103/PhysRevB.100.060410.

[13] Lebing Chen et al. "Magnetic Field Effect on Topological Spin Excitations in CrI_3". In: *Phys. Rev. X* 11 (3 Aug. 2021), p. 031047. DOI: 10.1103/PhysRevX.11.031047.

[14] N. Bazazzadeh et al. "Symmetry enhanced spin-Nernst effect in honeycomb antiferromagnetic transition metal trichalcogenide monolayers". In: *Phys. Rev. B* 103 (1 Jan. 2021), p. 014425. DOI: 10.1103/PhysRevB.103.014425.

[15] Fengjun Zhuo et al. *Topological Phases in Magnonics: A Review*. 2023. arXiv: 2305.14861 [cond-mat.mes-hall].

[16] Alexander Mook et al. "Interaction-Stabilized Topological Magnon Insulator in Ferromagnets". In: *Phys. Rev. X* 11 (2 June 2021), p. 021061. DOI: 10.1103/PhysRevX.11.021061.

[17] Hosho Katsura, Naoto Nagaosa, and Patrick A. Lee. "Theory of the Thermal Hall Effect in Quantum Magnets". In: *Phys. Rev. Lett.* 104 (6 Feb. 2010), p. 066403. DOI: 10.1103/PhysRevLett.104.066403.

[18] Xiaoou Zhang et al. “Thermal Hall Effect Induced by Magnon-Phonon Interactions”. In: *Phys. Rev. Lett.* 123 (16 Oct. 2019), p. 167202. DOI: 10.1103/PhysRevLett.123.167202.

[19] Sungjoon Park and Bohm-Jung Yang. “Topological magnetoelastic excitations in noncollinear antiferromagnets”. In: *Phys. Rev. B* 99 (17 May 2019), p. 174435. DOI: 10.1103/PhysRevB.99.174435.

[20] F. Körmann et al. “Temperature Dependent Magnon-Phonon Coupling in bcc Fe from Theory and Experiment”. In: *Phys. Rev. Lett.* 113 (16 Oct. 2014), p. 165503. DOI: 10.1103/PhysRevLett.113.165503.

[21] Haoran Man et al. “Direct observation of magnon-phonon coupling in yttrium iron garnet”. In: *Phys. Rev. B* 96 (10 Sept. 2017), p. 100406. DOI: 10.1103/PhysRevB.96.100406.

[22] Jiaming Luo et al. “Evidence for Topological Magnon–Phonon Hybridization in a 2D Antiferromagnet down to the Monolayer Limit”. In: *Nano Letters* 23.5 (Apr. 2023), pp. 2023–2030. ISSN: 1530-6984. DOI: 10.1021/acs.nanolett.3c00351.

[23] J. Fransson et al. “Microscopic theory for coupled atomistic magnetization and lattice dynamics”. In: *Phys. Rev. Materials* 1 (7 Dec. 2017), p. 074404. DOI: 10.1103/PhysRevMaterials.1.074404.

[24] C. M. Jaworski et al. “Spin-Seebeck Effect: A Phonon Driven Spin Distribution”. In: *Phys. Rev. Lett.* 106 (18 May 2011), p. 186601. DOI: 10.1103/PhysRevLett.106.186601.

[25] Pablo Maldonado and Yaroslav O. Kvashnin. “Microscopic theory of ultrafast out-of-equilibrium magnon-phonon dynamics in insulators”. In: *Phys. Rev. B* 100 (1 July 2019), p. 014430. DOI: 10.1103/PhysRevB.100.014430.

[26] Bahman Sheikhi, Mehdi Kargarian, and Abdollah Langari. “Hybrid topological magnon-phonon modes in ferromagnetic honeycomb and kagome lattices”. In: *Phys. Rev. B* 104 (4 July 2021), p. 045139. DOI: 10.1103/PhysRevB.104.045139.

[27] Even Thingstad et al. “Chiral Phonon Transport Induced by Topological Magnons”. In: *Phys. Rev. Lett.* 122 (10 Mar. 2019), p. 107201. DOI: 10.1103/PhysRevLett.122.107201.

[28] Bowen Ma and Gregory A. Fiete. “Antiferromagnetic insulators with tunable magnon-polaron Chern numbers induced by in-plane optical phonons”. In: *Phys. Rev. B* 105 (10 Mar. 2022), p. L100402. DOI: 10.1103/PhysRevB.105.L100402.

[29] Gyungchoon Go, Se Kwon Kim, and Kyung-Jin Lee. “Topological Magnon-Phonon Hybrid Excitations in Two-Dimensional Ferromagnets with Tunable Chern Numbers”. In: *Phys. Rev. Lett.* 123 (23 Dec. 2019), p. 237207. DOI: 10.1103/PhysRevLett.123.237207.

[30] Ryuji Takahashi and Naoto Nagaosa. “Berry Curvature in Magnon-Phonon Hybrid Systems”. In: *Phys. Rev. Lett.* 117 (21 Nov. 2016), p. 217205. DOI: 10.1103/PhysRevLett.117.217205.

[31] Otfried Madelung. *Introduction to Solid-State Theory*. Ed. by Dr.-Ing. Helmut and K.V. Lotsch. Translated by B.C. Taylor. Springer, 1995, pp. 129–155. ISBN: 3-540-60443-X.

[32] P.J. Bussey. “The phonon as a model for elementary particles”. In: *Physics Letters A* 176.3 (1993), pp. 159–164. ISSN: 0375-9601. DOI: https://doi.org/10.1016/0375-9601(93)91027-3.

[33] A. Sudbø et al. *Quantum Theory of Solids*. pp. 49-70. Digitalized lecture notes for the course "TFY4210 Quantum Theory of Many-Particle Systems". Course website; https://www.ntnu.edu/studies/courses/TFY4210#tab=omEmnet. 2021.

[34] Jin Ho Kwak and Sungpyo Hong. *Linear Algebra*. 1. Birkhäuser Boston, MA, 1997, pp. 210, 263. ISBN: 978-1-4757-1200-1. DOI: https://doi.org/10.1007/978-1-4757-1200-1.

[35] P.C. Hemmer. *Kvantemekanikk*. Tapir Akademisk Forlag, 2005, pp. 122, 178–179, 297–300, 336. ISBN: 978-82-519-2028-5.

[36] L.A. Falkovsky. "Symmetry constraints on phonon dispersion in graphene". In: *Physics Letters A* 372.31 (2008), pp. 5189–5192. ISSN: 0375-9601. DOI: https://doi.org/10.1016/j.physleta.2008.05.085.

[37] Even Thingstad et al. "Phonon-mediated superconductivity in doped monolayer materials". In: *Phys. Rev. B* 101 (21 June 2020), p. 214513. DOI: 10.1103/PhysRevB.101.214513.

[38] Eros Mariani and Felix von Oppen. "Flexural Phonons in Free-Standing Graphene". In: *Phys. Rev. Lett.* 100 (7 Feb. 2008), p. 076801. DOI: 10.1103/PhysRevLett.100.076801.

[39] L. A. Falkovsky. "Phonon dispersion in graphene". In: *Journal of Experimental and Theoretical Physics* 105.2 (Aug. 2007), pp. 397–403. ISSN: 1090-6509. DOI: 10.1134/S1063776107080122.

[40] Jia-An Yan, W. Y. Ruan, and M. Y. Chou. "Phonon dispersions and vibrational properties of monolayer, bilayer, and trilayer graphene: Density-functional perturbation theory". In: *Phys. Rev. B* 77 (12 Mar. 2008), p. 125401. DOI: 10.1103/PhysRevB.77.125401.

[41] Nicolas Mounet and Nicola Marzari. "First-principles determination of the structural, vibrational and thermodynamic properties of diamond, graphite, and derivatives". In: *Phys. Rev. B* 71 (20 May 2005), p. 205214. DOI: 10.1103/PhysRevB.71.205214.

[42] Terunobu Miyazaki and Hanmin Jin. *The Physics of Ferromagnetism*. 1. Springer Series in Materials Science. Springer Berlin, Heidelberg, 2012, pp. 97–104, 125–128. ISBN: 978-3-642-25583-0. DOI: https://doi.org/10.1007/978-3-642-25583-0.

[43] Robert M. White. *Quantum Theory of Magnetism*. 3. Springer Series in Solid-State Sciences. Springer Berlin, Heidelberg, 2007, p. 153. ISBN: 978-3-540-69025-2. DOI: https://doi.org/10.1007/978-3-540-69025-2.

[44] V. Baltz et al. "Antiferromagnetic spintronics". In: *Rev. Mod. Phys.* 90 (1 Feb. 2018), pp. 015005–11, 015005–12. DOI: 10.1103/RevModPhys.90.015005.

[45] Daniel D. Stancil Anil Prabhakar. *Spin Waves*. Springer New York, NY, 2009, pp. 49–60. ISBN: 978-0-387-77865-5. DOI: https://doi.org/10.1007/978-0-387-77865-5.

[46] F. Bloch. "Zur Theorie des Ferromagnetismus". In: *Zeitschrift für Physik* 61.3 (Mar. 1930), pp. 206–219. ISSN: 0044-3328. DOI: 10.1007/BF01339661.

[47] Paul A. McClarty. "Topological Magnons: A Review". In: *Annual Review of Condensed Matter Physics* 13.1 (2022). DOI: 10.1146/annurev-conmatphys-031620-104715.

[48] Pietro M. Bonetti and Walter Metzner. "Spin stiffness, spectral weight, and Landau damping of magnons in metallic spiral magnets". In: *Phys. Rev. B* 105 (13 Apr. 2022), p. 134426. DOI: 10.1103/PhysRevB.105.134426.

[49] Wolfgang Nolting and Anupuru Ramakanth. *Quantum Theory of Magnetism*. Springer Berlin, Heidelberg, 2009, pp. 28, 175–178, 280, 282, 346–350. ISBN: 978-3-540-85415-9.

[50] Mathias Getzlaff. *Fundamentals of magnetism*. Springer-Verlag Berlin Heidelberg, 2008, pp. 9–10, 41–46, 89–97. ISBN: 978-3-540-31150-8. DOI: https://doi.org/10.1007/978-3-540-31152-2.

[51] I. Dzyaloshinsky. "A thermodynamic theory of "weak" ferromagnetism of antiferromagnetics". In: *Journal of Physics and Chemistry of Solids* 4.4 (1958), pp. 241–255. ISSN: 0022-3697. DOI: https://doi.org/10.1016/0022-3697(58)90076-3.

[52] P. W. Anderson. "New Approach to the Theory of Superexchange Interactions". In: *Phys. Rev.* 115 (1 July 1959), pp. 2–13. DOI: 10.1103/PhysRev.115.2.

[53] Tôru Moriya. "Anisotropic Superexchange Interaction and Weak Ferromagnetism". In: *Phys. Rev.* 120 (1 Oct. 1960), pp. 91–98. DOI: 10.1103/PhysRev.120.91.

[54] Sungjoon Park, Naoto Nagaosa, and Bohm-Jung Yang. "Thermal Hall Effect, Spin Nernst Effect, and Spin Density Induced by a Thermal Gradient in Collinear Ferrimagnets from Magnon–Phonon Interaction". In: *Nano Letters* 20.4 (Apr. 2020), pp. 2741–2746. ISSN: 1530-6984. DOI: 10.1021/acs.nanolett.0c00363.

[55] S A Owerre. "A first theoretical realization of honeycomb topological magnon insulator". In: *Journal of Physics: Condensed Matter* 28.38 (July 2016), p. 386001. DOI: 10.1088/0953-8984/28/38/386001.

[56] T. Holstein and H. Primakoff. "Field Dependence of the Intrinsic Domain Magnetization of a Ferromagnet". In: *Phys. Rev.* 58 (12 Dec. 1940), pp. 1098–1113. DOI: 10.1103/PhysRev.58.1098.

[57] Ran Cheng, Satoshi Okamoto, and Di Xiao. "Spin Nernst Effect of Magnons in Collinear Antiferromagnets". In: *Phys. Rev. Lett.* 117 (21 Nov. 2016), p. 217202. DOI: 10.1103/PhysRevLett.117.217202.

[58] Franz G. Utermohlen. "Magnetic Properties of Two-Dimensional Honeycomb-Lattice Materials". English. PhD thesis. The Ohio State University, 2021, pp. 119–121. URL: https://www.proquest.com/dissertations-theses/magnetic-properties-two-dimensional-honeycomb/docview/2689580861/se-2.

[59] Se Kwon Kim et al. "Realization of the Haldane-Kane-Mele Model in a System of Localized Spins". In: *Phys. Rev. Lett.* 117 (22 Nov. 2016), p. 227201. DOI: 10.1103/PhysRevLett.117.227201.

[60] V Bonbien et al. "Topological aspects of antiferromagnets". In: *Journal of Physics D: Applied Physics* 55.10 (Nov. 2021), p. 103002. DOI: 10.1088/1361-6463/ac28fa.

[61] Sergio M. Rezende, Antonio Azevedo, and Roberto L. Rodríguez-Suárez. "Introduction to antiferromagnetic magnons". In: *Journal of Applied Physics* 126.15 (2019), p. 151101. DOI: 10.1063/1.5109132.

[62] F. Keffer, H. Kaplan, and Y. Yafet. "Spin Waves in Ferromagnetic and Antiferromagnetic Materials". In: *American Journal of Physics* 21.4 (1953), pp. 250–257. DOI: 10.1119/1.1933416.

[63] Haakon T. Simensen et al. "Magnon-polarons in cubic collinear antiferromagnets". In: *Phys. Rev. B* 99 (6 Feb. 2019), p. 064421. DOI: 10.1103/PhysRevB.99.064421.

[64] A. N. Bogdanov, A. V. Zhuravlev, and U. K. Rößler. "Spin-flop transition in uniaxial antiferromagnets: Magnetic phases, reorientation effects, and multidomain states". In: *Phys. Rev. B* 75 (9 Mar. 2007), p. 094425. DOI: 10.1103/PhysRevB.75.094425.

[65] Charles Kittel. "Physical Theory of Ferromagnetic Domains". In: *Rev. Mod. Phys.* 21 (4 Oct. 1949), pp. 541–583. DOI: 10.1103/RevModPhys.21.541.

[66] C. Kittel. "Model of Exchange-Inversion Magnetization". In: *Phys. Rev.* 120 (2 Oct. 1960), pp. 335–342. DOI: 10.1103/PhysRev.120.335.

[67] Andreas Rückriegel et al. "Magnetoelastic modes and lifetime of magnons in thin yttrium iron garnet films". In: *Phys. Rev. B* 89 (18 May 2014), p. 184413. DOI: 10.1103/PhysRevB.89.184413.

[68] Bowen Ma. "Thermal transport and topological aspects of magnons". PhD thesis. The University of Texas Austin, 2021. DOI: http://dx.doi.org/10.26153/tsw/14618.

[69] R. M. White, M. Sparks, and I. Ortenburger. "Diagonalization of the Antiferromagnetic Magnon-Phonon Interaction". In: *Phys. Rev.* 139 (2A July 1965), A450–A454. DOI: 10.1103/PhysRev.139.A450.

[70] Ryo Matsumoto, Ryuichi Shindou, and Shuichi Murakami. "Thermal Hall effect of magnons in magnets with dipolar interaction". In: *Phys. Rev. B* 89 (5 Feb. 2014), p. 054420. DOI: 10.1103/PhysRevB.89.054420.

[71] J.H.P. Colpa. "Diagonalization of the quadratic boson hamiltonian". In: *Physica A: Statistical Mechanics and its Applications* 93.3 (1978), pp. 327–353. ISSN: 0378-4371. DOI: https://doi.org/10.1016/0378-4371(78)90160-7.

[72] Hiroki Kondo, Yutaka Akagi, and Hosho Katsura. "Non-Hermiticity and topological invariants of magnon Bogoliubov–de Gennes systems". In: *Progress of Theoretical and Experimental Physics* 2020.12 (Oct. 2020). 12A104. ISSN: 2050-3911. DOI: 10.1093/ptep/ptaa151.

[73] Binghai Yan and Claudia Felser. "Topological Materials: Weyl Semimetals". In: *Annual Review of Condensed Matter Physics* 8.1 (2017), pp. 337–354. DOI: 10.1146/annurev-conmatphys-031016-025458.

[74] Di Xiao, Ming-Che Chang, and Qian Niu. "Berry phase effects on electronic properties". In: *Rev. Mod. Phys.* 82 (3 July 2010), pp. 1959–2007. DOI: 10.1103/RevModPhys.82.1959.

[75] M. V. Berry. "Quantal Phase Factors Accompanying Adiabatic Changes". In: *Proceedings of the Royal Society of London. Series A, Mathematical and Physical Sciences* 392.1802 (1984), pp. 45–57. ISSN: 00804630. URL: http://www.jstor.org/stable/2397741 (visited on 06/07/2023).

[76] Ryuichi Shindou et al. "Topological chiral magnonic edge mode in a magnonic crystal". In: *Phys. Rev. B* 87 (17 May 2013), p. 174427. DOI: 10.1103/PhysRevB.87.174427.

[77] Ryo Matsumoto and Shuichi Murakami. "Theoretical Prediction of a Rotating Magnon Wave Packet in Ferromagnets". In: *Phys. Rev. Lett.* 106 (19 May 2011), p. 197202. DOI: 10.1103/PhysRevLett.106.197202.

[78] O. Vafek, A. Melikyan, and Z. Te sanovi ć. "Quasiparticle Hall transport of d-wave superconductors in the vortex state". In: *Phys. Rev. B* 64 (22 Nov. 2001), p. 224508. DOI: 10.1103/PhysRevB.64.224508.

[79] Bo Li, Shane Sandhoefner, and Alexey A. Kovalev. "Intrinsic spin Nernst effect of magnons in a noncollinear antiferromagnet". In: *Phys. Rev. Res.* 2 (1 Jan. 2020), p. 013079. DOI: 10.1103/PhysRevResearch.2.013079.

[80] Gyungchoon Go and Se Kwon Kim. "Tunable large spin Nernst effect in a two-dimensional magnetic bilayer". In: *Phys. Rev. B* 106 (12 Sept. 2022), p. 125103. DOI: 10.1103/PhysRevB.106.125103.

[81] Lucas Webster, Liangbo Liang, and Jia-An Yan. "Distinct spin–lattice and spin–phonon interactions in monolayer magnetic CrI3". In: *Phys. Chem. Chem. Phys.* 20 (36 2018), pp. 23546–23555. DOI: 10.1039/C8CP03599G.

[82] Alexey Kartsev et al. "Biquadratic exchange interactions in two-dimensional magnets". In: *npj Computational Materials* 6.1 (Oct. 2020), p. 150. ISSN: 2057-3960. DOI: 10.1038/s41524-020-00416-1.

[83] A. R. Wildes et al. "Evidence for biquadratic exchange in the quasi-two-dimensional antiferromagnet FePS3". In: *Journal of Applied Physics* 127.22 (2020), p. 223903. DOI: 10.1063/5.0009114.

[84] Sahar Izadi Vishkayi et al. "Strain and electric-field control of spin-spin interactions in monolayer CrI_3". In: *Phys. Rev. Mater.* 4 (9 Sept. 2020), p. 094004. DOI: 10.1103/PhysRevMaterials.4.094004.

[85] P. A. McClarty et al. "Topological magnons in Kitaev magnets at high fields". In: *Phys. Rev. B* 98 (6 Aug. 2018), p. 060404. DOI: 10.1103/PhysRevB.98.060404.

[86] Inhee Lee et al. “Fundamental Spin Interactions Underlying the Magnetic Anisotropy in the Kitaev Ferromagnet CrI_3”. In: *Phys. Rev. Lett.* 124 (1 Jan. 2020), p. 017201. DOI: 10.1103/PhysRevLett.124.017201.

[87] Thomas Halloran et al. “Geometrical frustration versus Kitaev interactions in $BaCo_2(AsO_4)_2$”. In: *Proceedings of the National Academy of Sciences* 120.2 (2023), e2215509119. DOI: 10.1073/pnas.2215509119.

[88] Jiefu Cen and Hae-Young Kee. “Determining Kitaev interaction in spin-S honeycomb Mott insulators”. In: *Phys. Rev. B* 107 (1 Jan. 2023), p. 014411. DOI: 10.1103/PhysRevB.107.014411.

[89] Andi Cong et al. “Exchange-mediated magnon-phonon scattering in monolayer CrI_3”. In: *Phys. Rev. B* 106 (21 Dec. 2022), p. 214424. DOI: 10.1103/PhysRevB.106.214424.

[90] Lifa Zhang and Qian Niu. “Chiral Phonons at High-Symmetry Points in Monolayer Hexagonal Lattices”. In: *Phys. Rev. Lett.* 115 (11 Sept. 2015), p. 115502. DOI: 10.1103/PhysRevLett.115.115502.

[91] Alexey A. Kovalev and Vladimir Zyuzin. “Spin torque and Nernst effects in Dzyaloshinskii-Moriya ferromagnets”. In: *Phys. Rev. B* 93 (16 Apr. 2016), p. 161106. DOI: 10.1103/PhysRevB.93.161106.

[92] P. G. de Oliveira and A. S. T. Pires. *Magnon Hall effect in antiferromagnetic lattices*. 2023. arXiv: 2305.09077 [cond-mat.str-el].

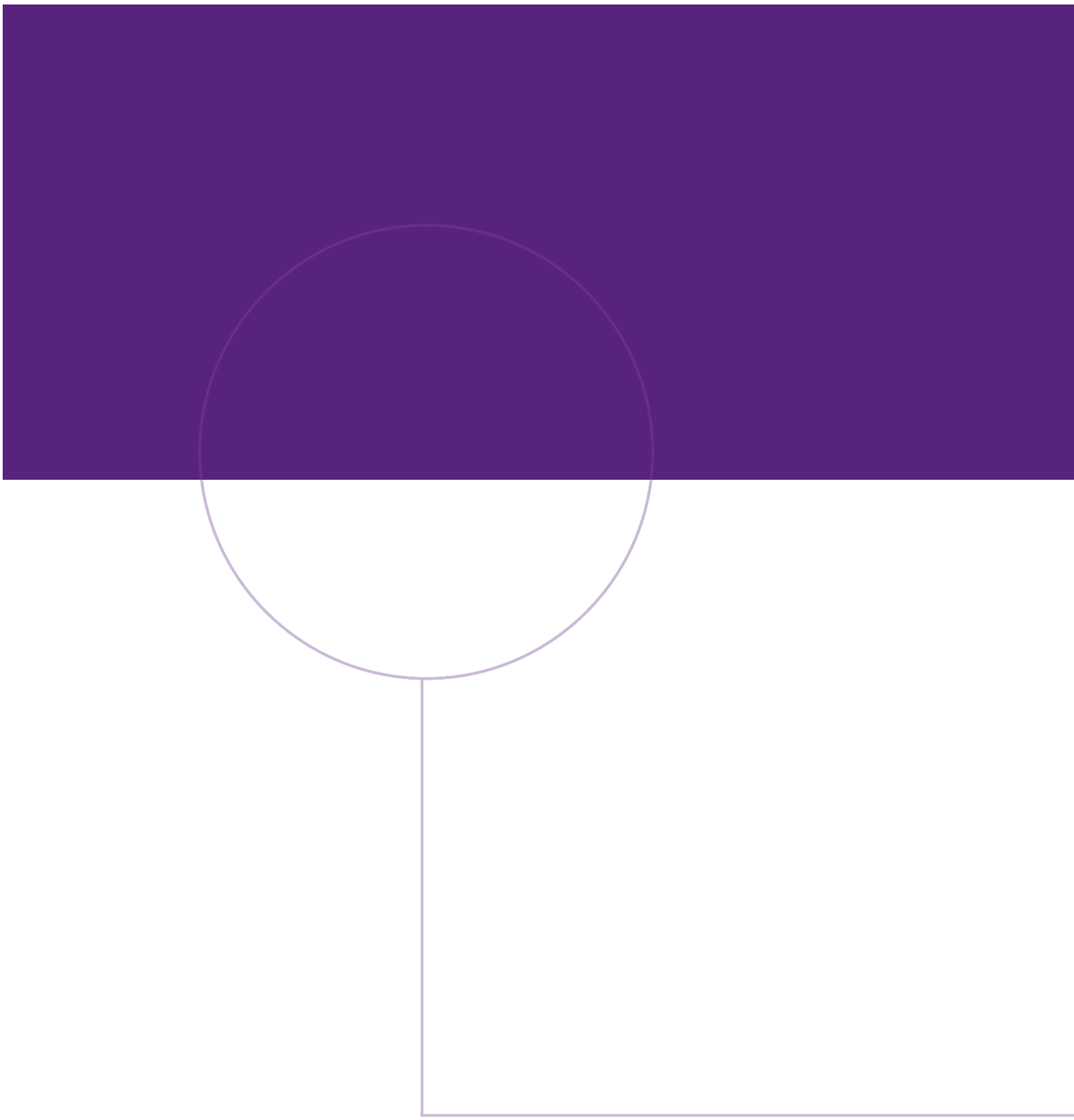

NTNU

Norwegian University of
Science and Technology